issn 0424-7116
An open-access journal by the German Quaternary Association
Editor-in-chief: Christopher Lüthgens

E&G

Quaternary Science Journal

Eiszeitalter und Gegenwart

Special issue

Connecting disciplines – Quaternary archives and geomorphological processes in a changing environment (proceedings of the Central European Conference on Geomorphology and Quaternary Sciences)

Guest editors: Johanna Lomax, Thomas Kolb and Markus Fuchs

Copernicus Publications
The Innovative Open Access Publisher

E&G Quaternary Science Journal

An open-access journal of the German Quaternary Association

E&G Quaternary Science Journal (EGQSJ) is an interdisciplinary open-access journal, which publishes peer-reviewed articles, express reports, and thesis abstracts covering the broad range of Quaternary research. It was established under the name "Eiszeitalter & Gegenwart" (i.e. "ice age and present" in German) in 1951. By linking insights from the past (i.e. the ice age) with the present, our publications provide an interdisciplinary understanding and knowledge that becomes even more important in the context of the current challenges of global climate change. EGQSJ is a non-profit, community-based effort: It is run by Quaternary scientists, financed by Quaternary scientists, and supporting Quaternary scientists, because any revenue generated is only used to support publications in the journal.

Copernicus Publications
The Innovative Open Access Publisher

Copernicus Publications
Bahnhofsallee 1e
37081 Göttingen
Germany

Phone: +49 551 90 03 39 0
Fax: +49 551 90 03 39 70

publications@copernicus.org
https://publications.copernicus.org

Printed in Germany.
Schaltungsdienst Lange o.H.G.

ISSN 0424-7116

Published by Copernicus GmbH (Copernicus Publications) on behalf of the German Quaternary Association (DEUQUA).

Image credit:
The river Elbe near Rathen, Saxony (Germany), deeply incised into Cretaceous sandstone, Markus Fuchs, 2016, all rights reserved

E&G Quaternary Sci. J., 68, 241–242, 2020
https://doi.org/10.5194/egqsj-68-241-2020

Open Access E&G Quaternary Science Journal

Preface: Introduction to the special issue "Connecting disciplines – Quaternary archives and geomorphological processes in a changing environment (proceedings of the Central European Conference on Geomorphology and Quaternary Sciences)"

Johanna Lomax, Thomas Kolb, and Markus Fuchs

Department of Geography, Justus Liebig University Giessen, Senckenbergstr. 1, 35390 Giessen, Germany

Correspondence: Johanna Lomax (johanna.lomax@geogr.uni-giessen.de)

Relevant dates: Published: 16 January 2020

How to cite: Lomax, J., Kolb, T., and Fuchs, M.: Preface: Introduction to the special issue "Connecting disciplines – Quaternary archives and geomorphological processes in a changing environment (proceedings of the Central European Conference on Geomorphology and Quaternary Sciences)", E&G Quaternary Sci. J., 68, 241–242, https://doi.org/10.5194/egqsj-68-241-2020, 2020.

This special issue contains five scientific papers, which were presented at the "Central European Conference on Geomorphology and Quaternary Sciences", held in Giessen (Germany) in September 2018. The conference was organized by the German Association on Geomorphology (AKG – Deutscher Arbeitskreis für Geomorphologie) and the German Quaternary Association (DEUQUA – Deutsche Quartärvereinigung) and was hosted by the Department of Geography at the Justus Liebig University Giessen.

The aim of the conference was to bring together the closely related fields of geomorphology and Quaternary sciences under the guiding theme "Connecting Disciplines". The necessity of connecting the two disciplines arises from the fact that Quaternary deposits, accumulated thousands or hundred thousands of years ago, can only be understood if the geomorphological processes forming these deposits are known. Vice versa, today's geomorphological processes are often a reorganization of Quaternary (or older) sediments. Therefore, the Quaternary history of deposits and landforms needs to be considered when studying recent morphodynamics. Further sessions of the conference concentrated on geoarchaeology and on recent methodological advances.

Over 260 scientists from 19 different countries participated in the meeting, presenting cutting-edge research from both disciplines as keynote lectures, talks and posters. Student prizes for best oral presentations were awarded to Stefanie Tofelde (Potsdam) for her talk on "Effects of deep-seated versus shallow hillslope processes on cosmogenic ^{10}Be concentrations in fluvial sand and gravel" and to Anna Schoch (Bonn) for her talk on "Outsize fan evolution – internal structure and influence on the upper Rhone Valley, Switzerland". Two prizes for best poster presentations were handed over to Sebastian Kreutzer (Bordeaux) for his poster on "The Mousterian Loess Sequence La Combette (France): Chronological Evidence of Rapid Environmental Changes in the MIS 4/3 Transition" and to Janek Walk (Aachen) for his poster on "The Guanillos fan complex – implications for the morphogenesis of Atacama's coastal alluvial fans".

Following the guiding theme of the conference, this special issue assembles papers from geomorphology, Quaternary sciences and geoarchaeology. Von Scheffer et al. (2019) reconstruct palaeoenvironmental change and human impact recorded in the Kleinwalser Valley (northern Central Alps, Austria), using X-ray fluorescence (XRF), pollen analysis,

and radiocarbon chronologies. They identify the first anthropogenic impact at around 5700 to 6300 BP, large-scale deforestation during the mid to late Bronze Age, and the arrival of the Walser people after around 1300 CE. Tinapp et al. (2019) investigate sediments from the lower Pleiße river in Saxony (Germany) using archaeological finds, plant remains, micromorphological and geochemical analysis and radiocarbon dating. They detect a prominent mid-Holocene black clay horizon, underlain by a sedge peat of Boreal and Preboreal age, as well as Weichselian sands. From 400 BCE onwards, overbank fines dominate, testifying land clearance activities, which intensified further during the Middle Ages. Marr et al. (2019) present ^{10}Be surface exposure ages of bedrock and boulder samples from southern Norway. These ages indicate an onset of deglaciation of the Scandinavian ice sheet at around 13 ka in southwestern Norway. The paper of Schellmann et al. (2019) focusses on electron spin resonance (ESR) dating of small gastropod shells in order to establish a chronology of Pleistocene gravel terraces from valleys in the Bavarian Alpine Foreland. Their results match the stratigraphy very well and agree well with luminescence ages where available, showing the high potential of ESR dating for constraining the age of Pleistocene fluvial deposits. Dietze and Dietze (2019) use end-member modelling analysis (EMMA) of grain size distributions in order to decipher grain size populations and infer sedimentary histories. They provide R protocols for a robust EMMA and present tests of their model on a synthetic data set of natural sediment types such as loess, dunes and floodplain deposits.

References

Dietze, E. and Dietze, M.: Grain-size distribution unmixing using the R package EMMAgeo, E&G Quaternary Sci. J., 68, 29–46, https://doi.org/10.5194/egqsj-68-29-2019, 2019.

Marr, P., Winkler, S., Binnie, S. A., and Löffler, J.: ^{10}Be-based exploration of the timing of deglaciation in two selected areas of southern Norway, E&G Quaternary Sci. J., 68, 165–176, https://doi.org/10.5194/egqsj-68-165-2019, 2019.

Schellmann, G., Schielein, P., Rähle, W., and Burow, C.: The formation of Middle and Upper Pleistocene terraces (Übergangsterrassen and Hochterrassen) in the Bavarian Alpine Foreland – new numeric dating results (ESR, OSL, 14C) and gastropod fauna analysis, E&G Quaternary Sci. J., 68, 141–164, https://doi.org/10.5194/egqsj-68-141-2019, 2019.

Tinapp, C., Heinrich, S., Herbig, C., Schneider, B., Stäuble, H., Miera, J., and von Suchodoletz, H.: Holocene floodplain evolution in a central European loess landscape – geoarchaeological investigations of the lower Pleiße valley in NW Saxony, E&G Quaternary Sci. J., 68, 95–105, https://doi.org/10.5194/egqsj-68-95-2019, 2019.

von Scheffer, C., Lange, A., De Vleeschouwer, F., Schrautzer, J., and Unkel, I.: 6200 years of human activities and environmental change in the northern central Alps, E&G Quaternary Sci. J., 68, 13–28, https://doi.org/10.5194/egqsj-68-13-2019, 2019.

E&G Quaternary Sci. J., 68, 13–28, 2019
https://doi.org/10.5194/egqsj-68-13-2019

Open Access E&G Quaternary Science Journal

Research article

6200 years of human activities and environmental change in the northern central Alps

Clemens von Scheffer[1,2], **Annika Lange**[1], **François De Vleeschouwer**[2,3], **Joachim Schrautzer**[1], **and Ingmar Unkel**[1]

[1]Institute for Ecosystem Research, Christian-Albrechts University, Olshausenstraße 75, 24118 Kiel, Germany
[2]EcoLab/Campus Ensat, Toulouse INP, Avenue de l'Agrobiopole, 31326 Castanet-Tolosan, France
[3]Instituto Franco-Argentino para el Estudio del Clima y sus Impactos (UMI IFAECI/CNRS-CONICET-UBA) Dpto. de Ciencias de la Atmosfera y los Oceanos, FCEN, Universidad de Buenos Aires Intendente Guiraldes 2160, Ciudad Universitaria (C1428EGA) Ciudad Autónoma de Buenos Aires, Argentina

Correspondence: Clemens von Scheffer (cscheffer@ecology.uni-kiel.de)

Relevant dates: Received: 19 December 2018 – Revised: 18 March 2019 – Accepted: 3 April 2019 – Published: 8 May 2019

How to cite: von Scheffer, C., Lange, A., De Vleeschouwer, F., Schrautzer, J., and Unkel, I.: 6200 years of human activities and environmental change in the northern central Alps, E&G Quaternary Sci. J., 68, 13–28, https://doi.org/10.5194/egqsj-68-13-2019, 2019.

Abstract: In this study, we combine erosion and anthropogenic proxies (Ti, Pb) from calibrated portable XRF with pollen and radiocarbon chronologies in peat from mires of the Kleinwalser Valley (Kleinwalsertal, Vorarlberg, Austria) to reconstruct palaeoenvironmental change and human impact in the northern central Alps. Favoured by a wetter climate, two analysed mires formed 6200 years ago in a densely forested valley. Landscape opening suggests that the first anthropogenic impact emerged around 5700 to 5300 cal BP. Contemporaneously, lead enrichment factors (Pb EFs) indicate metallurgical activities, predating the earliest archaeological evidence in the region. Pollen and erosion proxies show that large-scale deforestation and land use by agro-pastoralists took place from the mid- to late Bronze Age (3500 to 2800 cal BP). This period was directly followed by a prominent peak in Pb EF, pointing to metallurgical activities again. After 200 cal CE, a rising human impact was interrupted by climatic deteriorations in the first half of the 6th century CE, probably linked to the Late Antique Little Ice Age. The use of the characteristic Pb EF pattern of modern pollution as a time marker allows us to draw conclusions about the last centuries. These saw the influence of the Walser people, arriving in the valley after 1300 cal CE. Later, the beginning of tourism is reflected in increased erosion signals after 1950 cal CE. Our study demonstrates that prehistoric humans were intensively shaping the Kleinwalser Valley's landscape, well before the arrival of the Walser people. It also demonstrates the importance of palaeoenvironmental multiproxy studies to fill knowledge gaps where archaeological evidence is lacking.

Kurzfassung: In dieser Studie kombinieren wir Paläoproxies für Erosion und menschliche Aktivitäten (Ti, Pb) aus Messungen eines mobilen RFA- bzw. XRF-Analysators mit Pollen und Radiokohlenstoffdatierungen in Torfproben aus Mooren des Kleinwalsertals (Vorarlberg, Österreich). Auf diese Weise sollen der Wandel der Paläoumweltbedingungen sowie der Einfluss des Menschen auf die Landschaft der nördlichen Zentralalpen untersucht werden. Begünstigt durch feuchteres Klima, begann vor ca. 6200 Jahren im damals dicht bewaldeten Tal die Torfbildung in zwei der untersuchten Moore. Au-

flichtungen des Waldes deuten auf den ersten menschlichen Einfluss zwischen cal B.P. 5700 und 5300 hin. Gleichzeitig suggerieren Bleianreicherungen (Pb EF) metallurgische Aktivitäten, die weit vor jeglichen archäologischen Beweisen in der Region liegen. Pollen und Erosionsproxies bezeugen eine weitläufige Entwaldung und Landnutzung durch Landwirtschaft und Beweidung in der mittleren und späten Bronzezeit (3500 bis 2800 cal B.P.). Dieser Phase folgte ein vorläufiger Höchstwert des Pb EF zum Beginn der Eisenzeit, der erneut auf Bergbau oder Metallurgie in der näheren Umgebung hindeutet. Eine im cal A.D. 3. Jahrhundert einsetzende verstärkte Landnutzung wird im cal A.D. 6. Jahrhundert unvermittelt durch klimatisch ungünstigere Bedingungen unterbrochen, welche der sogenannten spätantiken kleinen Eiszeit zugeschrieben werden können. Unter Zuhilfenahme des charakteristischen Verlaufs der modernen Bleiemissionen als Zeitmarker, konnten die Analyseergebnisse der letzten Jahrhunderte eingeordnet werden. Diese waren von der Ansiedlung der Walser im cal A.D. 14. Jahrhundert geprägt. Nach cal A.D. 1950 zeigt sich außerdem der erstarkende Tourismus anhand höherer Erosionsspuren. Unsere Ergebnisse machen deutlich, dass die Landschaft des Kleinwalsertals schon weit vor Ankunft der Walser vom Menschen genutzt und verändert wurde. Unsere Studie betont zudem die Wichtigkeit der Anwendung unterschiedlicher Paläoproxies, insbesondere, wenn archäologische Anhaltspunkte zur Landnutzungsgeschichte fehlen.

1 Introduction

Humans have been recurringly present in Alpine environments since the last deglaciation (e.g. Cornelissen and Reitmaier, 2016). These harsh landscapes are heterogeneous and sensitive to climate (Barry, 2002), which requires specific human adaptation (Clegg et al., 1970). Half nomadic lifestyles or transhumance have been strategies to survive, and are still today the basis for seasonal livestock management practice in mountainous regions (e.g. Reitmaier et al., 2018). There is however no consensus on the human colonisation of European mountains during the Holocene. In the Alps, the onset of human impact is still not fully understood because occupation pulses were radiating from different regions and societies at different time periods (e.g. Bätzing, 2015; Carcaillet, 1998; Dietre et al., 2017; Oeggl and Nicolussi, 2009; Valese et al., 2014). It is therefore important to document human occupation and its impact on mountain environments to a certain level of detail, as each region or each valley reveals pieces of information on the complex spatial linkages between humans and environmental and climatic conditions.

Another challenge in reconstructing past human impacts in the Alps is the general scarcity of suitable palaeoenvironmental archives in high mountain areas. Archaeological records and historical sources cannot provide continuous information and may bias interpretations towards separate findings. These gaps are generally closed by environmental archives, such as trees, lakes, glaciers or mires, which potentially provide uninterrupted records of past environmental changes (anthropogenic or natural). However, except for pollen or dendrochronological studies, mountain mires are so far rarely used as environmental archives.

In this paper, we present a multiproxy study of the Kleinwalser Valley (Kleinwalsertal) in the Austrian northern central Alps, using small mountain mires as environmental archives. The valley is historically known for its human occupation, animal husbandry and forestry only since the Late Middle Ages (Fink and von Klenze, 1891; Wagner, 1950). Before that, the human impact on this valley is unclear. While Romans were present in the Alpine foreland (Mackensen, 1995; Weber, 1995), there are no records of their presence in the valley. Palaeovegetation information suggests prehistoric land use (Dieffenbach-Fries, 1981; Grosse-Brauckmann, 2002) but chronologies and data are limited. Other evidence points to early activities at archaeological sites in the valley (Bachnetzer, 2017; Gulisano, 1994, 1995; Leitner, 2003), which are located close to our study sites (Fig. 1). These spots may have acted as strategic points between Alpine foreland and the surrounding mountain ranges, leading prehistoric humans to cross and occupy the Kleinwalser Valley.

By combining geochemical and palynological data together with radiocarbon chronologies, we aim at better understanding the points in time and impacts of human occupation in the Kleinwalser Valley's landscape and beyond. We also aim at detecting early metallurgical activities, possibly where archaeological evidence is lacking. By looking into the past, using multiple proxies on chronologically constrained peat sequences from a key area, we provide new insights into the development and interaction of landscape, climate and humans from mid-Holocene to modern times in the northern central Alps.

2 Study sites

The Kleinwalser Valley belongs to the federal state of Vorarlberg in the north-western part of Austria (Fig. 1) and is located at the junction of the geological units of the Northern Calcareous Alps, Penninic flysch and Helvetic (Völk, 2001). The valley floor elevates around 1100 m a.s.l. and is

surrounded by mountains ranging from 2000 to 2500 m a.s.l. Geologically speaking, the watershed is composed of calcareous as well as silicate rocks. During the late Pleistocene, the valley was glaciated (Völk, 2001) and several moraines are still present. Iron (Fe), lead (Pb), zinc (Zn) and copper (Cu) ores are present outside the valley. Within 20 km N-NE, iron had been exploited since 1471 CE in Sonthofen (Merbeler, 1995). Pb–Zn deposits are known to the NE at Himmelschrofen (Fig. 1) (von Gümbel, 1861) and in the Ostrach Valley since 1620 cal CE (Oblinger, 1996). To the south, Zn–Pb deposits exist at Zug, at St. Anton at Arlberg, and at St. Christoph at Arlberg and Cu can be found at Bartholomäberg (Weber, 1997) within 35 km off the lower Kleinwalser Valley.

A temperate climate in the Kleinwalser Valley is reflected by a mean annual temperature of 5.7 °C and 1863 mm of mean annual precipitation (HDÖ, 1994). In combination with impermeable sediments of glacial or postglacial lacustrine origin, these climate conditions foster the development of many mires in the valley (Schrautzer et al., 2019; El Balti et al., 2017; Völk, 2001).

The main study site, Hoefle Mire (HFL, GPS: 47°21′52.5″ N, 10°10′37.2″ E, Fig. 1), is at an elevation of 1020 m a.s.l. and in immediate proximity of the early Mesolithic archaeological site "Egg" (Bachnetzer, 2017) (Fig. 1a) on a small rise almost in the middle of the valley bottom. Its sheltered position between the rivers Breitach and Schwarzwasser protects it from both river erosion and direct sediment input from the mountainsides. Therefore, this mire is a suitable archive to record atmospheric signals, undisturbed by small-scale processes. The current vegetation consists of typical bog species such as *Sphagnum* spp., *Eriophorum vaginatum* and several species of the family *Ericaceae*. Glacial ground moraine material and localised lake clays form the underlying sediment (Zacher, 1990). Mowing and a drainage ditch, accompanied by a gravelled hiking road, affect the mire at present.

A second study site, the Ladstatt Mire (LAD, GPS: 47°21′28.1″ N, 10°09′26.9″ E), is situated at a distance of 1.7 km to the south-west of Hoefle Mire at 1140 m a.s.l., just at the foot of a forested slope (Küren Valley) to the Gottesacker plateau and downhill of the archaeological site "Schneiderkürenalpe" (Fig. 1b). This slope is characterised by almost no surface runoff. All precipitation disappears into the karstic underground (Goldscheider, 1998). LAD is comparable to HFL in terms of size and surface vegetation, although *Sphagnum* is more dominant. A road with ditches separates the mire from the valley's slope.

A third peat profile at "Halden-Hochalpe" (HHA, GPS: 47°20′18.3″ N, 10°03′49.2″ E) (Fig. 1) was only surveyed in 2017. The HHA mire developed on a sediment-filled glacial cirque form (de Graaff et al., 2003) at 1660 m a.s.l. The uppermost Subersach River meanders through the peatland, which allowed sampling of the bottom of the profile to date the onset of peat formation.

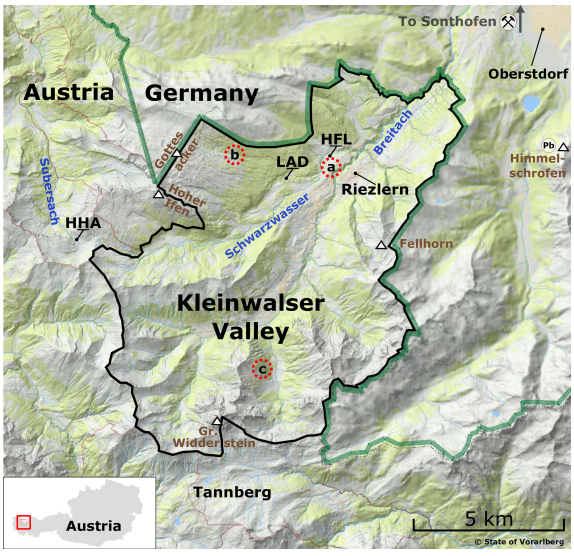

Figure 1. The Kleinwalser Valley and surrounding areas. Archaeological sites (red dotted circles): Egg **(a)**, Schneiderkürenalpe **(b)**, Neolithic flint mine **(c)**. Sampled mire sites: Hoefle Mire (HFL), Ladstatt Mire (LAD), Halden-Hochalpe (HHA). Mountains (white triangles). Modified from data source: state of Vorarlberg – http://data.vorarlberg.gv.at (last access: 6 October 2018).

3 Methods

3.1 Coring and sampling

Field sampling was performed in early August 2016 in the centre of HFL. A peat sequence of 240 cm was recovered in three parallel, overlapping cores (B, C, D) using a Russian peat corer with a chamber of 5 cm in diameter. Additionally, a 10 × 10 × 30 cm monolith of the topmost part was sampled with a serrated ceramic blade, to avoid compression in the fibrous living part of the acrotelm. Similarly, we recovered an 83 cm long sediment core and a 28 cm monolith at LAD. All cores and monoliths were wrapped into cling film, transferred to PVC half-tubes in closed plastic hoses and stored at 3 °C. At HHA, only a charred wood sample was collected for ^{14}C dating, just below the bottom peat layers.

After freezing the cores for 2 d at −18 °C, each of the sections was cut into 1 cm thick slices with a stainless-steel band saw. Subsamples of every slice were cut with ceramic knives, stored in ziplock bags and frozen again. Contamination was minimised following cutting protocols by De Vleeschouwer et al. (2010a) and Givelet et al. (2004). The dimensions of the subsamples dedicated to geochemistry were measured with a Vernier calliper. These were then freeze-dried and weighed to obtain dry bulk density. To cover the gap between the first two core sections in HFL, an overlapping part of core (C) was subsampled and fitted to the main core (B) by using dry bulk density and element concentration profiles.

3.2 Radiocarbon dating and chronology

Sphagnum stems and leaves were selected for radiocarbon dating from fresh samples in ultrapure water. When *Sphagnum* was absent (in deeper/more decomposed peat layers), other plant remains (*Eriophorum* spindles, seeds, *Ericaceae* leaves, wood) as well as bulk peat were selected and sent to Poznan AMS Radiocarbon Laboratory (Poland). The calibrated ages (Table 1) and age–depth models (Fig. 2) were produced in R, version 3.4.2 (R Core Team, 2017), by using the packages clam version 2.3.2 (Blaauw, 2010) and rbacon version 2.3.3 (Blaauw and Christen, 2011). Both packages work with the IntCal13 radiocarbon calibration curve (Reimer et al., 2013). Unless denoted otherwise, ages are given as calibrated before present (cal BP, i.e. years before 1950) for prehistoric times. For a more convenient comparison to historical sources, interpretations for the last 2000 years are made in cal CE. The classification of cultural periods was performed based on the study of Roepke and Krause (2013).

3.3 Pollen analysis

A volume of 2 mL was taken from 14 peat samples of cores HFL-B and HFL-C in the overlapping section and prepared for pollen analysis, following the method described by Moore et al. (1991). The material was pretreated in separate steps in 10 % HCl and 10 % KOH to get rid of carbonates and humic substances. Macro remains were removed with a 200 µm mesh. The sample was first cooked for 4 min in a 9 : 1 solution of acetic anhydride and concentrated sulfuric acid and centrifuged. Particles below 6 µm were removed with ultrasonic sieving. The absence of siliciclastic sediment layers in the analysed samples made the use of HF obsolete. Pollen were counted to a sum of 200 tree pollen (excluding *Corylus*). Fern spores without perine were counted as indeterminate pteridophytes. The counts were compiled with Tilia version 2.0.60 (Grimm, 2018).

3.4 Geochemistry

This study concentrated on calcium (Ca), lead (Pb) and titanium (Ti) for interpretation. While Ca can yield information on the trophic state of a mire, Ti can be used as an erosion or human impact proxy (Hölzer and Hölzer, 1998). Pb often originates from anthropogenic sources when it exceeds its natural background (e.g. Weiss et al., 1999). Using portable X-ray fluorescence spectrometry (pXRF) on peat samples in palaeoenvironmental research has rarely been done so far and is hence not well understood, despite some studies that were assessing its general potential (Kalnicky and Singhvi, 2001; Mejía-Piña et al., 2016; Shand and Wendler, 2014; Shuttleworth et al., 2014). Therefore, a regression analysis was conducted to evaluate and calibrate the semi-quantitative pXRF by several parallel quantitative measurements with inductively coupled plasma mass spectrometry (ICP-MS). In HFL-B and HFL-C, a total of 187 and 51 samples were selected for pXRF scanning and ICP-MS analyses, respectively. A total of 62 samples were selected from the LAD core for pXRF scanning. The samples were transferred into Falcon tubes together with eight glass beads (4 mm) and ground 3×20 s using a FastPrep-24® mixer at maximum speed.

Samples dedicated to pXRF were transferred into 12.5 mL polypropylene vials, closed with Fluxana TF-240-255 film and rubber band. All samples were measured using a Thermo Fisher Niton XL3t pXRF equipped with an Au anode and a 50 kV X-ray tube. The predefined "soil mode" was used with 180 s of measurement time each for the main and low filter, which is 60 s above the minimum duration recommended by Shuttleworth et al. (2014). Every sample was measured at least three times and shaken after each scan to control the reproducibility of measurements (precision). In addition to the Certified Reference Materials (CRM) used with ICP-MS (see below), BCR-060 (aquatic plants), IAEA-336 (lichen), IPE-176 (reed/*Phragmites*) and NIST-1575a (pine needles) were scanned. Table 2 shows the quality control of pXRF. Estimated standard sample deviations (SD) based on n repeated measurements remained mostly below or around 10 %. Only for Ti, did a higher SD of 18.8 % occur in NJV941. All three elements were above the certified concentrations.

Samples dedicated to ICP-MS were digested using HNO_3, HF and H_20_2 in a class 100 clean room following the protocol of Vanneste et al. (2015). Depending roughly on the dry bulk density of the peat sediment sample, the final aliquots were diluted to total factors between 2500 and 28 500. To verify the analytical quality, precision and accuracy of the ICP-MS results, the CRMs (GBW-07603 bush branches and leaves, NIST-1515 apple leaves, NIST-1547a peach leaves, NJV-941 *Carex*/sedge peat, NJV-942 *Sphagnum* peat) were digested and measured along with the samples. Procedural blanks were added to monitor possible contamination or systematic errors. Measurements were performed on an Agilent 7500 CE at Observatoire Midi-Pyrénées, Toulouse, France. The internal ICP-MS calibration with a multi-element standard was run every 10th sample. Measured concentrations were within 11 % of the certified values (Table 3). Only NJV941 deviated more than 10 % for Ca and Pb.

4 Results

4.1 Age–depth model

Median ages were extracted from the age–depth model for further interpretation. The accumulation rates for the model of each core were calculated as the median of 1000 estimates by rbacon for each depth. In the lowermost 60 cm of HFL, an accumulation of almost 0.9 mm a^{-1} is observed (Fig. 2), while rates of 0.3 to 0.6 mm a^{-1} prevailed up to 37 cm in depth. The following section of 12 cm was characterised by a very low accumulation of 0.2 to 0.1 mm a^{-1} and comprised almost 900 years. In contrast, accumulation or growth

Table 1. List of radiocarbon samples including information about origin, depth, dated material, ^{14}C ages and calibrated ages within a 95 % confidence interval (probabilities < 1 % excluded).

Lab. no.	Site	Depth (cm)	Material	^{14}C age (BP)	Cal age (BP)	Comment
Poz-101727	HFL	21.3	*Sphagnum* stems and leaves, few *Eriophorum* spindles	127 ± 0.35 pMC	−32 to −29.9 (80.8 %) −12.1 to −12 (4.2 %) −9.7 to −9.4 (10 %)	
Poz-104865	HFL	29.9	*Eriophorum* spindles, *Sphagnum* stems and leaves	65 ± 30	31–138 (71.4 %) 222–257 (23.5 %)	0.5 mg C
Poz-92252	HFL	36.0	*Eriophorum* spindles	1110 ± 30	939–959 (1.4 %) 951–1071 (93.5 %)	0.7 mg C
Poz-101728	HFL	48.3	*Sphagnum* stems and leaves, *Eriophorum* spindles	1525 ± 30	1348–1424 (55.6 %) 1428–1444 (4.3 %) 1454–1522 (34.9 %)	
Poz-92255	HFL	80.0	*Sphagnum* leaves	2410 ± 30	2351–2496 (81.2 %) 2596–2612 (2.9 %) 2637–2684 (10.9 %)	
Poz-92251	HFL	120.3	*Sphagnum* stem, *Eriophorum* remains	3065 ± 35	3180–3200 (4.6 %) 3206–3363 (90.4 %)	
Poz-86728	HFL	152.0	Bulk peat	4105 ± 35	4453–4461 (1 %) 4521–4713 (70.5 %) 4753–4814 (22.7 %)	
Poz-96113	HFL	176.7	Wood and *Eriophorum* remains,	4710 ± 40	5322–5419 (46.4 %) 5439–5486 (20.8 %) 5507–5581 (27.6 %)	
Poz-92253	HFL	202.0	Ligneous material, wood	2730 ± 35	2759–2883 (93.5 %) 2911–2918 (1.5 %)	Excluded outlier, 0.2 mg C
Poz-86726	HFL	235.0	Wood	5330 ± 40	5996–6208 (93.9 %) 5254–6260 (1 %)	
Poz-86729	HFL	175.0	Bulk peat	4400 ± 35	4860–5054 (91 %) 5190–5256 (3.3 %)	Core D
Poz-95963	HHA	∼ 145.0	Charred wood, tree age outer age ring, > 50	3195 ± 35	3357–3479 (94.8 %)	
Poz-99319	LAD	24.8	*Sphagnum* stems and leaves	127.74 ± 0.37 pMC	−32 to −29.3 (81.9 %) −12.1 to −12 (5.8 %) −9.7 to −9.4 (7.3)	0.7 mg C
Poz-103202	LAD	31.2	*Eriophorum* spindles	40 ± 30	−5 to 2 (6.9 %) 32–83 (52.1 %) 97–108 (3 %) 112–137 (13.8 %) 223–255 (19 %)	0.8 mg C
Poz-99198	LAD	63.5	*Eriophorum* spindles	3185 ± 35	2253–3475 (95 %)	
Poz-86730	LAD	102.5	Bulk peat	5320 ± 40	5991–6210 (93.5 %) 6250–6262 (1.5 %)	

Table 2. Repeated pXRF measurements (n) of Ca, Pb and Ti versus certified (Cert.) concentrations in organic Certified Reference Materials (CRM). Sample standard deviations (SDs) from certified values as a percentage.

Element	Ca				Pb				Ti			
Value Unit	Cert. (mg kg^{-1})	pXRF (mg kg^{-1})	SD (%)	n	Cert. (mg kg^{1})	pXRF (mg kg^{-1})	SD (%)	n	Cert. (mg kg^{1})	pXRF (mg kg^{-1})	SD (%)	n
BCR060	–	54 013	2.0	8	64	92.5	4.3	8	–	280.5	11.6	8
GBW07603	16 800	42 761	0.4	5	47	73.7	3.0	5	95	214.4	4.1	5
IAEA336	–	8262	5.2	4	4.9	6.2	10.1	4	–	219.6	6.0	4
IPE176	4160	8736	6.1	5	8.24	13.4	8.7	5	–	1172.5	6.8	5
NIST1515	15 260	44 634	1.9	3	0.47	–	–	–	–	15.9	–	1
NIST1547a	15 600	41 795	0.1	3	0.87	–	–	–	–	18.7	0.1	2
NIST1575a	2500	8882	0.3	3	0.167	–	–	–	–	15.3	12.4	2
fNJV941	10 200	33 937	4.4	8	2.4	2.3	10.8	8	–	64.1	18.8	8
NJV942	1200	4024	2.5	6	10.1	14.3	3.4	6	–	262.0	2.9	6

Table 3. Quality control of Ca, Ti and Pb. Measurements by ICP-MS of procedural blanks and in organic Certified Reference Materials (CRM). Total deviations (Dev.) from certified values as a percentage.

CRM/blank	Ca			Ti			Pb		
	Cert.	ICP-MS	Dev.	Cert.	ICP-MS	Dev.	Cert.	ICP-MS	Dev.
	(mg kg^{-1})	(mg kg^{-1})	(%)	(mg kg^{-1})	(mg kg^{-1})	(%)	(mg kg^{-1})	(mg kg^{-1})	(%)
Blank 1	–	0.03	–	–	0.000	–	–	0.000	–
Blank 2	–	0.01	–	–	0.000	–	–	0.000	–
Blank 3	–	0.01	–	–	0.000	–	–	0.000	–
NIST1515 (a)	15 250	14 216	−6.8	–	13.3	–	0.47	0.44	−5.7
NIST1515 (b)	15 250	13 900	−8.8	–	12.4	–	0.47	0.49	3.7
GBW07603 (a)	16 800	16 143	−3.9	95	92.1	−3.0	47	47.32	0.7
GBW07603 (b)	16 800	16 696	−0.6	95	90.2	−5.1	47	48.60	3.4
NJV941 (a)	10 200	8766	−14.1	–	34.5	–	2.4	2.09	−13.1
NJV941 (b)	10 200	8743	−14.3	–	33.6	–	2.4	2.11	−11.9
NJV941 (c)	10 200	8689	−14.8	–	27.1	–	2.4	2.10	−12.6
NJV942 (a)	1200	1262	5.2	–	51.8	–	10.1	9.48	−6.1
NJV942 (b)	1200	1232	2.7	–	115.2	–	10.1	9.13	−9.6
NJV942 (c)	1200	1181	−1.6	–	49.6	–	10.1	9.48	−6.2
NIST1547a	15 600	14 652	−6.1	–	24.1	–	0.87	0.86	−1.1

rates of the topmost layers reached a maximum of more than 8 mm a^{-1}. The age–depth model of LAD (Fig. 2) had a net accumulation rate of only 0.15 mm a^{-1}. However, the model is less constrained than in HFL, with a modern age at 25 cm in depth and 3450 cal BP at 62 cm in depth. Especially in the uppermost 30 cm, peat growth took a development similar to HFL, with accumulation or growth rates reaching 9 mm a^{-1}.

4.2 Pollen profile

A detailed interpretation of the pollen record from HFL Mire (Fig. 3) is provided in the discussion below. We can, however, point out major changes in the pollen profile. The deepest part was strongly characterised by *Picea* pollen. A significant change is observed between 200 and 175 cm (5700 to 5300 cal BP) when deciduous forest pollen and herbs appeared. After tree pollen were dominating again at 140 cm (4000 cal BP), the sudden and strong signals of *Poaceae*, herbs and cultural plants illustrate a diversification in the spectrum between 125 and 115 cm (3450 to 3150 cal BP). The opposite trend started above, although the overall pattern did not return to a complete dominance of tree pollen. Only in the uppermost 37 cm (1000 cal CE), did *Poaceae*, herbs and cultural plants represent a larger proportion of the spectrum once again. In order to facilitate the interpretation of palynological data in the discussion, we have assembled pollen into six groups (Fig. 3): 1 – cultural and pastoral; 2 – open grassland; 3 – herbs and heather; 4 – forest border; 5 – swamp/wetland; 6 – ferns.

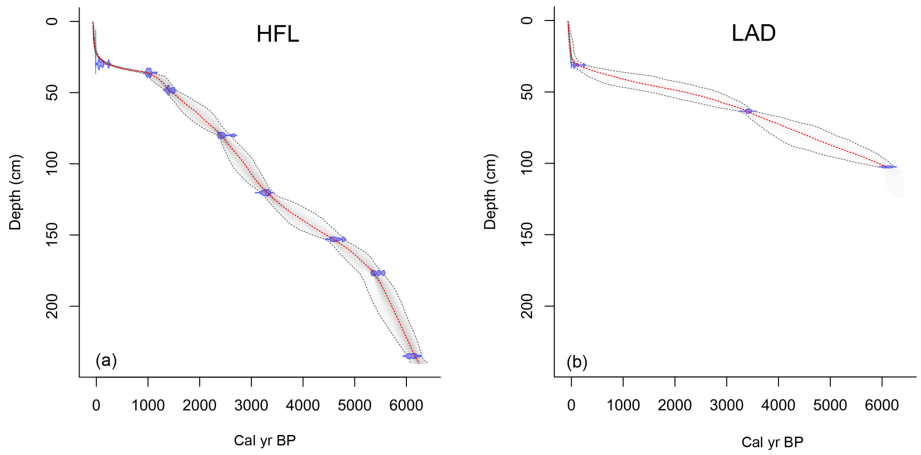

Figure 2. Age–depth models of Hoefle Mire **(a)** and Ladstatt Mire **(b)**. The median is plotted as a red dotted line amidst the confidence range of 95 % in grey.

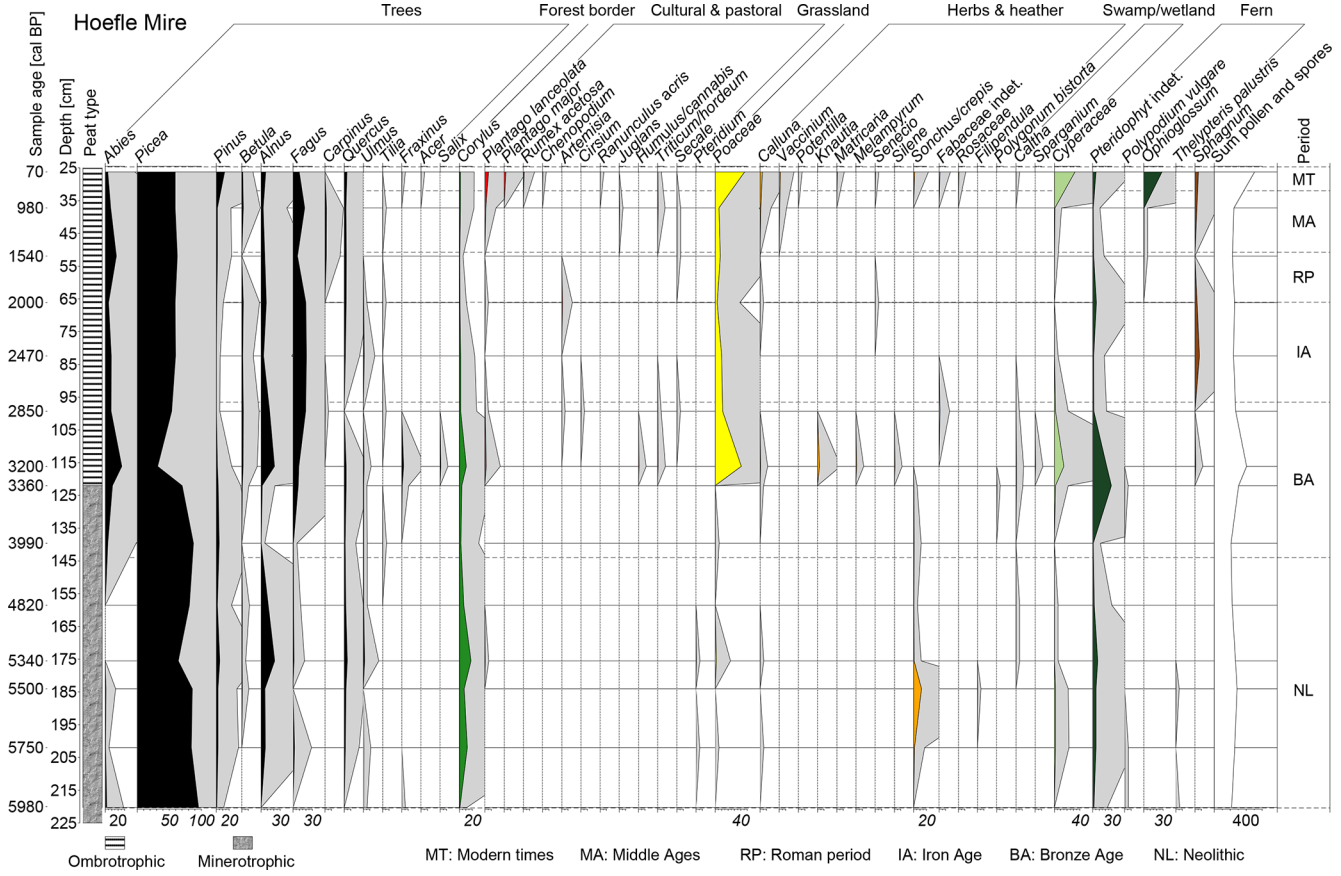

Figure 3. Pollen diagram of HFL Mire. Fully coloured profiles represent pollen percentages, shaded areas enhanced by factor 12. Black: trees; green: forest border (*Corylus*); yellow: open grassland (*Poaceae*); red: cultural and pastoral indicators; orange: herbs and heather; light green: swamp/wetland; dark green: fern; brown: *Sphagnum*; white: total spores and pollen. Vertical lines depict calibrated sample ages. Vertical dashed lines are boundaries of cultural periods.

4.3 Geochemistry

The quantitative and validated ICP-MS results of HFL were compared to the pXRF scans of the same sample, which allowed us to constrain our calibration. The regression analysis in the HFL peat samples showed high adjusted R^2 values or coefficient of determination (R^2), as a measure for the fit of the model ($R^2_{Ca} = 0.95$, $R^2_{Ti} = 0.97$, $R^2_{Pb} = 0.99$, Fig. 2). As the two deepest samples (240–230 cm) were composed of sediment and not peat, they plotted as outliers and were excluded. In the range of measured ICP-MS concentrations (Ca: 2000–14 000, Pb: 2–110 and Ti: 25–400 mg kg^{-1}), pXRF values were generally higher than the concentrations obtained by ICP-MS. Transfer functions were therefore calculated to calibrate the pXRF scans of all 187 samples (Fig. 4).

The element-specific overestimation of the pXRF output illustrates that this method cannot be used to quantify element concentrations in peat without a cross-calibration against quantitative methods. Specification and type of sample need to be considered during such a calibration. Shuttleworth et al. (2014) used a Niton XL3t with an Ag anode to evaluate the applicability of pXRF for Pb contents in peat. Their results suggested a linear relationship between pXRF and ICP-OES (optical emission spectrometry), which was confirmed in this study. However, their observed overestimation by pXRF was much lower and was attributed to an incomplete Pb extraction with aqua regia. As a complete digestion was performed in this study, the overestimation by pXRF for Pb cannot have a similar explanation. Additionally, the high content of light organic matter in peat should rather result in an underestimation of heavier elements in XRF analysis (Löwemark et al., 2011). Nevertheless, the regression analysis allowed us to generate quantitative results of Ca, Pb and Ti in both minerotrophic and ombrotrophic peat. The only exception was the measurement of mineral-rich bottom layer samples with a high element load, which plotted outside the linear regression.

The Pb enrichment factor (Pb EF) was calculated following (Weiss et al., 1999) using Ti as a conservative element, which is not affected by dissolution in acidic environments (Nesbitt and Markovics, 1997).

Here we used the background Pb/Ti ratio of the bottom sediment, measured by ICP-MS (0.0037), which is close to the generally used upper continental crust (UCC) value (0.004) from McLennan (2001). It is explained by the local geology consisting of limestone, marl and sandstone, resulting in a mixed weathering product.

$$\mathrm{Pb\,EF} = \frac{(\mathrm{Pb/Ti})_{\mathrm{sample}}}{(\mathrm{Pb/Ti})_{\mathrm{background}}}$$

Titanium originates from natural local erosion/sources and is therefore used as a human-impact proxy. Following Shotyk et al. (2002), we calculated a mineral accumulation rate (MAR) on the mires' surfaces in g m^{-2} a^{-1} with a Ti (UCC) of 0.41 %:

$$\mathrm{MAR} = 100/0.41 \times \mathrm{Ti} \times \delta \times \mathrm{pa},$$

where δ is the dry bulk density and pa is the peat accumulation rate.

The temporal variability of Ca, Pb EF and MAR shown in Fig. 5 is based on the calibrated pXRF concentrations, calibrated ages, densities and accumulation rates (tables in Supplement). Ca concentrations in HFL constantly declined towards the top. After a max. of 15 000 mg kg^{-1} in the deepest peat layers (6000 cal BP), they fell permanently below 6000 mg kg^{-1} after 122 cm (3250 cal BP). Above 62 cm (1950 cal BP) they decreased to a level below 3000 mg kg^{-1}.

The concentrations of Ti in HFL decreased from 1040 to around 50 mg kg^{-1} in the deepest 12 cm of the core (6250 to 6000 cal BP) and remained low until an increasing trend started above 133 cm (3700 cal BP), which culminated at 122 cm (3250 cal BP) with over 385 mg kg^{-1}. Although higher than in the lower half of the profile, concentrations returned to values between 40 and 110 mg kg^{-1} until an increasing trend, which was shortly interrupted around 48 cm (500 cal CE), started above 58 cm (200 cal CE). This trend turned after reaching 360 mg kg^{-1} at 32 cm (1500 cal CE) and ultimately came to a halt at the surface.

Excluding the deepest samples of HFL, Pb was below the detection limit from 230 to 190 cm (6250 to 5600 cal BP) and did not exceed 9 mg kg^{-1} until 98 cm in depth. From 97 to 91 cm (2800 to 2650 cal BP), concentrations rose to values around 25 mg kg^{-1}. From then on, Pb oscillated around 15 mg kg^{-1} until it increased between 50 and 20 cm (500 to 1970 cal CE) to a maximum of 115 mg kg^{-1}. Thereafter, the profile sharply dropped to 6 mg kg^{-1} within the next 7 cm and fell below the detection limit at the subsurface.

In the LAD core, Ti concentrations were above 1000 mg kg^{-1} until 85 cm in depth (4900 cal BP) and briefly dropped to 200 mg kg^{-1} at 78 cm (4800 cal BP). A peak, exceeding 1000 mg kg^{-1}, appeared at 61 cm (3200 cal BP), after which the profile stayed slightly below 600 mg kg^{-1}. The concentrations decreased from 34 cm to 20 cm in depth (1700–1982 CE) and continued to less than 30 mg kg^{-1} at the surface.

5 Discussion

5.1 Mire formation

Peat formation in HFL and LAD began around 6200 cal BP. Pollen proportions suggest a *Picea* swamp in a densely forested valley at 6000 cal BP, fitting well to the findings of Dieffenbach-Fries (1981). For the same period, other studies reported a wetter and colder climate in the central Alps (Haas et al., 1998; Van der Knaap et al., 2004; Wurth et al., 2004). The fine clayey sediment of a glacial till followed by gyttja at the bottom of both HFL and LAD indicates standing water

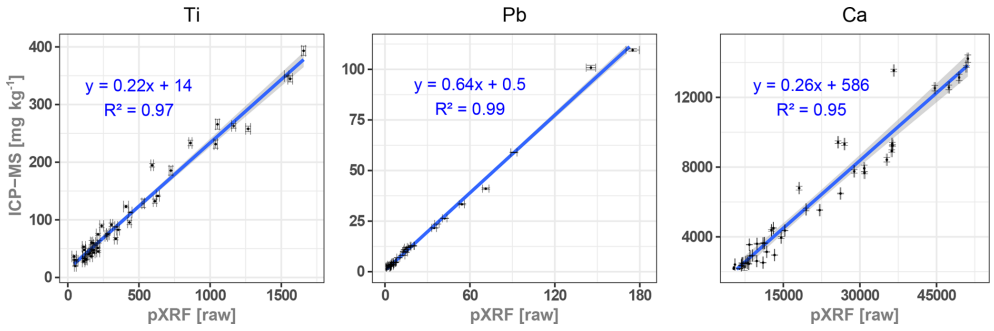

Figure 4. Cross-plots of measured concentrations of Ca, Ti and Pb with ICP-MS (mg kg^{-1}) versus measured values with pXRF (raw) for regression analyses.

conditions, which favoured peat formation. Land- or rockslides in the watershed (Schmidt-Thomé, 1960; Völk, 2001) could have resulted from a wetter climate as well and may have reorganised the valley's hydrology, which is very complex (Goldscheider, 1998). This could have further promoted mire formation in certain places, as suggested by Grosse-Brauckmann (2002).

5.2 5800 to 3500 cal BP: early human occupation

Only very little archaeological evidence suggests early human occupation in the area (Bachnetzer, 2017; Leitner, 2003). Similarly, little palaeoecological evidence exists on early local land use. Regional studies showed evidence for fire practices (Clark et al., 1989) and crop cultivation around Lake Constance (Jacomet, 2009; Rösch, 1992) and at Oberstdorf, north of the valley (Fig. 1) (Dieffenbach-Fries, 1981). In HFL, increasing *Poaceae* pollen and the presence of *Plantago* as well as the emergence of *Corylus* suggest anthropogenic landscape opening around 5550 cal BP. This interpretation is further strengthened by a significantly elevated erosion signal (MAR) in HFL. Prehistoric fire practices in the valley can be inferred from the presence of *Pteridium* and *Calluna*. While not dendrochronologically dated, a charred tree trunk was pierced (horizontally) at parallel depth in the parallel HFL-D core (not analysed in detail). Although the cause of this fire (anthropogenic or natural) cannot be deciphered, it supports the other indicators in suggesting prehistoric patchy land clearances, possibly for livestock grazing.

Almost simultaneously to the observed pollen signals in HFL, the Pb EF rose significantly to 50 at 5450 cal BP and remained around an average value of 22 until 3500 cal BP. While this elevated Pb EF period falls in the minerotrophic part of the core, several authors showed that Pb, an immobile element, could carefully be used as an anthropogenic indicator in minerotrophic peat (e.g. Baron et al., 2005; Shotyk et al., 2001). Archaeological evidence shows that metal tools were circulating in the central Alps (e.g. Artioli et al., 2017). Metallurgy was dominated by Cu at that time, but Pb can be present as an impurity (Höppner et al., 2005; Lutz and

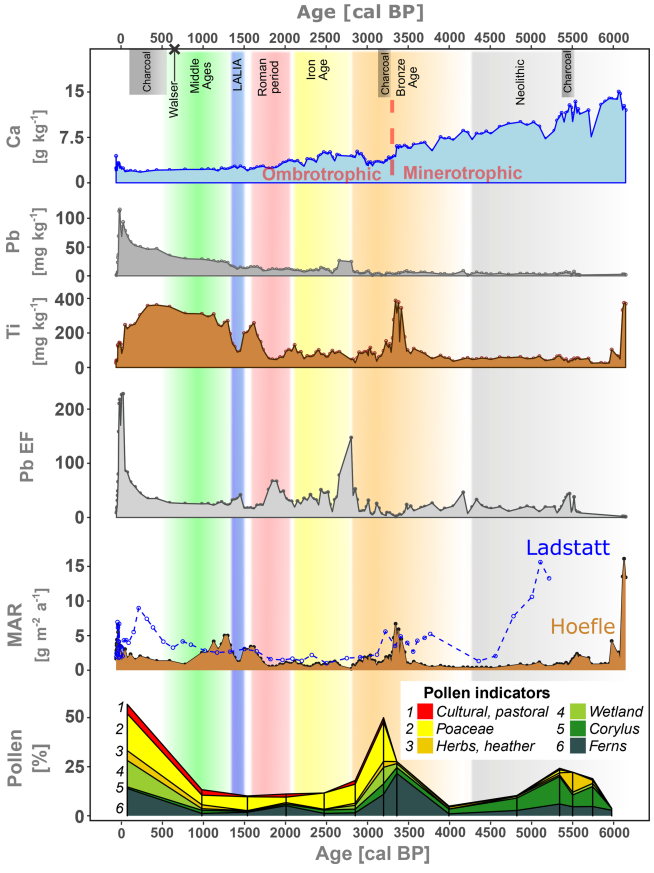

Figure 5. Chronological profile of Ca, Pb and Ti concentrations in HFL, Pb EF in HFL, and mineral accumulation rates (g m^{-2} a^{-1}) in HFL and LAD. Pollen groups as a percentage of total pollen (%) in HFL. Colours of shaded areas represent cultural periods in the northern central Alps: grey – Neolithic; orange – Bronze Age; yellow – Iron Age; red – Roman period; green – Middle Ages.

Pernicka, 2013). Despite the existence of different ore deposits in the region (see Sect. 2), archaeological evidence suggests that the closest and earliest copper mining emerged in the Lower Inn Valley in the early to mid-Bronze Age around 3600 cal BP (Breitenlechner et al., 2013; O'Brien,

2015; Tomedi et al., 2013). Our HFL record strongly suggests that metallurgical activities around the Kleinwalser Valley could have already taken place around 5500 cal BP, which would be almost 2000 years earlier. Our findings are, however, in agreement with other studies, which indicate that Alpine metallurgy started well before 5000 cal BP (Bartelheim et al., 2002; Frank and Pernicka, 2012; Höppner et al., 2005).

5.3 3500 to 2800 cal BP: Bronze Age

The start of this period saw the evolution from minerotrophic to ombrotrophic conditions in HFL, characterised by the occurrence of *Sphagnum* and a stabilisation of Ca values, which suggests an independence from bottom sediment influence. The landscape opened, as shown by the emergence of *Poaceae, Cyperaceae* and *Corylus*, while tree pollen sank below 50 %. Moreover *Calluna*, *Plantago*, cereals and other cultural indicators *(Triticum/Hordeum, Humulus/Cannabis)* support the interpretation of a landscape opening with human presence. A drastic MAR peak in HFL and LAD (Fig. 5) suggests that deforestation and openness strongly promoted soil and slope erosion between 3500 and 3200 cal BP. A bottom layer of partly charred wood debris at HHA was dated to 3360–3480 cal BP, which points to deforestation by fire and further supports land openness. Archaeological evidence from Schneiderkürenalpe (Fig. 1) also suggests pastoral activities in the valley (Leitner, 2003), which would have promoted soil erosion on the karstic western slopes. On the same slopes, a speleothem record from the Hölloch cave (Wurth et al., 2004) showed a contemporary negative $\delta^{13}C$ excursion, which could have been caused by an enhanced input of soil-derived carbon. Cultural pollen indicators and pastoral weeds were observed locally by Dieffenbach-Fries (1981), while Walde and Oeggl (2004) documented fire clearings in the Tannberg area (Fig. 1) between 3600 and 3300 cal BP. Several lake and mire records showed an increasing human impact on the central Alp's landscape during that period (Festi et al., 2014; Schmidl and Oeggl, 2005; Vorren et al., 1993; Wick and Tinner, 1997). Contemporaneously, settlement patterns changed after 3500 cal BP as a result of climatic deteriorations and new sites appeared at higher elevations in the central Alps (Della Casa, 2013). The same author saw technical and agricultural innovations as a driver of higher impact during the middle to late Bronze Age. In terms of climate, a trend to wetter and colder conditions began after approximately 3300 cal BP (Hormes et al., 2001; Ivy-Ochs et al., 2009; Magny et al., 2009; Vorren et al., 1993), which could have promoted such erosive events by both descending the timberline and bringing more precipitation on an open landscape. While some studies suggested that warmer conditions can promote human activities (Tinner et al., 2003; Vorren et al., 1993), our pollen record does not allow conclusions about warmer or colder conditions. We can however argue that the large erosive event observed in the Kleinwalser Valley and the specific cultural pollen assemblage were a direct consequence of a strong and deliberate human land use rather than being the direct result of climate factors.

5.4 2800 cal BP to 600 cal CE: Iron Age and Roman period

The pressure of agro-pastoralism progressively disappeared from 2800 to 2500 cal BP as shown by the disappearance of *Artemisia, Fabacea, Cirsium* and *Plantago*. Cerealia pollen (*Hordeum/Triticum* and *Secale)* also go missing around 2500 cal BP. Forests progressively recovered in a stable landscape with minimum erosion, as also reflected in the low MAR. The decreasing human impact in the Kleinwalser Valley after the late Bronze Age may have been triggered by a cold phase (Ivy-Ochs et al., 2009), making harsh mountain environments less attractive. However, several studies discussed or contested a climate-deterministic view on the widespread decline of human activities around this period (e.g. Armit et al., 2014; Röpke et al., 2011; Tinner et al., 2003). Decreasing cultural indicators during this period were also documented elsewhere in the central Alps (Vorren et al., 1993). Yet, a general decline contrasts with human impact in the neighbouring Tannberg area (Walde and Oeggl, 2003, 2004). Why human impact in the Kleinwalser Valley decreased therefore remains unclear at this stage. We can however hypothesise that humans never abandoned the valley completely. The favourable warm and dry period starting around 2000 cal BP (Büntgen et al., 2011) attracted people again for hunting and pastoralism as suggested by pollen (*Artemisia, Plantago*) and by archaeological evidence (Leitner, 2003).

While anthropogenic impact in the Kleinwalser Valley declined from 2800 to 2000 cal BP, Pb EF suggests that metallurgical activities continued in the area. A Pb EF of up to 175 hints at intensive metallurgical activities not far from HFL between 2800 and 2600 cal BP. The exact locations of these activities remain unclear, but may be local to regional, as metallurgy became widespread in the eastern Alps around 3500 cal BP (Höppner et al., 2005; Lutz and Pernicka, 2013). The signal is in line with the technological introduction of the first Pb alloys (Tomedi et al., 2013). Afterwards (2600–2300 cal BP), short episodes of moderate Pb EF indicate ongoing metallurgy in the region. Part of it could have been connected to Celtic cultures (e.g. La Tène), as metal artefacts and metallurgy evidence were found in the northern central Alps (Bächtiger, 1982; Mansel, 1989).

During early Roman times (ca. 2000 cal BP in this region) HFL and LAD show a low MAR, indicating little erosion and therefore decreased land use, as Walde and Oeggl (2003, 2004) already suggested. In contrast, Friedmann and Stojakowits (2017) reported higher land use in the Alpine foreland. Later on, the study of Büntgen et al. (2011) suggested warm summers with moderately low precipitation from 200 to 300 cal CE. Simultaneously, rising mineral input in HFL

indicates increased land use in the Kleinwalser Valley. The local and regional human activity and connectivity of the valley can only be inferred by connecting historical sources (Dertsch, 1974; Fink and von Klenze, 1891; von Raiser, 1830; Weber, 1995), archaeological finds (Gulisano, 1995) and a Roman trade route completion (Via Decia) through Sonthofen (20 km N) around 250 CE (Heuberger, 1955). We therefore suggest that people may have used the valley's slopes, which led to the observed MAR rise in HFL and LAD around the 3rd century cal CE. We also observe an elevated Pb EF around 100 cal CE, but in contrast to Mackensen (1995), we cannot firmly connect that to local Roman mining around Sonthofen. As strong Pb emissions of Roman origin are recorded across Europe (e.g. De Vleeschouwer et al., 2010b), we tend to attribute the enrichment in HFL to diffuse distal sources.

After 400 cal CE, increased *Abies alba* pollen indicate forest expansion in cool and humid conditions. The absence of herbs (e.g. *Plantago*) and *Corylus* suggests a low human influence in the Kleinwalser Valley. In parallel to the forest expansion and decreased anthropogenic pollen indicators, the MAR dropped significantly in the first half of the 6th century cal CE. Similar patterns were observed in the Kleinwalser Valley (Grosse-Brauckmann, 2002) as well as north of it (Rösch, 1992; Stojakowits, 2014). A wetter climate around 400 cal CE was directly followed by colder summer temperatures from 536 to 660 cal CE (Büntgen et al., 2011, 2016), called the Late Antique Little Ice Age (LALIA). Around this period, Holzhauser et al. (2005) observed glacier advances in the Swiss Alps. The comparison of our data with these palaeoclimate records suggests that due to a climatic deterioration between 500 and 600 cal CE, human activities in the Kleinwalser Valley and its surroundings declined significantly. Moreover, erosion decreased as a combined result of forest expansion and soil stabilisation.

5.5 600 cal CE to 2016 CE: from early Middle Ages to modern times

This period saw the expansion of the Frankish empire to higher elevations, but little is known about it in this part of the northern central Alps, as neither Roman nor Middle Age historical sources exist (Babucke, 1995). We nevertheless observe a growing human impact in HFL, reflected in increasing cultural pollen proportions (*Juglans*, Cerealia, *Plantago*), which fits to deforestation and settlement expansion in the Alpine foreland suggested by Friedmann and Stojakowits (2017). The MAR in HFL also increased sharply after the LALIA to peak around 700 cal CE, which is in accordance with observations in the Alps of Tinner et al. (2003). However, a sharp drop at 770 cal CE was then followed by a decreasing trend along with the Medieval climatic optimum (900 to 1300 CE) (Mann, 2002) until the onset of the Little Ice Age glacier progressions (1300 to 1850 CE) (Matthews and Briffa, 2005). The MAR decrease indicates a landscape stabilisation. Historical sources indeed suggested that the Kleinwalser Valley has been managed for cattle herding and hunting since at least the 11th century CE (Amann, 2013a). The Walser arrived in the early 14th century CE and should have been responsible for most of the changes since then (Wagner, 1950). The presence of macro-charcoal (> 1 mm) in HFL after 1350 cal CE is in line with the onset of Walser settlements and indicates intense use of fire across the valley. The uppermost pollen sample in HFL shows the highest proportion of cultural and open landscape indicators (Fig. 3). However, our palynological resolution is coarse and our age–depth model is limited for that period, placing this uppermost sample in the early period of industrialisation (ca 1880 cal CE). We can therefore assume that the Walser intensified deforestation until the mid-19th century, as shown on a land cover map from 1857 CE (State of Vorarlberg, 2018). The MAR progressively increased from the 13th century cal CE towards the industrial period, reflecting a growing population, increasing forestry and agro-pastoral activities (dairy and meat production). However, this accelerating trend to landscape opening may have been buffered by early land (forest) management regulations (Amann, 2014; Fink and von Klenze, 1891), mitigating further destabilisation of land cover.

In contrast to HFL, the MAR in LAD seems to have taken another development between the Middle Ages and industrialisation. Even if the accumulation rates in this part need to be considered with caution, the MAR rose quite strongly after around 1400 cal CE. Particularly this western side of the valley started to be used for cattle grazing after 1450 CE (Amann, 2013b). Consequently, the vulnerable slopes suffered from erosion, induced by timber cutting and cattle trampling.

Pb EF has also increased since around 1400 cal CE. Part of this increase may be attributed to the Sonthofen mining district, where exploitation was first documented for 1471 cal CE (Merbeler, 1995). However, the emergence of widespread European mining activities in the Middle Ages (e.g. Forel et al., 2010; Le Roux et al., 2005) could have contributed to the signal in HFL. The interpretation of the late Middle Ages in the LAD record is however limited by the age constraint. A more detailed discussion would therefore be speculative. We can however observe that the trends described above for Pb EF, the MAR, and pollen in HFL continued towards the 19th century. We can moreover suggest several interpretations from our geochemical data for the late 19th and 20th centuries. As a result of heavy industry and the introduction of leaded gasoline in Europe, the Pb EF in HFL strongly increased continuously from 1850 cal CE to a maximum of 250 in the 1980s and a sharp decline thereafter, perfectly fitting to the maximum use of leaded fuel and its subsequent ban (Pacyna and Pacyna, 2001). The chronology of the last centuries is however not well constrained. This could have been caused partly by drainage of Hoefle Mire, which temporarily reduced peat accumulation and enhanced

decomposition at intermediate depth. However, our Pb EF profile is strikingly similar to the well-dated Pb EF profile of several Swiss mires (Shotyk et al., 1998; Weiss et al., 1999) and, hence, provides another chronological reference point for the topmost part of the Hoefle core. We can therefore say that, during the first half of the 20th century, the MAR remained low in both mires. The tourism intensification in the valley (Fritz, 1981) and the construction of related infrastructure increased the MAR in both mires again after 1950 cal CE.

6 Conclusions

We present two peat records of the central Alps covering the last 6200 years. By combining geochemical, palynological and chronological tools, we are able to understand the occupation and high human impact on the landscape in a valley of the northern central Alps and beyond. Calibrating a portable geochemical tool with ICP-MS also allows us to quantify geochemical elements in peat at a resolution that is rarely obtained and demonstrates its potential in (palaeo)environmental studies.

A cooler and wetter climate around 6200 cal BP promoted mire formation in the Kleinwalser Valley. Pollen spectra and erosion suggest human presence in the valley as early as around 5700 cal BP, lasting over several centuries, which is in line with studies on regional occupation. Increased Pb EF values around the same time suggest metallurgical activities in the area, which predates regional archaeological evidence by almost 2000 years. Large-scale deforestation and land use (agro-pastoralism) took place between 3500 and 2800 cal BP causing a drastic landscape opening and high initial erosion rates at both low and high elevations. At the end of this period, a prominent Pb EF points to metallurgical activities. However, landscape stabilised and forests recovered thereafter until well into the Roman period. A second period of increased erosion and land use started after 230 cal CE to a climax at around 700 cal CE. This increased land use period was interrupted by climatic deteriorations around 500 to 600 cal CE. Pb EF increased during the Roman period. It is however challenging to identify an origin as Roman Pb pollution was widespread. The Middle Ages saw progressive land management and the arrival of the Walser people. While historical sources point to a strong Walser influence on the area, our data only allow us to suggest that deforestation, agriculture and pastoralism continued during that period. The extent of those activities remains unclear however. The Pb EF increased during Late Middle Ages. It then rose faster during the industrial revolution and peaked before leaded gasoline was banned, allowing us to use it as a chronological marker to constrain the last century, which saw increasing tourism and its consequences taking place in the Kleinwalser Valley.

Although several archaeological findings and sites gave evidence for three prehistoric hotspots of human activity before, our pollen and geochemical data allow us to detail the evolution of the local and regional landscape and its use in the northern central Alps. The combination of historical sources with erosion indicators and pollen points to local land use and human presence in the valley thousands of years before the Walser arrival. Because the landscape had already undergone strong anthropogenic changes before, the recorded impact of the Walser was ultimately less prominent than could be expected.

Data availability. The geochemical data underlying this study are given either in the tables of the article or in the Supplement published with this article. The pollen data can be requested by contacting the first author.

Supplement. The supplement related to this article is available online at: https://doi.org/10.5194/egqsj-68-13-2019-supplement.

Author contributions. As corresponding author, CvS was responsible for planning and carrying out field work, geochemical analyses, data processing, and designing and writing of the paper. The pollen analyses were conducted by AL, whereas FDV contributed to sample preparation, geochemical analyses and designing of the paper. Both IU and JS helped in planning and conducting field sampling and contributed to the interpretation process.

Competing interests. The authors declare that they have no conflict of interest.

Special issue statement. This article is part of the special issue "Connecting disciplines – Quaternary archives and geomorphological processes in a changing environment". It is a result of the First Central European Conference on Geomorphology and Quaternary Sciences, Gießen, Germany, 23–27 September 2018.

Acknowledgements. We would like to thank Karl Keßler (landscape conservation Kleinwalser Valley), Alexander Suhm (Kiel University), Chuxian Li, Marie-Jo Tavella and Gaël Le Roux (all EcoLab) for their help and advice during field and laboratory phases. Clemens von Scheffer benefited from several travel grants from PPP (no. 57316724)/PHC-PROCOPE, no. 37646SG from DAAD/Campus-France (funded by the BMBF – German Federal Ministry of Education and Research), "*Soutien à la Mobilité Internationale 2017*" from the Institut National Polytechnique de Toulouse and a co-tutelle grant from the Deutsch-Französische Hochschule/Université franco-allemande (DFH/UFA). The project was co-funded through the graduate school *"Human development in landscapes"* (DFG-Excellence Initiative, GSC-208).

References

Amann, A.: Alpleben im Walsertal – ein kulturhistorischer Abriss, in: Das Buoch soll Kraft und Macht haben, Alpbücher im Kleinwalsertal, 1541–1914, edited by: Amann, A. and Willand, D., 11–80, Brüüge, Riezlern/Kleinwalsertal, 2013a.

Amann, A.: Kaleidoskop der Alpbücher, in: Das Buoch soll Kraft und Macht haben, Alpbücher im Kleinwalsertal 1541–1914, edited by: Willand, D. and Amann, A., 103–164, Brüüge, Riezlern/Kleinwalsertal, 2013b.

Amann, A.: Alpgenossenschaften im Kleinwalsertal – Eine Vignette aus früherer Zeit "Berichte aus Alpbüchern des Alters 1592 AD", in: Genossenschaftswissenschaft zwischen Theorie und Geschichte: Festschrift für Prof. Dr. Johann Brazda zum 60. Geburtstag, edited by: Laurinkari, J., Schediwy, R., and Todev, T., 49–63, BoD – Books on Demand, 2014.

Armit, I., Swindles, G. T., Becker, K., Plunkett, G., and Blaauw, M.: Rapid climate change did not cause population collapse at the end of the European Bronze Age, P. Natl. Acad. Sci. USA, 111, 17045–17049, 2014.

Artioli, G., Angelini, I., Kaufmann, G., Canovaro, C., Dal Sasso, G., and Villa, I. M.: Long-distance connections in the Copper Age: New evidence from the Alpine Iceman's copper axe, edited by: Hart, J. P., PLoS One, 12, e0179263, https://doi.org/10.1371/journal.pone.0179263, 2017.

Babucke, V.: Das frühe Mittelalter, in Kempten und das Allgäu, Führer zu archäologischen Denkmälern in Deutschland 30, edited by: Czysz, W., Dietrich, H., and Weber, G., 70–78, Theiss, Stuttgart, 1995.

Bachnetzer, T.: Prähistorischer Feuersteinbergbau im Kleinwalsertal, Vorarlberg, Silex- und Bergkristallabbaustellen in Österreich, Praearchos, 5, 2017.

Bächtiger, K.: Die Erzvorkommen und Lagerstätten Graubündens und der ehemalige Bergbau, Mitteilungen, Verein der Freunde des Bergbaues Graubünden, 21, 2–12, 1982.

Baron, S., Lavoie, M., Ploquin, A., Carignan, J., Pulido, M., and De Beaulieu, J. L.: Record of metal workshops in peat deposits: History and environmental impact on the Mont Lozère Massif, France, Environ. Sci. Technol., 39, 5131–5140, https://doi.org/10.1021/es048165l, 2005.

Barry, R. G.: Changes in mountain environments: a review, in Mountain Environments in Changing Climates, edited by: Beniston, M., 496, Taylor & Francis, 2002.

Bartelheim, M., Eckstein, K., Huijsmans, M., Krauß, R., and Pernicka, E.: Kupferzeitliche Metallgewinnung in Brixlegg, Österreich, in: Die Anfänge der Metallurgie in der Alten Welt, edited by: Bartelheim,M., Pernicka, E., and Krause, R., 33–82, Rahden, Westfalia: Verlag Marie Leidorf, Rahden, 2002.

Bätzing, W.: Die Alpen: Geschichte und Zukunft einer europäischen Kulturlandschaft, 4th ed., C.H. Beck, Munich, 2015.

Blaauw, M.: Methods and code for "classical" age-modelling of radiocarbon sequences, Quat. Geochronol., 5, 512–518, 2010.

Blaauw, M. and Christen, J. A.: Flexible paleoclimate age-depth models using an autoregressive gamma process, Bayesian Anal., 6, 457–474, https://doi.org/10.1214/11-BA618, 2011.

Breitenlechner, E., Goldenberg, G., Lutz, J., and Oeggl, K.: The impact of prehistoric mining activities on the environment: A multidisciplinary study at the fen Schwarzenbergmoos (Brixlegg, Tyrol, Austria), Veg. Hist. Archaeobot., 22, 351–366, https://doi.org/10.1007/s00334-012-0379-6, 2013.

Büntgen, U., Tegel, W., Nicolussi, K., McCormick, M., Frank, D., Trouet, V., Kaplan, J. O., Herzig, F., Heussner, K. U., Wanner, H., Luterbacher, J., and Esper, J.: 2500 years of European climate variability and human susceptibility, Science, 80, 331, 578–582, https://doi.org/10.1126/science.1197175, 2011.

Büntgen, U., Myglan, V. S., Ljungqvist, F. C., McCormick, M., Di Cosmo, N., Sigl, M., Jungclaus, J., Wagner, S., Krusic, P. J., Esper, J., Kaplan, J. O., De Vaan, M. A. C., Luterbacher, J., Wacker, L., Tegel, W., and Kirdyanov, A. V.: Cooling and societal change during the Late Antique Little Ice Age from 536 to around 660 AD, Nat. Geosci., 9, 231–236, https://doi.org/10.1038/ngeo2652, 2016.

Carcaillet, C.: A spatially precise study of Holocene fire history, climate and human impact within the Maurienne valley, North French Alps, J. Ecol., 86, 384–396, https://doi.org/10.1046/j.1365-2745.1998.00267.x, 1998.

Clark, A. J. S., Merkt, J., and Muller, H.: Post-Glacial Fire, Vegetation, and Human History on the Northern Alpine Forelands, South-Western Germany, J. Ecol., 77, 897–925, 1989.

Clegg, E. J., Harrison, G. A. and Baker, P. T.: The impact of high altitudes on human populations, Hum. Biol., 42, 486–518, 1970.

Cornelissen, M. and Reitmaier, T.: Filling the gap: Recent Mesolithic discoveries in the central and south-eastern Swiss Alps, Quatern. Int., 423, 9–22, https://doi.org/10.1016/j.quaint.2015.10.121, 2016.

de Graaff, L. W. S., de Jong, M. G. G., Busnach, T., and Seijmonsbergen, A. C.: Geomorphologische Studie hinterer Bregenzerwald, Bericht an das Amt der Vorarlberger Landesregierung, Abt. Raumplanung und Baurecht Landhaus Bregenz, Amsterdam, 2003.

Della Casa, P.: Switzerland and the Central Alps, in The Oxford Handbook of the European Bronze Age, edited by: Harding, A. and Fokkens, H., 706–722, OUP Oxford, 2013.

Dertsch, R.: Ortsnamensbuch des Landkreises Sonthofen, Historisches Ortsnamenbuch von Bayern, Schwaben, Bd. 7, Kommission für Bayerische Landesgeschichte, München, 1974.

De Vleeschouwer, F., Chambers, F. M., and Swindles, G. T.: Coring and sub-sampling of peatlands for palaeoenvironmental research, Mires Peat, 7, 1–10, https://doi.org/10.1016/j.ssi.2010.01.014, 2010a.

De Vleeschouwer, F., Le Roux, G., and Shotyk, W.: Peat as an archive of atmospheric pollution and environmental change: A case study of lead in Europe, PAGES Mag., 18, 20–22, https://doi.org/10.22498/pages.18.1.20, 2010b.

Dieffenbach-Fries, H.: Zur spät- und postglazialen Vegetationsentwicklung bei Oberstdorf (Oberallgäu) und im kleinen Walsertal (Vorarlberg), Technische Hochschule Darmstadt, 1981.

Dietre, B., Walser, C., Kofler, W., Kothieringer, K., Hajdas, I., Lambers, K., Reitmaier, T., and Haas, J. N.: Neolithic to Bronze Age (4850–3450 cal. BP) fire management of the Alpine Lower Engadine landscape (Switzerland) to establish pastures and cereal fields, Holocene, 27, 181–196, https://doi.org/10.1177/0959683616658523, 2017.

El Balti, N., Christ, L., Kempke, M., Martens, T., Bork, H., and Schrautzer, J.: Die Moore im Kleinwalsertal – Aktueller Zustand und Entwicklungsmöglichkeiten, Ina. – Forsch. online, 40.1, 2017.

Festi, D., Putzer, A., and Oeggl, K.: Mid and late holocene land-use changes in the Ötztal alps, territory of the neolithic iceman "Ötzi", Quatern. Int., 353, 17–33, https://doi.org/10.1016/j.quaint.2013.07.052, 2014.

Fink, J. and von Klenze, H.: Der Mittelberg. Geschichte, Landes- und Volkskunde des ehemaligen gleichnamigen Gerichtes (Reprint), Kösel, Kempten, 1891.

Forel, B., Monna, F., Petit, C., Bruguier, O., Losno, R., Fluck, P., Begeot, C., Richard, H., Bichet, V., and Chateau, C.: Historical mining and smelting in the Vosges Mountains (France) recorded in two ombrotrophic peat bogs, J. Geochem. Explor., 107, 9–20, https://doi.org/10.1016/j.gexplo.2010.05.004, 2010.

Frank, C. and Pernicka, E.: Copper artefacts of the Mondsee group and their possible sources, in: Lake Dwellings after Robert Munro, Proceedings from the Munro International Seminar: The Lake Dwellings of Europe. 22nd 23rd October 2010, University of Edinburgh, edited by: Midgley, M. S. and Sanders, J., 113–138, Sidestone press, Leiden, 2012.

Friedmann, A. and Stojakowits, P.: Zur spät- und postglazialen Vegetationsgeschichte des Allgäu mit Alpenanteil, Kontrakpunkte: Festschrift für Manfred Rösch, edited by: Lechterbeck, J. and Fischer, E., Verlag Dr. Rudolf Habelt GmbH, Bonn, 2017.

Fritz, W.: Kleinwalsertal einst und jetzt: heimatkundliche Betrachtungen, Verlag Walserdruck, Erich Stöckeler, Riezlern/Kleinwalsertal, 1981.

Givelet, N., Le Roux, G., Cheburkin, A., Chen, B., Frank, J., Goodsite, M. E., Kempter, H., Krachler, M., Noernberg, T., Rausch, N., Rheinberger, S., Roos-Barraclough, F., Sapkota, A., Scholz, C., and Shotyk, W.: Suggested protocol for collecting, handling and preparing peat cores and peat samples for physical, chemical, mineralogical and isotopic analyses, J. Environ., 6, 481–492, https://doi.org/10.1039/B401601G, 2004.

Goldscheider, N.: Hydrogeologische Untersuchungen im alpinen Karstgebiet Gottesacker und Schwarzwassertal (Allgäu/Vorarlberg), Vor. Naturschau, 4, 247–294, available at: http://www.biologiezentrum.at (last access: 17 September 2018), 1998.

Grimm, E. C.: Tilia software v. 2.0.60, Illinois State Museum, Springf., 2018.

Grosse-Brauckmann, G.: Paläobotanische Befunde von zwei Mooren im Gebiet des Hohen Ifen, Vorarlberg (Österreich), Telma, 32, 17–36, 2002.

Gulisano, G.: Neue mittelsteinzeitliche Fundplätze im oberen Illertal und im Kleinwalsertal, Archäologische Informationen, 17, 79–84, https://doi.org/10.11588/ai.1994.1.35418, 1994.

Gulisano, G.: Die Besiedlung des Kleinwalsertales und seiner angrenzenden Gebiete in Bayern und Vorarlberg von der Steinzeit bis zur Einwanderung der Walser, Archäologische Informationen, 18, 53–65, https://doi.org/10.11588/ai.1995.1.35421, 1995.

Haas, J. N., Richoz, I., Tinner, W., and Wick, L.: Synchronous holocene climatic oscillations recorded on the Swiss plateau and at timberline in the alps, Holocene, 8, 301–309, https://doi.org/10.1191/095968398675491173, 1998.

HDÖ: Die Niederschläge, Schneeverhältnisse und Lufttemperaturen in Österreich im Zeitraum 1981–1991, Beiträge zur Hydrographie Österreichs, Vienna, 1994.

Heuberger, R.: Der Bodenseeraum im Altertum, in Aus Verfassungs- und Landesgeschichte, Festschrift für Theodor Mayer zum 70. Geb. Band 2. Geschichtliche Landesforschung, Wirtschaftsgeschichte u. Hilfswissenschaften, edited by: Büttner, H., Feger, O., and Meyer, B., 7–21, Lindau/Konstanz, 1955.

Hölzer, A. and Hölzer, A.: Silicon and titanium in peat profiles as indicators of human impact, Holocene, 8, 685–696, https://doi.org/10.1191/095968398670694506, 1998.

Holzhauser, H., Magny, M., and Zumbühl, H. J.: Glacier and lake-level variations in west-central Europe over the last 3500 years, Holocene, 15, 789–801, https://doi.org/10.1191/0959683605hl853ra, 2005.

Höppner, B., Bartelheim, M., Huijsman, M., Krauss, R., Martinek, K.-P., Pernicka, E., and Schwab, R.: Prehistoric copper production in the Inn Valley (Austria), and the earliest copper in Cental Europe, Archaeometry, 47, 293–315, https://doi.org/10.1111/j.1475-4754.2005.00203.x, 2005.

Hormes, A., Müller, B. U., and Schlüchter, C.: The Alps with little ice: Evidence for eight holocene phases of reduced glacier extent in the Central Swiss Alps, Holocene, 11, 255–265, https://doi.org/10.1191/095968301675275728, 2001.

Ivy-Ochs, S., Kerschner, H., Maisch, M., Christl, M., Kubik, P. W., and Schlüchter, C.: Latest Pleistocene and Holocene glacier variations in the European Alps, Quaternary Sci. Rev., 28, 2137–2149, https://doi.org/10.1016/j.quascirev.2009.03.009, 2009.

Jacomet, S.: Plant economy and village life in Neolithic lake dwellings at the time of the Alpine Iceman, Veg. Hist. Archaeobot., 18, 47–59, https://doi.org/10.1007/s00334-007-0138-2, 2009.

Kalnicky, D. J. and Singhvi, R.: Field portable XRF analysis of environmental samples, J. Hazard. Mater., 83, 93–122, https://doi.org/10.1016/S0304-3894(00)00330-7, 2001.

Le Roux, G., Aubert, D., Stille, P., Krachler, M., Kober, B., Cheburkin, A., Bonani, G., and Shotyk, W.: Recent atmospheric Pb deposition at a rural site in southern Germany assessed using a peat core and snowpack, and comparison with other archives, Atmos. Environ., 39, 6790–6801, https://doi.org/10.1016/j.atmosenv.2005.07.026, 2005.

Leitner, W.: Der Felsüberhang auf der Schneiderkürenalpe – Ein Jäger- und Hirtenlager der Vorzeit, Bergschau, 1, 1–32, 2003.

Löwemark, L., Chen, H. F., Yang, T. N., Kylander, M., Yu, E. F., Hsu, Y. W., Lee, T. Q., Song, S. R., and Jarvis, S.: Normalizing XRF-scanner data: A cautionary note on the interpretation of high-resolution records from organic-rich lakes, J. Asian Earth Sci., 40, 1250–1256, https://doi.org/10.1016/j.jseaes.2010.06.002, 2011.

Lutz, J. and Pernicka, E.: Prehistoric copper from the Eastern Alps, Open J. Archaeom., 1, 122–127, https://doi.org/10.4081/arc.2013.e25, 2013.

Mackensen, M.: Die spätrömische Grenze im Gebiet von Cambidano-Kempten, in: Kempten und das Allgäu, Führer zu archäologischen Denkmälern in Deutschland 30, edited by: Czysz, W., Dietrich, H., and Weber, G., 61–69, Theiss, Stuttgart, 1995.

Magny, M., Galop, D., Bellintani, P., Desmet, M., Didier, J., Haas, J. N., Martinelli, N., Pedrotti, A., Scandolari, R., Stock, A., and Vannière, B.: Late-Holocene climatic variability south of the Alps as recorded by lake-level fluctuations at Lake Ledro, Trentino, Italy, Holocene, 19, 575–589, https://doi.org/10.1177/0959683609104032, 2009.

Mann, M. E.: Medieval Climatic Optimum, Encycl. Glob. Environ. Chang., 1, 514–516, 2002.

Mansel, K.: Ein latènezeitlicher Schlüssel mit Stierplastik aus Sonthofen im Allgäu, Germania, 67, 572–587, 1989.

Matthews, J. A. and Briffa, K. R.: The "Little Ice Age": Re-evaluation of an evolving concept, Geogr. Ann. Ser. A, 87, 17–36, https://doi.org/10.1111/j.0435-3676.2005.00242.x, 2005.

McLennan, S. M.: Relationships between the trace element composition of sedimentary rocks and upper continental crust, Geochem. Geophy. Geosy., 2, 2000GC000109, https://doi.org/10.1029/2000GC000109, 2001.

Mejía-Piña, K. G., Huerta-Diaz, M. A., and González-Yajimovich, O.: Calibration of handheld X-ray fluorescence (XRF) equipment for optimum determination of elemental concentrations in sediment samples, Talanta, 161, 359–367, https://doi.org/10.1016/j.talanta.2016.08.066, 2016.

Merbeler, J.: Erzbergbau und Verhüttung im Starzlachtal, in: Kempten und das Allgäu, Führer zu archäologischen Denkmälern in Deutschland 30, edited by: Czysz, W., Dietrich, H., and Weber, G., 149–152, Theiss, Stuttgart, 1995.

Moore, P., Webb, J., and Collinson, M.: Pollen Analysis, Blackwell Scientific Publications Ltd, Oxford, 1991.

Nesbitt, H. W. and Markovics, G.: Weathering of granodioritic crust, long-term storage of elements in weathering profiles, and petrogenesis of siliciclastic sediments, Geochim. Cosmochim. Ac., 61, 1653–1670, https://doi.org/10.1016/S0016-7037(97)00031-8, 1997.

Oblinger, H.: Blei- und Zinkerz am Roßkopf (Ostrachtal/Allgäuer Alpen), Berichte des Naturwissenschaftlichen Vereins für Schwaben e.V., 100, 85–90, 1996.

O'Brien, W.: Prehistoric Copper Mining in Europe: 5500–500 BC, Oxford University Press, 2015.

Oeggl, K. and Nicolussi, K.: Prähistorische Besiedlung von zentralen Alpentälern in Bezug zur Klimaentwicklung, in: Klimawandel in Österreich: die letzten 20.000 Jahre und ein Blick voraus, edited by: Schmidt, R., Psenner, R., and Matulla, C., 77–86, Innsbruck university press, 2009.

Pacyna, J. M. and Pacyna, E. G.: An assessment of global and regional emissions of trace metals to the atmosphere from anthropogenic sources worldwide, Environ. Rev., 9, 269–298, https://doi.org/10.1139/er-9-4-269, 2001.

R Core Team: R: A Language and Environment for Statistical Computing, available at: https://www.r-project.org/ (last access: 14 April 2019), 2017.

Reimer, P. J., Bard, E., Bayliss, A., Beck, J. W., Blackwell, P. G., Ramsey, C. B., Buck, C. E., Cheng, H., Edwards, R. L., Friedrich, M., Grootes, P. M., Guilderson, T. P., Haflidason, H., Hajdas, I., Hatté, C., Heaton, T. J., Hoffmann, D. L., Hogg, A. G., Hughen, K. A., Kaiser, K. F., Kromer, B., Manning, S. W., Niu, M., Reimer, R. W., Richards, D. A., Scott, E. M., Southon, J. R., Staff, R. A., Turney, C. S. M., and van der Plicht, J.: IntCal13 and Marine13 Radiocarbon Age Calibration Curves 0–50 000 Years cal BP, Radiocarbon, 55, 1869–1887, https://doi.org/10.2458/azu_js_rc.55.16947, 2013.

Reitmaier, T., Doppler, T., Pike, A. W. G., Deschler-Erb, S., Hajdas, I., Walser, C., and Gerling, C.: Alpine cattle management during the Bronze Age at Ramosch-Mottata, Switzerland, Quatern. Int., 484, 19–31, https://doi.org/10.1016/j.quaint.2017.02.007, 2018.

Roepke, A. and Krause, R.: High montane-subalpine soils in the Montafon Valley (Austria, northern Alps) and their link to land-use, fire and settlement history, Quatern. Int., 308–309, 178–189, https://doi.org/10.1016/j.quaint.2013.01.022, 2013.

Roepke, A., Stobbe, A., Oeggl, K., Kalis, A. J., and Tinner, W.: Late-Holocene land-use history and environmental changes at the high altitudes of St Antönien (Switzerland, Northern Alps): Combined evidence from pollen, soil and tree-ring analyses, Holocene, 21, 485–498, https://doi.org/10.1177/0959683610385727, 2011.

Rösch, M.: Human impact as registered in the pollen record: some results from the western Lake Constance region, Southern Germany, Veg. Hist. Archaeobot., 1, 101–109, https://doi.org/10.1007/BF00206090, 1992.

Schmidl, A. and Oeggl, K.: Land Use in the Eastern Alps During the Bronze Age – an Archaeobotanical Case Study of a Hilltop Settlement in the Montafon (Western Austria), Archaeometry, 47, 455–470, https://doi.org/10.1111/j.1475-4754.2005.00213.x, 2005.

Schmidt-Thomé, P.: Zur Geologie und Morphologie des Ifengebirgsstockes (Allgäu): Erläuterungen zur topographisch-morphologischen Kartenprobe VI 3: Alpiner Karst und Bergsturz (On the Geology and Morphology of the Hohe Ifen), Erdkunde, 14, 181–195, 1960.

Schrautzer, J., Bork, H.-R., Christ, L., El-Balti, N., Martens, T., Kempke, M., von Scheffer, C., and Unkel, I.: Classification, ecological characterization and development of montane mires, Phytocoenologia – J. Veg. Ecol., in press, 2019.

Shand, C. A. and Wendler, R.: Portable X-ray fluorescence analysis of mineral and organic soils and the influence of organic matter, J. Geochem. Explor., 143, 31–42, https://doi.org/10.1016/j.gexplo.2014.03.005, 2014.

Shotyk, W., Weiss, D., Appleby, P. G., Cheburkin, A. K., Frei, R., Gloor, M., Kramers, J. D., Reese, S., and Van der Knaap, W. O.: History of atmospheric lead depostion since 12,370^{14}C yr BP from a Peat bog, Jura Mountains, Switzerland, Science, 281, 1635–1640, https://doi.org/10.1126/science.281.5383.1635, 1998.

Shotyk, W., Weiss, D., Kramers, J. D., Frei, R., Cheburkin, A. K., Gloor, M., and Reese, S.: Geochemistry of the peat bog at Etang de la Gruère, Jura Mountains, Switzerland, and its record of atmospheric pb and lithogenic trace metals (Sc, Ti, Y, Zr, and REE) since 12,370^{14}C yr bp, Geochim. Cosmochim. Ac., 65, 2337–2360, https://doi.org/10.1016/S0016-7037(01)00586-5, 2001.

Shuttleworth, E. L., Evans, M. G., Hutchinson, S. M., and Rothwell, J. J.: Assessment of lead contamination in peatlands using field portable XRF, Water Air. Soil Pollut., 225, https://doi.org/10.1007/s11270-013-1844-2, 2014.

State of Vorarlberg: VoGIS, Vorarlberg Atlas, Urmappe 1857, available at: http://vogis.cnv.at/, last access: 17 August 2018.

Stojakowits, P.: Pollenanalytische Untersuchungen zur Rekonstruktion der Vegetationsgeschichte im südlichen Iller-Wertach-Jungmoränengebiet seit dem Spätglazial (PhD-Thesis), Universität Augsburg, 2014.

Tinner, W., Lotter, A. F., Ammann, B., Conedera, M., Hubschmid, P., Van Leeuwen, J. F. N., and Wehrli, M.: Climatic change and contemporaneous land-use phases north and south of the Alps 2300 BC to 800 AD, Quaternary Sci. Rev., 22, 1447–1460, https://doi.org/10.1016/S0277-3791(03)00083-0, 2003.

Tomedi, G., Staudt, M., and Töchterle, U.: Zur Bedeutung des prähistorischen Bergbaus auf Kupfererze im Raum Schwaz-Brixlegg, in: Cuprum Tyrolense – 5550 Jahre Bergbau und Kupferverhüttung in Tirol, edited by: Oeggl, K. and Schaffer, V., 55–70, Edition Tirol, 2013.

Valese, E., Conedera, M., Held, A. C. C., and Ascoli, D.: Fire, humans and landscape in the European Alpine region during the Holocene, Anthropocene, 6, 63–74, https://doi.org/10.1016/j.ancene.2014.06.006, 2014.

Van der Knaap, W. O., van Leeuwen, J. F. N., and Ammann, B.: The first rise and fall of Fagus sylvatica and interactions with Abies alba at Faulenseemoos (Weiss Plateau) 6900–6000 cal yr BP, Acta Palaeobot., 44, 249–266, 2004.

Vanneste, H., De Vleeschouwer, F., Martínez-Cortizas, A., von Scheffer, C., Piotrowska, N., Coronato, A., and Le Roux, G.: Late-glacial elevated dust deposition linked to westerly wind shifts in southern South America, Sci. Rep., 5, 11670, https://doi.org/10.1038/srep11670, 2015.

Völk, H. R.: Geomorphologie des Kleinwalsertales und seiner Gebirgsumrahmung, Landschaftsformen zur Eiszeit und Nacheiszeit unter Einbeziehung der geologischen Verhältnisse, Vor. Naturschau, 10, 7–95, 2001.

von Gümbel, C. W.: Geognostische Beschreibung des Königreichs Bayern: Geognostische Beschreibung des bayerischen Alpengebirges und seines Vorlandes, bayer. Staatsministerium der Finanzen, Gotha, 1861.

von Raiser, J. N.: Der Ober-Donau-Kreis des Königreichs Bayern unter den Römern, Die Römer-Male von Augusta rauracum bis Augusta Vindelicorum: 1, Kranzfelder, Augsburg, 1830.

Vorren, K.-D., Mørkved, B,. and Bortenschlager, S.: Human impact on the Holocene forest line in the Central Alps, Veg. Hist. Archaeobot., 2, 145–156, https://doi.org/10.1007/BF00198585, 1993.

Wagner, G.: Rund um Hochifen und Gottesackergebiet, Verlag der Hohenloheschen Buchhandlung Ferdinand Rau, Öhringen, 1950.

Walde, C. and Oeggl, K.: Blütenstaub enthüllt 3000-jährige Siedlungsgeschichte im Tannberggebiet, Walserheimat Vor., Tirol und Liechtenstein, 73, 1–6, available at: https://www.vorarlberger-walservereinigung.at/vwvwp/bluetenstaub (last access: 6 March 2019), 2003.

Walde, C. and Oeggl, K.: Neue Ergebnisse zur Siedlungsgeschichte am Tannberg. Die Pollenanalysen aus dem Körbersee, Walserheimat Vor., Tirol und Liechtenstein, 75, 4–7, available at: https://www.vorarlberger-walservereinigung.at/vwvwp/neue-ergebnisse (last access: 6 March 2019), 2004.

Weber, L.: Handbuch der Lagerstätten der Erze, Industrieminerale und Energierohstoffe Österreichs: Erläuterungen zur metallogenetischen Karte von Österreich 1:500 000 unter Einbeziehung der Industrieminerale und Energierohstoffe, Geologische Bundesanstalt, 1997.

Weber, M.: Die frühe und mittlere römische Kaiserzeit, in Kempten und das Allgäu, Führer zu archäologischen Denkmälern in Deutschland 30, edited by: Czysz, W., Dietrich, H., and Weber, G., 49–60, Theiss, Stuttgart, 1995.

Weiss, D., Shotyk, W., Appleby, P. G., Kramers, J. D., and Cheburkin, A. K.: Atmospheric Pb Deposition since the Industrial Revolution Recorded by Five Swiss Peat Profiles: Enrichment Factors, Fluxes, Isotopic Composition, and Sources, Environ. Sci. Technol., 33, 1340–1352, https://doi.org/10.1021/es980882q, 1999.

Wick, L. and Tinner, W.: Vegetation Changes and Umbertine Fluctuations in the Central Alps as Indicators of Holocene Climatic Oscillations, Arct. Alp. Res., 29, 445–458, https://doi.org/10.2307/1551992, 1997.

Wurth, G., Niggemann, S., Richter, D. K., and Mangini, A.: The Younger Dryas and Holocene climate record of a stalagmite from Hölloch Cave (Bavarian Alps, Germany), J. Quaternary Sci., 19, 291–298, https://doi.org/10.1002/jqs.837, 2004.

Zacher, W.: Geologische Karte von Österreich: Blatt 113 Mittelberg 1:50 000, Geologische Bundesanstalt, Wien, 1990.

E&G Quaternary Sci. J., 68, 95–105, 2019
https://doi.org/10.5194/egqsj-68-95-2019

Open Access E&G Quaternary Science Journal

Research article

Holocene floodplain evolution in a central European loess landscape – geoarchaeological investigations of the lower Pleiße valley in NW Saxony

Christian Tinapp[1,4], **Susann Heinrich**[2], **Christoph Herbig**[3], **Birgit Schneider**[1], **Harald Stäuble**[4], **Jan Miera**[5], **and Hans von Suchodoletz**[6,1]

[1]University of Leipzig, Institute of Geography, Johannisallee 19a, 04103 Leipzig, Germany
[2]Max-Planck-Institute for Evolutionary Anthropology, Deutscher Platz 6, 04103 Leipzig, Germany
[3]Am Dorf 12, 63517 Rodenbach, Germany
[4]Saxonian Archaeological Heritage Office, Zur Wetterwarte 7, 01109 Dresden, Germany
[5]University of Leipzig, Historical Seminar, Ritterstraße 14, 04109 Leipzig, Germany
[6]University of Technology Dresden, Institute of Geography, Helmholtzstraße 10, 01069 Dresden, Germany

Correspondence: Christian Tinapp (christian.tinapp@lfa.sachsen.de)

Relevant dates: Received: 8 March 2019 – Revised: 17 May 2019 – Accepted: 13 June 2019 – Published: 15 July 2019

How to cite: Tinapp, C., Heinrich, S., Herbig, C., Schneider, B., Stäuble, H., Miera, J., and von Suchodoletz, H.: Holocene floodplain evolution in a central European loess landscape – geoarchaeological investigations of the lower Pleiße valley in NW Saxony, E&G Quaternary Sci. J., 68, 95–105, https://doi.org/10.5194/egqsj-68-95-2019, 2019.

Abstract: Undisturbed sediments are an important source for the reconstruction of the Holocene development of valleys. Wide floodplains with relatively small rivers in a region settled since 5500 BCE offer opportunities for investigations regarding climatic and anthropogenic landscape change. In the context of a motorway construction, excavations were carried out by the Saxonian Heritage Office in the year 2015. At one of the sites it was possible to get a view of the sediments of the Pleiße valley less than 100 m distance from large cross sections described by Neumeister (1964) in a former open cast mine. Archaeological finds and features, plant remains and radiocarbon dating as well as micromorphological and geochemical investigations helped to decipher the age and the characteristics of the Holocene sediments: above Weichselian loamy sands a sedge peat developed in small depressions during the Preboreal and Boreal. The sands and the sedge peat are covered by a "black clay", which was still the topsoil during the Atlantic period. The sedimentation of 2.3 m thick overbank fines began after 4000 BCE. A depth of 1 m below the surface a medieval Slavic find layer was excavated. These results show that sedimentation processes in the lower Pleiße valley significantly changed after 4000 BCE. It is obvious that the increase in silty material in the floodplain is caused by the land clearance in the Neolithic period. More than half of the silty overbank fines were deposited before the Middle Ages began.

Kurzfassung: Ungestörte Sedimente in fluvialen Systemen sind ein wichtiges Archiv zur Rekonstruktion der holozänen Talentwicklung. Seit 5500 BCE besiedelte Altsiedellandschaften mit breiten, von relativ kleinen Flüssen durchflossenen Tälern bieten besonders gute Voraussetzungen für die Untersuchung klimatis-

cher und anthropogener Einflüsse auf Landschaftsveränderungen. Im Rahmen eines Autobahnprojektes südlich von Leipzig wurden vom Landesamt für Archäologie Sachsen Ausgrabungen durchgeführt. An einer der Grabungsflächen konnten die Sedimente des Pleißetales in weniger als 100 m Entfernung zu den von Neumeister (1964) in einem Tagebau beschriebenen Profilen aufgenommen und beprobt werden. Archäologische Befunde und Funde, Pflanzenreste, Radiocarbondatierungen, mikromorphologische und geochemische Untersuchungen führten zur Eingrenzung des Alters der holozänen Sedimente: Über weichselzeitlichem lehmigen Sand lagern in kleinen Vertiefungen Seggentorflagen aus dem Präboreal und Boreal. Sand sowie Torf werden von einem "Schwarzen Ton" überdeckt, der bis weit in das Atlantikum hinein den Oberboden bildete. Nach 4000 BCE begann die Sedimentation von etwa 2,3 m Auenlehm. Einen Meter unter der Geländeoberfläche befindet sich eine mittelalterliche, slawische Fundschicht. Die Ergebnisse belegen, dass sich nach der Ankunft der ersten Ackerbauern die Sedimentationsprozesse im Tal der unteren Pleiße nach 4000 BCE signifikant änderten. Der deutliche Anstieg von schluffreicherem Material in der Aue geht auf die Unterkulturnahme weiter Teile des Einzugsgebietes im Neolithikum zurück. Mehr als die Hälfte der Auenlehmdecke entstand vor dem Mittelalter.

1 Introduction

Alluvial valley sediments are important archives of the Holocene landscape evolution, since besides internal processes the dynamics of rivers are controlled by external factors such as base level changes, tectonic activity, climate changes and anthropogenic activity (Bridgland and Westaway, 2008; Faust and Wolf, 2017). Therefore, to investigate the Holocene landscape evolution of central Europe, alluvial sediments of several rivers have been studied during recent years (Starkel et al., 2006; Hoffmann et al., 2008; Erkens et al., 2009; Kaiser et al., 2012; Houben et al., 2013; Notebaert et al., 2018).

Considering central Germany with a long settlement history since ca. 7.5 ka (Heynowski and Reiß, 2010), only sediments of the lower Weiße Elster River were intensively studied during recent decades (Händel, 1967; Hiller et al., 1991; Fuhrmann, 1999; Tinapp, 2002; Tinapp et al., 2008). However, given that the fluvial dynamics can show individual behaviour even between neighbouring river systems (Faust and Wolf, 2017; von Suchodoletz et al., 2018a), the results from the lower Weiße Elster should ideally be complemented by investigations from other regional river systems to derive sound conclusions about the regional paleoenvironmental evolution. Generally, the Holocene landscape evolution of central Germany is not well known so far: besides investigations of the alluvial sediments from the lower Weiße Elster valley, current knowledge is based on non-continuous pollen, snail or ostracod data from different archives, as well as on lacustrine sediments from the former lake Salziger See (Litt, 1992; Mania, 1980; Fuhrmann, 2008; Wennrich et al., 2005).

In contrast to the Weiße Elster River, the lower part of its eastern tributary Pleiße has rarely been investigated so far (Neumeister, 1964; Händel, 1967). According to Neumeister (1964) the stratigraphy for large parts of the lower Pleiße valley is as follows: the base is formed by Late Weichselian silty fine sand that is sporadically covered by peat, and both are covered by a so-called "black clay" ("Schwarzer Ton"; Neumeister, 1964) that is overlain by older and younger overbank fines. New geoarchaeological investigations of a long-known site in the lower Pleiße valley in 2015 offered the chance to re-evaluate and reanalyse the fluvial stratigraphy of the lower Pleiße valley with modern radiocarbon, sedimentological and micromorphological methods.

Therefore, the goal of this study was to reconstruct environmental change in the lower Pleiße floodplain and to compare these results with those from the neighbouring lower Weiße Elster valley (Figs. 1 and 2) but also with other floodplains from central Europe. This will allow sound conclusions about the regional paleoenvironmental evolution of central Germany compared with other regions of central Europe.

2 Study area

The area south of Leipzig belongs to the North German Plain, and the mostly flat landscape is covered with Pleistocene sediments: in the northern part, glacial till, gravel and sand deposits of Elsterian and Saalian age are covered by Weichselian sandy loess with a thickness of ca. 50 cm. Towards the south, the sandy loess grades into typical loess and increases its thickness to more than 7 m in the Altenburg-Zeitz loess hills (Eissmann, 2002).

The once 115 km long Pleiße River is a right-hand tributary of the Weiße Elster. Most of its former valley was destroyed by mining activities during the 20th century. Therefore the river flows through a canal today, and only small parts of its original floodplain are still preserved. The courses of the Weiße Elster and Pleiße River were formed during the Elsterian glaciation more than 400 000 years ago (Eissmann, 2002; Lauer and Weiss, 2018). Subsequently, fluvial gravels and sand were deposited under periglacial conditions

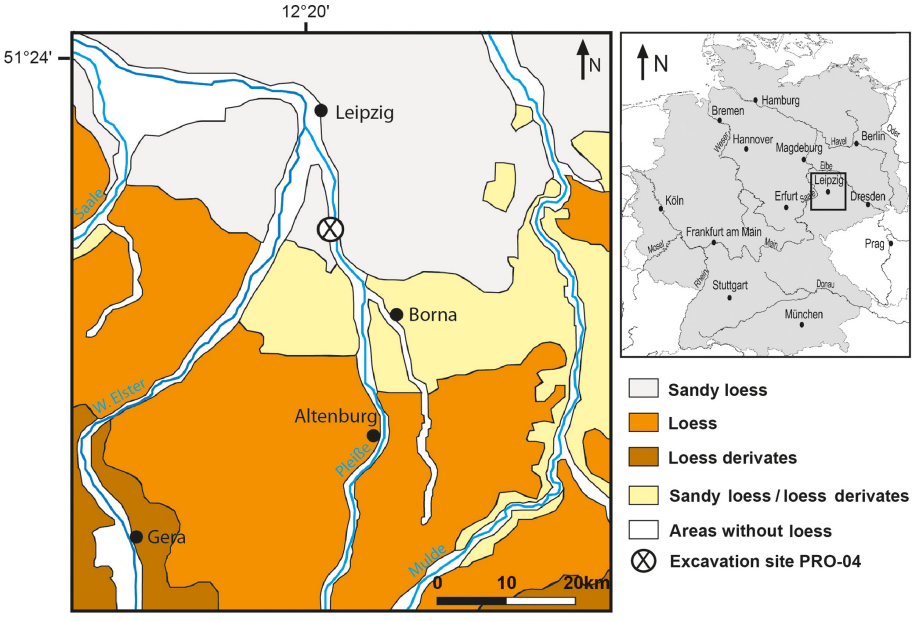

Figure 1. The excavation site near the Pleiße River south of Leipzig with the distribution of loess and loess-like deposits (according to Eissmann, 2002).

during the Saalian and Weichselian glacial periods. In both river systems the current floodplains are found at the eastern sides of the once wider valleys, whereas the western parts are mainly occupied by Saalian gravel terraces. In the remaining smaller floodplains Weichselian gravels and sands form the bases of the Holocene deposits. The branched Weichselian river systems changed towards meandering systems during the latest Weichselian period (Mol, 1995). After the Younger Dryas cold spell, the so far dominant steppe vegetation was replaced by open forests that developed in the floodplains and the surrounding areas (Litt, 1994). The first Neolithic settlers already arrived in the region 7500 years ago (Heynowski and Reiß, 2010). This was the start of a long history of land use in the region with varying intensities during different periods (Tinapp and Stäuble, 2000).

3 Methods

In the context of a motorway construction, archaeological excavations were carried out by the Saxonian Heritage Office in 2015. In one of the four excavation sites east of the village Großdeuben, sediments of the lower Pleiße floodplain were exposed probably less than 100 m distance from the cross sections that were described by Neumeister (1964) in the open cast lignite mine Espenhain more than 50 years ago.

In preparation for the excavation, the topsoil was removed in a 20×83 m wide area by an excavator up to 1 m below the current surface. At this level a small channel and a lot of Slavic remnants (900–1000 CE) were discovered. During the excavations of the Slavic features three cross sections were opened by the excavator: Profile 1 was 15 m long and 2.1 m deep, and Profile 2 was 10 m long and 1.8 m deep. Both east–west directed parallel cross sections started on the level of the Slavic features, while the smaller (2 m long) and 1.6 m deep Profile 3 was dug at the edge of the excavation area (Fig. 3). From the sediments in Profile 3, 6 samples were taken for geochemical analyses, and in Profile 2, 22 samples were taken for geochemical analyses and another 6 for radiocarbon dating. In Profile 1, 1 sample was taken for thin section analysis.

Plant macro remains were extracted from two sediment samples each in Profile 1 and 2 by flotation and wet sieving (mesh width: 2, 0.5 and 0.25 mm), and determined under magnifications from $\times 6.3$ to $\times 40$ using standard literature (e.g. Cappers et al., 2012) and the reference collection at the Laboratory of Archaeobotany, Institute of Prehistoric Archaeology, Goethe University Frankfurt. Attribution of the taxa to ecological units followed Oberdorfer (2001). Several discovered fruits and seeds, as well as pieces of charcoal from two layers of the overbank fines under the Slavic surface at Profile 2, were used for radiocarbon dating (Table 1).

A thin section for micromorphological analysis was prepared from an oriented and undisturbed soil sample taken from the transition of the black clay to the overlying overbank deposits in Profile 1 and was impregnated with resin. The thin section was analysed using a petrographic microscope under plane-polarized light (PPL), crossed polarized light (XPL) and oblique incident light (OIL). The microscopic description mainly followed the terminology according to Bullock et al. (1985) and Stoops (2003).

The particle size distribution was determined by dry sieving of the sand fraction, and silt and clay were measured

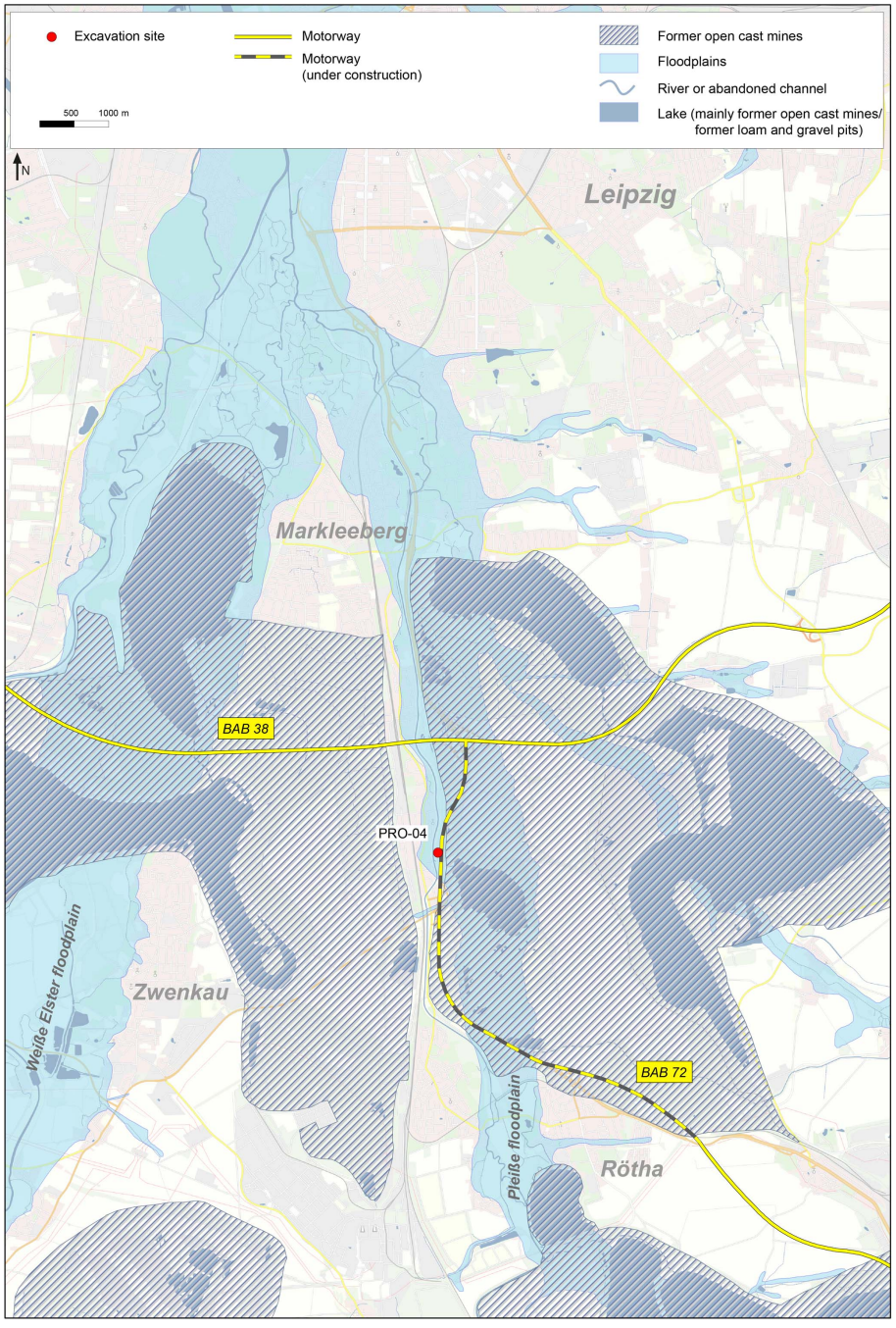

Figure 2. Location of the excavation site (PRO-04) with mining areas and the floodplains of Weiße Ester and Pleiße (map: Geodaten© Staatsbetrieb Geoinformation und Vermessung Sachsen 2018).

based on settling velocities using a sedigraph (Micrometrics). An element analyser was used for the determination of the total contents of carbon, nitrogen and sulfur. The determination of the carbonate content was carried out using the volumetric method with a Eijkelkamp calcimeter according to Scheibler. Subtraction of the inorganic carbon from the total carbon resulted in the organic carbon.

4 Results

In the following, the stratigraphic succession of the lower Pleiße valley with analytical and dating results is described from the base to the top (Fig. 4):

– The base of the Holocene floodplain is formed by Late Weichselian loamy sands. These are waterlogged and do

Table 1. Results of ^{14}C analyses, performed by Ronny Friedrich, Curt-Engelhorn-Zentrum Archäometrie in Mannheim (CEZ), and calibrated using INTCAL 13 and SwissCal 1.0.

MAMS	Material	^{14}C age (years)	Error (years)	$\delta^{13}C$ ($^0/00$)	1σ Cal. BCE (years)	2σ Cal. BCE (years)	C (%)
27 110	peat	9876	35	−25.0	9353–9283	9402–9265	52.8
27 111	charcoal	9408	34	−30.7	8730–8638	8785–8612	59.7
27 112	wood fragments	8702	33	−26.6	7736–7613	7811–7599	56.4
27 113	wood fragments	5152	27	−27.7	3984–3951	4038–3816	51.5
27 114	charcoal	4474	27	−31.7	3327–3095	3337–3029	2.2
27 115	charcoal	3604	25	−28.1	2015–1924	2026–1895	38.4

not contain any organic remnants, with the exception of fine roots.

– The loamy sands are sporadically covered by peat layers, where C_{org} values reach > 30 %, and the pH is < 3 (Fig. 5). The peat is compacted and contains plant material mostly consisting of *Carex* species. Other plants which could be identified were *Betula* spec. and some herbs like *Comarum palustre* and *Filipendula ulmaria*, indicating the existence of a *Carex* peat. Radiocarbon dates prove a Preboreal age of the peat layers (Fig. 4 and Table 1): peat fragments date between 9402 and 9265 cal. BCE, while the charcoal has a younger age of 8785–8612 cal. BCE. In contrast, dated wood pieces probably have their origin in roots and are about 1000 years younger.

– A black clay ca. 25 cm thick covers the loamy sand and the peat. Clay contents > 80 % demonstrate calm sedimentation conditions during its deposition. pH values rise to > 4, and C_{org} values are > 6 %. Root traces start at the top and pass downwards through the black clay layer. Plant macro remains could not be found, with the exception of root fragments and one charcoal piece. The root fragments gave a radiocarbon age of 4038–3816 cal. BCE (Fig. 4). The lowest part of the thin section, representing the upper part of the black clay, was made up of dark-grey-coloured, very fine-grained material (fine silt and clay). The microstructure of the sediment was spongy, as it mainly consisted of more or less oval and round-shaped voids that were encircled by filigree sediment covers and bridges between the covered voids (Fig. 6a, b). Their shape implies its genesis by plant pseudomorphs: plants (stems) were embedded into the sediments and subsequently completely decomposed so that only the embedding material was preserved. Plants standing upright would have created vertical structures. Therefore, the horizontal pseudomorphs suggest a surface-parallel bedding of the plant stems. This process is regularly observed during flood events. Obviously, the thin section illustrates the remnants of the last vegetation that covered the black clay before the deposition of overbank fines began.

– The black clay is overlain by overbank fines with a thickness of ca. 2.3 m. The deposits directly overlying the black clay already have a much higher silt content, while clay percentages drop from 80 % to around 50 % (Fig. 5). The colour changes from black (2.5Y2.5/1) to dark greyish brown (10YR4/2), while the pH values are between 4 and 5. The C_{org} content of the overbank fines fluctuates between 0.5 % and 1 %, and redoximorphic features prove temporal waterlogging. Charcoal pieces were taken from two levels of the overbank fines of Profile 2, i.e. at 117.1 and 117.8 m a.s.l. (Fig. 4). Both radiocarbon ages prove a Subboreal age (3337–3029, 2026–1895 cal. BCE; Table 1). The upper part of the thin section, representing the lowest overbank fines, shows closely packed fine-grained sediments. The material has a light grey colour with dark-grey-coloured channel infillings, consisting of the underlying black clay that was mixed in by bioturbation (Fig. 6). Furthermore, abundant biogenic voids underline a high intensity of bioturbation processes. The grey colour of the sediments is mainly a consequence of reducing conditions due to a high groundwater level. Nevertheless, the thin section reveals features of groundwater oscillations: larger voids allowing oxygen intrusion into the sediment display coatings, hypocoatings and fibrous crystals of ferric oxides and hydroxides (Fig. 6e, f).

– Above the lower level of overbank fines with an Atlantic to Subboreal age, a lot of potsherds of the Slavic period (ca. 900–1000 CE) mark the base of ca. 1 m of loamy material that was deposited during the last ca. 1000 years (Fig. 3). Higher sand values below and above the Slavic layer prove less calm conditions during the sedimentation process (Fig. 5). Missing settlement features give evidence for just a short period of human activity on the valley floor during the Slavic period.

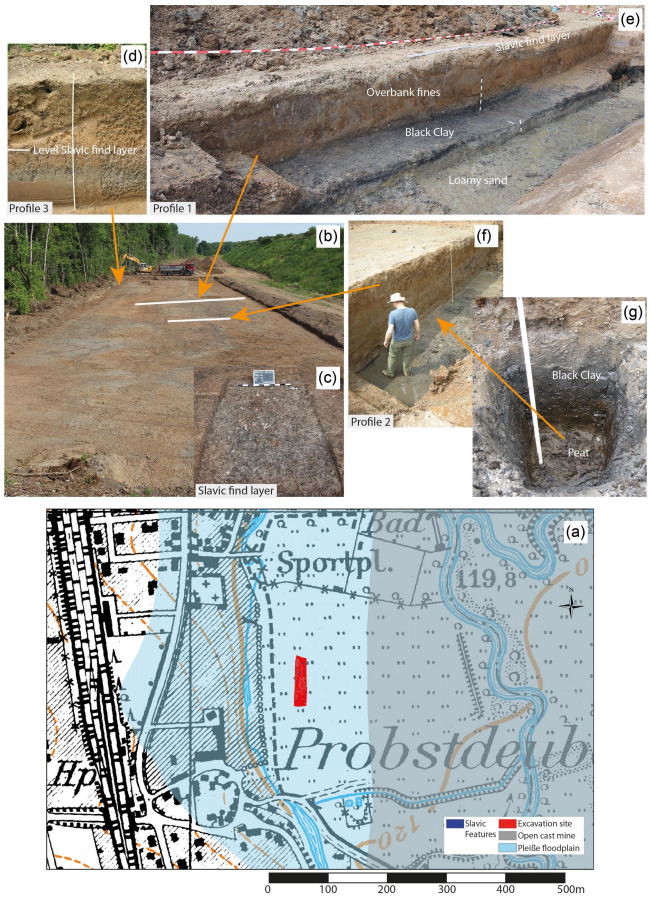

Figure 3. The excavation site, the profiles and the sediments near Probstdeuben. **(a)** The excavation site in the floodplain and the topographic situation during the first half of the last century (Geodaten© Staatsbetrieb Geoinformation und Vermessung Sachsen 2018). **(b)** The excavation site after removal of ca. 1 m of overbank fines by an excavator with the positions of the three profiles. **(c)** Slavic finds in the overbank fines ca. 1 m below the recent surface. **(d)** The uppermost overbank fines with the level of the Slavic find layer in Profile 3. **(e)** Profile 1 with the waterlogged loamy sands that are covered by the black clay and overbank fines. **(f)** Profile 2 with the black clay at the bottom. In a small hand-dug pit beneath the base of the profile a peat layer was found under the black clay **(g)**.

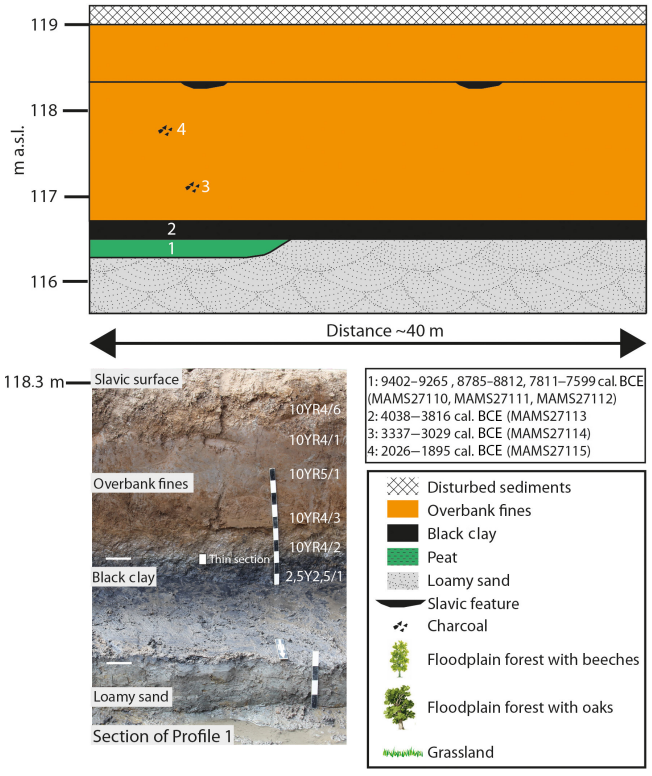

Figure 4. The valley sediments of the Pleiße according to Profile 1 to 3 with ^{14}C ages and the position of the thin section.

5 Discussion

5.1 Deposition of peat and black clay sediments during the Early to Middle Holocene

The oldest Holocene sediments in the lower Pleiße valley are peats that developed in small depressions of the Weichselian valley floor during the Preboreal period (Fig. 7a). Similar layers were formerly also described by Neumeister (1964) and Händel (1967). Organic sediments in the same stratigraphic position are also known from the lower Weiße Elster valley (Hiller et al., 1991; Tinapp, 2002), and organic deposition since that period is also known from other European catchments (Rittweger, 2000; Notebaert et al., 2018). Probably wetter conditions and higher groundwater levels in the valleys during the Preboreal resulted in the formation of many small peat layers on the Weichselian sediment base.

Sedimentation of the black clay in the Pleiße valley started during the Boreal and stopped during the Atlantic period when it was covered by overbank fines. According to the high clay content we assume mainly limnic conditions during the time of its sedimentation. According to Neumeister (1964) our investigations confirm that the black clay is pedologically a gyttja; i.e. it was formed under waterlogging conditions. The black clay discordantly covers the Weichselian sand and the Preboreal peat (Fig. 7b). Deposition of these more limnic sediments with a lower organic content during the Boreal compared with the Preboreal indicates a change towards more humid environmental conditions on the valley floor of the lower Pleiße River. However, iron and manganese features and roots that start in the black clay and reach the underlying loamy Weichselian sands also prove temporal drier periods. It is likely that the repeated changes of wetter and drier conditions on the valley floor were caused by fluctuations of the water table of the river. A similar black clay layer was not found in the neighbouring lower Weiße Elster river system. There, overbank fines directly cover Weichselian sand and gravel and sporadically also Preboreal peats (Hiller et al., 1991; Tinapp, 2002). We assume that the val-

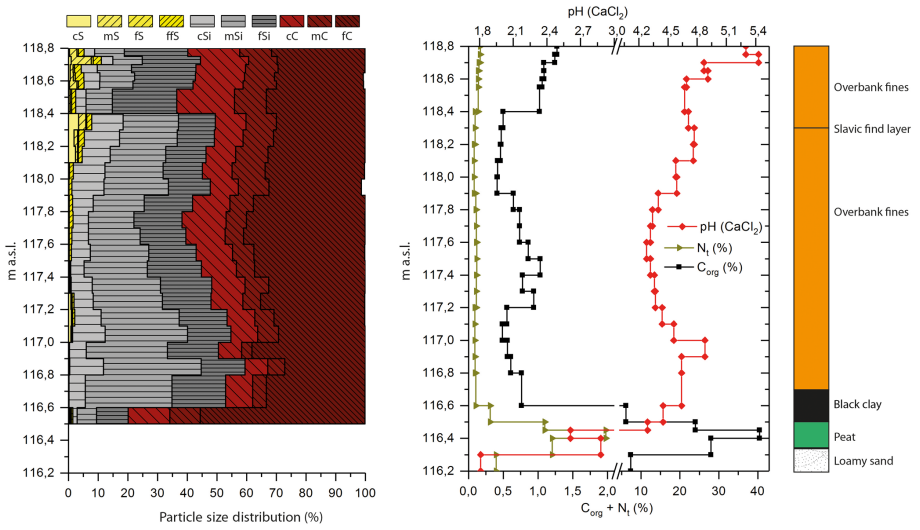

Figure 5. Particle size distribution, pH values and organic carbon of the sediments of Profile 1 to 3.

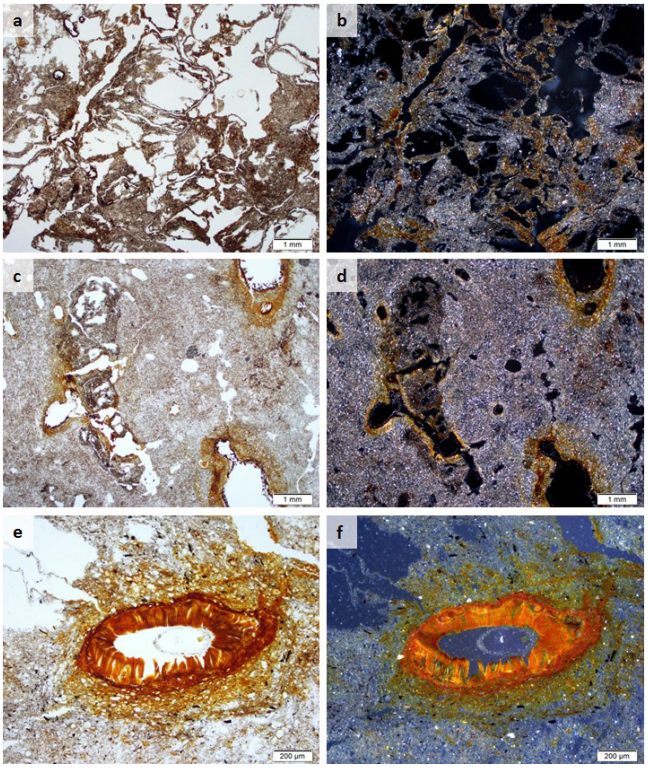

Figure 6. Microphotographs of the black clay (**a**, **b**) and the oldest overbank fines (**c**–**f**). **(a)** Voids encircled by filigree sediment covers and bridges between the covered voids (PPL). **(b)** Like **(a)** (XPL). **(c)** Light-grey-coloured material with dark-grey-coloured channel infillings consisting of the underlying black clay mixed in by bioturbation (PPL). **(d)** Like **(c)** (XPL). **(e)** Ferric coating, hypocoating and fibrous crystals of goethite (PPL). **(f)** Like **(e)** (OIL).

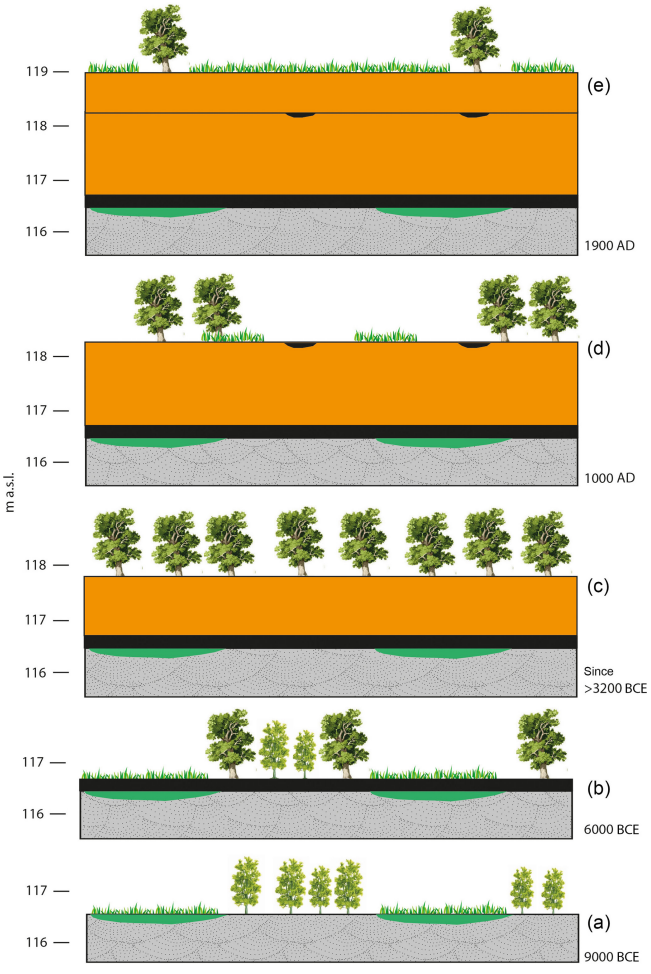

Figure 7. Holocene floodplain development of the lower Pleiße in five stages (legend in Fig. 4).

ley of the lower Weiße Elster, 2 km wide, was better drained than the lower Pleiße valley with a width of only ca. 1 km, and therefore a black clay could not develop in the former. It is also possible that the very slight slope of less than 1 % from here towards the drainage base a few kilometres in the north that is formed by the Weiße Elster valley stimulated the temporary development of limnic conditions in the lower Pleiße valley, allowing the deposition of the black clay layer.

It can be questioned whether black Holocene floodplain sediments should generally be interpreted as "Black Floodplain Soils" (Rittweger, 2000). However, the widespread existence of black-coloured organic-rich and clayey sediments in the same stratigraphic positions of different loess-influenced central European floodplains (Brunnacker, 1959; Schirmer, 1983; Bork, 1983; Brosche, 1984; Pretzsch, 1994; Schellmann, 1994; Hilgart, 1995; Rittweger, 2000; Bos et al., 2008; Brown et al., 2018) suggests similar conditions during the Boreal and Atlantic period for central Europe: wet valley floors and high organic load obviously caused the formation of clay-rich limnic layers with high contents of organic carbon. Rittweger (2000) discussed Chernozem-derived material as one factor in the formation of these dark layers. However, Chernozem and Phaeozem soils are found in the catchment of the lower Weiße Elster valley where no black clay was formed (Tinapp et al., 2008). In contrast, for the Pleiße catchment where a black clay exists such soils do not exist today. Instead, Stagnogleys and Luvisols are the main soil types in the catchment of the lower Pleiße River and probably also existed prior to Neolithic settlement (von Suchodoletz et al., 2019). Therefore, for the lower Pleiße valley a genesis of the black clay from Chernozem- and Phaeozem-derived material can clearly be rejected.

5.2 Alluvial overbank sedimentation since the Neolithic period

The covering of the black clay by ca. 2.3 m of younger overbank deposits indicates an environmental change at all sites: the sedimentation of the black clay in an environment with fluctuating water tables in the floodplain passed over into the deposition of more silty and sandy material. Human deforestation and agricultural land use in the catchment of the Pleiße river since 5500 BCE obviously resulted in the aggradation of coarser-grained and less organic overbank deposits that started between since ca. 4000 and ca. 3200 BCE (Fig. 7c and d). The growing thickness of the overbank fines led to less wet conditions and a more frequently dry topsoil. Similar to our results Rittweger (2000) dated the so-called Black Floodplain Soil into the Boreal and Atlantic period. He suggested relatively dry conditions after its formation, since the Black Floodplain Soil was strongly overprinted by soil development, and archaeological features on its surface proved human activities in the floodplain. However, that could be denied for the lower Pleiße valley: during the Early Neolithic period the floodplain was muddy and wet, and only the continuous rise of the valley floors by subsequent overbank deposition allowed longer-lasting anthropogenic activities in the floodplain during a later period. Accordingly, the oldest archaeological features in the lower Pleiße valley originate from the Bronze Age (Grahmann and Braune, 1933). The moment of sedimentation change from the black clay to the overlying overbank deposits could obviously be detected by our thin section analysis: holes at the surface of the black clay must have been caused by rotten plant material (Fig. 6). These should derive from sedges that were bent over during a flood event and buried by the oldest overbank fines. During subsequent drier periods the organic material was decomposed, whereas the holes remained since bioturbation was prevented by the new sediment cover.

Similar to the neighbouring lower Weiße Elster floodplain where significant overbank sedimentation was recorded in ca. 4500 to 4000 BCE (Tinapp et al., 2008), this demonstrates a start of overbank sedimentation during the Neolithic period. Therefore, the fairly early start of overbank sedimentation obviously represents a regional reaction of the landscape in this part of central Germany following Neolithic settlement activities (Fig. 8). This demonstrates the dominant influence of quite intensive human activity on the development of overbank fines (Hiller et al., 1991; Tinapp, 2002; Tinapp et al., 2008), especially against the background that major climatic changes are not detectable in central Germany for this time (Litt, 1994; Wennrich, 2005).

The start of overbank sedimentation in central Germany already during the Neolithic period was significantly earlier than in many other catchments of central Europe, where despite Neolithic settlement activities this process started at the earliest between ca. 4.2 and ca. 2 ka (Rittweger, 2000; Niller, 2001; Mäckel et al., 2002; Fuchs et al., 2011; Houben et al., 2013; Notebaert et al., 2018; Brown et al., 2018). Delayed overbank sedimentation compared with the onset of Neolithic land use and the deposition of corresponding colluvial slope sediments in the latter is explained with temporally variable hydrosedimentary connectivity between hillslopes and floodplains, leading to a sediment cascade in the landscape (Brown, 2009; Fuchs et al., 2011; Houben et al., 2013). In contrast, the early start of overbank deposition in the Weiße Elster catchment was explained with good hillslope–channel coupling due to missing small sediment traps along the lower Weiße Elster valley since the Neolithic period (Tinapp et al., 2008). However, given the obviously regional character of early overbank sedimentation in this part of central Germany we think that other factors could have also caused the high regional Neolithic sediment connectivity. Possible factors could, for example, have been the spatial structure of regional Neolithic settlement activity or climatic factors in this relatively dry area with precipitation down to 500 mm a^{-1}. However, these are only hypotheses so far that need further investigations.

No clear sediment unconformities were detected in the overbank fines, although geomorphologically stable periods

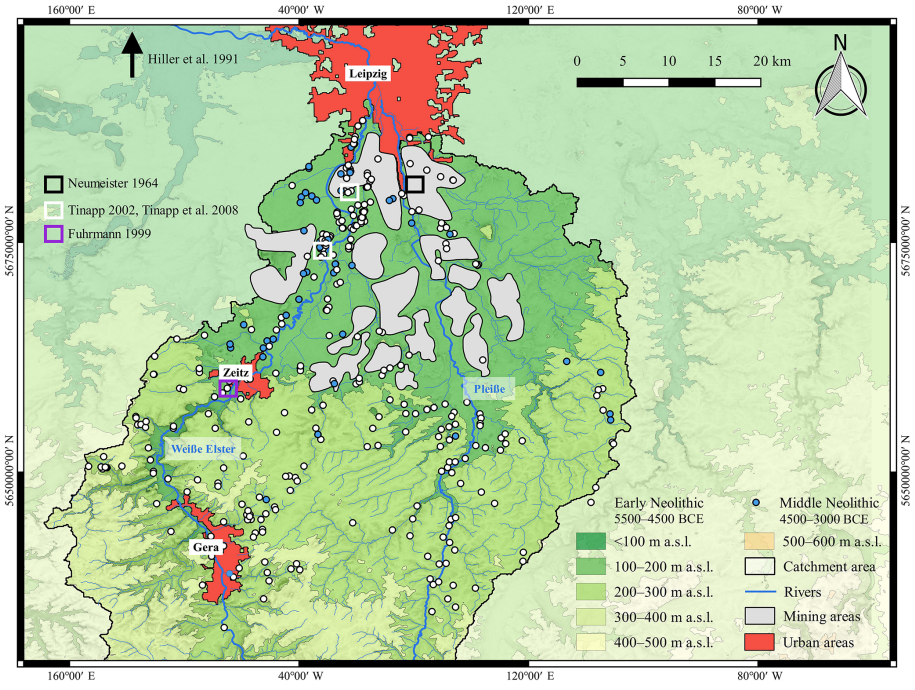

Figure 8. Early and Middle Neolithic find spots around the valleys of Weiße Elster and Pleiße and the positions of the main study sites. Mining activities destroyed great parts of the lower Pleiße floodplain and the surrounding plains, and most of these areas were archaeologically not investigated prior to 1993. The extent of the open cast mines on the map dates back to the year 1990 (Standke et al., 2010).

with less flooding often led to soil formation with the accumulation of organic material in floodplains of other regions (Zielhofer et al., 2009; May et al., 2015; von Suchodoletz et al., 2018b). Even at the Slavic level initial enrichment of organic material could not be detected (Fig. 5). Generally, unlike in many other river systems of western central Europe (Hoffmann et al., 2008; Fuchs et al., 2011; Houben et al., 2013; Notebaert et al., 2018) no strong increase of overbank sedimentation during the last 1000 years was observed along the lower Pleiße and Weiße Elster River: whereas at the lower Weiße Elster River ca. 0.8–1 m of overbank sediments compared with a total thickness of ca. 3–4 m was deposited over the last 1000 years (Fig. 7e), along the lower Pleiße River ca. 1 m of overbank sediments compared with a total thickness of ca. 2.3 m was observed. Thus, more than half of the fine-grained sediment cover of these valleys was formed prior to the Middle Ages. Therefore, unlike in most other river systems of central Europe this demonstrates a relatively continuous high regional sediment connectivity in this part of central Germany since the Neolithic period.

6 Conclusions

Our investigations in the lower Pleiße valley were conducted at a mostly undisturbed site with predominant sedimentation and negligible erosion processes during the Holocene. We compared our results with those of Neumeister (1964) that were carried out less than 100 m east of our study site and that were based on field investigations that extended over ca. 900 m. This comparison demonstrates that our investigated stratigraphy is representative of this part of the lower Pleiße valley, so we were able to build up a well-based reconstruction of its Holocene landscape development. In doing so, it was possible to define the turning point from extremely clayey and organic-rich, mostly limnic sedimentation (black clay) in the Boreal and Atlantic periods towards the deposition of coarser-grained and less organic overbank fines during the following period. This change occurred more than 1000 years after the beginning of Early Neolithic settlement between 4000 and 3300 BCE and was obviously linked with land clearance by these first farmers. The fairly early start of overbank sedimentation during the Neolithic period seems to be the exception rather than the rule in central Europe. During the following 6000 years sedimentation conditions did not change significantly (Fig. 4). Even initial organic enrichment could not be detected, although some geomorphologically stable periods with less flooding should have led to initial soil development. We also did not find a strong increase of the sediment deposition rates during and after the Middle Ages that was detected in many other catchments of central Europe, since more than half of the sediment cover of the lower Pleiße valley was deposited prior to that period. Further research in other river catchments of central Europe is needed to prove or to deny the singularity of the Holocene sedimentation history in the river catchments of lower Pleiße and Weiße Elster.

Data availability. Data relating to this paper can be found in the Supplement.

Supplement. The supplement related to this article is available online at: https://doi.org/10.5194/egqsj-68-95-2019-supplement.

Author contributions. CT and HS organized the project. CT, SH and HvS carried out the fieldwork. The concept and structure of the paper were organized by CT and HvS. The laboratory work was done by CH (plant macro remains) and BS (geochemistry, particle size distribution). Thin section analysis were carried out by SH. Archaeological investigations were performed by HS and JM. CT and HvS took the lead in writing the manuscript, with input from SH, CH, BS and HS. All authors discussed the results and contributed to the final manuscript.

Competing interests. The authors declare that they have no conflict of interest.

Special issue statement. This article is part of the special issue "Connecting disciplines – Quaternary archives and geomorphological processes in a changing environment". It is a result of the First Central European Conference on Geomorphology and Quaternary Sciences, Gießen, Germany, 23–27 September 2018.

Acknowledgements. We thank Yvonne Heine and the excavation team. Constructive comments by Knut Kaiser and an anonymous reviewer helped us to improve the manuscript.

References

Bork, H.-R.: Die holozäne Relief- und Bodenentwicklung in Lössgebieten, Catena, Suppl.-Band, 1–93, 1983.

Bos, J. A. A., Dambeck, R., Kalis, A. J., Schweizer, A., and Thiemeyer, H.: Palaeoenvironmental changes and vegetation history of the northern Upper Rhine Graben (southwestern Germany) since the Lateglacial, Netherlands J. Geosc. Geol. Mijnb., 87, 65–88, 2008.

Bridgland, D. and Westaway, R.: Climatically controlled river terrace staircases: A worldwide Quaternary phenomenon, Geomorphology, 98, 285–315, 2008.

Brosche, K. H.: Zur jungpleistozänen und holozänen Entwicklung des Werratales zwischen Hannoversch Münden und Phillipsthal, Eiszeitalter u. Gegenwart, 34, 105–129, 1984.

Brown, A. G.: Colluvial and alluvial response to land use change in Midland England: an integrated geoarchaeological approach, Geomorphology, 108, 92–106, 2009.

Brown, A. G., Lespez, L., Sear, D. A., Macaire, J.-J., Houben, P., Klimek, K., Brazier, R. E., Van Oost, K., and Pears, B.: Natural vs anthropogenic streams in Europe: History, ecology and implications for restoration, river-rewilding and riverine ecosystem services, Earth-Sci. Rev., 180, 185–205, 2018.

Brunnacker, K.: Junge Deckschichten und 'schwarzerdeähnliche' Böden bei Schweinfurt, Geol. Bl. Nordost-Bayern, 9, 2–14, 1959.

Bullock, P., Fedoroff, N., Jongerius, A., Stoops, G., and Tursina, T. (Eds.): Handbook for soil thin section description, Waine Research Publications, Albrighton, Wolverhampton, 1985.

Cappers, R. T. J., Bekker, R. M., and Jans, J. E. A.: Digitale zadenatlas van Nederland – Digital seed atlas of the Netherlands, Groningen Archaeological Studies 4, 2nd edn., Barkhuis Publishing, Eelde, 2012.

Eissmann, L.: Quaternary geology of eastern Germany (Saxony, Saxon-Anhalt, South Brandenburg, Thüringia, type area of the Elsterian and Saalian stages in Europe, Quat. Sci. Rev., 21, 1275–1346, 2002.

Erkens, G., Dambeck, R., Volleberg, K. P., Bouman, M. T. I. J., Bos, J. A. A., Cohen, K. M., Wallinga, J., and Hoek, W. Z.: Fluvial terrace formation in the northern Upper Rhine Graben during the last 20 000 years as a result of allogenic controls and autogenic evolution, Geomorphology, 103, 476–495, 2009.

Faust, D. and Wolf, D.: Interpreting drivers of change in fluvial archives of the Western Mediterranean – A critical review, Earth-Sci. Rev., 174, 53–83, 2017.

Fuchs, M., Will, M., Kunert, E., Kreutzer, S., Fischer, M., and Reverman, R.: The temporal and spatial quantification of Holocene sediment dynamics in a meso-scale catchment in northern Bavaria, Germany, The Holocene, 21, 1093–1104, 2011.

Fuhrmann, R.: Klimaschwankungen im Holozän nach Befunden aus Talsedimenten Mitteldeutschlands – Beiträge zur Klimageschichte und Stratigraphie des jüngeren Quartärs, Altenbg. nat.wiss. Forsch., 11, 3–41, 1999.

Fuhrmann, R.: Die Ostrakoden- und Molluskenfauna des Auelehmprofils Zeitz (Landkreis Burgenland) und ihre Aussage zum Klima sowie zur Landnutzung im jüngeren Holozän Mitteldeutschlands, Mauritiana, 20, 253–281, 2008.

Grahmann, R. and Braune, K.: Braune, Bronzezeitliche und slawische Herdstellen in der Pleißeaue bei Markkleeberg, "Die Fundpflege", Jg. 1, H. 6, Beitrag d. Mitteldt. Bl. f. Volkskunde, 1933.

Händel, D.: Das Holozän in den nordwestsächsischen Flußauen, Hercynia, Bd. 4 Leipzig, 2, 152–198, 1967.

Heynowski, R. and Reiß, R. (Eds): Atlas zur Geschichte und Landeskunde von Sachsen, Beiheft zur Karte BI 1.1-1.5, Ur- und Frühgeschichte Sachsens, Leipzig/Dresden, 2010.

Hilgart, M.: Die geomorphologische Entwicklung des Altmühl- und Donautales im Raum Dietfurt-Kelheim-Regensburg im jüngeren Quartär, Forschungen zur deutschen Landeskunde, 242, Deutsche Akademie für Landeskunde, Trier, 1995.

Hiller, A., Litt, T., and Eissmann, L.: Zur Entwicklung der jungquartären Tieflandstäler im Elbe-Saale-Gebiet unter besonderer Berücksichtigung von ^{14}C-Daten, Eiszeitalter u. Gegenwart, 41, 26–46, 1991.

Hoffmann, T., Lang, A., and Dikau, R.: Holocene river activity: Analysing ^{14}C-dated fluvial and colluvial sediments from Germany, Quaternary Sci. Rev., 27, 2031–2040, 2008.

Houben, P.: Sediment budget for five millennia of tillage in the Rockenberg catchment (Wetterau loess basin, Germany), Quaternary Sci. Rev., 52, 12–23, 2012.

Houben, P., Schmidt, M., Mauz, B., Stobbe, A., and Lang, A.: Asynchronous Holocene colluvial and alluvial aggradation: A matter of hydrosedimentary connectivity, The Holocene, 23, 544–555, 2013.

Kaiser, K., Lorenz, S., Germer, S., Juschus, O. Küster, M, Libra, J., Bens, O. and Hüttl, R. F.: Late Quaternary evolution of rivers, lakes and peatlands in northeast Germany reflecting past climatic and human impact – an overview, Quaternary Sci. J., 61, 2, 103–132, 2012.

Lauer, T. and Weiss, M.: Timing of the Saalian- and Elsterian glacial cycles and the implications for Middle- Pleistocene hominin presence in central Europe, Nature, Sci. Rep., 8, 5111, https://doi.org/10.1038/s41598-018-23541-w, 2018.

Litt, T.: Fresh investigations into the natural and anthropogenically influenced vegetation of the earlier Holocene in the Elbe-Saale Region, Central Germany, Veg. Hist. Archaeobot., 1, 69–74, 1992.

Litt, T.: Paläoökologie, Paläobotanik und Stratigraphie des Jungquartärs im nord-mitteleuropäischen Tiefland unter besonderer Berücksichtigung des Elbe-Saale-Gebietes, Dissertationes Botanicae, Halle, 227, 1994.

Mäckel, R., Schneider, R., Friedmann, A., and Seidel, J.: Environmental changes and human impact on the relief development in the Upper Rhine valley and Black Forest (South-West Germany) during the Holocene, Z. Geomorphol., Supplement 128, 31–45, 2002.

Mania, D.: Zur spät- und nacheiszeitlichen Besiedlung in ihrer Beziehung zur natürlichen Umwelt, in: Wissenschaftliche Beiträge der Martin-Luther-Universität Halle-Wittenberg 1980/6, Halle/S, 29–31, 1980.

May, J.-H., Plotzki, A., Rodrigues, L., Preusser, F., and Veit, H.: Holocene floodplain soils along the Río Mamoré, northern Bolivia, and their implications for understanding inundation and depositional patterns in seasonal wetland settings, Sediment. Geol., 330, 74–89, 2015.

Mol, J.: Weichselian and Holocene river dynamics in relation to climate change in the Halle-Leipziger Tieflandsbucht (Germany), Eiszeitalter und Gegenwart, 45, 32–41, 1995.

Neumeister, H.: Beiträge zum Auenlehmproblem des Pleiße- und Elstergebietes, Wiss. Veröff. Dt. Inst. Länderkde., 21, 65–132, 1964.

Niller, H. P.: Wandel prähistorischer Landschaften, Erdkunde, 55, 32–48, 2001.

Notebaert, B., Broothaerts, N., and Verstraeten, G.: Evidence of anthropogenic tipping points in fluvial dynamics in Europe, Global Planet. Change, 164, 27–38, 2018.

Oberdorfer, E.: Pflanzensoziologische Exkursionsflora für Deutschland und angrenzende Gebiete, 8th edn., Ulmer, Stuttgart, 2001.

Pretzsch, K.: Spätpleistozäne und holozäne Ablagerungen als Indikatoren der fluvialen Morphodynamik im Bereich der mittleren Leine, Göttinger Geogr. Abh., Göttingen, 99, 1994.

Rittweger, H.: The "Black Floodplain Soil" in the Amöneburger Becken, Germany: a lower Holocene marker horizon and indicator of an upper Atlantic to Subboreal dry period in Central Europe?, Catena, 41, 143–164, 2000.

Schellmann, W.: Die Talentwicklung der unteren Oberweser im jüngeren Quartär, Düsseld. Geogr. Schr., 34, 11–43, 1994.

Schirmer, W.: Die Talentwicklung an Main und Regnitz seit dem Hochwürm, Geol. Jahrb., 71, 11–43, 1983.

Standke, G., Escher, D., Fischer, J., and Rascher, J: Das Tertiär Nordwestsachsens, Ein geologischer Überblick, LfULG Sachsen, Dresden, 2010.

Starkel, L., Soja, R., and Michczynska, D. J.: Past hydrological events reflected in Holocene history of Polish rivers, Catena, 66, 24–33, 2006.

Stoops, G.: Guidelines for analysis and description of soil and regolith thin sections, Soil Science Society of America, Inc., Madison, 2003.

Tinapp, C: Geoarchäologische Untersuchungen zur holozänen Landschaftsentwicklung der südlichen Leipziger Tieflandsbucht, Trierer Geographische Studien, 26, Trier, 2002.

Tinapp, C. and Stäuble, H.: Auenentwicklung und Besiedlungsgeschichte im Tal der Weissen Elster südlich von Leipzig, Trierer Geographische Studien, 23, 31–48, 2000.

Tinapp, C., Meller, H., and Baumhauer, R.: Holocene accumulation of colluvial and alluvial sediments in the Weiße Elster river valley in Saxony, Germany, Archaeometry, 50, 696–709, 2008.

von Suchodoletz, H., Gärtner, A., Zielhofer, C., and Faust, D.: Eemian and post-Eemian fluvial dynamics in the Lesser Caucasus, Quaternary Sci. Rev., 191, 189–203, 2018a.

von Suchodoletz, H., Zielhofer, C., Hoth, S., Umlauft, J., Schneider, B., Zeeden, C., Sukhishvili, L., and Faust, D.: North Atlantic influence on Holocene flooding in the southern Greater Caucasus, The Holocene, 28, 609–620, 2018b.

von Suchodoletz, H., Tinapp, C., Lauer, T., Glaser, B., Stäuble, H., Kühn, P., and Zielhofer, C.: Distribution of Chernozems and Phaeozems in Central Germany during the Neolithic period, Quat. Int., in press, https://doi.org/10.1016/j.quaint.2017.10.041, 2019.

Wennrich, V., Wagner, B., Melles, M., and Morgenstern, P.: Late Glacial and Holocene history of former Salziger See, Central Germany, and its climatic and environmental implications, Int. J. Earth Sci. (Geol Rundsch), 94, 275–284, 2005.

Zielhofer, C., Recio-Espejo, J. M., Nunez-Granados, M. A., and Faust, D.: Durations of soil formation and soil development indices in a Holocene Mediterranean floodplain, Quaternary Int., 209, 44–65, 2009.

E&G Quaternary Sci. J., 68, 165–176, 2019
https://doi.org/10.5194/egqsj-68-165-2019

Open Access E&G Quaternary Science Journal

Research article

^{10}Be-based exploration of the timing of deglaciation in two selected areas of southern Norway

Philipp Marr[1], **Stefan Winkler**[2], **Steven A. Binnie**[3], **and Jörg Löffler**[1]

[1]Department of Geography, University of Bonn, Meckenheimer Allee 166, 53115 Bonn, Germany
[2]Department of Geography and Geology, University of Würzburg, Am Hubland, 97074 Würzburg, Germany
[3]Institute for Geology and Mineralogy, University of Cologne, Zülpicherstr., 49B, 50674 Cologne, Germany

Correspondence: Philipp Marr (marr@uni-bonn.de)

Relevant dates: Received: 18 January 2019 – Revised: 2 May 2019 – Accepted: 13 June 2019 – Published: 30 July 2019

How to cite: Marr, P., Winkler, S., Binnie, S. A., and Löffler, J.: ^{10}Be-based exploration of the timing of deglaciation in two selected areas of southern Norway, E&G Quaternary Sci. J., 68, 165–176, https://doi.org/10.5194/egqsj-68-165-2019, 2019.

Abstract: We present new ^{10}Be surface exposure ages from two selected locations in southern Norway. A total of five ^{10}Be samples allow a first assessment of local deglaciation dynamics of the Scandinavian Ice Sheet at Dalsnibba (1476 m a.s.l.) in southwestern Norway. The bedrock ages from the summit of Dalsnibba range from 13.3 ± 0.6 to 12.7 ± 0.5 ka and probably indicate the onset of deglaciation as a glacially transported boulder age (16.5 ± 0.6 ka) from the same elevation likely shows inheritance. These ages indicate initial deglaciation commencing at the end of the Bølling–Allerød interstadial ($\sim$ 14.7–12.9 kyr BP) and ice-free conditions at Dalsnibba's summit during the Younger Dryas. Bedrock samples at lower elevations imply vertical ice surface lowering down to 1334 m a.s.l. at 10.3 ± 0.5 ka and a longer overall period of downwasting than previously assumed. Two further ^{10}Be samples add to the existing chronology at Blåhø (1617 m a.s.l.) in south-central Norway. The ^{10}Be erratic boulder sample on the summit of Blåhø sample yields 20.9 ± 0.8 ka, whereas a ^{10}Be age of 46.4 ± 1.7 ka for exposed summit bedrock predates the Late Weichselian Maximum. This anomalously old bedrock age infers inherited cosmogenic nuclide concentrations and suggests low erosive cold-based ice cover during the Last Glacial Maximum. However, due to possible effects of cryoturbation and frost heave processes affecting the erratic boulder age and insufficient numbers of ^{10}Be samples, the glaciation history on Blåhø cannot conclusively be resolved. Comparing the different timing of deglaciation at both locations in a rather short west–east distance demonstrates the complex dynamics of deglaciation in relation to other areas in southern Norway.

Kurzfassung: Es werden neue ^{10}Be Oberflächenexpositionsdatierungsalter zweier ausgewählter Lokalitäten in Südnorwegen vorgestellt. Insgesamt fünf ^{10}Be Altersdatierungen erlauben eine erste Bewertung der lokalen Deglaziationsdynamiken des Skandinavischen Eisschildes auf Dalsnibba (1476 m ü.d.M., über dem Meeresspiegel) im westlichen Südnorwegen. Die Expositionsalter des anstehenden Grundgesteins zwischen 13.3 ± 0.6 und 12.7 ± 0.5 ka vom Gipfel der Dalsnibba indizieren den Beginn der Deglaziation, da das Alter des glazial transportierten Blocks (16.5 ± 0.6 ka) von ähnlicher Höhenlage stammt und dieser wahrscheinlich eine ererbte kosmogene Nuklidkonzentration besitzt. Dies

deutet auf eine beginnende initiale Deglaziation am Ende des Bølling–Allerød interstadial (∼ 14.7–12.9 kyr BP) und einen eisfreien Gipfel der Dalsnibba während der Jüngeren Dryas hin. Expositionsalter für Grundgestein in niedrigerer Höhenlage weisen auf ein anschließendes Absinken der vertikalen Eisausdehnung auf 1334 m ü.d.M. um 10.3 ± 0.5 ka sowie auf eine länger anhaltende Eisschmelzperiode als bisher angenommen hin. Es werden zwei zusätzliche Datierungen zur bereits bestehenden Deglaziationschronologie von Blåhø (1617 m ü.d.M.) im zentralen Südnorwegen präsentiert. Das ^{10}Be Alter eines erratischen Blocks auf Blåhø ergibt 20.9 ± 0.8 ka und das erzielte Alter von 46.4 ± 1.7 ka eines Grundgesteinsaufschluss am Gipfel liegt zeitlich vor dem Spätweichsel-Maximum (LGM). Das ungewöhnlich hohe Grundgesteinsalter lässt sich auf eine ererbte kosmogene Nuklidkonzentration sowie eine Bedeckung mit wenig erosivem, kaltbasalen Eis auf Blåhø während des LGM schließen. Allerdings ist eine abschließende Bewertung der Vergletscherungsgeschichte Blåhø schwierig, da mögliche Effekte von Kryoturbation und Frosthebungsprozessen das Alter des Blocks beeinflusst haben könnten und die Anzahl der Expositionsdatierungen unzureichend ist. Der Vergleich des unterschiedlichen Beginns der Deglaziation in beiden Untersuchungsgebieten in geringer West–Ost Distanz deutet auf komplexe dynamische Deglaziationsprozesse in Relation zu anderen Gebieten in Südnorwegen hin.

1 Introduction

The growth and decay of Quaternary glaciers and ice sheets has had fundamental implications for environmental changes worldwide (Ehlers and Gibbard, 2007). Based on numerical terrestrial or marine radiocarbon and cosmogenic nuclide surface exposure ages in addition to pollen stratigraphy, the chronology of the last deglaciation of the Scandinavian Ice Sheet (SIS) following the Last Glacial Maximum (LGM, 26.5–20 kyr; Clark et al., 2009) and related ice marginal positions in Norway are generally perceived as well constrained (Hughes et al., 2016; Stroeven et al., 2016; Patton et al., 2017). The detailed vertical extent of the SIS in Norway for this period remains, however, uncertain over large areas. Scenarios ranging from maximum models with a central ice dome (Sollid and Reite, 1983; Mangerud, 2004) to minimum models implying a thin multi-domed ice sheet and larger ice-free areas (Dahl et al., 1997; Wohlfarth, 2010) are the topic of ongoing discussion. The knowledge of the vertical dimension of the LGM ice sheet could provide crucial information on palaeoenvironmental factors like sea-level changes, atmospheric and oceanic circulation, (de-)glaciation patterns, ice-sheet erosion rates, landscape evolution, and englacial thermal boundaries (Winguth et al., 2005; Rinterknecht et al., 2006; Goehring et al., 2008). The interpretation of bedrock with different degree of weathering in mountain areas affected by Quaternary glaciation can, therefore, be important for determining ice-sheet behaviour and thickness during the last glaciation periods (Brook et al., 1996; Briner et al., 2006; McCarroll, 2016). There are several concepts to explain the limit between differently weathered bedrock (trimline) separating highly weathered uplands comprising blockfields and tors from relatively unweathered lower exposures of freshly eroded glacial features (Rea et al., 1996; Briner et al., 2006). The two most discussed scenarios suggest on the one hand the preservation of highly weathered uplands by a cover of non-erosive cold-based ice; thus the trimline would reflect an englacial thermal boundary. The alternative explanation suggests that the trimline represents the true upper vertical ice surface and erosional limit of a former warm-based ice sheet with ice-free nunatak areas above that boundary (Stroeven et al., 2002).

The rise of terrestrial cosmogenic nuclides (TCNs) for surface exposure dating as a key tool to yield numerical ages of landforms and bedrock surfaces representing specific glacier and ice sheet dynamics has revolutionized deglaciation chronologies (Dunai, 2010), especially for settings where organic material is not available for dating. TCNs have been frequently used to reconstruct glacial chronologies worldwide, often utilizing ages derived from erratic boulders or bedrock surfaces (Dunai, 2010; Stroeven et al., 2016, and references therein). To successfully apply TCNs and to establish timing and rates of the last deglaciation, it is necessary that any cosmogenic nuclide produced prior to the last deglaciation has been removed by erosion (Briner et al., 2006; Dunai, 2010). Consequently, the erosive capacity of an ice sheet is mirrored in the concentration of cosmogenic nuclides, as the degree of erosion governs the level of inheritance (Harbor et al., 2006). Erosive capacity is largely causally connected to the basal temperature regime of the ice and its related ability to move by basal sliding. Therefore, cosmogenic nuclide concentrations may also serve as a tool to identify englacial thermal boundaries between warm-based and cold-based zones or estimate palaeo-ice thickness of entirely warm-based glaciers (Kleman, 1994).

The SIS constituted the largest unit of the Eurasian ice sheet (Hughes et al., 2016). Despite the progress with reconstructing volume, margins and timing, the information from terrestrial sources about the former ice cover is limited (Patton et al., 2016). Only a few deglaciation studies have

been carried out in the Geiranger Fjord area in southwestern Norway, where our first selected site, Dalsnibba, is located (e.g. Fareth, 1987; Aarseth et al., 1997). These studies have mostly relied on ^{14}C dates which have repeatedly been questioned (e.g. Donner, 1996). Hence, only limited numerical age data are available and there is a need for more reliable data for a better understanding of deglaciation dynamics in this area. Our second selected site at Blåhø was previously studied by several authors focussing on deglaciation following the LGM (e.g. Nesje et al., 1994; Goehring et al., 2008; Marr et al., 2018). We provide additional ages from an erratic boulder and from a bedrock outcrop to improve the image of the glaciation history.

In the wake of growing evidence for a more dynamic SIS through the last glacial cycle (Rinterknecht et al., 2006; Mangerud et al., 2010), it is essential to establish a robust deglaciation chronology, particularly for its inner mountainous region, to understand landform evolution and ice sheet dynamics. Given the importance of ice sheets with respect to the climate system, a better understanding of their evolution and the rate and timing of their ice retreat across the mountainous parts of southern Norway is necessary. Here, we report cosmogenic ^{10}Be surface exposure ages from boulder and bedrock surfaces of two selected mountain sites in southwestern and south-central Norway to improve our knowledge on the (de)glaciation history (Fig. 1). Our main study objectives were as follows:

1. to apply terrestrial cosmogenic ^{10}Be dating and to determine ^{10}Be surface exposure ages from the collected boulder and bedrock samples
2. to present the first estimate for the timing of initial local deglaciation for Dalsnibba in Opplendskedalen based on ^{10}Be
3. to assess and further improve the existing deglaciation chronology for Blåhø in the light of new ^{10}Be ages presented in this study
4. to explore the ice sheet dynamics and characteristics during the deglaciation in the selected areas in southern Norway.

2 Study area

2.1 Dalsnibba

Dalsnibba (62°4′43 N, 7°17′35 E; 1476 m a.s.l.) is located in Opplendskedalen on the Geirangerfjellet in the western part of south-central Norway. The summit area is dominated by glacially eroded bedrock outcrops which are moderately weathered, but there is no blockfield on Dalsnibba. The general morphology was strongly influenced by Quaternary glaciations with well-developed glacial valleys and deep fjords constituting prevailing macro-landforms (Holtedahl, 1967; Klemsdal and Sjulsen, 1988). Four bedrock samples from glacially eroded bedrock surfaces and one glacially transported boulder sample taken at four elevations ranging from 1334 to 1476 m a.s.l. were analysed. We aimed for sampling along a vertical transect from Dalsnibba to the valley bottom of Opplendskedalen at ∼ 1050 m a.s.l. However, inaccessibility and/or inappropriate sampling sites prohibited us from doing so. Sub-oceanic climatic conditions prevail at the site with mean annual air temperature between 0 and 2 °C (1971–2000) and mean annual precipitation between 2000 and 3000 mm a^{-1} (1971–2000) (http://www.senorge.no, last access: 18 April 2019). The gneiss bedrock is mainly quartz dioritic to granitic and partly migmatitic and is part of the so-called Western Gneiss Region (Tveten et al., 1998). The sampled boulder had the equivalent lithological composition.

The ice retreat following the LGM probably saw the ice margin approaching the inner parts of Storfjorden during the Bølling–Allerød interstadial (∼ 14.7–12.9 kyr BP; Patton et al., 2017) when the glacier probably experienced several short standstills in the Geiranger Fjord (Longva et al., 2009). Glaciers readvanced during the Younger Dryas (YD, 12.9–11.7 cal. kyr BP; Lohne et al., 2013) and created moraines at the fjord mouth (Longva et al., 2009). Little is known about the vertical ice limit during the YD; Andersen et al. (1995) suggest a thickness of 800–1200 m in fjords that became ice-free during the Bølling–Allerød interstadial. The final deglaciation following the YD in the fjords in western Norway generally falls between 11.2 ± 0.4 and 10.9 ± 0.2 cal. kyr BP (cf. Nesje and Dahl, 1993; calibration from Hughes et al., 2016, applied).

2.2 Blåhø

Blåhø (61°53′51 N, 9°16′58 E; 1617 m a.s.l.) is located in Ottadalen in the central part of southern Norway. Smooth undulating surfaces at summit level are present, with three lower peaks – Rundhø (1556 m a.s.l.), Veslrundhø (1514 m a.s.l.) and Storhøi (1455 m a.s.l.) – part of the mountain ridge. The Blåhø summit is covered by an autochthonous blockfield extending down to a trimline at ∼ 1500 m a.s.l. (Nesje et al., 1994). Two samples were collected at the summit: one from a bedrock slab at the eastern edge of the blockfield and one from an erratic boulder. Climatic conditions are continental, with a mean annual temperature of −2 to −1 °C and a mean annual precipitation of 750–1000 mm a^{-1} at the summit and less than 500 mm a^{-1} (1971–2000) in the valley (http://www.senorge.no); it is among the driest areas in Norway. The area is dominated by quartz-rich Precambrian bedrock. The summit itself is dominated by meta-conglomerate and meta-sandstone on higher and lower slopes, respectively (Tveten et al., 1998). The sampled erratic boulder from the summit is quartz pegmatite.

The (de)glaciation history of Blåhø has attracted researchers' attention for decades (e.g. Nesje et al., 1994; Goehring et al., 2008; Marr and Löffler, 2017). It has been debated whether the summit was covered by cold-based ice

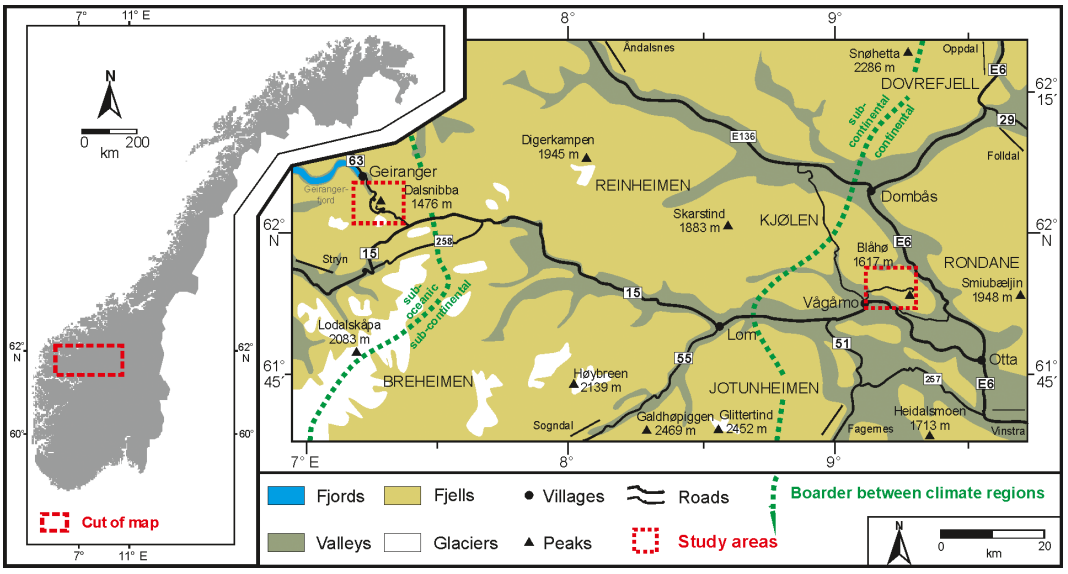

Figure 1. Study areas in southern Norway and the location of Dalsnibba in the west and Blåhø in the east (modified after Löffler and Pape, 2004).

(Goehring et al., 2008) or remained ice-free during the LGM (Nesje et al., 1994). Goehring et al. (2008) established a deglaciation chronology following the LGM, commencing at 25.1 ± 1.8 ka based on a ^{10}Be age from an erratic boulder at the summit to 11.7 ± 1.0 ka at the lowermost sample (1086 m a.s.l.).

3 Methods

3.1 Material and measurement

Surface exposure dating utilizes the in situ build-up of cosmogenic nuclides like ^{10}Be, ^{26}Al or ^{36}Cl by secondary cosmic rays to assess the duration of surface exposure at or near the earth's surface (Balco et al., 2008). The calculation of surface exposure ages using cosmogenic nuclide concentrations from glacial landforms is based on several assumptions. Exposure ages obtained using a single nuclide species are often considered minimum ages, as it is assumed that the samples were constantly exposed at the surface during one single period only, and that they neither contain an inherited nuclide concentration nor were they affected by significant snow shielding or erosion (Stroeven et al., 2002; Briner et al., 2006). In this study, we measured the ^{10}Be concentration of five bedrock (-bed) and two boulder (-bo) samples (Fig. 2). We targeted bedrock outcrops to provide additional new data to existing datasets (Goehring et al., 2008) and to explore the potential thermal and erosional properties of the ice sheet (Harbor et al., 2006; Dunai, 2010) because erratics on top of (glacially modified) bedrock may (Fabel et al., 2002; Dunai, 2010), but not necessarily, provide deglaciation ages (cf. Heymann et al., 2011). It has to be acknowledged, however, that our limited ^{10}Be ages ($n = 7$), especially in the eastern study area, allow us to improve and assess the existing deglaciation chronology rather than construct an independent one.

The samples were collected by hammer and chisel, and only boulders broader than 20 cm in diameter were selected for measurement to minimize the probability of post-depositional disturbance. All samples were obtained from flat surfaces (dip $< 5°$) with at least 25 cm distance from any edges for the large boulder and the longest distance possible from the edges of the smaller boulder. Both bedrock samples were obtained from locations with weathered surfaces and/or lichen cover to avoid surfaces so intensively weathered that slabs had potentially broken off the boulder surfaces (Fig. S5 in the Supplement). We sampled from local topographic highs to minimize the influence of snow cover. Geographical coordinates and elevations of sampling locations were recorded with a handheld GPS. Topographic shielding was derived from compass and clinometer measurements at each sample site.

After crushing and sieving, between ca. 10 to 44 g of purified quartz was extracted from the rock samples using the approach of Kohl and Nishiizumi (1992). Quartz samples were spiked with around 300 µg of a commercial beryllium solution (Scharlab, 1000 mg L^{-1}, density 1.02 g cm^{-3}) before being dissolved in a concentrated HF/HNO_3 mixture. Preparation of the purified quartz as AMS (accelerator mass spectrometry) targets was undertaken in tandem with a reagent blank. Target preparation chemistry was undertaken in the clean laboratory at the University of Cologne using the single-step column approach described by Binnie et al. (2015). Beryllium hydroxide was co-precipitated with Ag, according to Stone et al. (2004), for pressing

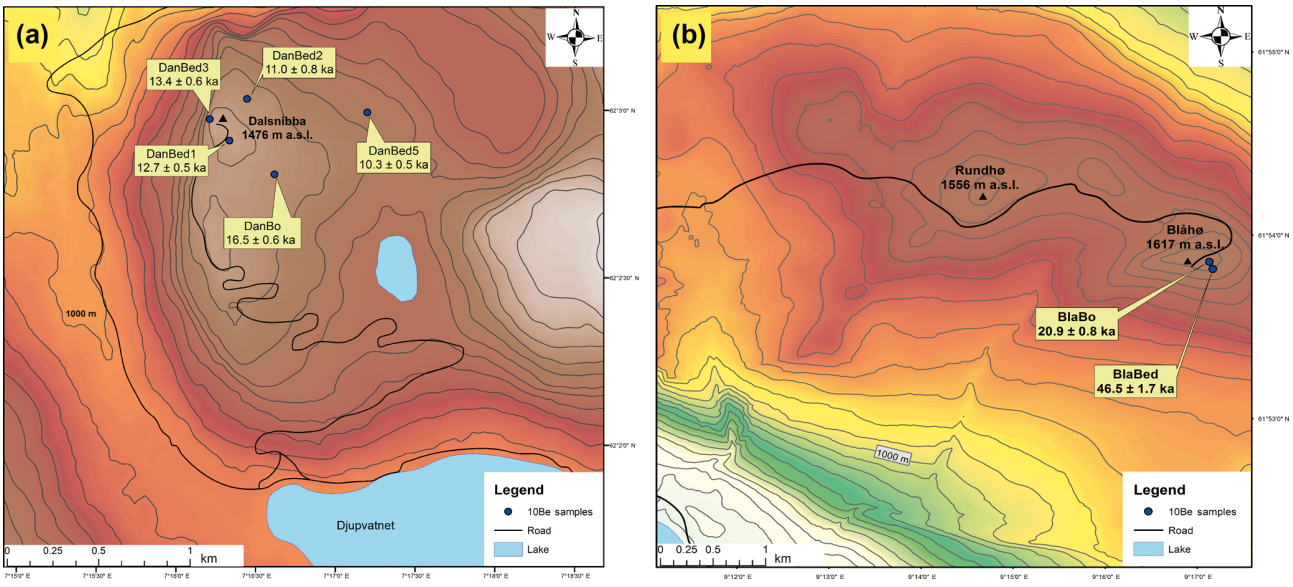

Figure 2. Detailed sampling locations at **(a)** Dalsnibba and **(b)** Blåhø. The bedrock samples in both study areas are labelled as -bed, the boulder samples as -bo. The calculated ^{10}Be ages of every sample are reported with 1σ uncertainty in ka. The contour line intervals are a distance of 50 m (source: http://www.kartverket.no, last access: 14 January 2019).

into AMS targets. Measurements of ^{10}Be/^{9}Be were undertaken at CologneAMS (Dewald et al., 2013), normalized to the revised standard values reported by Nishiizumi et al. (2007). Uncertainties in the blank-corrected ^{10}Be concentrations were derived by propagating (summing in quadrature) the 1 SD uncertainties in the AMS measurements of the blanks and the samples along with an estimated 1 % uncertainty (1 SD) in the mass of ^{9}Be added as a carrier.

3.2 Exposure age calculations

The ^{10}Be surface exposure ages were calculated with the online exposure age calculator version 3, formerly known as the CRONUS-Earth online exposure age calculator (Balco et al., 2008; Balco, 2017; http://hess.ess.washington.edu/, last access: 30 April 2019). The spallation-induced regional production rate for western Norway (normalized to sea-level high latitude) was used, as surfaces of unknown age can be dated more precisely due to the proximity of the calibration site (Goehring et al., 2012a, b). We applied the time-dependent LSD scaling model of Lifton et al. (2014) and used the 07KNSTD flag in the online calculator. A rock density of 2.6 g cm^{-3} was applied for all samples. We did not correct our ages for atmospheric pressure anomalies, temporal shielding by snow, sediment or vegetation. Erosion of 1 mm kyr^{-1} was applied in the online calculator, a comparable erosive capacity in summit areas as presented by Andersen et al. (2018a) for Reinheimen, close to Blåhø.

One parameter required within the calibration process for calculating ^{10}Be age is the elevation of the sampled bedrock or boulder surface. Any correction for the effect of post-glacial glacio-isostatic uplift is, however, quite challenging. No detailed local uplift data for Dalsnibba are available, but an estimate of ca. 100 m total uplift based on reports of former shoreline displacement or modelling attempts seems reasonable (Svendsen and Mangerud, 1987; Fjeldskaar et al., 2000; Steffen and Wu, 2011). For Blåhø, the total postglacial uplift is estimated at around 300 m (Morén and Påsse, 2001). However, this postglacial uplift cannot be described as a linear function as data from other localities in western Norway highlight (e.g. Fjeldskaar, 1994; Helle et al., 2007). An initial strong uplift during Allerød halted during the Younger Dryas and resumed after its termination with high uplift rates in the Early Holocene that subsequently significantly decreased (Lohne et al., 2007). According to newest modelling by Fjeldskaar and Amatonov (2018) the calculated uplift between Allerød and Younger Dryas at around Dalsnibba would summarize to around 50 m, i.e. half of the suggested total postglacial glacio-isostatic uplift. Because postglacial uplift first becomes relevant for ^{10}Be age calculation after exposure of the sampled surface, a circular reference emerges as surface exposure age (the unknown factor itself) needed to be known to precisely determine the amount of uplift that had already occurred according to established models (cf. Jones et al., 2019). To resolve this problem and simplify the correction for postglacial uplift, we assume initial fast uplift between 13 and 11.5 kyr totaling 50 m following Fjeldskaar and Amatonov (2018), followed by linear uplift during the Holocene that accounts for the remaining 50 m. The resulting reduction for sample elevation is ca. 30 m for Dalsnibba. Following similar considerations for Blåhø, a maximum reduction of 150 m in relation to modern elevation is

considered. However, the alternative influence of ca. 100 m reduction and no uplift correction are also assessed because of a likely non-linear uplift function, with maximum uplift during or immediately following deglaciation. The results of different uplift scenarios on Blåhø ages are presented in Table S3 in the Supplement. A reduction of sample elevation of ca. 100 m averaged over the entire surface exposure time seems reasonable and needs to be treated as a maximum value as Early Holocene uplift rates may be underestimated. Finally, with respect to all potential uncertainties with the calculation and calibration of ^{10}Be surface exposure age estimates (production rates, selected scaling schemes, etc.), our simplified postglacial uplift correction appears appropriate.

4 Results

AMS analysis gave ^{10}Be/^{9}Be ratios ranging from 1.65×10^{-12} to 8.69×10^{-14}. The reagent blank prepared alongside the samples gave a ^{10}Be/^{9}Be value of 6.47×10^{-15}, and the blank subtractions were < 4 % of the total number of ^{10}Be atoms measured in the samples, aside from sample DanBed2, which yielded less quartz, resulting in a blank subtraction that was 7.5 % of the total.

The cosmogenic exposure ages calculated for all samples from Dalsnibba and Blåhø are shown in Fig. 2 and Table 1. The boulder sample from the summit of Dalsnibba (DanBo) was the oldest from this site at 16.5 ± 0.6 ka. The ^{10}Be ages from Blåhø are 46.4 ± 1.7 ka (BlaBed) for the bedrock from the blockfield, whereas the boulder resting on the blockfield gave 20.9 ± 0.8 ka (BlaBo). The recalculated ages for Goehring et al. (2008) are presented in Table S4. Results for the effect of different glacio-isostatic uplift rates for Dalsnibba and Blåhø are presented in Tables S2 and S3. The considered uplift of 30 m vs. no uplift for Dalsnibba results in a ~ 3 % age increase. An uplift of 100 m at Blåhø leads to ~ 9 % older ages if compared to no correction for no uplift. For the maximum scenario of 150 m uplift the corresponding value is a ~ 14 % age increase.

5 Discussion

5.1 Methodological considerations and processes affecting ^{10}Be concentrations

We collected our rock samples from three different settings: bedrock outcrops from weathered debris/blockfields, glacially eroded bedrock surfaces, and boulders. Erosion of the sampled surfaces or undetected shielding (e.g. snow or vegetation cover) would lower the nuclide concentrations and consequently lead to underestimated ages (Stroeven et al., 2002; Hughes et al., 2016). Further, samples collected above the weathering limit, where outcrops are prone to surface degradation by severe frost weathering, also result in an underestimation of the true surface exposure (Brook et al., 1996).

The uplift model used by Goehring et al. (2008) applied on Blåhø reveals ~ 22 % older ages from high-elevation samples (> 1400 m a.s.l.). The recalculated data from Goehring et al. (2008) applying our uplift correction approach (with 100 m) give an estimated age difference of ~ 9 %. A total uplift of 150 m results in ~ 14 % older ages, which is closer to the value obtained by Goehring et al. (2008). For further discussion we rely on the most realistic option with a total uplift of 100 m for Blåhø.

The impact of snow cover on the ^{10}Be ages was estimated on the basis of Gosse and Philipps (2001) with recent snow conditions (data from http://www.senorge.no, averaged 1958–2019). By assuming 150 cm during 9–10 months in the west and 40 cm for 7–8 months (snow density 0.3 g cm^{-3}) in the east are representative of this interglacial, the ^{10}Be calculations could result in 18 %–20 % too young ages in the west and 4.2 %–4.8 % in the east. It needs, however, to be pointed out that it is impossible to assess whether modern snow conditions are representative of the conditions during the entire Holocene with its known climate variability (Nesje, 2009). We are aware that due to our limited dataset it is impossible to make conclusive statements about the glaciation history, especially for Blåhø, and to definitively identify geological bias and sample outliers (Stroeven et al., 2016). Furthermore, our restrictions to a single cosmogenic nuclide (^{10}Be) does not allow us to obtain information on any complex burial history that would require pairing ^{10}Be with other nuclides like ^{26}Al (Fabel et al., 2002). Nevertheless, we assume our results to have the capacity to contribute to the discussion of the timing of deglaciation in both areas because of their generally coherent ages in relation to previously published timings of deglaciation between 11.2 ± 0.4 and 10.9 ± 0.2 cal. kyr BP (cf. Nesje and Dahl, 1993; calibration from Hughes et al., 2016, applied) in the west and 21.8 ± 1.6 ka (Goehring et al., 2008, recalculated) in the east. Recent findings indicate the timing of the last deglaciation at 11 ± 0.2 ka in Reinheimen, located between our study areas (Andersen et al., 2018a).

5.2 Timing of deglaciation at Dalsnibba

The obtained ^{10}Be surface exposure ages from Dalsnibba offer the possibility of presenting the first age constraints for local deglaciation based on cosmogenic nuclides. The internal consistency of our ^{10}Be exposure ages from glacially eroded bedrock surfaces with their post-LGM age implies that glacial erosion was sufficient to remove any inherited nuclide concentration, and that the bedrock had been continuously exposed since. This supports the concept that glaciers in fjord landscapes were highly effective erosional agents and consequently warm-based (Aarseth et al., 1997; Matthews et al., 2017), especially in the valleys. This is in agreement with Landvik et al. (2005), who claim that frozen-bed conditions throughout the growth and decay of glaciers in coastal environments are unlikely. However, there are blockfield-covered summits between the fjords which are mostly located at a

Table 1. Sample and laboratory data and calculated ^{10}Be surface exposure ages.

Sample ID	Sample type	Latitude (°)	Longitude (°)	Altitude (m a.s.l.)	Sample thickness (cm)	Topographic shielding	Blank-corrected ^{10}Be conc. (10^5 at g^{-1})	Uncertainty (1σ) blank-corrected ^{10}Be conc. (10^3 at g^{-1})	External uncertainty (year)	Exposure age (year)
DanBed1	Bedrock	62.047639	7.274044	1476	4.8	0.999935	2.04	8	1100	12 700 ± 500
DanBed2	Bedrock	62.049925	7.275275	1418	3.5	0.999997	1.70	13	1200	11 000 ± 800
DanBed3	Bedrock	62.049314	7.270258	1464	5.9	0.999976	2.10	8	1200	13 300 ± 600
DanBed5	Bedrock	62.048295	7.287856	1334	4.7	0.999544	1.48	6	900	10 300 ± 500
DanBo	Boulder	61.897524	9.282407	1438	6.5	1	2.60	10	1500	16 500 ± 600
BlaBed	Bedrock	61.897700	9.284238	1615	2.4	1	7.49	26	4200	46 400 ± 1700
BlaBo	Boulder	62.044505	7.274839	1617	2.8	1	3.59	14	1900	20 900 ± 800

All ages are calculated using version 3 of the calculator code found at https://hess.ess.washington.edu/ (last access: 30 April 2019) (Balco et al., 2008; Balco, 2017). The western Norway ^{10}Be production rate (Goehring et al., 2012a, b) is applied with standard atmosphere and pressure "std" and a rock density of 2.6 g cm^{-3}. The time-dependent LSD scaling model of Lifton et al. (2014) was used. An uplift for 30 m for Dalsnibba and 100 m for Blåhø was assumed as well as an erosion of 1 mm kyr^{-1}.

higher altitude above the blockfield boundary, indicating that they were potentially protected by cold-based ice (Brook et al., 1996). The two uppermost bedrock ages and the glacial boulder are from comparable altitudinal settings, whereas the boulder is ∼ 3.8 to 3.2 ka older than the bedrock samples. This points to inherited cosmogenic nuclide inventory, and we therefore interpret the uppermost bedrock ages ranging from 13.3 ± 0.6 to 12.7 ± 0.5 ka as the timing of deglaciation on Dalsnibba. The bedrock ages mark the subsequent lowering of the ice surface; by plotting sample age with altitude (Fig. S4, $R^2 = 0.91$) the dynamics of ice surface lowering through time becomes clear. As the lowermost sample in this study is at 1334 m a.s.l. (which cannot cover the spectrum until the final downmelt of the ice), the exposure age of the valley bottom of Opplendskedalen (7.47 ± 0.73 ka at 1045 m a.s.l.; Marr et al., 2019) is used to determine the ice surface lowering rate. This gives an ice surface lowering of about 430 m within ∼ 5.8 ka. We calculate a thinning rate of ∼ 7.3 cm a^{-1}, which is comparable to the inland thinning rate determined by Linge et al. (2007) of 5 cm a^{-1}. We explain this with the persistence of a small ice cap on Dalsnibba and/or glacial readvances (with related fluctuations of the vertical ice limit) as the YD in the valleys probably led to a prolonged ice coverage. Our results from the western study site have three important implications in terms of the local glaciation history:

1. We suggest that the vertical ice limit must have exceeded 1476 m a.s.l. to be able to transport and deposit the boulder at its location. This contrasts to some extent with the view that ice thickness in coastal areas was supposed to be relatively thin due to effective ice drainage (Nesje et al., 1987), but it needs to be considered that Dalsnibba is located at the innermost fjord head of the Geiranger Fjord. Some authors anyway infer the possibility of nunataks on high coastal surfaces in western Norway (Mangerud, 2004; Winguth et al., 2005). In the light of our results, we have to reject the possibility that Dalsnibba was a nunatak during the LGM but suggest that the summit was covered by warm-based ice.

2. The timing of deglaciation between 13.3 ± 0.6 and 12.7±0.5 ka overlaps with the Bølling–Allerød interstadial, during which the summit of Dalsnibba was probably ice-free, and coincides with when the deglaciation reached Storfjord (Longva et al., 2009). Subsequently, Dalsnibba was not affected by the Younger Dryas readvance. Our results indicate that the deglaciation on Dalsnibba began at the end of the Bølling–Allerød or later, and Dalsnibba constituted a nunatak during the Younger Dryas.

3. There is only sparse information on the final deglaciation in the Scandinavian mountains; it is supposed to have commenced shortly after ∼ 10 ka (cf. Hughes et al., 2016). In Reinheimen, east of Dalsnibba, Andersen et al. (2018a) suggest 11 ± 0.2 ka as the timing of the last deglaciation. With our ^{10}Be results it is difficult to constrain the final deglaciation as our lowermost sample was collected at 1334 m a.s.l. However, we can clearly state that the ice persisted at ∼ 1330 m a.s.l. until 10.3 ± 0.5 ka when the final local deglaciation was partly inferred for the region 11.2±0.4 and 10.9±0.2 cal. kyr BP (cf. Nesje and Dahl, 1993; calibration from Hughes et al., 2016, applied). Therefore, our results open up the possibility that the ice coverage at Dalsnibba lasted longer than previously anticipated and also longer than in the Reinheimen area, unless the last part of deglaciation was characterized by a sudden collapse of the remaining ice.

5.3 Implications of ^{10}Be exposure ages from Blåhø

The ^{10}Be ages from the blockfield support the overall interpretation that these relict features have survived glaciation with little or no erosion, which indicates long-term landform preservation (Rea et al., 1996; Linge et al., 2006). By acknowledging the widely accepted scenario that anoma-

lously high ^{10}Be concentrations of bedrock samples, such as BlaBed, are the consequence of cold-based ice cover, the blockfield boundary might represent the former englacial boundary between cold-based and warm-based ice (Fabel et al., 2002; Marquette et al., 2004). This implies that the bedrock sample is likely compromised by inherited ^{10}Be from previous exposure followed by preservation beneath cold-based ice (Linge et al., 2006). This scenario appears realistic for the Blåhø bedrock sample, which, consequently, confirms the presence of non-erosive cold-based ice in line with several models suggesting thick ice coverage for this part of Norway (Stroeven et al., 2002; see Goehring et al., 2008). Notably, few of the weighted average bedrock ages from Reinheimen (Andersen et al., 2018a) show inheritance and provide ages of ∼ 11 ka. This may point towards different thermal basal ice conditions within a short distance. Cosmogenic ^{10}Be and ^{26}Al nuclide concentration data indicate that some repeatedly glaciated sites have experienced negligible glacial erosion over the entire Quaternary (Briner et al., 2006; Harbor et al., 2006). Therefore, the inherited cosmogenic nuclides must have accumulated during multiple phases of exposure and have subsequently been preserved by cold-based ice (Hughes et al., 2016). Subtracting the exposure age since deglaciation (∼ 21 ka) the surface experienced ∼ 25 kyr of prior exposure. By using the ice coverage modelled by Mangerud et al. (2010) and Hughes et al. (2016), we evaluate the ^{10}Be concentration accumulation over time (Stroeven et al., 2002). With this approach it seems possible that the bedrock sample on Blåhø was first exposed at the surface during the Early Weichselian or the Eemian interglacial. Some authors suggest even older blockfield ages (e.g. Linge et al., 2006). In this scenario, boulder ages are often considered to reflect the timing of deglaciation (Marquette et al., 2004; Goehring et al., 2008). Following this, our boulder age of 20.9 ± 0.8 ka reflects the beginning of deglaciation, which agrees with the termination of the LGM (Fig. 3). This and the recalculated boulder age of 21.8 ± 1.6 ka (Goehring et al., 2008) supports their statement of the onset of deglaciation around this time. However, alternative interpretations of these boulder ages cannot be rejected, e.g. age overestimation due to post-depositional shielding by burial and subsequent exhumation by frost heave, deposition prior to LGM followed by long-term shielding, or deposition during a readvance following LGM (Briner et al., 2006; Heymann et al., 2011). But Marr et al. (2018) show evidence that the blockfield stabilized ∼ 18 ka during severe periglacial conditions, which indicates the absence of ice cover close to the inferred time of boulder deposition.

The alternative interpretation of the bedrock ^{10}Be nuclide concentration assumes continuous surface exposure since at least 46.4 ± 1.7 ka. Geomorphic evidence, such as periglacial activity of the summit blockfield until 18 ka, challenges the inferred presence of cold-based ice on Blåhø during the LGM (Marr et al., 2018). Recently, Andersen et al. (2018b) stated that high-elevation low-relief areas in south-central Norway

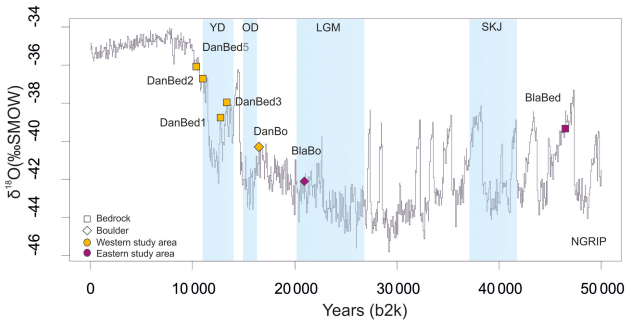

Figure 3. The ages are plotted against the North Greenland Ice Core Project (North Greenland Ice Core Project members, 2004) δ^{18}O with ^{10}Be ages. The key cold climate events are the Younger Dryas (YD), Older Dryas (OD), Last Glacial Maximum (LGM) and Skjonghelleren Stadial (SKJ); data are from Clark et al. (2009), Mangerud et al. (2010), Lohne et al. (2013) and Hughes et al. (2016).

were not covered by cold-based but warm-based ice as they calculated significant erosion rates. Therefore, whether the consistent trimline represents an englacial boundary remains ambiguous as englacial thermal boundaries may change frequently and may be unstable over long time periods (Nesje et al., 1987). However, decisive statements on glaciation history based on a single age are not possible; to resolve this issue on Blåhø, more numerical age data are necessary.

5.4 Implications for the regional glaciation history

The time difference of about 6–9 kyr for deglaciation between Dalsnibba and Blåhø is noteworthy. Taking into account the timing of deglaciation at 11 ± 0.2 ka in Reinheimen (Andersen et al., 2018a), located between our study areas, the deglaciation pattern in southern Norway was spatially and temporally variable. In relation to these ages the summit of Blåhø became apparently ice-free relatively early during deglaciation, whereas Dalsnibba at the inner fjord head of Geiranger Fjord became ice-free around 2 kyr later than the Reinheimen plateau. This means that during the YD readvance Reinheimen must have still been ice-covered, but the summit of Dalsnibba was already ice-free.

6 Conclusion

In this paper we present seven in situ cosmogenic ^{10}Be surface exposure ages from two selected mountain locations in southern Norway. Despite uncertainties related to the uncertainties of our ^{10}Be surface exposure ages and the limited dataset, we can delineate age constraints for the timing of deglaciation in the Geirangerfjellet in southwestern Norway. Further, we contribute new age estimates to the previously established deglaciation chronology for Blåhø in south-central Norway. The following conclusions can be drawn from this study:

1. According to the summit bedrock exposure ages ranging from 13.3 ± 0.6 to 12.7 ± 0.5 ka, deglaciation of the summit of Dalsnibba in Opplendskedalen commenced during the termination of the Bølling–Allerød interstadial. The summit successively remained ice-free during the Younger Dryas. However, the ice cover in the valley below the summit lasted longer (until 10.3 ± 0.5 ka) than previously assumed. In contrast to other studies, our results conclude that Dalsnibba was not a nunatak but covered by warm-based ice during the LGM.

2. The bedrock age from Blåhø (46.4 ± 1.7 ka) indicates long-term weathering history and exposure predating the LGM. Most likely, inherited cosmogenic nuclides preserved through shielding by non-erosive cold-based ice are responsible for its old age. However, possible post-depositional disturbance of the boulder and the lack of larger suitable datasets restrict its interpretation.

3. The different timing of deglaciation in both selected sites and in nearby Reinheimen implies complex deglaciation patterns within a spatially limited area. The vertical extent of the Younger Dryas readvance seems to have been less pronounced in the inner fjord areas.

Data availability. All data sources are publicly accessible online; supporting ground imagery can be found in the Supplement.

Supplement. The supplement related to this article is available online at: https://doi.org/10.5194/egqsj-68-165-2019-supplement.

Author contributions. PM prepared the manuscript with contributions from all co-authors. SAB was responsible for the ^{10}Be measurements at CologneAMS.

Competing interests. The authors declare that they have no conflict of interest.

Special issue statement. This article is part of the special issue "Connecting disciplines – Quaternary archives and geomorphological processes in a changing environment". It is a result of the First Central European Conference on Geomorphology and Quaternary Sciences, Gießen, Germany, 23–27 September 2018.

Acknowledgements. We thank Peter Wilson and one anonymous reviewer for very constructive and thoughtful comments that helped to improve the manuscript. We also thank Tibor Dunai for his expertise and his help. We further acknowledge permission to conduct field work in the Geiranger World Natural Heritage and Landscape Protection Area for over 20 years.

Financial support. This research has been supported by the Friedrich-Ebert-Stiftung (PhD scholarship grant).

References

Aarseth, I., Austbo, P. K., and Risnes, H.: Seismic stratigraphy of Younger Dryas ice-marginal deposits in western Norwegian fjords, Norsk Geol. Tidsskr., 77, 65–85, 1997.

Andersen, B. G., Mangerud, J., Sørensen, R., Reite, A., Sveian, H., Thoresen, M., and Bergström, B.: Younger Dryas ice-marginal deposits in Norway, Quatern. Int., 28, 147–169, https://doi.org/10.1016/1040-6182(95)00037-J, 1995.

Andersen, J. L., Egholm, D. L., Knudsen, M. F., Linge, H., Jansen, J. D., Goodfellow, B. W., Pedersen, V. K., Tikhomirov, D., Olsen, J., and Fredin, O.: Pleistocene Evolution of a Scandinavian Plateau Landscape, J. Geophys. Res.-Earth, 123, 3370–3387, https://doi.org/10.1029/2018JF004670, 2018a.

Andersen, J. L., Egholm, D. L., Knudsen, M. F., Linge, H., Jansen, J. D., Pedersen, V. K., Nielsen, S. B., Tikhomirov, D., Olsen, J., Fabel, D., and Xu, S.: Widespread erosion on high plateaus during recent glaciations in Scandinavia, Nat. Commun., 9, 830, https://doi.org/10.1038/s41467-018-03280-2, 2018b.

Balco, G.: Production rate calculations for cosmic-ray-muon-produced ^{10}Be and ^{26}Al benchmarked against geological calibration data, Quat. Geochronol., 39, 150–173, https://doi.org/10.1016/j.quageo.2017.02.001, 2017.

Balco, G., Stone, J. O., Lifton, N. A., and Dunai, T. J.: A complete and easily accessible means of calculating surface exposure ages or erosion rates from ^{10}Be and ^{26}Al measurements, Quat. Geochronol., 3, 174–195, https://doi.org/10.1016/j.quageo.2007.12.001, 2008.

Binnie, S. A., Dunai, T. J., Voronina, E., Goral, T., Heinze, S., and Dewald, A.: Separation of Be and Al for AMS using single-step column chromatography, Nucl. Instrum. Methods Phys. Res. Sect. B Beam Interact. Mater. Atoms, 361, 397–401, https://doi.org/10.1016/j.nimb.2015.03.069, 2015.

Briner, J. P., Miller, G. H., Thompson Davis, P., and Finkel, R. C.: Cosmogenic radionuclides from fiord landscapes support differential erosion by overriding ice sheets, Geol. Soc. Am. B., 118, 406–420, https://doi.org/10.1130/B25716.1, 2006.

Brook, E. J., Nesje, A., Lehman, S. J., Raisbeck, R. M., and Yiou, F.: Cosmogenic nuclide exposure ages along a vertical transect in western Norway: Implications for the height of the Fennoscandian ice sheet, Geology, 24, 207–210, https://doi.org/10.1130/0091-7613(1996)024<0207:CNEAAA>2.3.CO;2, 1996.

Clark, P. U., Dyke, A. S., Shakun, J. D., Carlson, A. E., Clark, J., Wohlfarth, B., Mitrovica J. X., Hostetler, S. W., and McCabe, A. M.: The last glacial maximum, Science, 325, 710–714, https://doi.org/10.1126/science.1172873, 2009.

Dahl, S. O., Nesje, A., and Øvstedal, J.: Cirque glaciers as morphological evidence for a thin Younger Dryas ice sheet in east-central southern Norway, Boreas, 26, 161–180, https://doi.org/10.1111/j.1502-3885.1997.tb00850.x, 1997.

Dewald, A., Heinze, S., Jolie, J., Zilges, A., Dunai, T., Rethemeyer, J., Melles, M., Staubwasser, M., Kuczewski, B., Richter, J., Radtke, U., von Blanckenburg, F., and Klein, M.: CologneAMS, a dedicated center for accelerator mass spectrometry in Germany,

Nucl. Instrum. Methods Phys. Res. Sect. B Beam Interact. Mater. Atoms, 294, 18–23, https://doi.org/10.1016/j.nimb.2012.04.030, 2013.

Donner, J.: The early and middle Weichselian Interstadials in the central area of the Scandinavian glaciations, Quaternary Sci. Rev., 15, 471–479, https://doi.org/10.1016/0277-3791(96)00002-9, 1996.

Dunai, T. J.: Cosmogenic Nuclides: Principles, Concepts and Applications in the Earth Surface Sciences, Cambridge University Press, Cambridge, https://doi.org/10.1017/CBO9780511804519, 2010.

Ehlers, J. and Gibbard, P. L.: The extent and chronology of Cenozoic Global Glaciation, Quatern. Int., 164–165, 6–20, https://doi.org/10.1016/j.quaint.2006.10.008, 2007.

Fabel, D., Stroeven, A. P., Harbor, J., Kleman, J., Elmore, D., and Fink, D.: Landscape preservation under Fennoscandian ice sheets determined from in situ produced ^{10}Be and ^{26}Al, Earth Planet. Sc. Lett., 201, 397–406, https://doi.org/10.1016/S0012-821X(02)00714-8, 2002.

Fareth, O. W.: Glacial geology of Middle and Inner Nordfjord, western Norway, Technical Report 408, Geological Survey of Norway, Trondheim, 1987.

Fjeldskaar, W.: Viscosity and thickness of the asthenosphere detected from the Fennoscandian uplift, Earth Planet. Sc. Lett., 126, 399–410, https://doi.org/10.1016/0012-821X(94)90120-1, 1994.

Fjeldskaar, W. and Amatonov, A.: Younger Dryas transgression in western Norway: a modelling approach, Norsk Geol. Tidsskr., 98, 127–139, https://doi.org/10.17850/njg98-1-08, 2018.

Fjeldskaar, W., Lindholm, C., Dehls, J. F., and Fjeldskaar, I.: Postglacial uplift, neotectonics and seismicity in Fennoscandia, Quaternary Sci. Rev., 19, 1413–1422, https://doi.org/10.1016/S0277-3791(00)00070-6, 2000.

Goehring, B. M., Brook, E. J., Linge, H., Raisbeck, G. M., and Yiou, F.: Beryllium-10 exposure ages of erratic boulders in Southern Norway and implications for the history of the Fennoscandian Ice Sheet, Quaternary Sci. Rev., 27, 320–336, https://doi.org/10.1016/j.quascirev.2007.11.004, 2008.

Goehring, B. M., Lohne, Ø. S., Mangerud, J., Svendsen, J. I., Gyllencreutz, R., Schaefer, J., and Finkel, R.: Late glacial and Holocene ^{10}Be production rates for western Norway, J. Quaternary Sci., 27, 89–96, https://doi.org/10.1002/jqs.2548, 2012a.

Goehring, B. M., Lohne, Ø. S., Mangerud, J., Svendsen, J. I., Gyllencreutz, R., Schaefer, J., and Finkel, R.: Erratum. Late glacial and Holocene ^{10}Be production rates for western Norway, J. Quaternary Sci., 27, 544, https://doi.org/10.1002/jqs.2548, 2012b.

Gosse, J. C. and Phillips, F. M.: Terrestrial in situ cosmogenic nuclides: theory and application, Quaternary Sci. Rev., 20, 1475–1560, https://doi.org/10.1016/S0277-3791(00)00171-2, 2001.

Harbor, J., Stroeven, A. P., Fabel, D., Clarhäll, A., Kleman, J., Li, Y., Elmore, D., and Fink, D.: Cosmogenic nuclide evidence for minimal erosion across two subglacial sliding boundaries of the late glacial Fennoscandian ice sheet, Geomorphology, 75, 90–99, https://doi.org/10.1016/j.geomorph.2004.09.036, 2006.

Helle, S. K., Rye, N., Stabell, B., Prösch-Danielsen, L., and Hoel, C.: Neotectonic faulting and the Late Weichselian shoreline gradients in SW Norway, J. Geodyn., 44, 96–128, https://doi.org/10.1016/j.jog.2007.01.001, 2007.

Heymann, J., Stroeven, A. P., Harbor J. M., and Caffee, M. W.: Too young or too old: Evaluating cosmogenic exposure dating based on an analysis of compiled boulder exposure ages, Earth Planet. Sc. Lett., 302, 71–80, https://doi.org/10.1016/j.epsl.2010.11.040, 2011.

Holtedahl, H.: Notes on the formation of fjord and fjord-valleys, Geogr. Ann. A., 49, 188–203, https://doi.org/10.1080/04353676.1967.11879749, 1967.

Hughes, A. L. C., Gyllencreutz, R., Lohne, Ø. S., Mangerud, J., and Svendsen, J. I.: The last Eurasian ice sheets – a chronological database and time-slice reconstruction, DATED-1, Boreas, 45, 1–45, https://doi.org/10.1111/bor.12142, 2016.

Jones, R. S., Whitehouse, P. L., Bentley, P. M., Small, S., and Dalton, A. S.: Impact of glacial isostatic adjustment on cosmogenic surface-exposure dating, Quaternary Sci. Rev., 212, 206–212 https://doi.org/10.1016/j.quascirev.2019.03.012, 2019.

Kleman, J.: Preservation of landforms under ice sheets and ice caps, Geomorphology, 9, 19–32, https://doi.org/10.1016/0169-555X(94)90028-0, 1994.

Klemsdal, T. and Sjulsen, E.: The Norwegian macrolandforms: Definition, distribution and system of evolution, Norsk Geogr. Tidsskr., 42, 133–147, https://doi.org/10.1080/00291958808552192, 1988.

Kohl, C. P. and Nishiizumi, K.: Chemical isolation of quartz for measurement of in-situ produced cosmogenic nuclides, Geochim. Cosmochim. Ac., 56, 3583–3587, 1992.

Landvik, J. Y., Ingólfsson, Ó., Mienert, J., Lehman, S. J., Solheim, A., Elverhøi, A., and Ottesen, D.: Rethinking Late Weichselian ice-sheet dynamics in coastal NW Svalbard, Boreas, 34, 7–24, https://doi.org/10.1111/j.1502-3885.2005.tb01001.x, 2005.

Lifton, N., Sato, T., and Dunai, T. J.: Scaling in situ cosmogenic nuclide production rates using analytical approximations to atmospheric cosmic-ray fluxes, Earth Planet. Sc. Lett., 386, 149–160, https://doi.org/10.1016/j.epsl.2013.10.052, 2014.

Linge, H., Brook, E. J., Nesje, A., Raisbeck, G., Yiou, F., and Clark, H.: In situ ^{10}Be exposure ages from southeastern Norway: implications for the geometry of the Weichselian Scandinavian ice sheet, Quaternary Sci. Rev., 25, 1097–1109, https://doi.org/10.1016/j.quascirev.2005.10.007, 2006.

Linge, H., Olsen, L., Brook, E. J., Darter, J. R., Mickelson, D. M., Raisbeck, G. M., and Yiou, F.: Cosmogenic nuclide surface exposure ages from Nordland, northern Norway: implications for deglaciation in a coast to inland transect, Norsk Geol. Tidsskr., 87, 269–280, 2007.

Löffler, J. and Pape, R.: Across scale temperature modelling using a simple approach for the characterization of high mountain ecosystem complexity, Erdkunde, 58, 331–348, https://doi.org/10.3112/erdkunde.2004.04.04, 2004.

Lohne, Ø. S., Bondevik, S., Mangerud, J., and Svendsen, J. I.: Sea-level fluctuations imply that the Younger Dryas ice-sheet expansion in western Norway commenced during the Allerød, Quaternary Sci. Rev., 26, 2128–2151, https://doi.org/10.1016/j.quascirev.2007.04.008, 2007.

Lohne, Ø. S., Mangerud, J., and Birks, H. H.: Precise ^{14}C ages of the Vedde and Saksunarvatn ashes and the Younger Dryas boundaries from western Norway and their comparison with the Greenland Ice Core (GICC05) chronology, J. Quaternary Sci., 28, 490–500, https://doi.org/10.1002/jqs.2640, 2013.

Longva, O., Blikra, L. H., and Dehls, J. F.: Rock avalanches: distribution and frequencies in the inner part of Storfjorden, Møre og

Romsdal County, Norway, Technical Report 2009.002, Geological Survey of Norway, Trondheim, 2009.

Mangerud, J.: Ice sheets limits in Norway and on the Norwegian continental shelf, in: Quaternary Glaciations Extent and Chronology, edited by: Ehlers, J. and Gibbard, P. L., Elsevier, Amsterdam, 271–294, 2004.

Mangerud, J., Gulliksen, S., and Larsen, E.: ^{14}C-dated fluctuations of the western flank of the Scandinavian Ice Sheet 45–25 kyr BP compared with Bølling–Younger Dryas fluctuations and Dansgaard–Oeschger events in Greenland, Boreas, 39, 328–342, https://doi.org/10.1111/j.1502-3885.2009.00127.x, 2010.

Marquette, G. C., Gray, J. T., Gosse, J. C., Courchesne, F., Stockli, L., Macpherson, G., and Finkel, R.: Felsenmeer persistence under non-erosive ice in the Torngat and Kaumajet mountains, Quebec and Labrador, as determined by soil weathering and cosmogenic nuclide exposure dating, Can. J. Earth Sci., 41, 19–38, https://doi.org/10.1139/e03-072, 2004.

Marr, P. and Löffler, J.: Establishing a multi-proxy approach to alpine blockfield evolution in south-central Norway, AUC Geogr., 52, 219–236, https://doi.org/10.14712/23361980.2017.18, 2017.

Marr, P., Winkler, S., and Löffler, J.: Investigations on blockfields and related landforms at Blåhø (Southern Norway) using Schmidt-hammer exposure-age dating: palaeoclimatic and morphodynamic implications, Geogr. Ann. A., 100, 285–306, https://doi.org/10.1080/04353676.2018.1474350, 2018.

Marr, P., Winkler, S., and Löffler, J.: Schmidt-hammer exposure-age dating (SHD) performed on periglacial and related landforms in Opplendskedalen, Geirangerfjellet, Norway: Implications for mid- and late-Holocene climate variability, Holocene, 29, 97–109, https://doi.org/10.1177/0959683618804634, 2019.

Matthews, J. A., Shakesby, R. A., and Fabel, D.: Very low inheritance in cosmogenic surface exposure ages of glacial deposits: A field experiment from two Norwegian glacier forelands, Holocene, 27, 1406–1414, https://doi.org/10.1177/0959683616687387, 2017.

McCarroll, D.: Trimline trauma: the wider implications of a paradigm shift in recognising and interpreting glacial limits, Scottish Geogr. J., 132, 130–139, https://doi.org/10.1080/14702541.2016.1157203, 2016.

Morén, L. and Påsse, T.: Climate and shoreline in Sweden during Weichsel and the next 150,000 years, SKB Technical Report 01-19, Swedish Nuclear Fuel and Waste Management Co., Stockholm, 67, 2001.

Nesje, A.: Late Pleistocene and Holocene alpine glacier fluctuation in Scandinavia, Quaternary Sci. Rev., 28, 2119–2136, https://doi.org/10.1016/j.quascirev.2008.12.016, 2009.

Nesje, A. and Dahl, S. O.: Lateglacial and Holocene glacier fluctuations and climatic variations in western Norway: A review, Quaternary Sci. Rev., 12, 255–261, https://doi.org/10.1016/0277-3791(93)90081-V, 1993.

Nesje, A., Anda, E., Rye, N., Lien, R., Hole P. A., and Blikra, H.: The vertical extent of the Late Weichselian ice sheet in the Nordfjord-Møre area, western Norway, Norsk Geol. Tidsskr., 67, 125–141, 1987.

Nesje, A., McCarroll, D., and Dahl, S. O.: Degree of rock surface weathering as an indicator of ice-sheet thickness along an east–west transect across Southern Norway, J. Quaternary Sci., 9, 337–347, https://doi.org/10.1002/jqs.3390090404, 1994.

Nishiizumi, K., Imamura, M., Caffee, M. W., Southon, J. R., Finkel, R. C., and McAninch, J.: Absolute calibration of ^{10}Be AMS standards, Nucl. Instrum. Methods Phys. Res. Sect. B Beam Interact. Mater. Atoms, 258, 403–413, https://doi.org/10.1016/j.nimb.2007.01.297, 2007.

North Greenland Ice Core Project members: High-resolution record of Northern Hemisphere climate extending into the last interglacial period, Nature, 431, 147–151, https://doi.org/10.1038/nature02805, 2004.

Patton, H., Hubbard, A., Andreassen, K., Winsborrow, M., and Stroeven, A. P.: The build-up, configuration, and dynamical sensitivity of the Eurasian ice-sheet complex to Late Weichselian climatic and oceanic forcing, Quaternary Sci. Rev., 154, 97–121, https://doi.org/10.1016/j.quascirev.2016.10.009, 2016.

Patton, H., Hubbard, A., Andreassen, K., Auriac, A., Whitehouse, P. L., Stroeven, A. P., Shackleton, C., Winsborrow, M., Heyman, J., and Hall, A. M.: Deglaciation of the Eurasian ice sheet complex, Quaternary Sci. Rev., 169, 148–172, https://doi.org/10.1016/j.quascirev.2017.05.019, 2017.

Rea, B. R., Whalley, W., Rainey, M. M., and Gordon, J. E.: Blockfields, old or new? Evidence and implications from some plateaus in northern Norway, Geomorphology, 15, 109–121, https://doi.org/10.1016/0169-555X(95)00118-O, 1996.

Rinterknecht, V. R., Clark, P. U., Raisbeck, G. M., Yiou, F., Brook, E. J., Marks, L., Zelčs, V., Lunkka, J.-P., Pavlovskaya, I. E., Piotrowski, J. A., and Raukas, A.: The last deglaciation of the southeastern sector of the Scandinavian Ice Sheet, Science, 311, 1449–1452, https://doi.org/10.1126/science.1120702, 2006.

Sollid, J. L. and Reite, J. A.: The last glaciation and deglaciation of Central Norway, in: Glacial deposits of North-West Europe, edited by: Ehlers, J., Balkema, Rotterdam, 41–59, 1983.

Steffen, H. and Wu, P.: Glacial isostatic adjustment in Fennoscandia – A review of data and modeling, J. Geodyn., 52, 169–204, https://doi.org/10.1016/j.jog.2011.03.002, 2011.

Stone, J. O., Fifield, L. K., Beer, J., Vonmoos, M., Obrist, C., Grajcar, M., Kubik, P., Muscheler, R., Finkel, R., and Caffee, M.: Co-precipitated silver metal oxide aggregates for accelerator mass spectrometry of Be-10 and Al-26, Nucl. Instrum. Meth. B, 223–224, 272–277, https://doi.org/10.1016/j.nimb.2004.04.055, 2004.

Stroeven, A. P., Fabel, D., Hättestrand, C., and Harbor, J.: A relict landscape in the centre of Fennoscandian glaciation: cosmogenic radionuclide evidence of tors preserved through multiple glacial cycles, Geomorphology, 44, 145–154, https://doi.org/10.1016/S0169-555X(01)00150-7, 2002.

Stroeven, A. P., Hättestrand, C., Kleman, J., Heyman, J., Fabel, D., Fredin, O., Goodfellow, B. W., Harbor, J. M., Jansen, J. D., Olsen, L., Caffee, M. W., Fink, D., Lundqvist, J., Rosqvist, G. C., Strömberg, B., and Jansson, K. N.: Deglaciation of Fennoscandia, Quaternary Sci. Rev., 147, 91–121, https://doi.org/10.1016/j.quascirev.2015.09.016, 2016.

Svendsen, J. I. and Mangerud, J.: Late Weichselian and Holocene sea-level history for a cross-section of western Norway, J. Quaternary Sci., 2, 113–132, https://doi.org/10.1002/jqs.3390020205, 1987.

Tveten, E., Lutro, O., and Thorsnes, T.: Geologisk kart over Norge 1 : 250 000, Norges Geologiske Undersøkelse, Ålesund, 1998.

Winguth, C., Mickelson, D. M., Larsen, E., Darter, J. R., Moeller, C. A., and Stalsburg, K.: Thickness evolution of the Scandina-

vian Ice Sheet during the Late Weichselian in Nordfjord, western Norway: evidence from ice-flow modeling, Boreas, 34, 176–185, https://doi.org/10.1111/j.1502-3885.2005.tb01013.x, 2005.

Wohlfarth, B.: Ice-free conditions in Sweden during Marine Oxygen Isotope Stage 3?, Boreas, 39, 377–398, https://doi.org/10.1111/j.1502-3885.2009.00137.x, 2010.

E&G Quaternary Sci. J., 68, 141–164, 2019
https://doi.org/10.5194/egqsj-68-141-2019

Open Access E&G Quaternary Science Journal

Research article

The formation of Middle and Upper Pleistocene terraces (*Übergangsterrassen* and *Hochterrassen*) in the Bavarian Alpine Foreland – new numeric dating results (ESR, OSL, ^{14}C) and gastropod fauna analysis

Gerhard Schellmann[1], **Patrick Schielein**[1], **Wolfgang Rähle**[2], **and Christoph Burow**[3]

[1]Department of Physical Geography and Landscape Studies, University of Bamberg, Bamberg, Germany
[2]Engelfriedshalde 102, 72076 Tübingen, Germany
[3]Institute of Geography, University of Cologne, Cologne, Germany

Correspondence: Gerhard Schellmann (gerhard.schellmann@uni-bamberg.de)

Relevant dates: Received: 27 March 2019 – Accepted: 24 June 2019 – Published: 25 July 2019

How to cite: Schellmann, G., Schielein, P., Rähle, W., and Burow, C.: The formation of Middle and Upper Pleistocene terraces (*Übergangsterrassen* and *Hochterrassen*) in the Bavarian Alpine Foreland – new numeric dating results (ESR, OSL, ^{14}C) and gastropod fauna analysis, E&G Quaternary Sci. J., 68, 141–164, https://doi.org/10.5194/egqsj-68-141-2019, 2019.

Abstract: Until now, reliable chronological classifications based on numerical ages for many Pleistocene fluvial deposits in the Alpine Foreland were rare. In this study, new numeric data (ESR, OSL, ^{14}C) from Middle and Upper (Late) Pleistocene *Hochterrassen* (high terraces) and *Übergangsterrassen* (transitional terraces) in the Bavarian Alpine Foreland are presented. The dating results imply that the *Hochterrassen* gravel sensu stricto were deposited during the penultimate glacial (MIS 6, Rissian), and that underlying older gravel accumulation are predominantly of penultimate interglacial (MIS 7, Riss–Riss interglacial) age. In some areas of the *Hochterrassen* in the Danube valley south of Regensburg (interglacial *Hartinger Schichten*, Harting layers), and in some areas of the *Rainer Hochterrasse* (basal gravel unit I), *Hochterrassen* gravels are underlain by much older interglacial gravel deposits. These interglacial basal gravel deposits illustrate that the downcutting of these valleys far away from areas of Pleistocene foreland glaciations happened predominantly during warm-temperate interglacial or late-glacial periods. One last interglacial (MIS 5e, Riss–Würm interglacial) *Hochterrasse* is morphologically preserved in the Isar valley. This *Jüngere Moosburger Hochterrasse* is composed of the *Fagotienschotter* (Fagotia gravel, named after the gastropod *Fagotia acicularis*). The next younger terraces are the Early to Middle Würmian (MIS 5d to MIS 3?) *Übergangsterrassen* (transitional terraces), whereas the younger one of the two *Übergangsterrassen* was formed most probably during the Middle Würmian (MIS 3).

Kurzfassung: Chronostratigraphischen Einstufungen pleistozäner fluvialer Ablagerungen und Formen im Alpenvorland mangelt es bis heute an verlässlichen numerischen Altersdaten. Um diese Lücke etwas zu schließen, werden in diesem Beitrag neue numerische Altersdatierungen (ESR, OSL, ^{14}C) von den mittel- und ober (jung)-pleistozänen Hochterrassen und Übergangsterrassen im Bayerischen Alpenvorland vorgestellt. Danach wurden die Hochterrassenschotter sensu stricto im vorletzten Glazial

(MIS 6, Riss) und eventuell erhaltene ältere Sockelschotter vor allem im vorletzten Interglazial (MIS 7, inner-RißInterglazial) abgelagert. Das schließt allerdings nicht aus, dass unter einzelnen Hochterrassenschottern wie im Donautal südlich von Regensburg (interglaziale *Hartinger Schichten*) oder im Bereich der Rainer Hochterrasse (basaler Schotterkörper I) auch noch ältere interglaziale Kieskörper erhalten sein können. Die Relikte warmzeitlicher Sockelschotter weisen darauf hin, dass die Tieferlegung der Talsohlen in Tälern, die weiter von den alpinen Vorlandvergletscherungen entfernt sind, verstärkt in den Inter- und Spätglazialen stattgefunden hat. Letztinterglazialer (Eem, MIS 5e) Herkunft ist die im Isartal erhaltene Jüngere Moosburger Hochterrasse, deren Kieskörper nach den manchmal enthaltenen Schneckenschalen der Gattung *Fagotia acicularis* auch als Fagotienschotter bezeichnet wird. Die nächst jüngeren Terrassen sind die früh- bis mittelwürmzeitliche (MIS 5d bis MIS 3?) ältere Übergangsterrasse 1 und die mittelwürmzeitliche (MIS 3) jüngere Übergangsterrasse 2.

1 Introduction

In the Northern Alpine Foreland, large river valleys like the Danube (German: *Donau*) valley and its tributaries Iller, Lech and Isar (Fig. 1) are characterised by well-developed stepped fluvial terrace systems, which are partly connected to terminal moraines of Quaternary glaciations in front of the Alps. Penck and Brückner (1901–1909) described these morphostratigraphic relationships between terminal moraines and associated fluvial terraces (respectively fluvial gravel deposits) of different elevations for the first time. They named the four glaciations (from old to young) *Günz, Mindel, Riss*, and *Würm* and the associated terrace levels (from old to young) *Älterer Deckenschotter* (Older Cover Gravel), *Jüngerer Deckenschotter* (Younger Cover Gravel), *Hochterrasse* (HT, high terrace, high terrace gravels) and *Niederterrasse* (NT, lower terrace; lower terrace gravel). In later studies, additional glaciations like the "*Donau* glaciation" (Eberl, 1930) and "*Biber* glaciation" (Schaefer, 1957) as well as further fluvial terrace levels like the *Hochschotter* (highest cover gravel) by Graul (1943) or the *Übergangsterrassen* (ÜT, transitional terraces; transitional terrace gravel) by Schellmann (1988) have been differentiated.

This article focuses on the Middle to Upper (Late) Pleistocene *Hochterrassen* and *Übergangsterrassen* of the Danube, Isar, Lech and Iller rivers. It was Penck (1884) who for the first time used the morphostratigraphic term *Hochterrasse* for fluvial terraces that are situated some metres (mostly 7 to 15 m) above the valley floors, and the term *Niederterrasse* for those that are located in the valley floor usually up to 2.5 m above the floodplains. Penck and Brückner (1901–1909) attributed all *Hochterrassen* to the Rissian (penultimate glaciation, late Middle Pleistocene) and all *Niederterrassen* to the Würmian glaciation (last glaciation, Upper Pleistocene) of the Alpine Foreland. In more recent studies, further loess-covered terrace levels, the Lower to Middle Würmian *Übergangsterrassen* (e.g. Schellmann, 1988, 2010; Unger, 1999; Kroemer, 2010; Doppler et al., 2011; Schielein and Schellmann, 2016b), were described between the levels of the *Hochterrassen* and the *Niederterrassen* in some valleys (e.g. Danube, Isar, Lech valley). In general, the locally specific morphological position of the *Übergangsterrassen* and the loess cover is the reason for an occasionally incorrect stratigraphic interpretation of the *Übergangsterrassen* as *Niederterrasse* or *Hochterrasse*, respectively.

Each of these different levels of fluvial terraces within the range of some metres above the modern valley floors can be subdivided additionally into further terrace sublevels with individual fluvial gravel deposits: in some valleys of the Bavarian Alpine Foreland the *Hochterrassen* can be subdivided morphologically into two (e.g. Penck and Brückner, 1901–1909; Miara, 1996; Miara and Rögner, 1996) or three sublevels (e.g. Schellmann, 1988, 2017b, and further references therein). The terrace gravels are sometimes superimposed on older basal gravel units (e.g. Bibus and Strahl, 2000; Leger, 1988; Schellmann 1988, 1990, 2016b, 2017b; Schellmann et al., 2010; Schielein et al., 2015). Likewise, the Lower to Middle Würmian *Übergangsterrassen* are sporadically subdivided in two different sublevels (Schellmann, 2010, 2018b; Doppler et al., 2011).

A detailed review of the current stratigraphical system for Quaternary terrace units and for different terminal moraines in southern Bavaria was presented by Doppler et al. (2011). Here, we followed the stratigraphic nomenclature of the Bavarian Geological Survey, which correlates the Würmian to MIS 5d up to MIS 2, the Rissian to MIS 10 up to MIS 6, and the Mindelian to MIS12 and older (cf. Doppler et al., 2011: Table 3).

All in all, Doppler et al. (2011) showed that secure chronological classifications based on numerical ages are rare for many Pleistocene fluvial deposits in the Alpine Foreland. Whereas the age of the Holocene terrace gravels (H) and the Upper Würmian (MIS 2) *Niederterrassen* gravels in the Bavarian Alpine Foreland is relatively well established by numerous radiocarbon and dendrochronological data from river channel sediments, palaeochannel fills or overlaying floodplain deposits (e.g. Schellmann, 2010, 2016a, 2017a, 2018a; Doppler et al., 2011), numerical ages of the Middle Pleistocene *Hochterrassen* deposits (e.g. Schielein et al.,

2015; Rades et al., 2018, and further references therein) and of the Lower to Middle Würmian *Übergangsterrassen* deposits are much scarcer (e.g. Doppler et al., 2011; Schellmann, 2010).

The earliest attempts to numerically date the *Übergangsterrassen* and *Hochterrassen* in the Bavarian Alpine Foreland started in the late 1980s. Luminescence dating techniques were used focusing on the age determination of the loess cover and the palaeosols on top of the *Hochterrassen* (Rögner et al., 1988; Zöller, 1995; Miara, 1996; Miara and Rögner, 1996; Becker-Haumann and Frechen, 1997) or the *Übergangsterrassen* (Buch and Zöller, 1990, see also discussion by Schellmann, 2010; Zöller, 1995). Later, Fiebig and Preusser (2003) presented the first infrared stimulated luminescence (IRSL) measurements on feldspar extracted from sandy layers in *Hochterrassen* (see Sect. 5) deposits near Ingolstadt, Neuburg and Rain. Thus far, luminescence dating remains the mainly used dating method in the Northern Alpine Foreland. However, luminescence data from fluvial deposits in the Northern Alpine Foreland often suffer from a large scatter in equivalent dose estimates either due to insufficient signal intensities, aberrant luminescence properties, incomplete bleaching of the samples, fading phenomena or a combination of these (e.g. Klasen, 2008; Schielein et al., 2015; Klasen et al., 2016; Trauerstein et al., 2017; Rades et al., 2018).

In the light of these problems when dating fluvial sediments using luminescence, during the last few years we concentrated on electron spin resonance (ESR) dating of small gastropods from the aeolian loess cover on top of the fluvial gravel deposits and from shell-bearing clods of sandy loam and marl in the gravel deposits of the *Übergangsterrassen* and the *Hochterrassen*.

First ESR data have already been obtained by dating a relatively large land-snail shell from a clod of marl in the basal gravel of the *Langweider Hochterrasse* in the Lech valley northwest of Augsburg (Schielein et al., 2015). At that location, the upper gravel was dated by IRSL to the penultimate glaciation (Rissian, MIS 6) around 160 ± 15 to 179 ± 20 ka. One sample from the basal gravel unit yielded an IRSL age of 263 ± 29 ka, whereas four further samples could not be dated by IRSL. The land-snail shell of *Succinea putris*, embedded in a loamy clod at a depth of approximately 11 m below the surface, was dated by ESR to 204 ± 27 ka (Schielein et al., 2015), which indicates a deposition of this basal gravel most likely during MIS 7. The difficulty in dating this basal gravel unit by luminescence and the discrepancy between IRSL and ESR data illustrate the need for further investigations.

Recent ESR dating studies on small land-snail shells demonstrate that ESR is a valuable additional method whose upper dating limit supposedly extends beyond MIS 7, an age range similar to that of mollusc shells or corals (e.g. Schellmann et al., 2018). While the ESR dating method can also encounter methodological problems, the most severe problem of its application in this context is to find gastropods bearing sediments, especially in the investigated fluvial gravel deposits, with sufficient amount of dating material (> 5 g shell material), if present at all.

Here, we focused on the age of the *Übergangsterrassen* and the *Hochterrassen* deposits in the Bavarian Alpine Foreland in the light of new numerical dating results (ESR, OSL, and ^{14}C). We also present some new information about the gastropod fauna, which was found in the sampled aeolian and fluvial sediments leading to the question of the climatic conditions during terrace formation and its different gravel deposits.

2 Regional context and investigated areas

All sample sites are located in the Bavarian Alpine Foreland (Fig. 1) and were sampled during geological field mappings of larger parts of the valley floors of the Danube, Lech, Wertach and Isar rivers in the past years (Schellmann, 2010, 2016a, 2017a, 2018a). In these valleys, prominent flights of Middle Pleistocene *Hochterrassen* and of early to middle Late Pleistocene *Übergangsterrassen* are preserved. All of them are accumulation terraces and consist of some metres (mostly 4 to 7 m) thick deposits of fluvial gravels and sands which are often overlain by fine-grained aeolian loess or sandy loess deposits. In particular, in areas with unusually thick fluvial gravel accumulations, the *Hochterrassen* deposits are composed of two stacked gravel deposits with an older fluvial facies at the base and a cold climate *Hochterrassen* deposit sensu stricto at the top. This was described for the first time in the Danube valley downstream of Regensburg (Fig. 1), where an interglacial fluvial facies (determined by pollen analysis) named the *Hartinger Schichten* is preserved at the base of the oldest of three *Hochterrassen* levels (Schellmann, 1988, 1990; Schellmann et al., 2010). In the same area, the unusually thick (up to 11.5 to 13.5 m) fluvial gravel deposits of the youngest *Hochterrasse* consist of a basal, approximately 8 m thick sand-rich gravel unit with numerous limestone cobbles dislocated from the nearby Jurassic Alb. This basal gravel unit was overlain by an approximately 4 m thick, very coarse-grained gravel deposit (the younger *Hochterrassen* deposit sensu stricto) with numerous pebbles from the Alps, and with boulders up to $1.2\,\text{m} \times 0.8\,\text{m} \times 0.4\,\text{m}$ in diameter (Schellmann, 1988). Schellmann (1988, p. 124) did not address the question of whether the two gravel units have been deposited under different climatic conditions or if they only represent a local phenomenon.

A predominantly sandy gravel unit at the base of coarse-grained and cobble-rich *Hochterrassen* deposits has been found during geological mapping of the upper Danube valley (Fig. 1: *Dillinger Hochterrasse*) and in the Lech valley (Fig. 1: *Langweider Hochterrasse* and *Rainer Hochterrasse*. Geological maps of these areas including explanations were published by Schellmann (2016b, 2017b) and Schielein

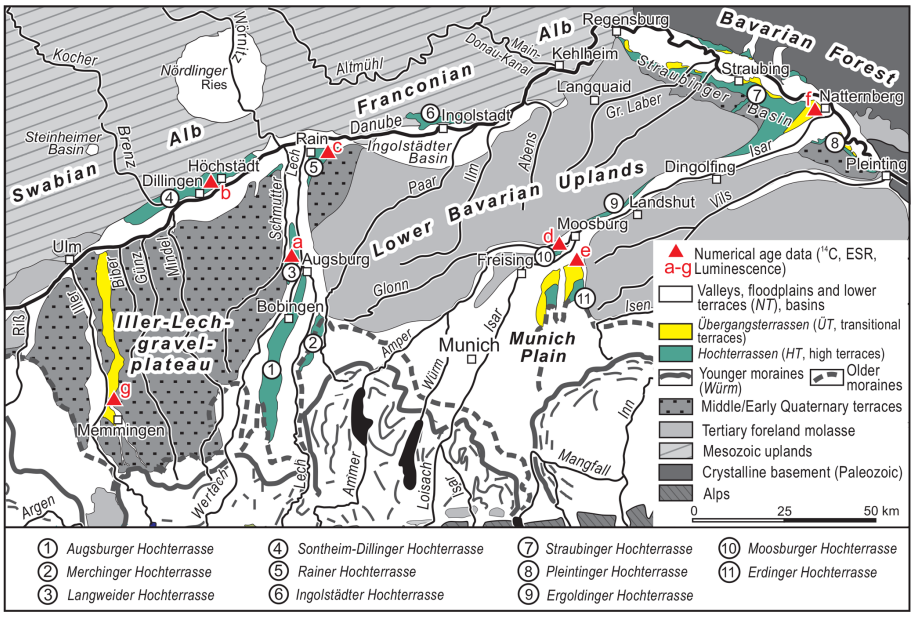

Figure 1. Location of Middle Pleistocene (Rissian) *Hochterrassen* and lower to middle Upper Pleistocene (Würmian) *Übergangsterrassen* in the Bavarian Alpine Foreland including sampling sites mentioned in the text.

and Schellmann (2016a, b). From a lithostratigraphic point of view, these basal gravel units could either be only several hundreds to several thousands years older or even one or more glacial–interglacial periods older than the superimposed penultimate glacial accumulation of the *Hochterrassen* gravel sensu stricto. In this respect, only numeric dating methods can give a more accurate chronostratigraphical classification.

Numeric dating results are also essential for a geochronological classification of the *Jüngere Moosburger Hochterrasse* in the Isar valley west of Moosburg (Fig. 1: sample site d). A geological map of this area including explanations has been published by Schellmann (2018b). Here, Nathan (1953) for the first time found sand lenses with an interglacial gastropod fauna like *Fagotia acicularis* embedded in the *Hochterrassen* gravel. Therefore, this *Hochterrassen* deposit is also known by the name "*Fagotienschotter*" (Fagotia gravel). Whereas Nathan (1953), Brunnacker and Brunnacker (1962), Brunnacker (1966), and Jerz (1993) postulated a last interglacial age, Kovanda (2006) assumed a much older age, older than *Mindel*.

More numeric age data are also needed for the loess-covered Lower to Middle Würmian *Übergangsterrassen* (e.g. Doppler et al., 2011, and further references therein). They are older than the pleniglacial (MIS 2) deposition of the oldest *Niederterrasse* (i.e. NT1), younger than the youngest penultimate glacial *Hochterrassen* deposits, and younger than the accumulation of the interglacial *Jüngere Moosburger Hochterrasse*. *Übergangsterrassen* are well preserved in the Danube valley near Dillingen (e.g. Schellmann, 2017b) and downstream of Regensburg (e.g. Schellmann, 2010), in the Isar valley near Moosburg (Schellmann, 2018b) and at the confluence of the Isar and Danube valley (e.g. Kroemer, 2010; Unger, 1999; Schellmann, 1988) for example.

3 Sample sites and methods

Samples of ESR dating (snail shells and the surrounding sediment within 30 cm in diameter) and for luminescence dating were collected during geological field mapping of Holocene, Late and Middle Pleistocene fluvial terraces along the Danube, Lech, Wertach and Isar rivers over the past 10 years (Schellmann, 2010, 2016a, 2017a, 2018a).

Shells from land snails were sampled from loamy or marly clods, which were embedded in fluvial gravel and sands of the *Langweider* and *Rainer Hochterrasse* (Fig. 1: sample site a and c), of the *Dillinger Hochterrasse* west of Höchstädt (Fig. 1: sample site b), and of the *Jüngere Moosburger Hochterrasse* west of Moosburg (Fig. 1: sample site d). These clods were eroded from the adjacent floodplain or from islands in the riverbed during the deposition of the terrace gravels. Shells from gastropods were also collected from the sandy loess cover on the *Übergangsterrasse* in the Isar valley south of Moosburg (Fig. 1: sample site e), and in the Danube valley west of Natternberg near the Isar–Danube confluence (Fig. 1: sample site f). Luminescence samples were collected and dated from the sandy loess cover on the *Übergangsterrasse* in the Iller valley northeast of Memmingen (Fig. 1: sample site g). Here, Schaefer (1940, 1953) and Brunnacker (1953) postulated that this loess-covered ter-

race (named *Fellheimer Feld*) is older than the Würmian pleniglacial *Niederterrasse* (named *Erolzheimer Feld*).

The accuracy of the ESR dating results was checked by parallel dating of two Upper Würmian snail shells by the accelerated mass-spectrometric (AMS) radiocarbon method (Table 1). In addition, at three localities, the ESR data could be compared with luminescence data (Fig. 1: sample sites a, f, g). A further check was made by ESR dating of land-snail shells from different clods of sandy loam, which were embedded in the basal facies of the *Dillinger Hochterrasse* of the Danube (Fig. 1: sample site b). The composition of the gastropod fauna at some sample sites gave helpful palaeoecological information on whether they lived in an interglacial or glacial period. This is also useful to verify the reliability of numeric dating results in general.

Samples for ESR dating were prepared in the sediment laboratory of the University of Bamberg. After cleaning manually, the thickness of the shell fragments was measured using a micrometer or reflection electron microscope (REM) measurements. REM investigations of some shell thicknesses were undertaken in the laboratory of the Department of Building Preservation Sciences of the University of Bamberg. Both techniques yielded congruent results after having measured the thickness from about 20 points per sample. Afterwards, the shells were carefully ground by hand and sieved with a final grain size of 125 to 250 µm. The ESR signals were measured in the ESR laboratory of the Institute of Geography at the University of Cologne. Due to the small amount of shell material it was necessary to put together a mixture of different individuals to obtain sufficient material for a single sample. In five cases, mixtures of different specimens from one sample site had to be used (Table 1: Ba32, Ba33, Ba42, Ba43, Ba56).

At some locations, particle sizes and carbonate content of the loess cover were determined using the pipette method after Köhn and Köttgen and volumetrically after Scheibler.

3.1 ESR measurements and equivalent dose (D_E) calculations

A multiple aliquot additive-dose procedure was applied for ESR D_E determination. Depending on the amount of available sample material, 18 to 20 aliquots per sample were used. For sample K5838 material for only 10 aliquots was available. Due to limited sample material each aliquot has a weight between 0.02 and 0.07 g (Table 1) instead of the commonly used 0.2 g. All aliquots were re-weighed after ESR measurement to correct the corresponding ESR signal amplitudes if needed.

All samples were γ-irradiated by a ^{60}Co source (Helmholtz Center in Munich, effective dose rates of 0.8–5.2 Gy min^{-1}) prior to ESR measurements with maximal doses up to 784 Gy for the Middle Pleistocene shells (Table 1).

The ESR measurements were performed at room temperature on a Bruker ESP 300E X-band spectrometer or on a Bruker ELEXSYS 500 X-band spectrometer working at a frequency of 9.7–9.8 GHz. Measurement conditions were microwave power of 10, 25 or 101 mW, modulation amplitude of 0.485 G, conversion time of 20.48 ms, time constant of 163.84 ms and sweep time of 20.972 s. Depending on the individual signal-to-noise ratio, between 5 and 40 scans were used to record the ESR spectra. The D_E was derived from the analysis of the dating signal at $g = 2.0007$ (Fig. 2), which was successfully used by Schellmann and Kelletat (2001) in the context of ESR dating of snail shells from aeolianites in Cyprus. The investigated shells are largely composed of aragonite, whereas some shells also contain some calcite layers (Table 1; Fig. 2). Already the smallest traces of calcite (< 2 %) exhibit six triplets of hyperfine Mn^{2+} lines in the ESR spectra (Fig. 2a; e.g. Low and Zeira, 1972; Molodkov, 1988, 1993; Inoue et al., 2000), which may overlap with the left shoulder of the ESR signal at $g = 2.0007$. In such cases ESR dating is not possible with the method used here. The signal peak at $g = 2.0007$ was determined by additional measurements of a DPPH standard, an aragonitic coral (*Acropora palmata*) from Cuba and an aragonitic mollusc shell (*Protothaca antiqua*) from the Patagonian Atlantic coast (Fig. 2b).

The D_E–D_{max} plot (DDP) procedure was used for D_E determination (Fig. 2c). This plateau screening method for D_E determination and some further details of ESR measurement parameters, number of aliquots and irradiations steps, timing of major U-uptake processes in mollusc shells and corals have been described in detail by Schellmann and Radtke (1999, 2001), and Schellmann et al. (2008). The D_E was calculated using a single saturation exponential function with the program "simplex-fit" (version 1993) written by Rainer Grün.

3.2 Dose rate and age calculations

The natural radioactivity of the surrounding sediments (external dose rate) was determined by measuring the radioactive elements uranium (U), thorium (Th) and potassium (K), and the radioactivity of the snail shells (internal dose rate) by measuring the internal U content. U and Th contents were determined at the Jülich Research Centre and some samples at the Landeslabor Berlin-Brandenburg by inductively coupled plasma mass spectrometry (ICP-MS). The K content was measured at the University of Bayreuth via inductively coupled plasma optical emission spectroscopy (ICP-OES) and partly at the Bavarian Geological Survey via X-ray fluorescence (XRF) analysis. For some samples double analyses of U, Th and K were performed and their mean value was used for ESR age calculations (Table 1). Cosmic dose rates were calculated following Prescott and Hutton (1994) using the current depth of the sample below terrain surface. These estimates were used in the "ESR-Data V-6" software (Grün,

Table 1. Samples and dose rate data, equivalent doses, ESR ages and AMS radiocarbon data.

Sample no.	Ba08	Ba13	Ba32	Ba33	Ba43	Ba55	Ba56
Locality	Do14/8b	Do14/8b	Is16/4	Is16/5	Is16/7	Is17/1b*1	Is17/1b*2
Stratigraphy	ÜT	ÜT	ÜT	ÜT	Jüngere Moosburger HT	Jüngere Moosburger HT	Jüngere Moosburger HT
Sample depth (cm)	380 ± 10	380 ± 10	50 ± 10	105 ± 10	250 ± 20	200 ± 30	200 ± 30
Species	*Succinea putris*	*Succinea putris*	*Succinea putris* *Succinella oblonga*	*Trochulus* sp. *Succinea putris* *Stagnicola* sp.	*Arianta arbustorum* *Aegopinella* cf. *nitens* *Succinella oblonga* *Trochulus hispidus*	*Arianta arbustorum*	*Aegopinella* cf. *nitens* *Trochulus hispidus*
[a] Calcite (ESR, XRD)	~ 2 %	~ 2 %	yes	yes	no	yes	yes
Thickness (µm)	290 ± 90	290 ± 90	100 ± 41	117 ± 39	214 ± 88	390 ± 104	112 ± 38
[b] Removed size (µm)	120	120	–	–	–	–	–
Weight/aliquot (g)	0.070	0.070	0.020	0.020	0.030	0.020	0.020
Aliquots (*n*)	20	20	19	18	20	20	20
Dmax (Gy)	784	592	140.2	131.9	562.9	544.25	544.25
U shell (ppm)	1.015 ± 0.015	1.015 ± 0.015	0.470 ± 0.130	0.530 ± 0.010	0.463 ± 0.012[f]	0.449 ± 0.006	0.430 ± 0.300
U sediment (ppm)	1.59 ± 0.015	1.59 ± 0.015	1.800 ± 0.040	1.000 ± 0.040	1.405 ± 0.065[f]	1.520 ± 0.030	1.520 ± 0.030
Th sediment (ppm)	7.70 ± 0.20	7.70 ± 0.20	3.10 ± 0.70	8.60 ± 0.50	6.50 ± 0.25[f]	5.10 ± 0.20	5.10 ± 0.20
K sediment (wt. %)	1.18 ± 0.03[f]	1.18 ± 0.03[f]	0.844 ± 0.02[f]	1.006 ± 0.06[f]	0.859 ± 0.02[f]	0.981 ± 0.07[f]	0.981 ± 0.07[f]
H_2O (wt. %)	21 ± 4	21 ± 4	16 ± 3	14 ± 3	10 ± 3	12 ± 2	12 ± 2
D' (µGy a^{-1}) total	1429 ± 83	1429 ± 83	1858 ± 77	1583 ± 69	1407 ± 75	1288 ± 68	1499 ± 74
D'_{int} (µGy a^{-1})	94 ± 14	94 ± 14	32 ± 10	40 ± 7	66 ± 12	69 ± 11	55 ± 39
D'_{cos} (µGy a^{-1})	127 ± 2	127 ± 2	199 ± 4	182 ± 3	147 ± 4	156 ± 7	156 ± 7
D_E (Gy)	43.6 ± 2.6	43.7 ± 2.6	30.4 ± 4.7	36.7 ± 1.6	182.3 ± 20.3	168.6 ± 16.4	177.6 ± 20
Age (EU)	30.5 ± 2.6 ka	30.6 ± 1.9 ka	16.4 ± 2.6 ka	23.2 ± 1.4 ka	130 ± 16	131 ± 14	119 ± 15
Age (LU)	31.6 ± 2.7 ka	31.8 ± 2.0 ka	16.4 ± 2.6 ka	23.5 ± 1.4 ka	130 ± 16	131 ± 14	119 ± 15
[c] ^{14}C age (years)			16 160 ± 40 ^{14}C BP	18 680 ± 60 ^{14}C BP			
[d] cal BP (2σ)			19 324–19 670 cal BP	22 385–22 715 cal BP			
[e] ^{14}C Lab. no.			Beta 470 771	Beta 485 050			

Sample no.	Ba12	Ba09	Ba11	Ba14	Ba15	Ba42	K5838
Locality	Le14/3	Do13/8	Do13/8li	Do13/8	Do14/9	Le16/5c	Le11/31
Stratigraphy	Langweider HT	Dillinger HT	Dillinger HT	Dillinger HT	Dillinger HT	Rainer HT, unit II	Rainer HT, unit II
Sample depth (cm)	200 ± 50	530 ± 15	530 ± 20	530 ± 15	560 ± 10	480 ± 20	660 ± 15
Species	*Trochulus hispidus*	*Arianta arbustorum*	*Arianta arbustorum*	*Fruticicola fruticum*	unknown	*Helicodonta obvoluta* *Aegopis verticillus*	unknown
[a] Calcite (ESR, XRD)	yes	~ 2 %	no	no	no	yes	no
Thickness (µm)	53 ± 10	283 ± 68	283 ± 68	220 ± 80	250 ± 30	168 ± 126	550 ± 50
[b] Removed size (µm)	–	–	–	–	–	–	–
Weight/aliquot (g)	0.020	0.060	0.050	0.026	0.035	0.020	0.022
Aliquots (*n*)	20	20	20	20	20	20	10
Dmax (Gy)	640	784	784	640	592	562.9	534
U shell (ppm)	1.140 ± 0.030	0.197 ± 0.006	0.183 ± 0.006	0.173 ± 0.004	0.330 ± 0.030	0.350 ± 0.020	0.500 ± 0.010
U sediment (ppm)	1.23 ± 0.01	1.59 ± 0.09	0.74 ± 0.06	0.68 ± 0.06	0.33 ± 0.10	1.906 ± 0.014	2.070 ± 0.030
Th sediment (ppm)	1.82 ± 0.01	4.70 ± 0.80	4.80 ± 0.20	4.75 ± 0.50	3.03 ± 0.10	5.10 ± 0.20	3.19 ± 0.10
K sediment (wt. %)	0.42 ± 0.10	1.11 ± 0.03[f]	1.12 ± 0.02[f]	1.12 ± 0.02[f]	1.02 ± 0.10	0.981 ± 0.07[f]	0.750 ± 0.020
H_2O (wt. %)	15 ± 5	17 ± 3	17 ± 3	20 ± 4	20 ± 4	21 ± 4	25 ± 5
D' (µGy a^{-1}) total	963 ± 73	1102 ± 62	1132 ± 53	1122 ± 72	926 ± 57	1391 ± 110	893 ± 43
D'_{int} (µGy a^{-1})	152 ± 29	34 ± 6	32 ± 6	32 ± 6	56 ± 11	58 ± 11	96 ± 4^
D'_{cos} (µGy a^{-1})	160 ± 10	106 ± 2	106 ± 3	106 ± 2	102 ± 1	111 ± 3	88 ± 2
D_E (Gy)	150.7 ± 16.6	222.1 ± 13.7	240.6 ± 19.5	223.2 ± 21.2	190.8 ± 13.8	291.7 ± 35.8	191.5 ± 18.5
age (EU)	156 ± 21 ka	202 ± 17 ka	213 ± 20 ka	199 ± 23 ka	206 ± 20 ka	210 ± 31	214 ± 23
age (LU)	172 ± 23 ka	202 ± 17 ka	213 ± 20 ka	199 ± 23 ka	206 ± 20 ka	210 ± 31	214 ± 23

[a] Calcite (ESR) yes or no indicates with Mn^{2+} or without Mn^{2+} lines. [b] Thickness (µm) reduced by etching with 2 % HCl approximately 1 to 2 min. [c] AMS ^{14}C ages (Beta Analytic Florida). [d] Calibrated with IntCal13 (CALIB Rev. 7.0.4); due to hard-water effect the real age is most probably younger than the atmospheric calibrated ^{14}C age. [e] Beta – Beta Analytic Florida. MAMS – Curt-Engelhorn-Zentrum Archäometrie Mannheim. [f] Mean value of double or triple analysis; U, Th analysis by ICP-MS, K analyses by ICP-OES or RFA. ESR age calculation uses: *k* factor of 0.07 ± 0.01 (Grün, 2007; Grün and Katzenberger, 1994); initial $^{234}U/^{238}U$ ratio 1.0 ± 0.2; density of shell 2.95 ± 0.02 g cm^{-3} EU – age calculation assuming early U uptake or LU – linear (continuous) U uptake.

2009) to calculate the age of a sample. The water content of the surrounding sediments was measured in the field using an electronic soil moisture meter. Measured values were used for ESR age calculations with relative errors of 15 % to 30 % (Table 1).

Fortunately, all dated snail shells have low internal U contents, often below 0.5 ppm (Table 1). Thus, ESR ages are the same or do not differ significantly when they are calculated under the assumption of an early (EU) or a linear (LU) U uptake model (Table 1). Even so, mollusc shells seem to incorporate U after death very quickly in a few thousand years (e.g. Schellmann et al., 2008), and consequently ESR age calculation of Pleistocene shells should prefer an early U uptake model, whereas ESR age calculations of Holocene shells should be checked with different U-uptake models.

In the context of ESR age calculation we further used (a) an alpha efficiency (*k* factor) of 0.07 ± 0.01 following Grün (2007) and Grün and Katzenberger (1994), and we assumed (b) an initial $^{234}U/^{238}U$ value of 1.0 ± 0.2, a value commonly found in soils and sediments (e.g. Borylo and Skwarzec, 2014; Vigier and Bourdon, 2012; Srivastava et al., 2012, and further references therein). Weißhaar (2000, Fig. 4.11) for example reported $^{234}U/^{238}U$ values of about 0.95 to 1.18 for fluvial gravel, sand, silts and clays in a 280 m

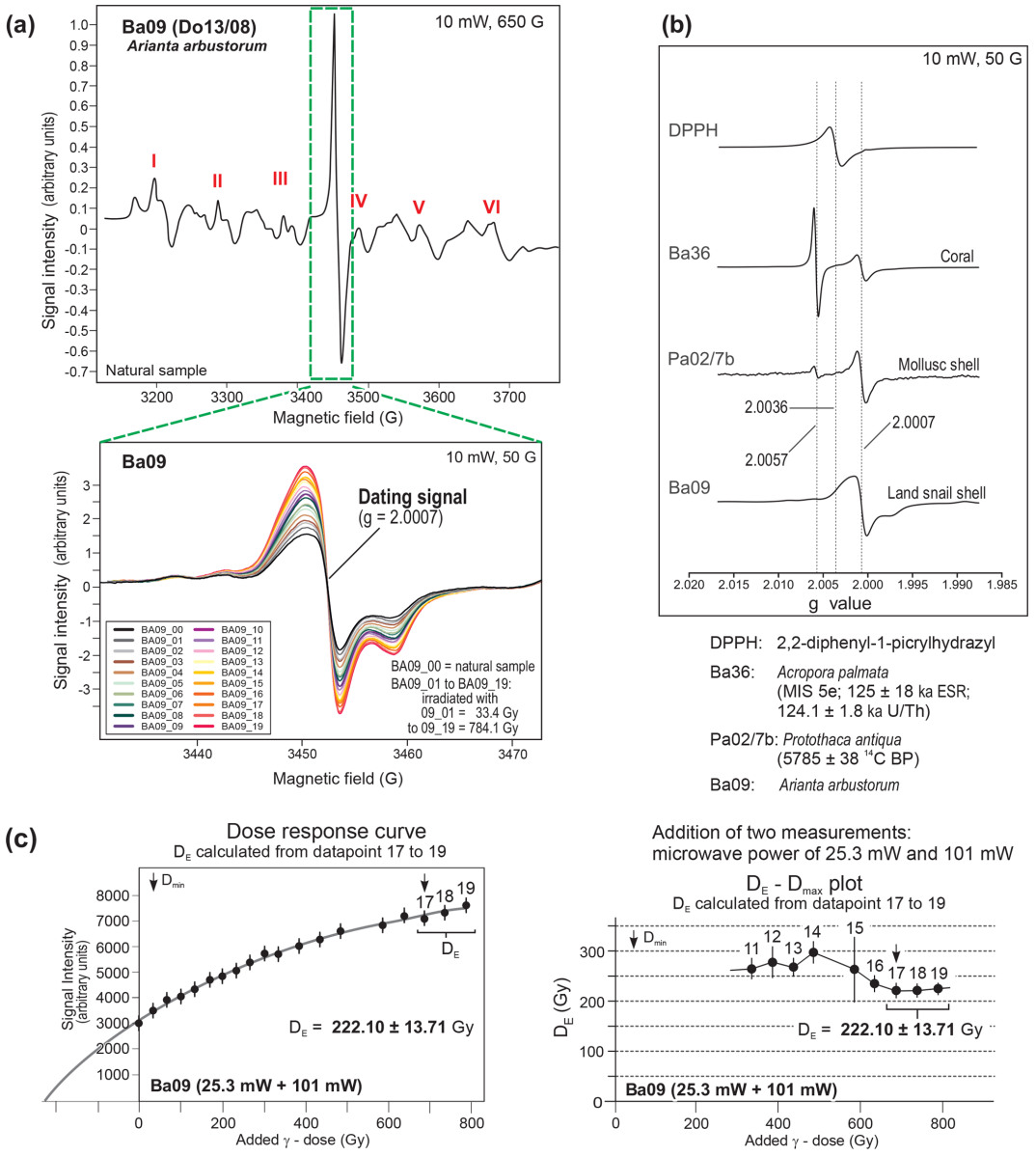

Figure 2. ESR spectra of a penultimate interglacial (MIS 7) land-snail shell (*Arianta arbustorum*) with aragonite and minor calcite crystal structure (calcite content approx. 2 % measured by XRD); **(a)** ESR screenings with a 650 G (top), and 50 G (bottom) scan width. The latter shows a strong signal growth of the dating signal at $g = 2.0007$ after gamma irradiation to doses of up to 784.1 Gy. The extra-wide ESR screening of 650 G shows six triplets (I to VI) of ESR hyperfine Mn^{2+} lines in the ESR spectrum; **(b)** g-value determination of the dating signal of Ba09 using a DPPH, a MIS 5e aragonite coral sample, and a Holocene aragonite mollusc shell for calibration; **(c)** additive dose response curve and D_E–D_{max} plot (DDP) of the sample Ba09. Only for this sample, the ESR signal amplitude is the mean value of two separate ESR measurements using different microwave powers of 25.3 and 101 mW, respectively.

deep sediment core of the Quaternary river Neckar alluvial fan deposit (southern Germany).

3.3 Radiocarbon and luminescence data

To check the reliability of the ESR dating results, two Late Würmian snail shells were also dated using the radiocarbon (^{14}C) method (Table 1). Data were calibrated without a hard-water correction using the atmospheric "IntCal13" calibration set (Reimer et al., 2013) and the software CALIB (version 7.0.2; Stuiver and Reimer, 1993). It needs to be considered that the hard-water effect, which may occur as a result of incorporating ^{14}C-free inorganic carbon from dissolved ancient carbonates during shell crystallisation (e.g. Xu et al., 2011, and further references therein), limits the reliability of land-snail ^{14}C age dating results. Measured ^{14}C ages can be a few years, some hundreds of years or even up to 2000

or 3000 years too old (e.g. Goodfriend and Stipp, 1983; Pigati et al., 2010; Xu et al., 2011). In our research area, the river channel and floodplain deposits of the Danube, Isar, and Lech rivers have high carbonate contents; hence ^{14}C ages should be influenced by a hard-water effect of some hundreds of years. This assumption is derived from radiocarbon dates of reworked charcoal or organic plant fragments and associated snail shells in fluvial deposits of the Alpine Foreland rivers Lech (Gesslein, 2013, p. 43) and Danube (Schellmann, 2017b), which have shown age differences of 570 and 500 years, respectively. Since the exact value of the hard-water effect is unknown, the calendar age should be younger than the atmospheric calibrated ^{14}C ages in Table 1.

ESR data are compared to published luminescence dating results from the same or neighbouring outcrops (Kroemer, 2010; Schielein et al., 2015). Additionally, we present two new OSL data (Table 2), sampled from the sandy loess cover on the *Übergangsterrasse* (i.e.,*Fellheimer Feld*) in the Iller valley (Fig. 1: sample site g). The luminescence samples were taken from the loess deposits in opaque tubes and prepared under subdued red light in the luminescence laboratory at the University of Bayreuth. Both samples were sieved and treated with 10 % HCl and 10 % H_2O_2 to remove any carbonates and organic material. The fine-grain (4–11 µm) quartz fraction was segregated by etching with H_2SiF_6 and enriched by settling using Stokes law. The suspension of demineralised water and 1.5 mg of fine-grain quartz was dispensed onto 9.8 mm wide stainless-steel discs. The measurements for D_E estimation were conducted on Risø DA-20 luminescence readers following the standard SAR protocol of Murray and Wintle (2003). OSL emission was filtered through a U-340 filter after stimulation with blue LEDs (125 °C, 40 s). The seven or nine measured aliquots of each sample were all accepted and yielded dose values from which median D_E values were calculated. For dose rate estimation, uranium and thorium concentrations were measured by alpha-counting and the potassium contents by ICP-OES. Conversion factors from Adamiec and Aitken (1998) were used. Furthermore, the geographic position, recent depth below surface, altitude, and density of the overlying sediment were included in the cosmic dose rate calculations (Prescott and Hutton, 1994) as well as water contents, which were measured in the field considering a relative error of 25 %. Dose rate and age calculations were conducted in ADELE software (Kulig, 2005).

4 Results

4.1 ESR, radiocarbon and luminescence data from the *Übergangsterrasse* in the Danube, Isar and Iller valley

Ages are obtained from the Upper Würmian sand loess cover on the *Übergangsterrasse* (ÜT) in the Danube valley north of the Isar valley mouth (Fig. 1: sample site f; Fig. 3 and Table 1: sample Ba33), in the Isar valley near Moosburg (Fig. 1: sample site e; Figs. 4, 5 and Table 1: sample Ba32), and in the Iller valley southwest of Fellheim (Fig. 7: sample site g; Table 2).

The ÜT in the Danube valley west of the Nattern-berg was first described by Schellmann (1988, 1990) and Unger (1999), and then later by Kroemer (2010), who published first numeric age data based on luminescence dating of feldspar (Fsp.) and quartz (Qu.) (Fig. 3). The luminescence dating was by Nicole Klasen (University of Cologne). The luminescence data from the base of the loess cover on the ÜT confirm an Upper Würmian (MIS 2) age of around 18.8 ± 1.0 ka (Fsp.) and 23.1 ± 2.8 ka (Qu.). Furthermore, a sandy layer in the fluvial gravel deposits of the ÜT was dated to 36.0 ± 1.9 ka (Fsp.) and 30.4 ± 3.7 ka (Qu.), implying a late Middle Würmian (MIS 3) age of the fluvial aggradations of the ÜT in this area (Kroemer, 2010).

In the current study, land-snail shells were sampled from the base of the sandy loess covering the unweathered sandy gravel deposits of the *Übergangsterrasse* (Fig. 3) and were dated by ESR and ^{14}C. Due to the small amount of shell material, sample Ba33 represents a mixture of the three species *Trochulus* sp., *Succinea putris* and *Stagnicola* sp. (Table 1). The resulting ESR age of 23.2 ± 1.4 ka agrees very well with the quartz age of ca. 23.1 ± 2.8 ka published by Kroemer (2010). Within error, it also agrees well with the AMS ^{14}C age of $18\,680 \pm 60$ BP of the gastropod collected in this study. The atmospheric calibrated age without hard-water correction is about 22 966 to 22 525 cal BP (Table 1: Ba33). If a hard-water effect of a few hundreds of years is assumed, the radiocarbon age would also be within the error range of the ESR age.

Further small terrestrial gastropods for ESR and radiocarbon dating were taken from the gravel pit Schulz in the younger *Übergangsterrasse 2* (ÜT2) of the Isar (Fig. 1: sample site e) west of Langenpreising (Figs. 4, 5). Some kilometres south of the location an older *Übergangsterrasse* (ÜT1) is preserved (Fig. 4), 0.5 to 2 m above the ÜT2. Details about the distribution and stratigraphy of the *Übergangsterrassen* and other Middle and Upper Pleistocene terraces of the Isar in this region, including some numeric data, are published in Schellmann (2018b). Similar to other valleys of the Bavarian Alpine Foreland, the gravelly, horizontal and occasionally also trough-bedded braided river deposits of the *Übergangsterrassen* are covered by sandy loess of fine to medium grain sizes (Fig. 5). The upper part of the 7 to 9 m thick gravel deposit of the ÜT2 and its loess cover are exposed in the gravel pit west of Langenpreising (Fig. 5; Table 1: sample Ba32). The calcareous, often sandy loess deposit is between 0.6 and 1.3 m thick and lies on top of the unweathered sandy gravel deposits of the *Übergangsterrasse*. A fossil palaeo-soil in the form of a very weak Gelic Gleysol and the high content of sandy grain sizes (Fig. 5) are characteristic of many Upper Würmian loess deposits in Bavaria.

An Upper Würmian age of this loess cover is confirmed by the ESR and ^{14}C dating results of land-snail shells. They

Table 2. Samples and dose rate data, equivalent doses, and OSL ages.

Sample	Location	Depth (m)	Grain size (µm)	Radionuclide concentrations			Water content (%)	Dose rate (Gy/ka)	No. aliquots	D_e (Gy)	Age (ka)
				U (ppm)	Th (ppm)	K (%)					
Iller12/1	ÜT (*Fellheimer Feld*)	1.65	4–11	3.05 ± 0.19	6.41 ± 0.63	1.23 ± 0.12	20 ± 5	2.46 ± 0.34	9	76.2 ± 4.0	31 ± 4
Iller12/3	ÜT (*Fellheimer Feld*)	1.50	4–11	3.59 ± 0.20	6.30 ± 0.64	1.25 ± 0.13	20 ± 5	2.60 ± 0.40	7	75.4 ± 5.3	29 ± 4

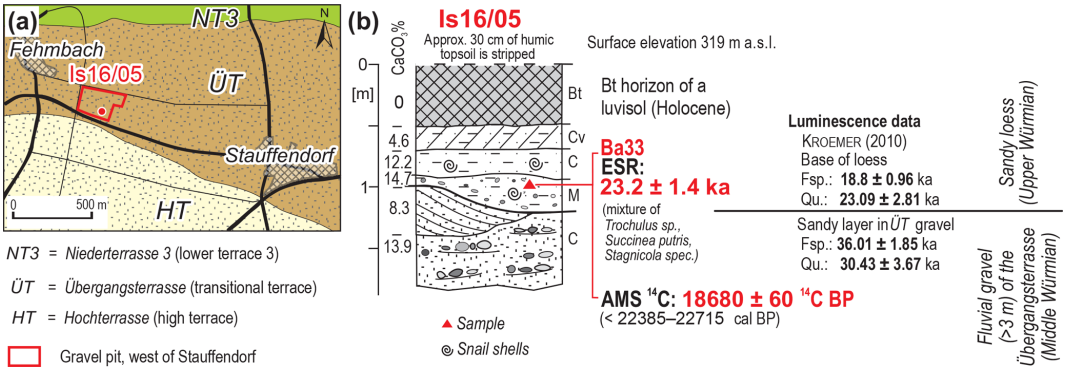

Figure 3. ESR, ^{14}C and luminescence data from the *Übergangsterrasse* in the Danube valley west of the village Stauffendorf; **(a)** geological map with location of sample site; **(b)** geological profile with ESR and ^{14}C dating results, and some luminescence data from Kroemer (2010) (Fig. 1: sample site f; Table 1: sample Ba33).

were sampled from the unweathered sandy loess layers above and below the weak Gelic Gleysol. The sample Ba32 is a mixture of several individuals of the species *Succinea putris* (Fig. 5; Table 1). The ESR age of 16.4 ± 2.6 ka seems underestimated compared to the atmospheric calibrated AMS ^{14}C age of 19 670–19 324 cal BP. Considering a hard-water effect of a few hundred years, the radiocarbon age would possibly agree with the ESR age within error range.

These data from the *Übergangsterrassen* in the Danube and Isar valley indicate an Upper Würmian age of the loess cover. This is also the case for the loess cover on the *Übergangsterrasse* in the Iller valley southwest of Fellheim (Fig. 1: sample site g). A formation prior to the Würmian pleniglacial of this loess-covered transitional terrace was first assumed by Schaefer (1940, 1953) and Brunnacker (1953). They demonstrated that the 1 to 2 m, sometimes more than 4 m thick, layers of Würmian loess and loess loam overlay the unweathered gravel deposit without any fossil interglacial soil horizon. In a gravel pit southwest of Fellheim, the more than 10 m thick, horizontally and trough-bedded gravel deposits (Fig. 6: Photo 1) and its up to 1.6 m thick cover of sandy loess (Fig. 7) were recently exposed. Only the upper 20 to 30 cm of the gravel layers were very slightly weathered with some mellow sandstones and dolomites, but without any significant decalcification (Fig. 7). A few species of cold-climate land-snail shells of *Succinella oblonga* ($n = 8$) and *Pupilla muscorum* ($n = 6$), and one shell of *Cochlicopa lubrica* were sampled from the bottom layer of the loess sediments. Unfortunately, not enough material for ESR dating could be sampled. However, two OSL samples of the bottom loess itself yielded ages of 29 ± 4 and 31 ± 4 ka, respectively (Fig. 7, Table 2).

All in all, the fluvial gravel deposits of the described *Übergangsterrassen* areas in the valleys of the Iller, Isar and Danube rivers are older than the Upper Würmian loess cover on top of their gravel deposits. Most probably, the younger one of the currently known two *Übergangsterrassen*, the ÜT2, is at least of late Middle Würmian age (MIS 3). This is indicated by the luminescence data of Kroemer (2010) from the *Übergangsterrasse* of the Danube west of Natternberg (Fig. 3). The age of the older ÜT1 is still unknown. This terrace is younger than the last interglacial Fagotia gravel (see next section), most probably of Early Würmian age (MIS 5d to MIS 4).

4.2 ESR data and gastropod fauna from the *Jüngere Moosburger Hochterrasse* (*Fagotienschotter*, Isar valley)

Two different levels of *Hochterrassen* are preserved between the Isar and lower Amper valley in the vicinity of Moosburg (Fig. 4) and were described in detail by Schellmann (2018b). The *Ältere Moosburger Hochterrasse* (Older Moosburger high terrace) is elevated about 15 to 16 m above the flood-

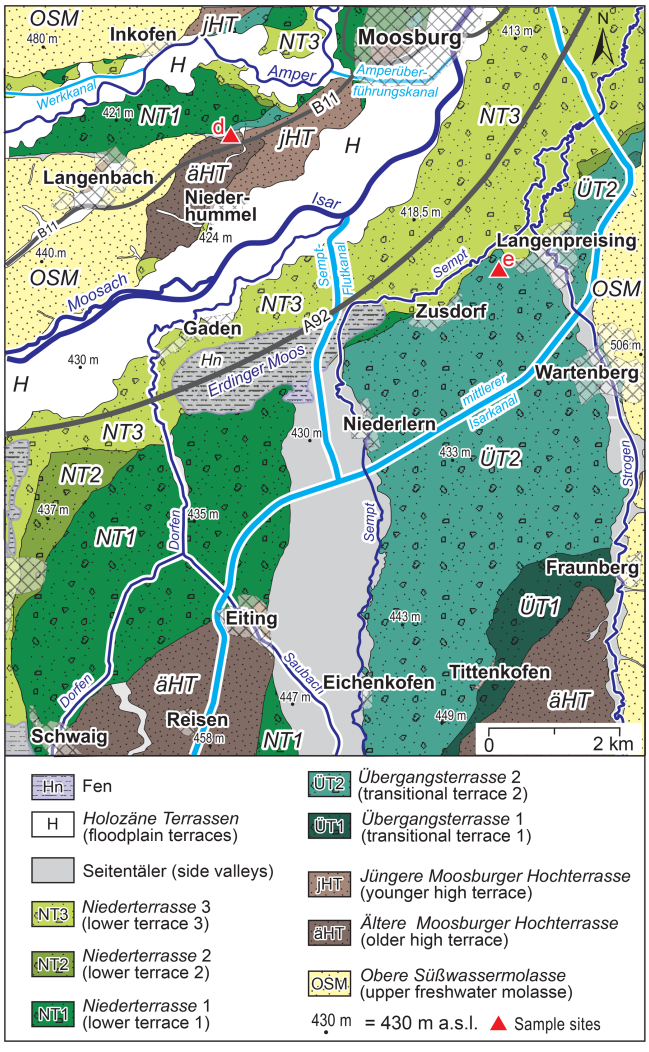

Figure 4. Middle and Late Pleistocene terraces of the Isar valley west and south of Moosburg modified after Schellmann (2018b).

plain of the river Isar, the *Jüngere Moosburger Hochterrasse* (Younger Moosburger high terrace) about 10 to 14 m.

The fluvial gravel deposits of both *Hochterrassen* have thicknesses of about 5 to 7 m, which are covered by Würmian loess mostly with thicknesses of 1 to 5 m. The Middle Pleistocene gravel deposits underlying the *Hochterrassen* are elevated above the fluvial gravel deposits of the adjacent Würmian and Holocene terraces of the Isar valley.

The *Jüngere Moosburger Hochterrasse* is situated between the valleys of Isar and Amper (Fig. 4). This terrace deposit has been known for many years under the name *Fagotienschotter* (Fagotia gravel), named after the gastropod *Fagotia acicularis*. Biostratigraphically (mollusc content) these gravel deposits are supposed to be as old as the last interglacial (Nathan, 1953; Brunnacker and Brunnacker, 1962; Brunnacker, 1966; Jerz, 1993) or older than the Elsterian glaciation in northern Germany as postulated by Kovanda (2006). All these authors agree on the interglacial habitus of the gastropod fauna; only the age interpretation is controversial.

Gastropod samples for dating were collected from a small gravel pit west of Moosham (Fig. 1: sample site d; Fig. 8). Here, marly clods bearing land-snail shells are intercalated in the *Fagotienschotter*. This new collection of land-snail species is similar to the collection of Nathan (1953). The interglacial character of the gastropod fauna is demonstrated by some interglacial species like *Aegopinella nitens* and by some further species that prefer warm temperate climatic conditions (Table 3). The floodplain of the river Isar, containing small standing waters and swamps and rich in high shrubs, could have been the habitat from which the snails derive. Species indicating dryness or open landscapes are almost completely absent.

Land-snail shells were collected from two separate marly clods (Fig. 8: Is 16/7 and Is17/1b) and dated by ESR. A mixture of land-snail shells of the species *Aegopinella* cf. *nitens*, *Arianta arbustorum, Succinella oblonga* and *Trochulus hispidus* yielded a last interglacial ESR age of 130 ± 16 ka (Table 1: Ba43). In the other marly clod, a few individuals of *Arianta arbustorum* also resulted in a last interglacial ESR age of 131 ± 14 ka (Table 1: Ba55) and a shell mixture of *Aegopinella* cf. *nitens* and *Trochulus hispidus* in an ESR age of 119 ± 15 ka (Table 1: Ba56).

From a morphostratigraphic point of view, the *Jüngere Moosburger Hochterrasse* (or Fagotia gravel) is older than both *Übergangsterrassen* deposits of Lower to Middle Würmian age southwest of Moosburg. And it also is younger than the Rissian *Ältere Moosburger Hochterrasse*, which is preserved in the west of the *Jüngere Moosburger Hochterrasse* (Fig. 4; details in Schellmann, 2018b). The gastropod fauna, which is preserved in marly or sandy clods or in sand lenses in the gravel deposits of the *Jüngere Hochterrassen*, indicates a warm temperate interglacial age of this deposit (Nathan; 1953, Brunnacker and Brunnacker, 1962; Brunnacker, 1965; Kovanda, 2006); the three ESR ages provide clear evidence for a deposition during the last interglacial (MIS 5e).

4.3 ESR data and gastropod fauna from the basal gravel unit of the *Dillinger Hochterrasse*

In the Danube valley between the villages Sontheim, Dillingen and Höchstädt (Fig. 9), *Hochterrassen* are widely preserved, especially north of the river. Graul (1962) was the first one to separate this extensive *Hochterrassen* area into three sublevels, and Leger (1988) and Bibus and Strahl (2000) found that the middle level of these three *Hochterrassen* levels, the *Dillinger Hochterrasse*, is composed of two stacked gravel deposits. This is the case in areas where the otherwise typically 5 to 8 m thick *Dillinger Hochterrassen* gravel reaches unusual thicknesses of about 10 to 13.5 m (Fig. 9). For details about the *Dillinger Hochterrasse* including the history of research, a geological map and

Table 3. Shells from gastropods collected from sand lenses and clods of marl and sand embedded in the *Jüngere Moosburger Hochterrassen* gravel (Fagotia gravel).

		Nathan (1953)	A	B1	B2
	1. Forest snails sensu stricto				
!	*Aegopinella nitens*	×	×	–	65
!	*Helicodonta obvoluta*	×	–	–	–
!	*Monachoides incarnatus*	×	–	–	–
!	*Platyla polita*	×	–	–	–
	2. Further shade-preferring species				
	Arianta arbustorum	–	×	1	17
!	*Cepaea* sp.	–	–	–	1
!	*Cepaea nemoralis*	×	–	–	–
!	*Discus rotundatus*	×	–	–	–
(!)	*Fruticicola fruticum*	×	–	–	–
	Trochulus striolatus	×	–	–	–
! ?	*Trochulus villosus*	–	–	–	1
	Vitrea crystallina	–	–	–	1
	Vitrea sp.	×	–	–	–
!	*Vitrinobrachium breve*	×	–	–	1
	3. Ubiquists				
	Agriolimacidae/Limacidae	×	–	–	–
!	*Carychium tridentatum*	×	–	–	–
	Cochlicopa lubrica	×	×		48
	Nesovitrea hammonis	–	–	–	17
	Nesovitrea petronella	–	×	–	1
	Succinella oblonga	–	×	–	17
	Trochulus hispidus	×	×	2	31
	4. Open-land species				
!	*Cecilioides acicula*	×	–	–	–
	Vallonia costata	–	×	–	1
	5. Water- and swamp-preferring molluscs				
(!)	*Ancylus fluviatilis*	×	–	–	–
	Anisus leucostoma	×	–	–	–
	Anisus vortex	×	–	–	–
(!)	*Bithynia tentaculata*	×	–	–	–
(!)	*Carychium minimum*	×	–	–	–
!!	*Esperiana daudebartii* (*Fagotia acicularis*)	×	–	–	–
	Galba truncatula	×	–	1	–
	Gyraulus acronicus	×	–	–	–
	Gyraulus laevis	×	–	–	–
!!	*Lithoglyphus* sp.	×	–	–	–
(!)	*Oxyloma elegans*	–	–	12	1?
	Pisidium amnicum	×	–	–	–
(!)	*Pisidium moitessierianum*	×	–	–	–
	Pisidium ponderosum	×	–	–	–
	Planorbis planorbis	×	–	–	–
	Radix balthica	×	–	–	–
(!)	*Segmentina nitida*	×	–	–	–
	Stagnicola corvus	×	–	–	–
	Valvata cristata	×	–	–	–
(!)	*Valvata piscinalis*	×	–	–	–
	Unionacea	×	–	–	–
	6. Indifferent				
	Clausiliidae	×	–	–	–

A – sample Is 16/97 collected 2016; B1 – sample Is 17/1a collected 2017; B2 – sample Is 17/1b collected 2017 in the gravel pit west of Moosham. !! interglacial indicator species: ! interglacial species; (!) predominately warm temperate species, sometimes also distributed in interstadials.

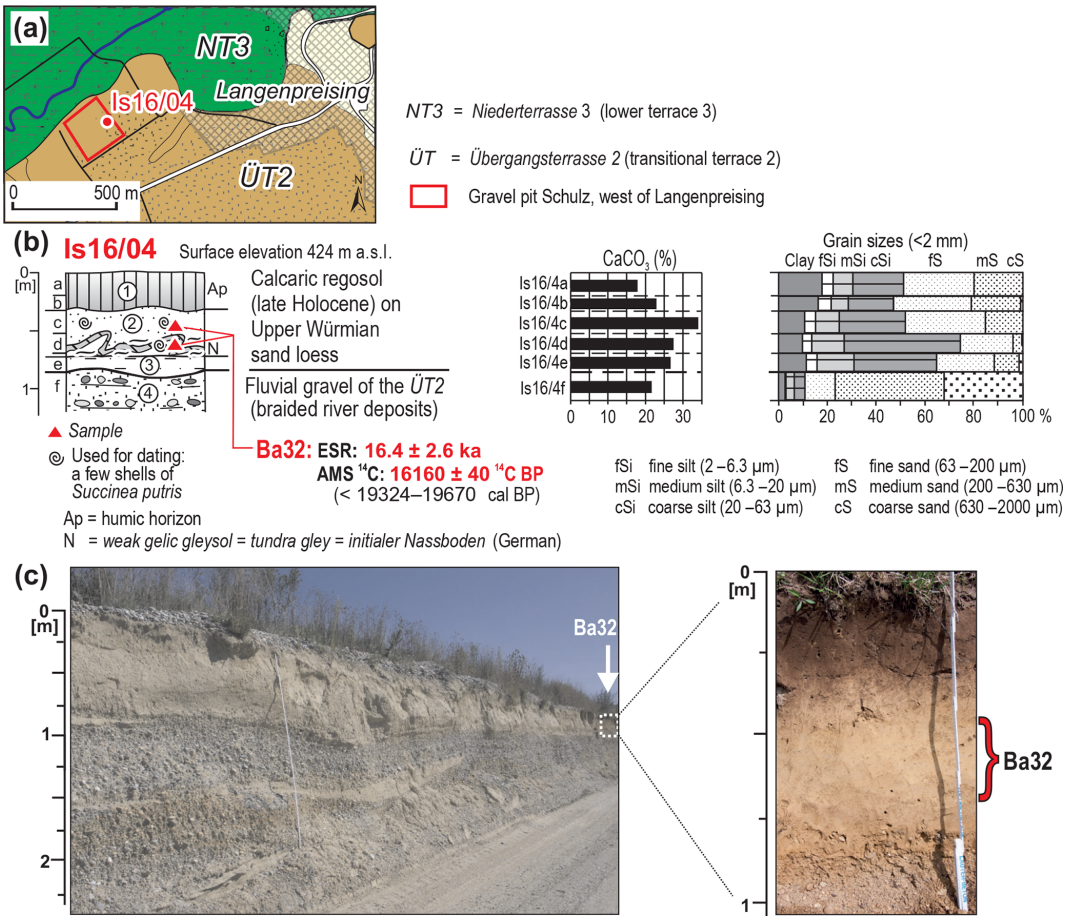

Figure 5. ESR and ^{14}C dating results of small terrestrial gastropods from the sand loess cover on the *Übergangsterrasse 2* west of Langenpreising, Isar valley (Fig. 1: sample site e; Table 1: sample Ba32); **(a)** geological map modified after Schellmann (2018b) with location of the sample site Ba32; **(b)** geological profile with dating results and some laboratory analysis (carbonate content, grain sizes); **(c)** photo of the *Übergangsterrassen* gravel (left) and its sandy loess cover with sample location Ba32 (right).

a revised fluvial terrace stratigraphy of the Danube valley in this region, see Schellmann (2017a, b).

Like the *Fagotienschotter* in the Isar valley, the basal gravel formation of the *Dillinger Hochterrasse* in the Danube valley west of Höchstädt (Fig. 1: sample site b, Fig. 9) also contains a warm-temperate interglacial mollusc fauna, which is embedded in sandy layers and predominantly in loamy and sandy clods. It was Leger (1988) who for the first time described an interstadial or interglacial gastropod fauna embedded in sandy gravel deposits of the *Dillinger Hochterrasse* west of the village of Höchstädt.

Gastropods shells have been collected from sandy layers and loamy and sandy clods at different sections in a gravel pit on the *Dillinger Hochterrasse* west of Höchstädt (Fig. 10). This location is only some hundred metres away from the site sampled by Leger (1988). The clods were deposited in frozen state in the basal gravel formation of the *Dillinger Hochterrasse* and have been reworked from a nearby former floodplain. Only in the eastern part of the gravel pit, this large-scale cross-bedded basal gravel unit reaches up to the gravel surface below the last glacial (Würmian) loess cover (Fig. 10b). In most parts of the gravel pit, the basal gravel unit is overlain by another few-metres-thick gravel unit deposited by a braided river (Fig. 10c). Gastropod shells were sampled in the eastern part of the gravel pit from two sandy layers (Table 4) and from two loamy and sandy clods (Fig. 10b). The collected gastropod fauna contain a few interglacial index species like *Discus perspectivus* and *Esperiana daudebartii* (*Fagotia acicularis*) and some other warm temperate species like *Helicodonta obvoluta* and *Monachoides incarnatus* (Table 4).

ESR dating of *Arianta arbustorum* (Ba09) and of *Fruticicola fruticum* species (Ba14) gave almost identical ages of 202 ± 17 and 199 ± 23 ka, respectively (Fig. 10b: Do13/8; Table 1: Ba09 and Ba14). The ESR age of 213 ± 20 ka of a further *Arianta arbustorum* shell from a neighbouring clod of loamy sand in this part of the gravel pit is within the error range of the other ages from this gravel unit (Fig. 10b:

Table 4. Shells from gastropods collected from sandy gravel deposits of the *Dillinger Hochterrasse* in the eastern part of the gravel pit Höchstädt.

		(1)	(2)	(3)	(4)	(5)	Total
	1. Shade-preferring species						
	1a. Forest snails						
!	*Acanthinula aculeata*	–	–	1	–	–	1
!	*Aegopinella* sp.	–	–	–	–	1	1
!!	*Discus perspectivus*	–	–	3	–	–	3
!	*Helicodonta obvoluta*	–	–	2	–	–	2
!	*Monachoides incarnatus*	–	–	1	2	–	3
	1b. Other shade-preferring species						
	Arianta arbustorum		–	5	5	6	16
!	*Cepaea hortensis*	1	–	?	–	–	1
	Clausilia pumila	–	–	3	3	–	6
(!)	Fruticicola fruticum	1	–	3	3	2	9
?	*Trochulus* cf. *coelomphalus*	–	–	4	6	4	14
	2. Ubiquists						
!	*Carychium tridentatum*	–	–	–	2	1?	2
	Eucobresia diaphana	–	–	–	1	–	1
	3. Open-land species						
(!)	*Vallonia pulchella*	–	–	1	–	2	3
	4. Water- and swamp-preferring mollusc						
!!	*Esperiana daudebartii (Fagotia acicularis)*	1	–	–	–	–	1
	Pisidium amnicum	–	1	–	–	–	1
	Succinea putris	1	–	–	–	–	1
	Helicidarum (indet.)	–	×	×××	×	××	

!! interglacial index species ! interglacial species (!) predominately warm temperate species. (1) gastropods collected from sandy layer during July 2013. (2) gastropods collected from sandy layer during October 2013 (Do 13/5). (3) gastropods collected from a loamy and sandy clod during October 2013 (Do 13/8li). (4) gastropods collected from another loamy and sandy clod during October 2013 (Do 13/8re). (5) gastropods collected from both loamy and sandy clods during October 2013 (Do 13/8).

Figure 6. Horizontally and trough-bedded gravel deposits of the *Übergangsterrasse* (*Fellheimer Feld* in the Iller valley south of the village Fellheim (Fig. 1: sample site g).

Do13/8li; Table 1: Ba11). Gastropod shells from the western part of the gravel pit (Fig. 10c: Do14/9, Ba15; Table 1: Ba15) also yield a MIS 7 age of 206 ± 20 ka. This shell-bearing clod was also deposited in the sandy and large-scale cross-bedded basal gravel unit. The overlying unit of a medium- to coarse-gravel facies is horizontally bedded, which is typical of braided river deposits. This overlying gravel unit was deposited by the Danube under cold climate conditions most probably during MIS 6. Under warm climate conditions like the Holocene the Danube is a meandering river in this region with sandy gravel channel deposits, which are large-scale cross-bedded (Schellmann, 2017b).

In general, these ESR dating results from the *Dillinger Hochterrasse* illustrate that ESR ages of different species of land-snail shells and from different clods of sandy loam in a gravel pit yield highly congruent ages. All ESR data from the basal gravel unit in the gravel pit west of the village Höchstädt are of penultimate interglacial (MIS 7) age. These

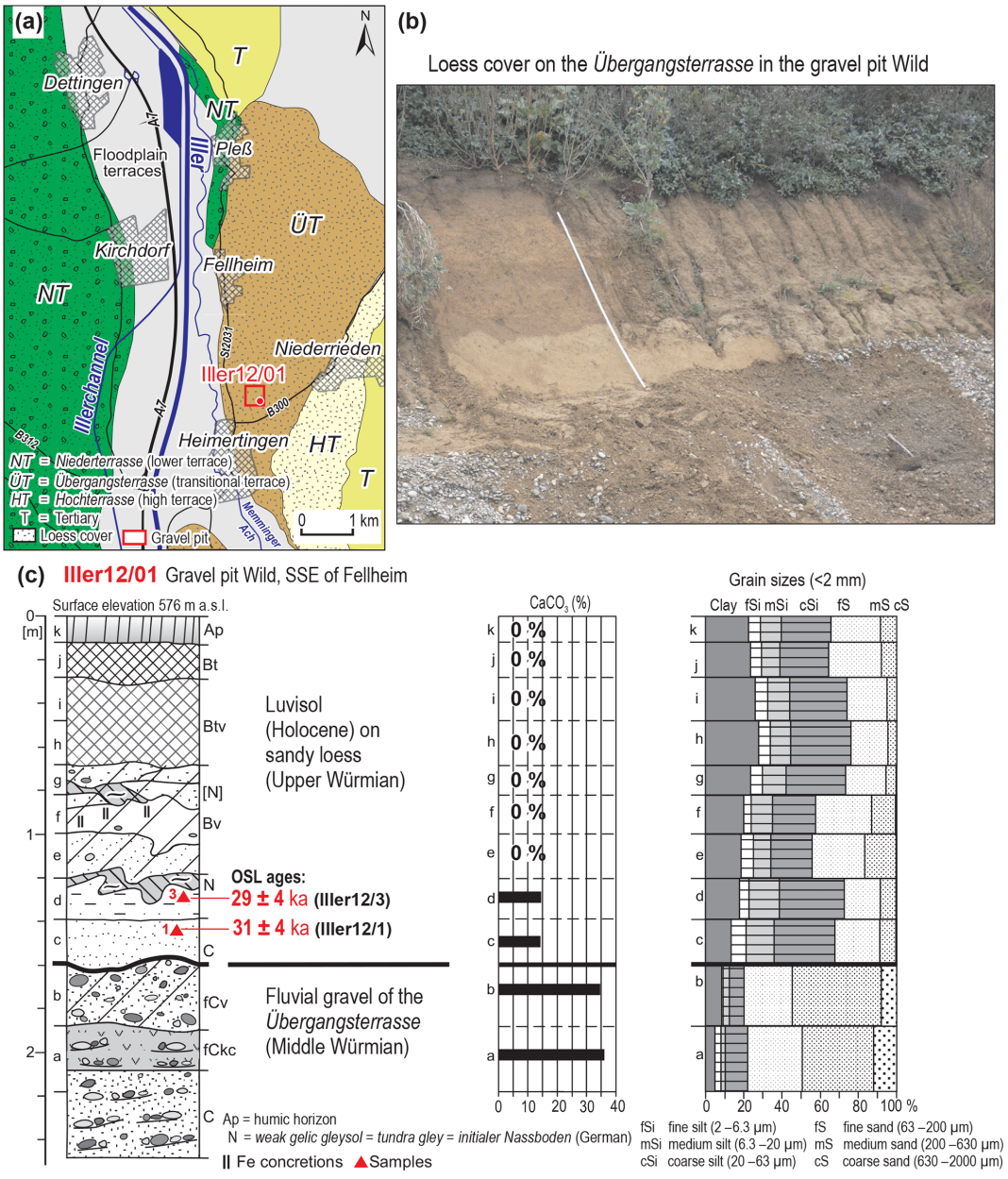

Figure 7. Luminescence dating results from the base of the sandy loess cover on top of the *Übergangsterrassen* gravel south of the village Fellheim (Fig. 1: sample site g; luminescence data are listed in Table 2); **(a)** geological map with location of the sample site Iller 12/01; **(b)** photo of the loess cover in the gravel pit Wild; **(c)** soil profile with some laboratory analysis (carbonate content, grain sizes), and two luminescence ages.

dating results confirm the regional stratigraphy (Schellmann, 2017b) and match the warm temperate climate indicated by the gastropod species. The 2 to 5 m thick superimposed gravel unit with its braided river facies type is most probably of penultimate glacial age (Rissian, MIS 6).

4.4 ESR and luminescence data from the *Langweider Hochterrasse* (Lech valley)

Similar to the *Dillinger Hochterrasse* in the Danube valley, a subdivision of the Middle Pleistocene fluvial gravel deposits of the *Langweider Hochterrasse* between Lech and Schmutter valley in two different gravel formations has been discussed for decades (Schäfer, 1957; Scheuenpflug, 1979, 1981; Aktas and Frechen, 1991; Schellmann, 2016b; Schielein and Schellmann, 2016a). All these studies assume

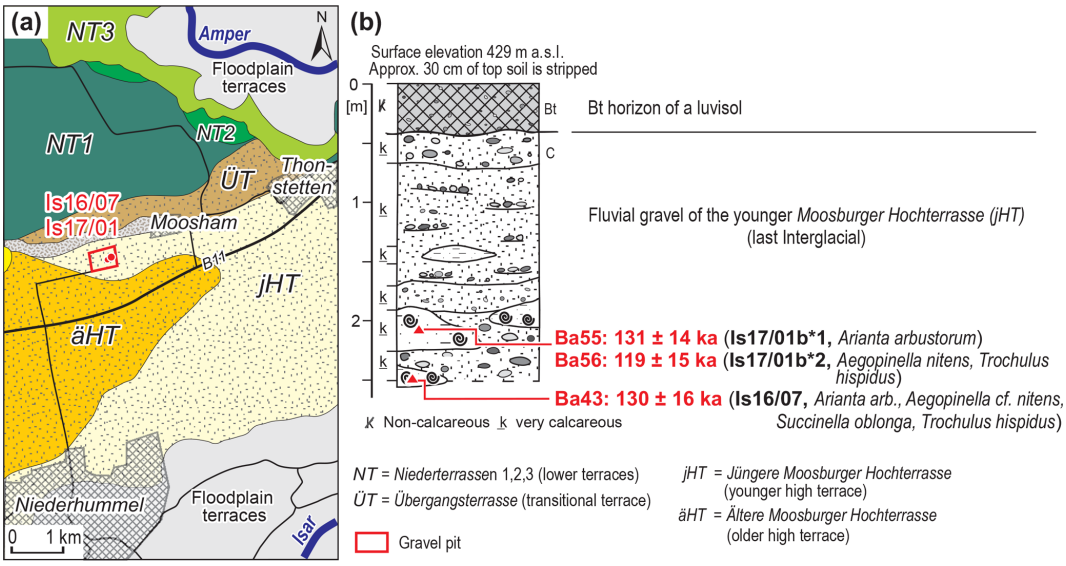

Figure 8. Marly and fine-sandy clods in the gravel deposits of the *Jüngere Moosburger Hochterrasse* (Fagotia gravel) west of Moosham, Amper valley (Fig. 1: sample site d; Table 1: samples Ba43, Ba55, Ba56). Small gastropods were collected and ESR dated from two separate clods in the years 2016 (sample Is16/07, Ba43) and 2017 (sample Is17/1, Ba55, Ba56); **(a)** geological map (modified after Schellmann, 2018b) with location of sample sites; **(b)** soil profile with ESR dated gastropod shells (species are listed in Table 3).

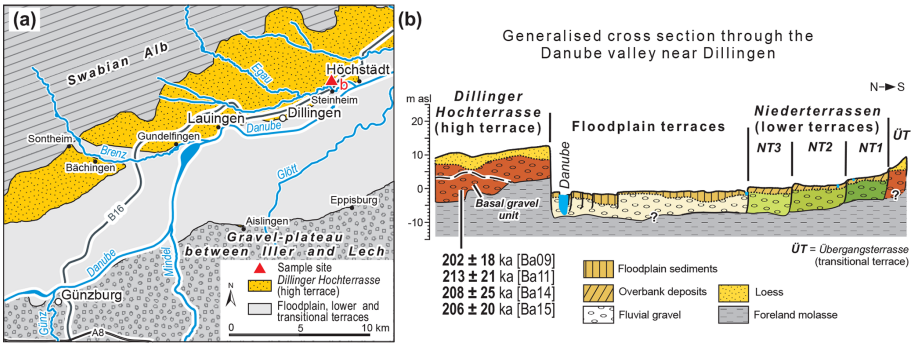

Figure 9. Distribution **(a)** and geological cross section **(b)** of the *Dillinger Hochterrasse* on the northern valley side of the river Danube between the villages Sontheim, Dillingen and Höchstädt (modified after Schellmann, 2017b).

a deposition of the 6 to 8 m thick top unit of the *Langweider Hochterrasse* during the penultimate glacial (Rissian), whereas the age of the basal gravel unit with thicknesses of 2 to 4 m remained uncertain. It was Schielein et al. (2015) who presented first luminescence data from both gravel units (Fig. 11) and one ESR age from the basal gravel deposit (Fig. 11: Le 11/26c; sample site: A11 Nachwegäcker). The luminescence data indicate a Rissian age of the superimposed gravel. Four IRSL samples from the basal gravel unit imply an age older than MIS 6, whereas the ESR dating of one large shell of *Succinea putris* refers to a deposition during the penultimate interglacial (MIS 7).

Small shells of the land-snail species *Trochulus hispidus* were collected from a clod of marl in the superimposed gravel (Fig. 11: sample site A7; Table 1: sample Ba12). The ESR age of 156 ± 21 ka is similar to IRSL ages of 160 ± 15 ka and of 163 ± 19 ka from sandy layers in the same gravel unit. Within error range, the ESR and luminescence ages also fit to two IRSL dates of 170 ± 18 and 179 ± 20 ka from the superimposed gravel in the neighbouring outcrop A8 Burghof W (Fig. 11). It can be stated that the superimposed gravel of the *Langweider Hochterrasse* was most likely accumulated during the penultimate glacial (MIS 6, Rissian), whereas the basal gravel unit has a minimum age of MIS 7 (Schielein et al., 2015). Most probably, the basal gravel formation may be correlated with the basal gravel deposit of the *Dillinger Hochterrasse*.

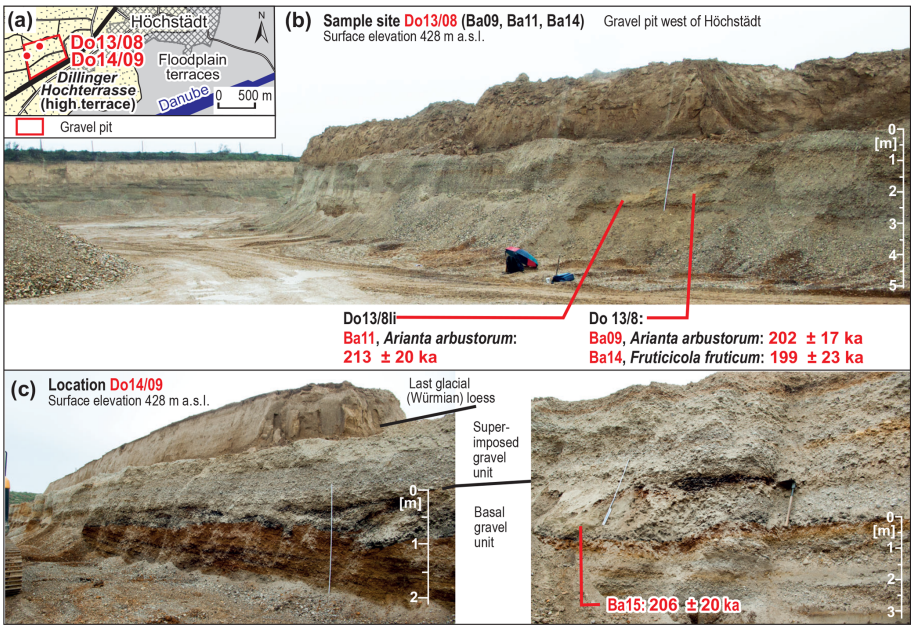

Figure 10. ESR dating results of an interglacial gastropod fauna from the basal gravel unit of the *Dillinger Hochterrasse* in the gravel pit Höchstädt W (Fig. 1: sample site b; Table 1: samples Ba09, Ba11, Ba14, Ba15); **(a)** geological map (modified after Schellmann, 2016b) with location of sample sites Do13/8 and Do14/9; **(b)** photo of sample site Do13/8 and ESR ages of the samples Ba09, Ba11, Ba14; **(c)** photos of the location Do14/9 with a large scale cross-stratified basal gravel unit and a horizontally bedded (braided river) top gravel unit (left), and the location and ESR age of sample Ba15 (right).

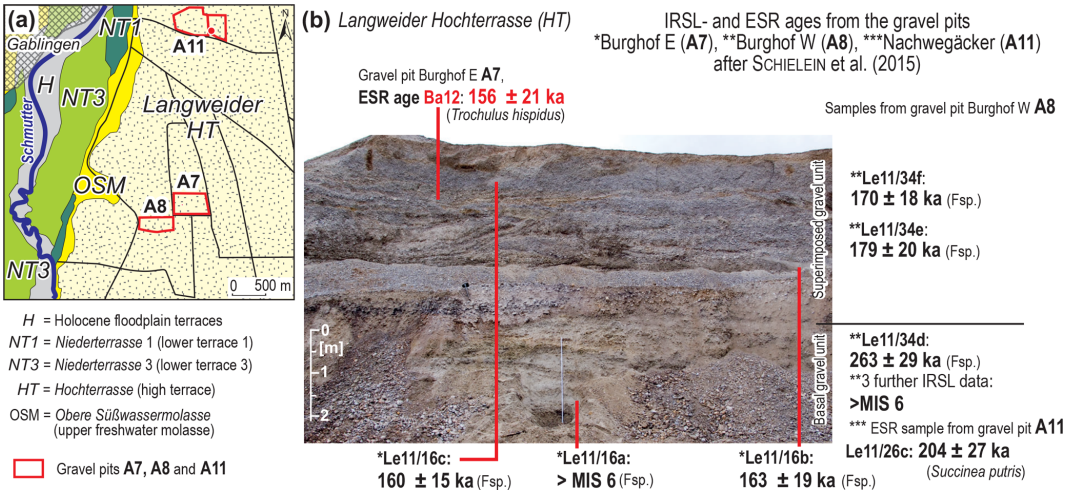

Figure 11. ESR and luminescence data from the stacked gravel deposits of the *Langweider Hochterrasse* in the gravel pit A7 Burghof E (Fig. 1: sample site a); **(a)** geological map (modified after Schellmann, 2018b; Schielein and Schellmann, 2016a) with location of sample sites; **(b)** photo with the newly dated ESR sample Ba12, and with some luminescence and ESR ages from Schielein et al. (2015). The latter are from the same outcrop (*), or from the nearby gravel pits A8 Burghof W (**) and A11 Nachwegäcker (***).

4.5 ESR and luminescence data from the *Rainer Hochterrasse* and from its loess cover (Lech valley)

Following the Lech valley downstream, a further high terrace is conserved near the confluence of Lech and Danube rivers: the *Rainer Hochterrasse* (Fig. 1: sample site c; Fig. 12). In contrast to Schaefer (1966), a clear morphostratigraphic subdivision of the Rainer Hochterrasse could not be confirmed (Schielein and Schellmann, 2016b) as already stated by Kilian and Löscher (1979). Only small areas of the significantly lower elevated surfaces of the *Übergangsterrasse* can be differentiated from the higher elevated areas of the *Rainer Hochterrasse* (Fig. 12).

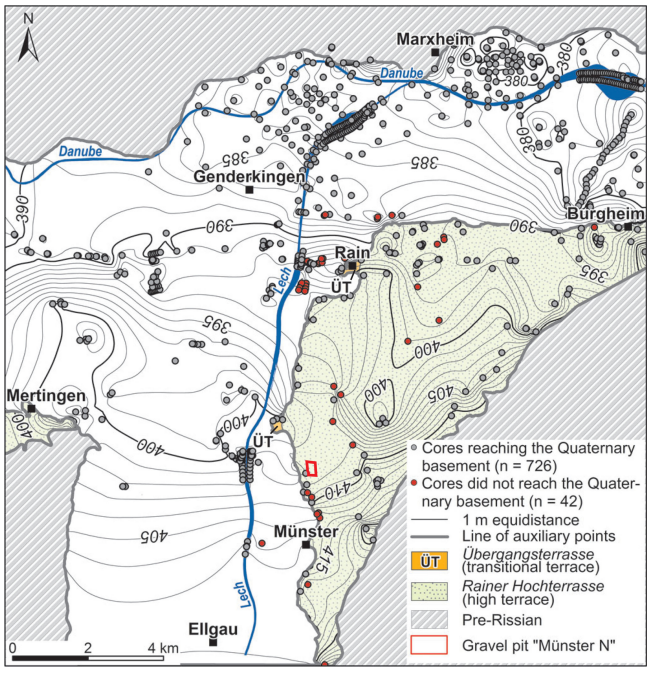

Figure 12. Geological map of the *Rainer Hochterrasse* with contour lines of the base level (m a. s.l.) of the Quaternary gravel deposits and location of the gravel pit Münster N mentioned in the text.

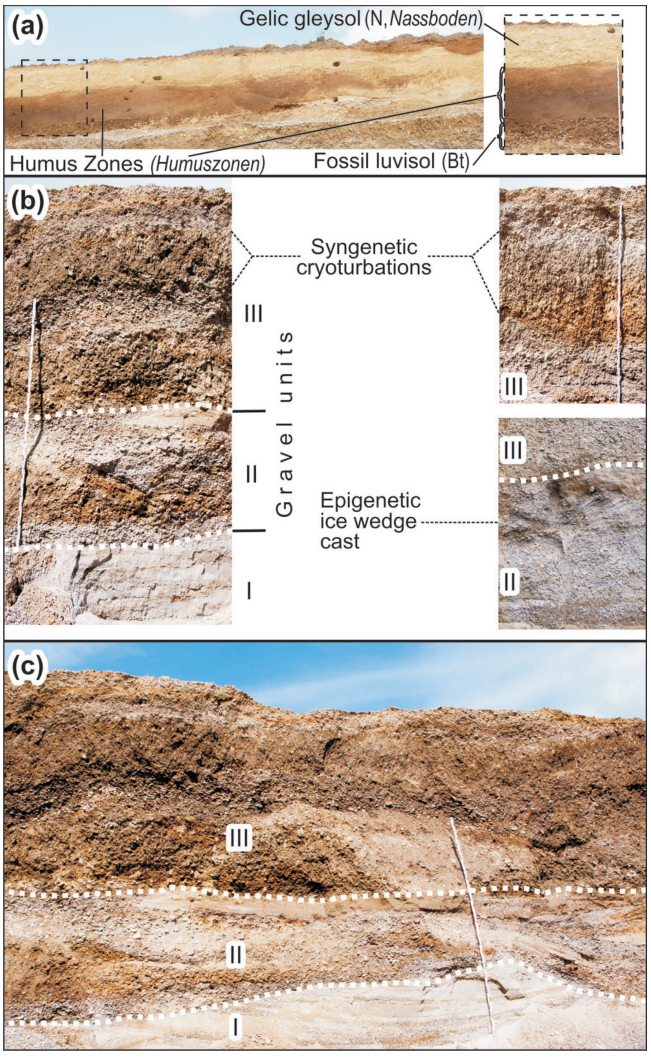

Figure 13. Images of the different fluvial gravel deposits of the *Rainer Hochterrasse* and the Würmian loess cover exposed in the gravel pit Münster N (Fig. 1: sample site c) during the last few years; **(a)** images of the loess cover exposed during the year 2009; **(b)** images of the three gravel units I to III exposed during the years 2016 and 2017; **(c)** image of the three gravel units I to III exposed during the year 2017.

The uniform terrace level of the *Rainer Hochterrasse* including some periglacial dry valleys is elevated about 10 to 14 m above the valley floor of the Lech and Danube rivers and its Würmian and Holocene terraces. The gravel deposits and the 1 to 3 m thick loess and sand loess cover reach thicknesses of 7 to 13 m in total. The base of the gravel deposits in the area of the *Rainer Hochterrasse* is about 8 to 10 m higher than the base level in the adjacent Upper Würmian and Holocene valley bottom (Fig. 12). In a southwest–northeast-orientated elongated depression extending in the central areas of the high terrace, a maximum thickness of the Quaternary sediments up to 15 m is reached (Fig. 12; Kilian and Löscher, 1979).

In one gravel pit north of the small village of Münster (gravel pit Münster N), which has been investigated by different researchers (e.g. Tillmanns et al., 1982, 1983; Schielein et al., 2015; Schielein and Schellmann, 2016b), the following summarised section has been exposed since 2016. Here, the *Hochterrassen* gravel is covered by 1 to 2.5 m thick loess sediments. In periglacial depressions, some decimetres thick layers of solifluidal reworked silts, sands and gravels (Fig. 14) are present. Up to three slightly rusty and grey Gelic Gleysols (tundra gley, *Nassboden*) may be preserved in the upper part of the fine-sandy loess cover. Similar weak Gelic Gleysols are most common in Upper Würmian loess deposits in Germany. In the lower part of a 2.6 m thick fine-grained infill of a periglacial trough valley, a stack of two humic horizons (*Humuszonen*) was preserved (details in Schielein and Schellmann, 2016b), which are comparable to the Lower (Early) Würmian *Mosbacher Humuszonen* (e.g. Semmel, 1968). Light reddish-brown spots in the upper part of the lower humic horizon correlate most probably to the "*gefleckten Horizont*" (spotted horizon) of Rohdenburg (1964) and might have been developed through acidic conditions by bleaching along plant roots. The Upper to Lower Würmian age of this loess cover is confirmed by the luminescence ages of 19.3 ± 2.2 ka (Fsp.) and 19.8 ± 2.7 ka (Qu.) from the top of the sandy loess cover, and of 95 ± 12 ka

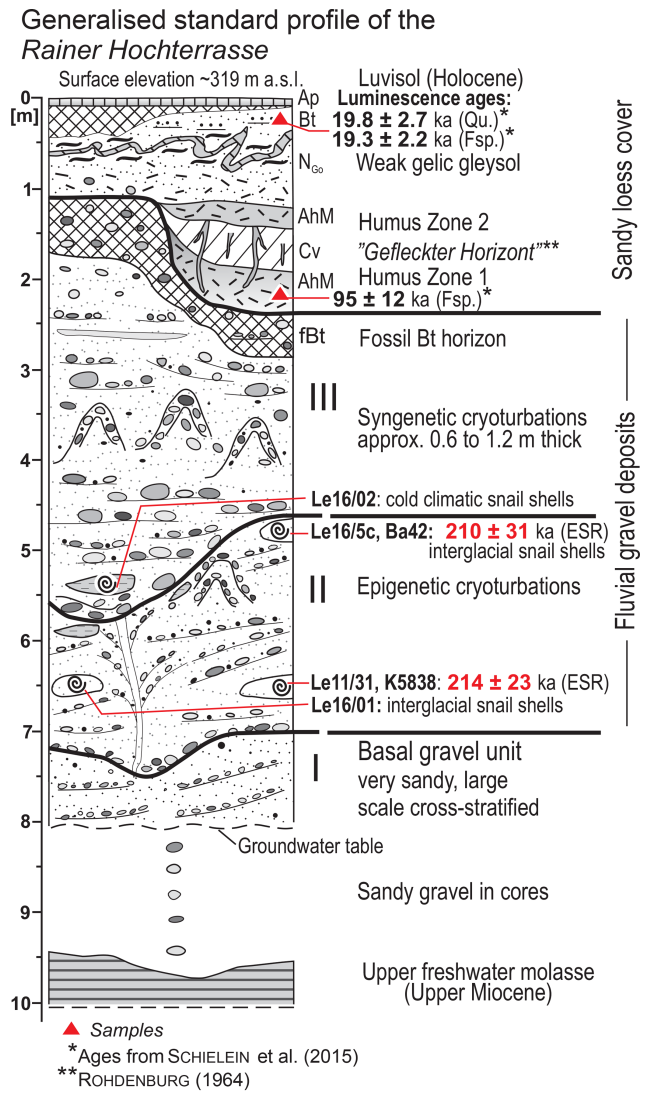

Wet sieving, one vertical sample per gravel unit	Gravel I	Gravel II	Gravel III
	wt.%	wt.%	wt.%
Sand, silt, clay (<0.2 cm)	35.5	16.2	19.5
Fine - middle gravel (0.2–2.0 cm)	64.3	61	32.6
Coarse gravel (2.0–6.3 cm)	0.2	19	26.3
Stones (>6.3 cm)		3.8	21.1
Max. diameter (cm)		8.5	11.5

Figure 14. Generalised standard profile of the different sediment units of the *Rainer Hochterrasse* exposed in the gravel pit Münster N (Fig. 1: sample site c) during the last few years. IRSL data from the loess cover are from Schielein et al. (2015); the ESR dating results of an interglacial gastropod fauna from the gravel unit II and the faunae collections are new.

(Fsp.) from the base of the lower humic horizon (Fig. 14; Schielein et al., 2015).

Below the loess cover, a fossil interglacial soil horizon (Bt horizon of a Luvisol; Fig. 14) with a mean thickness of 0.3 to 0.5 m is widely preserved on top of the *high terrace* gravels. In several outcrops, the 8 to 14 m thick sandy gravel deposits of the *Rainer Hochterrasse* can be subdivided into two stacked gravel units as previously mentioned by Tillmanns et al. (1982, 1983) and Schielein et al. (2015). In the aforementioned gravel pit Münster N, a third gravel unit is exposed below the other units near the groundwater table (Fig. 13). This very sandy and often large-scale cross-bedded or sometimes trough-bedded gravel unit I is often preserved approximately up to 1 to 2 m above the groundwater level (Fig. 14). The light colour of unit I is due to its high sand content of about 35 % and allows a clear separation from both superimposed gravel units, whose sand content is significantly lower (Fig. 14). The more than 1.5 m thick gravel unit II is predominately composed of fine to medium gravels but may contain coarse- and medium-sand layers with thicknesses of up to 1 m (Schielein et al., 2015). Sometimes epigenetic cryoturbations or small ice-wedge casts (Fig. 13) are preserved at the top of the gravel unit II. These periglacial features are overlain discordantly by the 2 to 5 m thick gravel deposits of unit III. The latter consists of medium and coarse gravel with many stones in a sandy matrix (Fig. 14), shows horizontal and trough-bedding, and exhibits strong syngenetic cryoturbations within the upper part of the unit (Fig. 13) as already described by Tillmanns et al. (1982, 1983).

In general, gravel units I and II are both large-scale cross-bedded, which indicate a deposition by a meandering or a moderate branching river like the Holocene river Lech. In contrast, the superimposed gravel unit III was accumulated by a braided river as it is characteristic of river morphology in this region under Pleistocene cold climate conditions.

Single clods of marl or sand can be preserved from the groundwater level up to the top of the gravel deposits. A separation of the whole gravel deposit by one significant layer of marly clods ("*Mergelbatzenhorizont*") as described by Tillmanns et al. (1982, 1983) was not comprehensible. All gravel units contain marly or loamy clods sometimes concentrated near the base of a gravel unit but often irregular within the gravel unit. As already described by Tillmanns et al. (1982, 1983) these clods sometimes contain shells of predominately cold (*Columella columella*, *Pupilla muscorum*, *Succinea oblonga*, *Trichia hispida*) and rarely warm (*Ena montana*, *Discus rotundatus*, *Aegopinella* sp., *Helicondonta obvoluta*, *Cepaea* sp.) gastropod fauna. A cold climatic or interstadial gastropod fauna could be sampled from a marly clod embedded at the base of gravel unit III at approx. 5.5 m below terrace surface (Fig. 14: Le16/2). This clod contained shells from the following species: *Cochlicopa lubrica*, *Pupilla muscorum*, *Neostyriaca corynodes*, *Succinella oblonga*, *Trochulus hispidus*, *Vallonia costata* and *Vallonia pulchella*. Shells from *Cochlicopa lubrica*, *Pupilla muscorum*, *Succinella oblonga*, *Vallonia costata* and *Vallonia pulchella* have been sampled also from marly clods with cold climatic gastropod fauna in 5 to 6 m below terrace surface by Tillmanns et al. (1982).

Both the cold climatic habitus of the gastropod fauna and the strong syngenetic cryoturbations clearly point to a deposition of gravel unit III under periglacial, stadial or intersta-

dial climatic conditions older than the Early to Late Würmian loess and older than the interglacial Bt horizon on top of the gravel deposits. The upper gravel unit is most probably of penultimate glacial (Rissian, MIS 6) age.

In contrast, two loamy clods from gravel unit II contain interglacial fauna. The following warm temperate species could be sampled from a loamy clod from gravel unit II in 4.8 m below surface (Fig. 14: Le16/5c): *Aegopis verticillus*, *Cepaea* sp. (*nemoralis*?), *Cochlodina laminata*, *Helicodonta obvoluta*, *Isognomostoma isognomostomos* and *Monachoides incarnatus*. A further loamy clod from gravel unit II in a depth of 6.5 m below surface contains shells of the warm temperate species *Aegopinella* sp., *Helicodonta obvoluta*, and *Monachoides incarnatus* (Fig. 14: Le16/1). These species have already been sampled by Tillmann et al. (1982) in this outcrop area from a marly clod with warm climatic gastropod fauna at approx. 5 m below terrace surface.

Helicodonta obvoluta and *Aegopis verticillus* shells from a loamy clod (Fig. 14: Ba42) and one large shell fragment from a layer of fine-sandy loam (Fig. 14: K5838) yielded almost identical ESR ages of 210 ± 31 and 214 ± 23 ka, respectively. Hence, the formation of gravel unit II during penultimate interglacial (MIS 7) is very likely. Schielein et al. (2015) published four luminescence (IRSL, OSL) ages from one sand layer at the top of gravel unit II in a nearby gravel pit, but the data scatter between MIS 7 and MIS 9.

The age of the underlying gravel unit I is still open. It could have been deposited under warm climate conditions as indicated by the sedimentological observations, perhaps during the MIS 7 interglacial period.

Table 5. Stratigraphical overview for the formation of Middle and Upper Pleistocene gravel deposits in the Bavarian Alpine Foreland.

	International			Bavaria		Terraces
Age (Ka)	Marine Isotop. Stage	System	(Sub-)Series	Strati-graphy		
11,5	1	QUATERNARY	Holocene	Würmian		H7 to H1 *Holozänterrassen* (Holocene terraces)
30	2		Upper (Late) Pleistocene		Upper	NT3 NT2 NT1 *Niederterrassen* (lower terraces)
70	3 - 4				Middle	ÜT2 loess cover is as old as 29 to 31 ka gravel deposition: 30.4 ± 3.7 (Qu.); 36.0 ± 1.9 (Fsp.)* *Übergangsterrassen* (transitional terraces)
115	5a - 5d				Lower	ÜT1
130	5e			*Riß/ Würmian*		JHT *Jüngere Moosburger Hochterrasse* (*Fagotia* gravel) (approx. 119 to 131 ka; ESR)
	6 - 10		Middle Pleistocene	Rissian		HT *Langweider, Dillinger, Rainer Hochterrasse* (high terraces) top gravel unit: MIS 6 (approx. 156 to 179 ka; ESR, luminescence) basal gravel, gravel unit II: MIS 7 (approx. 199 to 214 ka; ESR)
	11			*Mindel/ Rissian*		

* luminescence data from KROEMER (2010)

International and Bavarian stratigraphic nomenclature modified after DOPPLER et al. (2011)

5 Discussion

Numerical age data (ESR, OSL, ^{14}C) indicate that the formation of the two *Übergangsterrassen* (ÜT1, ÜT2) in the Bavarian Alpine Foreland took place before the Upper Würmian (MIS 2) and thus before the formation of the oldest *Niederterrasse* 1 (NT1) and the loess accumulation on top of the fluvial gravel deposit during MIS 2 (Table 5). In the valley of the river Isar in the vicinity of the village of Moosburg, it could be shown by geological mapping that both *Übergangsterrassen* are younger than the *Jüngere Moosburger Hochterrasse* (i.e. Fagotia gravel) of MIS 5e age. Luminescence data by Kroemer (2010) from a sandy layer in the fluvial gravel deposit of the ÜT2 in the Danube valley west of the Natternberg imply a late Middle Würmian age (MIS 3). This correlates well with the fact that only Upper Würmian loess covers the *Übergangsterrassen* gravel. Previously, Buch and Zöller (1990; see also discussion by Schellmann, 2010) published early Upper Würmian luminescence ages of 25.4 ± 2.4 and 24.1 ± 2.4 ka respectively from the base of the loess cover on the younger *Übergangsterrasse* (ÜT2; Schellmann, 2010) of the Danube southeast of Regensburg (Fig. 1). Buch and Zöller (1990) called this loess-covered terrace level "*Deckniveau der Niederterrasse*".

In contrast to the younger *Übergangsterrasse* (ÜT2), the age of the older ÜT1 is still unknown. But the ÜT1 is younger than the MIS 5e old *Jüngere Moosburger Hochterrasse*. Therefore, the ÜT1 is most likely of Early Würmian age (MIS 5d to MIS 4). Doppler et al. (2011, p. 354) assume that the relatively young OSL data of ∼ 70 to ∼ 90 ka by Fiebig and Preusser (2003) for parts of the *Rainer Hochterrasse*, for the *Neuburger* as well as the *Ingolstädter Hochterrasse* most likely point to a classification as *Übergangsterrasse*.

At this point, a short but stratigraphically important digression to northern Germany may be excused. In the Upper Weser valley between the villages of Hamelin (Hameln in German) and Rinteln, an *Übergangsterrasse* is preserved (Schellmann, 1994). The terrace is younger than the Drenthe glaciation (MIS 6; Lang et al., 2018) of the valley and older than the Upper Weichselian (Upper Pleistocene) *Niederterrasse 1*. At the gravel pit Franke (geological map in Schellmann, 1994: Fig. 6), Winsemann et al. (2015) postulated on the basis of one luminescence dated sample (79 ± 3 ka) a loess-covered lower middle terrace (*Untere Mittelterrasse*),

which can likely be correlated to the *Übergangsterrasse* mapped by Schellmann (1994) in this area.

Until now, the only known terrace of last interglacial age in the Bavarian Alpine Foreland was the *Jüngere Moosburger Hochterrasse* (Fagotia gravel). The interglacial formation of this gravel deposit has been known for many years by the finding of shells from interglacial gastropod fauna embedded in sand lenses and loamy clods. They were described first by Nathan (1953), Brunnacker and Brunnacker (1962), and Brunnacker (1965). The ESR data (Table 1) of three shell samples with ages of 131 ± 14, 130 ± 16 and 119 ± 15 ka point to a last interglacial (MIS 5e) age of this terrace (Table 5) instead of an age older than the Elsterian glaciation in northern Germany as postulated by Kovanda (2006).

Generally, the *Hochterrassen* in the Bavarian Alpine Foreland were formed under cold climatic conditions during the Rissian period. Therefore, they are covered by loess sediments of Würmian age only, and just a relict of one interglacial soil (Bt horizon of a Luvisol) may be preserved at the top of their fluvial gravel deposits. Most recently, Mayr et al. (2017) published new numeric age data with Würmian ages from the loess cover and its palaeosoils preserved on an interglacial soil relict (Bt horizon of a Luvisol) at the top of the fluvial gravel deposit of the *Augsburger Hochterrasse* (Fig. 1). In some river valleys, especially in such areas with unusual thick fluvial sediment accumulations, older gravel deposits (basal gravel) may have been covered by the extensive *Hochterrassen* gravel accumulations (top gravel) during the Rissian. IRSL and ESR data from the top gravel of the *Langweider Hochterrasse* in the Lech valley indicate a penultimate glacial (MIS 6) age of the top gravel unit (Table 5). Similar old luminescence data have been published by Becker-Haumann and Frechen (1997) and Frechen (1999) from the gravel deposits of the *Augsburger Hochterrasse*. This penultimate glacial age (MIS 6) corresponds very well with the MIS 6 age of the high terrace in the type locality of the Rissian (Penck and Brückner, 1901–1909) at the northeastern margin of the former Rhine glacier. There, Rades et al. (2018) dated "high terrace gravels" in the gravel pit Scholterhausen (Biberach am Riß) via single-grain feldspar luminescence to an age range between 149 ± 15 and 179 ± 17 ka. These ages may correspond with luminescence data of 116 ± 17 ka and 142 ± 15 (OSL), and 122 ± 18 and 210 ± 24 ka (IRSL) by Bickel et al. (2015) on sediments from glaciofluvial deposits linked to penultimate glaciation in the Eastern Alps. In contrast, Fiebig and Preusser (2003) dated sediments from the gravel pit Münster via IRSL, which they associated with the *Rainer Hochterrasse*. They yielded Early Würmian ages between ∼ 66 and ∼ 81 ka. Whereas Rades et al. (2018) assume an anomalous fading of these samples, Schielein et al. (2015) state that these samples could be derived from gravel deposits of the *Übergangsterrasse* and not of the *Rainer Hochterrasse*.

A penultimate glacial age of the superimposed top gravel unit in the *Langweider*, *Dillinger* and *Rainer Hochterrasse* is also implied by penultimate interglacial ages of the underlying older gravel units. But the luminescence (IRSL) dating of sandy layers in the basal gravel of the *Langweider Hochterrasse* seems to reach its upper dating limit (Schielein et al., 2015). Only one of the five luminescence samples allowed a proper age estimation. Its age of 263 ± 29 ka indicates a deposition between MIS 7 and MIS 8. In contrast, the ESR age of a *Succinea putris* shell of 204 ± 27 ka (Schielein et al., 2015) implies a deposition during the penultimate interglacial MIS 7. The latter agrees very well with the MIS 7 ESR ages of four land-snail shells from the basal gravel unit of the *Dillinger Hochterrasse* with ages of 199 ± 23, 202 ± 17, 206 ± 20, and 213 ± 20 ka, and two ESR ages of 210 ± 31 and 214 ± 23 ka from the medium-gravel unit II of the *Rainer Hochterrasse* (Table 1). The reliability of these MIS 7 dating results is additionally strengthened by the interglacial character of gastropod fauna collected from the basal, medium-gravel deposits of the *Dillinger* and *Rainer Hochterrasse*. Most probably, the basal gravel formation of the *Jüngere Hochterrasse* (HT1 sensu Schellmann, 1988) in the Danube valley downstream of Regensburg, which is also preserved in some metres deep troughs eroded in the Tertiary basement, may correlate with these older penultimate interglacial gravel deposits at the base of the *Rainer* and *Dillinger Hochterrasse*.

The oldest gravel units at the base of *Hochterrassen* deposits are the sand-rich gravel unit I of the *Rainer Hochterrasse* and the interglacial peat and gravel deposits of the "*Hartinger Schichten*" at the base of the oldest *Hochterrasse* south of Regensburg (Schellmann, 1988; Schellmann et al., 2010). Their ages are still unknown.

Interglacial gravel units at the base of superimposed cold climatic *Hochterrassen* gravels illustrate that fluvial downcutting in some valley parts far away from areas of Pleistocene glaciations happened not only in the Würmian late glacial and Early Holocene (e.g. Schellmann, 2010; Schielein et al., 2011), but also during older interglacial periods. In some valley parts, this erosion reached down to the surface of the recent valley floor or even below. In the Lech valley south of Augsburg, the deepest valley erosion most probably was reached during the last interglacial. There, older gravel deposits embedded in a deep trough in the Miocene molasse basement are distributed below calcareous sinter sediments, the "*Hurlacher Kalktuff*" (Jerz and Mangelsdorf, 1989; Gesslein, 2013). Both the fluvial and the sinter sediments contain an interglacial mollusc fauna (Kovanda, 1989). They were dated by uranium–thorium (U–Th) to approx. 120 ka (MIS 5e) (Jerz and Mangelsdorf, 1989). However, in many valleys of the Bavarian Alpine Foreland (Danube, lower Lech, Isar, Amper, Schmutter, Große Laber), the Würmian late glacial and Holocene erosion undercut the base level of older Pleistocene river dynamics (e.g. Schellmann, 2010; Schielein, 2012; Schellmann, 2016a, 2017a, 2018a).

As demonstrated, ESR dating of gastropods appears to be a viable alternative to luminescence methods applied to quartz (OSL) and feldspar (IRSL). The latter are the usually used methods for dating fluvial and glaciofluvial deposits in the Northern Alpine Foreland. However, luminescence data from Pleistocene fluvial deposits often show a large scattering of the dating results, and often show a low accuracy (e.g. Klasen, 2008; Klasen et al., 2016; Schielein et al., 2015; Rades et al., 2018; Trauerstein et al., 2017). In addition to providing an independent age control, ESR dating of gastropods also offers the advantage of a higher upper dating limit, which is supposedly larger than MIS 7, most probably similar to that of marine mollusc shells and corals (e.g. Schellmann et al., 2018). But in most fluvial–glaciofluvial and aeolian deposits, often only very small gastropod shells are preserved, which necessitates the reduction of the sample size of individual aliquots to a minimum (up to ca. 0.02 g instead of the commonly used 0.2 g). In some instances, it is even necessary to mix some specimen from the same or even different species. However, the mixture of individuals or different species as well as the reduction of sample weight seems not to influence the dating results.

6 Conclusions

In summary, the here presented new numeric age data permit a more accurate chronostratigraphic classification of the Würmian *Übergangsterrassen* ÜT1 and ÜT2, and of some of the stacked *Hochterrassen* deposits in the Bavarian Alpine Foreland. ESR, ^{14}C and luminescence data imply that loess sedimentation on the ÜT starts in the early Upper Würmian (MIS 2), and luminescence data by Kroemer (2010) imply an accumulation of the younger ÜT2 gravel deposit during the late Middle Würmian (MIS 3). The ÜT1 is older than the ÜT2 and younger than the last interglacial (MIS 5e) formation of the *Jüngere Moosburger Hochterrasse*. In this respect, the ÜT1 was formed after MIS 5e and before MIS 3. MIS 5e old ESR data from interglacial gastropod fauna embedded in the *Jüngere Moosburger Hochterrasse* (Fagotia gravel) indicate a formation during the last interglacial as it was already assumed on basis of morphostratigraphy (e.g. Brunnacker, 1965; Schellmann, 2018b) and gastropod assemblages (Nathan, 1953; Brunnacker and Brunnacker, 1962; Brunnacker, 1966). Most of the *Hochterrassen* deposits in the Bavarian Alpine Foreland were formed during the penultimate glacial (MIS 6). This is pointed out by luminescence and ESR data from the youngest gravel deposits (top gravel unit) of the *Langweider Hochterrasse*. A deposition under cold climate conditions is indicated by the occurrence of syngenetic cryoturbations and cold gastropod fauna, which were already described by many studies in the past. However, most remarkable are the ESR dating results of snail shells from the gravel unit below the MIS 6 top gravel unit in some areas of the *Langweider*, *Dillinger* and *Rainer Hochterrasse*. All ESR data imply a deposition of these sandy basal gravel units during the penultimate interglacial (MIS 7), and the warm temperate habitus of the gastropod assemblages supports this assumption.

All in all, the ESR ages and their error ranges are mostly within the age interval of luminescence (IRSL, OSL) or radiocarbon dating results. The ESR dating of small terrestrial gastropods allows differentiating land-snail shells of Upper or Middle Würmian (last glacial), penultimate glacial (MIS 6) or penultimate interglacial (MIS 7) age and with error ranges between ca. 10 % and 15 %.

Data availability. Most of the data are included in the paper. ESR raw data are stored at the Department of Physical Geography of the University of Bamberg. They are still part of further research but can be obtained upon reasonable request.

Author contributions. Fieldwork (geological mapping, descriptions, sampling) was carried out by GS and PS. ESR measurements were performed by CB and PS under the supervision of GS. ESR age calculations were done by GS and luminescence age calculations by PS. Analysis of the gastropod fauna remains was carried out by WR. GS prepared the manuscript and figures.

Competing interests. The authors declare that they have no conflict of interest.

Special issue statement. This article is part of the special issue "Connecting disciplines – Quaternary archives and geomorphological processes in a changing environment". It is a result of the First Central European Conference on Geomorphology and Quaternary Sciences, Gießen, Germany, 23–27 September 2018.

Acknowledgements. This study was funded by the Bavarian Environment Agency (LfU) in the framework of the EU-funded project "Informationsoffensive Oberflächennahe Geothermie" and by the University of Bamberg. We thank Ernst Kroemer and Gerhard Doppler (Bavarian Geological Survey) for numerous field excursions and technical support. We also would like to greatly thank Helmut Brückner (University of Cologne) for permission to use his ESR facilities and Rainer Drewello (University of Bamberg) for permission to use his REM facilities. We are also very thankful to Roland Beer (University of Bamberg), who did much of the necessary laboratory work, including thickness measurements of the shells and γ irradiation of the aliquots at the Helmholtz Center in Munich, and to Matthias Will, who did some luminescence measurements at the "Zöller" laboratory at the University of Bayreuth. Last but not least, we would also like to thank Silke Schwieger (Bamberg) for the very dedicated GIS and graphic work. The helpful comments of Ernst Kroemer, Johanna Lomax and an anonymous reviewer contributed to improving the manuscript.

References

Adamiec, G. and Aitken, M.: Dose-rate conversion factors: update, Ancient TL, 16, 37–50, 1998.

Aktas, A. and Frechen, M.: Mittel- bis jungpleistozäne Sedimente der Hochterrassen in der nördlichen Iller-Lech-Platte, Sonderveröff, Geol. Inst. Univ. zu Köln, 82, 19–41, 1991.

Becker-Haumann, R. and Frechen, M.: Vergleichende Lumineszenzdatierungen mit IRSL und TL am Deckschichtenprofil Bobingen/Lechtal, Z. Geol. Wiss., 25, 617–633, 1997.

Bibus, E. and Strahl, M.: Zur Gliederung und Altersstellung der bayerischen Hochterrassen nördlich des Donauriedes, Z. Geomorph. N.F., 44, 211–232, 2000.

Bickel, L., Luthgens, C., Lomax, J., and Fiebig, M.: Luminescence dating of glaciofluvial deposits linked to the penultimate glaciation in the Eastern Alps, Quaternary Int., 357, 110–124, 2015.

Borylo, A. and Skwarzec, B.: Activity disequilibrium between ^{234}U and ^{238}U isotopes in natural environment, J. Radioanal. Nucl. Chem., 300, 719–727, 2014.

Brunnacker, K.: Die bodenkundlichen Verhältnisse der würmeiszeitlichen Schotterfluren im Illergebiet, Geologica Bavarica, 18, 113–130, 1953.

Brunnacker, K.: Die Deckschichten und Paläoböden über dem Fagotien-Schotter westlich von Moosburg, N. Jb. Geol. Paläont. Mh., 1966, 214–227, 1966.

Brunnacker, M. and Brunnacker, K.: Weitere Funde pleistozäner Molluskenfaunen bei München, Eiszeitalter u. Gegenwart, 13, 129–137, 1962.

Buch, M. W. and Zöller, L.: Gliederung und Thermolumineszenz-Chronologie der Würmlösse im Raum Regensburg, Eiszeitalter u. Gegenwart, 40, 63–84, 1990.

Doppler, G., Kroemer, E., Rögner, K., Wallner, J., Jerz, H., and Grottenthaler, W.: Quaternary Stratigraphy of Southern Bavaria, E&G Quaternary Sci. J., 60, 23, https://doi.org/10.3285/eg.60.2-3.08, 2011.

Eberl, B.: Die Eiszeitenfolge im nordlichen Alpenvorlande – Ihr Ablauf, ihre Chronologie auf Grund der Aufnahmen des Lech- und Illergletschers, Benno Filser Verlag, Augsburg, 427 pp., 1930.

Fiebig, M. and Preusser, F.: Das Alter fluvialer Ablagerungen aus der Region Ingolstadt (Bayern) und ihre Bedeutung für die Eiszeitenchronologie des Alpenvorlandes, Z. Geomorph. N.F., 47, 449–467, 2003.

Frechen, M.: Upper Pleistocene loess stratigraphy in Southern Germany, Quat. Geochronol., 18, 243–269, 1999.

Gesslein, B.: Zur Stratigraphie und Altersstellung der jungquartären Lechterrassen zwischen Hohenfurch und Kissing unter Verwendung hochauflösender Airborne-LiDAR-Daten, Bamberger Geographische Schriften, SF 10, 148 pp., 2013.

Goodfriend, G. A. and Stipp, J. J.: Limestone and the problem of radiocarbon dating of land-snail shell carbonate, Geology, 11, 575–577, 1983.

Graul, H.: Zur Morphologie der Ingolstädter Ausräumungslandschaft, Forschungen zur deutschen Landeskunde, 43, 114 pp., 1943.

Graul, H.: Eine Revision der pleistozänen Stratigraphie des schwäbischen Alpenvorlandes, Petermann Geogr. Mitt., 106, 253–271, 1962.

Grün, R.: Electron Spin Resonance Dating, Encyclopedia of Quaternary Science, 2, 1505–1516, 2007.

Grün, R.: The DATA program for the calculation of ESR age estimates on tooth enamel, Quat. Geochronol., 4, 231–232, 2009.

Grün, R. and Katzenberger, O.: An alpha irradiator for ESR dating, Ancient TL, 12, 35–38, 1994.

Inoue, K., Hirai, M., Ikeya, M., and Yim, W.: Calibration method for ESR Signal intensity of calcitic shells, Appl. Magn. Reson., 19, 255–269, 2000.

Jerz, H.: Das Eiszeitalter in Bayern – Erdgeschichte, Gesteine, Wasser, Boden, Schweizerbart, Stuttgart, 243 pp., 1993.

Jerz, H. and Mangelsdorf, J.: Die interglazialen Kalksinterbildungen bei Hurlach nördlich Landsberg am Lech, Eiszeitalter u. Gegenwart, 39, 29–32, 1989.

Kilian, R. and Löscher, M.: Zur Stratigraphie des Rainer Hochterrassen-Schotters östlich des unteren Lechs, Heidelberger Geographische Arbeiten, 49, 210–217, 1979.

Klasen, N.: Lumineszenzdatierung glazifluvialer Sedimente im nördlichen Alpenvorland, Ph.D. thesis, University of Cologne, Germany, 209 pp., 2008.

Klasen, N., Fiebig, M., and Preusser, F.: Applying luminescence methodology to key sites of Alpine glaciations in Southern Germany, Quaternary Int., 420, 249–258, 2016.

Kovanda, J.: Fossile Mollusken in Kalksinterbildungen (Dauchen) am Lechufer östlich von Hurlach (nördlich Landsberg/Lech), Eiszeitalter u. Gegenwart, 39, 33–41, 1989.

Kovanda, J.: "Fagotia-Faunen" und quadriglazialistisches stratigraphisches System des Pleistozäns im nördlichen Alpenvorland im Vergleich zu einigen Fundorten im Bereich der nordischen Vereisung Deutschlands, J. Geol. Sci. Anthrop., 26, 5–37, 2006.

Kroemer, E.: Fluviale Geomorphodynamik der Donau im Bereich des Rückstaus durch das Isarmündungsgebiet bei Deggendorf (Niederbayern) und Aussagen zur späthochglazialen und spätglazialen Entwicklung, Bamberger Geographische Schriften, 24, 79–87, 2010.

Kulig, G.: Erstellung einer Auswertsoftware zur Altersbestimmung mittels Lumineszenzverfahren unter besonderer Berücksichtigung des Einflusses radioaktiver Ungleichgewichte in der 238U-Zerfallsreihe, B.Sc. Thesis, TU Bergakademie Freiberg, Germany, 2005.

Lang, J., Lauer, T., and Winsemann, J.: New age constraints for the Saalian glaciation in northern central Europe: Implication for the extent of ice sheets and related proglacial lake systems, Quaternary Sci. Rev., 180, 240–259, 2018.

Leger, M.: Géomorphologie de la vallée subalpine du Danube entre Sigmaringen et Passau, Thèse du doctorat, Univ. Paris VII, 621 pp., 1988.

Low, S. and Zeira, S.: ESR spectra of Mn^{2+} in heat-treated Aragonite, Am. Mineral., 57, 1115–11124, 1972.

Mayr, C., Matzke-Karasz, R., Stojakowits, P., Lowick, S. E., Zolitschka, B., Heigl, T., Mollath, R., Theuerkauf, M., Weckend, M.-O., Bäumler, R., and Gregor, H.-J.: Palaeoenvironments during MIS 3 and MIS 2 inferred from lacustrine intercalations in the loess–palaeosol sequence at Bobingen (southern Germany), E&G Quaternary Sci. J., 66, 73–89, https://doi.org/10.5194/egqsj-66-73-2017, 2017.

Miara, S.: Deckschichtenuntersuchungen zur Gliederung der Rißeiszeit beiderseits der Iller im Gebiet des Rhein- und Illergletschers (westliches Alpenvorland, Deutschland), Jahres-

berichte und Mitteilungen des oberrheinischen geologischen Vereins N.F., 78, 359–374, 1996.

Miara, S. and Rögner, K.: Die glazifluvialen Sedimente im unteren Günztal (Bayerisch Schwaben/Deutschland) nach morpho- und pedostratigraphischen Befunden sowie TL-Daten, Eiszeitalter u. Gegenwart, 45, 32–47, 1996.

Molodkov, A.: ESR Dating of Quaternary Shells: recent advances, Quaternary Sci. Rev., 7, 477–484, 1988.

Molodkov, A.: ESR-Dating of Non-marine Mollusc Shells, Appl. Radiat. Isot., 44, 145–148, 1993.

Murray, A. S. and Wintle, A. G.: The single aliquot regenerative dose protocol: Potential for improvements in reliability, Radiat. Meas., 37, 377–381, 2003.

Nathan, H.: Ein interglazialer Schotter südlich Moosburg in Oberbayern mit *Fagotia acicularis* Férussac (Melanopsenkies), Geologica Bavarica, 19, 315–334, 1953.

Penck, A.: Ueber Periodicität der Thalbildung, Verh. Ges. f. Erdkunde, XI, 39–59, 1884.

Penck, A. and Brückner, E.: Die Alpen im Eiszeitalter, 3 Bde., Tauchnitz, Leipzig, 1199 pp., 1901–1909.

Pigati, J. S., Rech, J. A., and Nekola, J. C.: Radiocarbon dating of small terrestrial gastropod shells in North America, Quat. Geochronol., 5, 519–532, 2010.

Prescott, J. R. and Hutton, J. T.: Cosmic ray contributions to dose rates for luminescence and ESR dating: large depths and long-term time variations, Radiat. Meas., 23, 497–500, 1994.

Rades, E. F., Fiebig, M., and Lüthgens, C.: Luminescence dating of the Rissian type section in southern Germany as a base for correlation, Quaternary Int., 478, 38–50, 2018.

Reimer, P. J., Bard, E., Bayliss, A., and Beck, J. W.: IntCal13 and Marine13 Radiocarbon Age Calibration Curves 0–50 000 Years cal BP, Radiocarbon, 55, 1869–1887, 2013.

Rögner, K., Löscher, M., and Zöller, L.: Stratigraphie, Paläogeographie und erste Thermolumineszenzdatierungen in der westlichen Iller-Lech-Platte (Nördliches Alpenvorland), Z. Geomorph. N.F., 70, 51–73, 1988.

Rohdenburg, H.: Ein Beitrag zur Deutung des "Gefleckten Horizonts", Eiszeitalter u. Gegenwart, 15, 66–71, 1964.

Schaefer, I.: Die Würmeiszeit im Alpenvorland zwischen Riß und Günz, Abhandlungen des Naturkunde- und Tiergartenvereins für Schwaben, Geologisch-Paläontologische Reihe 1, Schwabenlandverlag, Augsburg, 1940.

Schaefer, I.: Zur Gliederung der Würmeiszeit im Illergebiet, Geologica Bavarica, 18, 13–64, 1953.

Schaefer, I.: Geologische Karte von Augsburg und Umgebung 1 : 50 000 mit Erläuterungen, Bayerisches Geologisches Landesamt, München, Germany, 92 pp., 1957.

Schaefer, I.: Der Talknoten von Donau und Lech, Mitteilungen Geographische Gesellschaft München, 51, 59–111, 1966.

Schellmann, G.: Jungquartäre Talgeschichte an der unteren Isar und der Donau unterhalb von Regensburg, Ph.D. thesis, University of Düsseldorf, Germany, 332 pp., 1988.

Schellmann, G.: Fluviale Geomorphodynamik im jüngeren Quartär des unteren Isar- und angrenzenden Donautales, Düsseldorfer Geogr. Schr., 29, 131 pp., 1990.

Schellmann, G.: Zur Talgeschichte der unteren Oberweser im jüngeren Quartär, Düsseldorfer Geographische Schriften, 34, 1–56, 1994.

Schellmann, G.: Neue Befunde zur Verbreitung, geologischen Lagerung und Altersstellung der würmzeitlichen (NT1 bis NT3) und holozänen (H1 bis H7) Terrassen im Donautal zwischen Regensburg und Bogen, Bamberger Geographische Schriften, 24, 1–77, 2010.

Schellmann, G. (Ed.): Bamberger physisch-geographische Studien 2008–2015, Teil III: Geomorphologisch-quartärgeologische Kartierungen im bayerischen Lech-, Wertach- und Schmuttertal, Bamberger Geographische Schriften, 12, 356 pp., 2016a.

Schellmann, G.: Quartärgeologische Karte von Bayern 1 : 25 000 des Schmuttertals auf Blatt Nr. 7530 Gablingen mit Erläuterungen, Bamberger Geographische Schriften, 12, 1–40, 2016b.

Schellmann, G. (Ed.): Bamberger physisch-geographische Studien 2012–2014, Teil IV: Geomorphologisch-quartärgeologische Kartierungen im bayerischen Donautal zwischen Sontheim und Dillingen, Bamberger Geographische Schriften, 13, 237 pp., 2017a.

Schellmann, G.: Quartärgeologische Karte 1 : 25 000 des Donautals auf Blatt 7428 Dillingen West mit Erläuterungen, Bamberger Geographische Schriften, 13, 69–187, 2017b.

Schellmann, G. (Ed.): Bamberger physisch-geographische Studien 2008–2017, Teil V: Geomorphologisch-quartärgeologische Kartierungen im bayerischen Isar- und Donautal sowie im Tal der Großen und der Kleinen Laber, Bamberger Geographische Schriften, 14, 252 pp., 2018a.

Schellmann, G.: Quartärgeologische Karte 1 : 25 000 des Isar- und Ampertals auf Blatt 7537 Moosburg mit Erläuterungen, Bamberger Geographische Schriften, 14, 1–104, 2018b.

Schellmann, G. and Kelletat, D.: Chronostratigraphische Untersuchungen litoraler und äolischer Formen und Ablagerungen an der Südküste von Zypern mittels ESR-Altersbestimmungen an Mollusken- und Landschneckenschalen, Essener Geographische Arbeiten, 32, 75–98, 2001.

Schellmann, G. and Radtke, U.: Problems encountered in the determination of dose and dose rate in ESR dating of mollusc shells, Quaternary Sci. Rev., 18, 1515–1527, 1999.

Schellmann, G. and Radtke, U.: Progress in ESR dating of Pleistocene corals – a new approach for D_E determination, Quaternary Sci. Rev., 20, 1015–1020, 2001.

Schellmann, G., Beerten, K., and Radtke, U.: Electron sin resonance (ESR) dating of Quaternary materials, E&G Quaternary Sci. J., 57, 150–178, https://doi.org/10.3285/eg.57.1-2.6, 2008.

Schellmann, G., Irmler, R., and Sauer, D.: Zur Verbreitung, geologischen Lagerung und Alterstellung der Donauterrassen auf Blatt L7141 Straubing, Bamberger Geographische Schriften, 24, 89–178, 2010.

Schellmann, G., Brückner, H., and Brill, D.: Geochronology, in: Encyclopedia of Coastal Science, edited by: Finkl, C. W. and Makowski, C., Springer International Publishing AG, Cham, 1–11, 2018.

Scheuenpflug, L.: Die risszeitliche Hochterrasse des Lechs nördlich Augsburg und die Schutter (Bayerisch Schwaben), Heidelberger Geographische Arbeiten, 49, 194–209, 1979.

Scheuenpflug, L.: Die Schotterfazies des Augsburger Umlandes, Berichte des Naturwissenschaftlichen Vereins für Schwaben e.V., 85, 14–21, 1981.

Schielein, P.: Jungquartäre Flussgeschichte des Lechs unterhalb von Augsburg und der angrenzenden Donau, Bamberger Geographische Schriften, 9, 150 pp., 2012.

Schielein, P. and Schellmann, G.: Geologische Karte von Bayern 1 : 25 000, Blatt Nr. 7531 Gersthofen mit Erläuterungen, Bamberger Geographische Schriften, 12, 41–73, 2016a.

Schielein, P. and Schellmann, G.: Geologische Karte von Bayern 1 : 25 000, Blatt Nr. 7331 Rain mit Erläuterungen, Bamberger Geographische Schriften, 12, 141–166, 2016b.

Schielein, P., Schellmann, G., and Lomax, J.: Stratigraphy of Late Quaternary fluvial terraces at the confluence of the Lech and Danube valleys, E&G Quaternary Sci. J., 60, 27, https://doi.org/10.3285/eg.60.4.02, 2011.

Schielein, P., Schellmann, G., Lomax, J., Preusser, F., and Fiebig, M.: Chronostratigraphy of the Hochterrassen in the lower Lech valley (Northern Alpine Foreland), E&G Quaternary Sci. J., 64, 15–28, https://doi.org/10.3285/eg.64.1.02, 2015.

Semmel, A.: Studien über den Verlauf jungpleistozäner Formung in Hessen, Frankfurter Geographische Hefte, 45, 133 pp., 1968.

Srivastava, S. K., Balbudhe, A. Y., Vishwa Prasad, K., Paqdma Savithri, P., Tripathi, R. M., and Puranik, V. D.: Variation in the uranium isotopic ratios $^{234}U/^{238}U$, $^{238}U/$ total-U and $^{234}U/$ total-U in Indian soil samples: Application to environmental monitoring, Radioprotection, 2012, 1–12, 2012.

Stuiver, M. and Reimer, P. J.: Extended ^{14}C database and revised CALIB radiocarbon calibration program, Radiocarbon, 35, 215–230, 1993.

Tillmanns, W., Münzing, K., Brunnacker, K., and Löscher, M.: Die Rainer Hochterrasse zwischen Lech und Donau, Jahresberichte und Mitteilungen des oberrheinischen geologischen Vereins N.F., 64, 79–99, 1982.

Tillmanns, W., Brunnacker, K., and Löscher, M.: Erlauterungen zur Geologischen Übersichtskarte der Aindlinger Terrassentreppe zwischen Lech und Donau 1 : 50 000, Geologica Bavarica, 85, 83 pp., 1983.

Trauerstein, M., Lowick, S. E., Preusser, F., and Veit, H.: Testing the suitability of dim sedimentary quartz from Northern Switzerland for OSL burial dose estimation, Geochronometria, 44, 66–76, 2017.

Unger, H. J.: Zur Geologie im Donautal zwischen Straubing und Pleinting, Documenta Naturae, 128, 110 pp., 1999.

Vigier, N. and Bourdon, B.: Constraining Rates of Chemical and Physical Erosion using U-Series Radionuclides, in: edited by: Baskaran, M., Handbook of Environmental Isotope Geochemistry, 553–571, Springer Verlag, Berlin Heidelberg, 2012.

Weißhaar, R.: Isotopengeochemie des Heidelberger Neckarschwemmfächers, U/Th-Ungleichgewichte und Pb-Isotopie quartärer klastischer Sedimente, Diss. University of Heidelberg, Heidelberg, 2000.

Winsemann, J., Lang, J., Roskosch, J., Polom, U., Böhner, U., Brandes, Chr., Glotzbach, C., and Frechen, M.: Terrace styles and timing of terrace formation in the Weser and Leine valleys, northern Germany: Response of a fluvial system to climate change and glaciation, Quaternary Sci. Rev., 123, 31–57, 2015.

Xu, B., Gu, Z., Han, J., Hao, Q., Lu, Y., Wang, L., Wu, N., and Peng, Y.: Radiocarbon age anomalies of land snail shells in the Chinese Loess Plateau, Quat. Geochronol., 6, 383–389, 2011.

Zöller, L.: Würm- und Rißlöß-Stratigraphie und Thermolumineszenz-Datierung in Süddeutschland und angrenzenden Gebieten, habilitation thesis, University of Heidelberg, Germany, 224 pp., 1995.

E&G Quaternary Sci. J., 68, 29–46, 2019
https://doi.org/10.5194/egqsj-68-29-2019

Open Access E&G Quaternary Science Journal

Research article

Grain-size distribution unmixing using the R package EMMAgeo

Elisabeth Dietze[1,2] **and Michael Dietze**[3]

[1]Alfred Wegener Institute for Polar and Marine Research, Research Unit Potsdam, 14473 Potsdam, Germany
[2]GFZ German Research Centre for Geosciences, Section 3.2 Organic Geochemistry, 14473 Potsdam, Germany
[3]GFZ German Research Centre for Geosciences, Section 5.1 Geomorphology, 14473 Potsdam, Germany

Correspondence: Elisabeth Dietze (edietze@awi.de)

Relevant dates: Received: 3 December 2018 – Accepted: 2 April 2019 – Published: 16 May 2019

How to cite: Dietze, E., and Dietze, M.: Grain-size distribution unmixing using the R package EMMAgeo, E&G Quaternary Sci. J., 68, 29–46, https://doi.org/10.5194/egqsj-68-29-2019, 2019.

Abstract: The analysis of grain-size distributions has a long tradition in Quaternary Science and disciplines studying Earth surface and subsurface deposits. The decomposition of multi-modal grain-size distributions into inherent subpopulations, commonly termed end-member modelling analysis (EMMA), is increasingly recognised as a tool to infer the underlying sediment sources, transport and (post-)depositional processes. Most of the existing deterministic EMMA approaches are only able to deliver one out of many possible solutions, thereby shortcutting uncertainty in model parameters. Here, we provide user-friendly computational protocols that support deterministic as well as robust (i.e. explicitly accounting for incomplete knowledge about input parameters in a probabilistic approach) EMMA, in the free and open software framework of R.

In addition, and going beyond previous validation tests, we compare the performance of available grain-size EMMA algorithms using four real-world sediment types, covering a wide range of grain-size distribution shapes (alluvial fan, dune, loess and floodplain deposits). These were randomly mixed in the lab to produce a synthetic data set. Across all algorithms, the original data set was modelled with mean R^2 values of 0.868 to 0.995 and mean absolute deviation (MAD) values of 0.06 % vol to 0.34 % vol. The original grain-size distribution shapes were modelled as end-member loadings with mean R^2 values of 0.89 to 0.99 and MAD of 0.04 % vol to 0.17 % vol. End-member scores reproduced the original mixing ratios in the synthetic data set with mean R^2 values of 0.68 to 0.93 and MAD of 0.1 % vol to 1.6 % vol. Depending on the validation criteria, all models provided reliable estimates of the input data, and each of the models exhibits individual strengths and weaknesses. Only robust EMMA allowed uncertainties of the end-members to be objectively estimated and expert knowledge to be included in the end-member definition. Yet, end-member interpretation should carefully consider the geological and sedimentological meaningfulness in terms of sediment sources, transport and deposition as well as post-depositional alteration of grain sizes. EMMA might also be powerful in other geoscientific contexts where the goal is to unmix sources and processes from compositional data sets.

1 Introduction

1.1 Mixing of grain-size subpopulations in sedimentary deposits

Many studies in Quaternary Science aim to reconstruct past Earth surface dynamics using sedimentary proxies. Earth surface dynamics include a variety of processes that mix process-related components (Buccianti et al., 2006). Sediment from different sources can be transported and deposited by a multitude of sedimentological processes that have been linked to climate, vegetation, geological and geomorphological dynamics (Bartholdy et al., 2007; Folk and Ward, 1957; Macumber et al., 2018; Stuut et al., 2002; Tjallingii et al., 2008; Vandenberghe, 2013; Vandenberghe et al., 2004, 2018). During transport, grain-size subpopulations are affected by different transport energies, and, thus, distinct grain-size distributions are created upon deposition. Accordingly, it is possible to infer source areas, transport pathways and transport processes as well as the related sedimentary environment from measured grain-size distributions. This basic concept has been exploited for more than 60 years (Flemming, 2007; Folk and Ward, 1957; Hartmann, 2007; Visher, 1969). However, the approach is limited when sediments are transported by more than one process and become mixed during and after deposition (Bagnold and Barndorff-Nielsen, 1980; Vandenberghe et al., 2018).

The advent of fast, high-resolution grain-size measurements through laser diffraction allows the assessment of grain-size distributions of large sample sets in a short time and reveals the sediment mixing effects in multiple modes or distinct shoulders in the grain-size distribution curves. Although widely used, classic measures of bulk distributions such as sand, silt and clay contents or mean grain size, D_{50}, sorting, skewness or kurtosis (Folk and Ward, 1957) are non-informative in non-Gaussian, multi-modal distributions and allow only a qualitative interpretation and comparison of sedimentary processes that contributed to sediment formation.

To overcome these limitations and to improve process interpretation and attribution of associated drivers from sedimentary archives (Dietze et al., 2014), two ways have been proposed to decompose multi-modal grain-size distributions and to quantify the dominant grain-size subpopulation: parametric and non-parametric approaches. Among the former, commonly used curve fitting approaches describe a sediment sample as a combination of a finite number of parametric distribution functions such as (skewed) log-normal, log-hyperbolic or Weibull distributions (Bagnold and Barndorff-Nielsen, 1980; Gan and Scholz, 2017; Sun et al., 2002). However, curve fitting solutions are non-unique, and subpopulations might not be detected if a fixed number of functions are fitted to individual samples (Paterson and Heslop, 2015; Weltje and Prins, 2003), whereas other parametric approaches such as non- and semi-parametric mixture models (Hunter et al., 2011; Lindsay and Lesperance, 1995) are still very poorly explored in the field of grain-size distribution analyses.

Non-parametric end-member modelling or mixing analysis (EMMA) aims to describe a whole data set as a combination of discrete subpopulations, based on eigenspace analysis and compositional data constraints (Aitchison, 1986). A multidimensional grain-size data set $\mathbf{X}$ (i.e. m samples, each represented by n grain-size classes) can be described as a linear combination of transposed end-member loadings ($\mathbf{V}^{\mathrm{T}}$, representing individual grain-size subpopulations), end-member scores ($\mathbf{M}$, the relative contribution of the end-member subpopulations to each sample) and an error matrix $\mathbf{E}$ using the function

$$\mathbf{X} = \mathbf{M} \cdot \mathbf{V}^{\mathrm{T}} + \mathbf{E}. \quad (1)$$

Hence, it is possible to identify (using end-member loadings) and quantify (using end-member scores) sediment sources, transport and depositional regimes from mixed grain-size data sets. EMMA has been successfully applied to interpret and quantify past sedimentary processes from sediment deposits, beyond classical measures, for example in marine, lacustrine, aeolian, fluvial, alluvial and periglacial environments, across multiple spatial and temporal scales (Borchers et al., 2015; Dietze et al., 2013, 2016; Schillereff et al., 2016; Strauss et al., 2012; Toonen et al., 2015; Varga et al., 2019; Vriend and Prins, 2005; Wündsch et al., 2016).

1.2 Non-parametric grain-size unmixing approaches

Five approaches of non-parametric EMMA have been proposed: Weltje (1997) has developed a FORTRAN algorithm based on simplex expansion, which has been translated to a set of scripts for R (R Core Team, 2017) called RECA (R-based Endmember Composition Algorithm), including a fuzzy c-means clustering approach (Seidel and Hlawitschka, 2015). Available as MATLAB scripts, the algorithm by Dietze et al. (2012) has included eigenvector rotation, whereas Yu et al. (2015) have introduced a Bayesian EMMA (BEMMA) and Paterson and Heslop (2015) have used approaches from hyperspectral image processing (AnalySize). Based on the MATLAB algorithm by Dietze et al. (2012), Dietze and Dietze (2016) compiled a prototype R package (EMMAgeo v. 0.9.4).

Most EMMA approaches are deterministic (i.e. one single model solution without any uncertainty estimates) and require the user to set a fixed number of end-members q and further model parameters. In natural systems, however, q is rarely known and, thus, often one of the reasons to employ EMMA. Different approaches have been proposed to estimate q, such as the inflection point in a q–R^2 plot (Paterson and Heslop, 2015; Prins and Weltje, 1999) or the iterative adjustment of model parameters such as the weight transformation limit (Dietze et al., 2012), maximum convexity error, number of iterations and weighting exponent (Weltje, 1997; Seidel and Hlawitschka, 2015).

Previous studies of EMMA performance (Weltje and Prins, 2007; Seidel and Hlawitschka, 2015; Paterson and Heslop, 2015) either used measured data without information on the true loadings and scores or were based on ideally designed synthetic data. However, natural process end-members can overlap substantially and may have a varying or multi-modal grain-size distribution shape due to unstable transport conditions (e.g. gradual fining of aeolian dust with transport distance) and deposition (e.g. reworking by soil formation; Dietze et al., 2016; Vandenberghe et al., 2018).

Recently, van Hateren et al. (2018) compared the concepts and performances of AnalySize, RECA, BEMMA, EMMAgeo and a diffuse reflectance spectroscopy (DRS) unmixing approach (Heslop et al., 2007). They used numerically mixed real-world grain-size samples and compared the modelled end-member loadings with the real-world distributions and modelled scores with randomised mixing ratios, as suggested by Schulte et al. (2014). Van Hateren and others confirmed former studies and highlighted that geological background knowledge is crucial for end-member interpretation, but they also pointed to strong differences in model performance. However, the descriptions of van Hateren et al. (2018) are mainly based on verbal comparisons of graphic data representations, and the validation data are not available for future comparative studies.

Here, we introduce new operational modes and protocols for the comprehensive open-source R package EMMAgeo as a tool for quantifying process-related grain-size subpopulations in mixed sediments. We aim to clarify information provided by the reference documentation of the first version of the package (v. 0.9.4; Dietze and Dietze, 2016) and by Dietze et al. (2014), regarding parameter estimation and optimisation, and we add a new approach of uncertainty estimation of the end-member scores. We evaluate the performance and validity of EMMAgeo using a real-world grain-size data set with fully known end-member compositions and unbiased quantitative measures. For comparison, the same data set is modelled with other available grain-size end-member algorithms. An evaluation and validation of both process end-member distribution shapes and mixing ratios are provided. Finally, general constraints for the interpretation of end-members are discussed. The detailed Supplement shall help users to apply the EMMAgeo protocols and to reproduce the results, making use of the raw data published along with this study.

2 The R package EMMAgeo

2.1 Background

EMMAgeo in its current version 0.9.6 (Dietze and Dietze, 2019) contains 22 functions (Table S1 in the Supplement), the example data set for this study and full documentation of these items. EMMAgeo provides a systematic chain of data pre-processing, parameter estimation and optimisation, the actual modelling and the inference of model uncertainties.

EMMAgeo is based on the EMMA MATLAB code by Dietze et al. (2012), which was slightly modified, i.e. vectorisation of looped calculations to increase computation speed, a new coding of the scaling procedure (Miesch, 1976) and additional measures of model performance. Following Dietze et al. (2012), the core function `EMMA()` rescales the grain-size data matrix $\mathbf{X}$ to constant row sums (i.e. m rows of samples, n columns of grain-size classes). Then, a weight transformation (Klovan and Imbrie, 1971) is performed using a weight constant l to yield a weight matrix $\mathbf{W}$ that is not biased by variables with large standard deviations (Weltje, 1997). The similarity matrix $\mathbf{A}$ is returned as the minor product of $\mathbf{W}$. From the similarity matrix, the eigenspace is computed, and eigenvalues ($\mathbf{L}$) and their cumulative sums are calculated. Eigenvectors are inferred and sorted by decreasing explained variance ($\mathbf{V}_f$). These eigenvectors are then rotated, by default using the Varimax rotation (Dietze et al., 2012), in R using the package GPArotation (Bernaards and Jennrich, 2005). Their order is inverted to yield unscaled end-member loadings ($\mathbf{V}_q$). Then, normalised end-member loadings ($\mathbf{V}_{q\mathrm{n}}$) are computed by row-wise data normalisation of $\mathbf{V}_q$ or are user-defined; i.e. a known $\mathbf{V}_{q\mathrm{n}}$ can be used. A factor score matrix ($\mathbf{M}_q$) is calculated as a non-negative least squares estimate of $\mathbf{V}_{q\mathrm{n}}$ and $\mathbf{W}$. Then, the data set can be described as a minor product of $\mathbf{M}_q$ and $\mathbf{V}^{\mathrm{T}}$ to yield the modelled weight matrix $\mathbf{W}_{\mathrm{m}}$. These values are back-transformed and yield rescaled end-member loadings ($\mathbf{V}_{q\mathrm{sn}}$) and quantitative scores ($\mathbf{M}_{\mathrm{qs}}$). A linear combination of $\mathbf{M}_{\mathrm{qs}}$ and $\mathbf{V}^{\mathrm{T}}$ yields $\mathbf{X}'$, the modelled data set (see the mathematical formulation in Dietze et al., 2012). Model evaluation measures are calculated by comparing $\mathbf{X}$ and $\mathbf{X}'$: row-wise (sample) and column-wise (grain-size class) absolute model deviation, data variance and root mean square errors (MAD_m and MAD_n, R^2_m and R^2_n and RMSE_m and RMSE_n), explained variance of each end-member (M_{qsvar}) and total mean $\mathrm{MAD}_{\mathrm{t}}$ and R^2_{t} of the model, as well as the number of overlapping end-member loadings (ol), defined as one end-member having its main mode within the area of another end-member.

2.2 Theory of operational modes and protocols

A deterministic and a robust operational EMMA mode can be run by a function and two protocols, respectively. First, EMMA can be performed with a user-based decision on all parameters, which is comparable to existing algorithms. This *deterministic EMMA* is mainly useful for exploratory studies, such as investigating the effect of different numbers of end-members q, weight transformation limits l or factor rotation types. The function call `EM_det <-EMMA(X = X, q = 4, plot = TRUE)`, with `X` being the data set and `q` the number of suggested end-members, returns the final end-member loadings and scores, the modelled data set and several quality criteria. Additional function arguments can be

provided, such as `l`, other factor rotation methods, predefined unscaled end-member loadings, the grain-size class limits of the input data set or a series of plot arguments in standard R language.

The second and third protocol of *robust EMMA* account for the real mixing conditions being generally unknown. In such cases, it is reasonable to evaluate different model realisations within meaningful parameter ranges; i.e. `q` and `l` can be varied to infer the range of uncertainty associated with the set of model scenarios in a probabilistic framework. The central goal of robust EMMA is to set the boundary conditions for these two parameters `q` and `l`, which allows all resulting scenarios to be modelled to identify emergent robust end-members and to describe these by statistical measures. There are two ways to run robust EMMA (Fig. 1). An extended protocol is suitable for more exploratory studies, in which parameter settings can be explored and manipulated in detail (Fig. 1a). A compact protocol allows calculation of all important input and output parameters in five steps (Fig. 1b). Both protocols follow the same workflow but with different requirements and possibilities to interact.

The *extended protocol of robust EMMA* (Fig. 1a) starts with defining $l_{\min}$, a lower limit for `l` (step 1). By default, $l_{\min}$ is set to zero (according to Miesch, 1976). The upper limit $l_{\max}$ (step 2) represents the maximum possible value that still allows eigenspace calculation and is either found by testing the possibility of eigenspace computation for a sequence of possible `l` values (function `test.l()`) or by iteratively approximating the highest possible `l` value (`function test.l.max()`). When `l` approaches $l_{\max}$, EMMA generates increasingly unreliable output (e.g. negative loadings), which is why $l_{\max}$ should be set to a lower value, for example, the default value 95 % of $l_{\max}$. Based on $l_{\min}$ and $l_{\max}$, a sequence of likely values for `l` is created (step 3). The number of these values (here $n = 20$) should balance sufficient `q` scenarios and reasonable computational time.

The range of the number of end-members q is then modelled for each element of this sequence of `l`. Step 4 sets $q_{\min}$ by testing how much of the data variance can be explained with a given q prior to eigenspace rotation. Dietze et al. (2012) suggested a minimum R^2 of 0.95. A reasonable estimate of the highest meaningful value $q_{\max}$ (step 5) can be the first local maximum of total mean R^2_t after all end-members were modelled. In EMMA (Dietze et al. 2012), R^2_t rises as more end-members are included until, after a local maximum, it drops again, which is related to the forced constant-sum constraints (Paterson and Heslop, 2015). Alternative criteria can be a fixed upper threshold of R^2_t or a fixed user-defined value for $q_{\max}$ (step 5). Note that this approach differs from the way that other models identify q. While Weltje (1997) and Prins and Weltje (1999) use the inflection point of the q–R^2 relationship to set one fixed q, robust EMMA provides a range of $\boldsymbol{q}$ that include this inflection point. In step 6, the ranges of `q` and `l` are combined to a parameter matrix `P`, used to model all likely end-member scenarios. In `P`, $\boldsymbol{q}_{\min}$ must be at least 2, $\boldsymbol{q}_{\max}$ must be at least as high as the corresponding $\boldsymbol{q}_{\min}$ and there must be no NA (not available) values (see Supplement).

End-member loadings from different model parameter settings tend to cluster at similar main mode positions, which Dietze et al. (2012, 2014) used to manually identify robust end-members. To identify these mode clusters within EMMAgeo (step 7), `EMMA()` is evaluated for each combination of $\boldsymbol{q}$ between $q_{\min}$ and $q_{\max}$ for each element of $\boldsymbol{l}$. Step 8 generates the limits around the mode clusters of the robust end-member loadings. The limits are a two-column matrix with the lower and upper limit class for each robust end-member. With these class limits, all robust end-member loadings can be extracted (step 9), and their class-wise means and standard deviations are calculated.

With the mean robust loadings, i.e. the unweighted mean of all similarly likely loadings of step 9, it is possible to optimise the model with respect to different quality criteria by changing `l` to yield an optimal EM solution (l_{opt}, step 10). The default quality criterion is R^2_t. Other possible criteria are thresholds in mean sample- and class-wise R^2 and $\boldsymbol{E}$ and the number of overlapping end-members. With the uncertainty ranges of robust loadings and l_{opt} (or any other user-defined l values), it is possible to quantify the uncertainties of end-member scores using Monte Carlo simulations (step 11). The simulations generate many sets of unscaled end-member loadings, by default 100 times `q`. `EMMA()` is performed with each subset of loadings, and the scores are extracted. Their overall scatter is described by the sample-wise standard deviation. The Monte Carlo approach cannot propagate a specific $\boldsymbol{l}$ to the scores calculation because loadings are randomly sampled with no information about the initial l with which they have been created. Hence, the Monte Carlo approach only delivers an estimate of the standard deviation of the scores (default) or asymmetric confidence intervals, whereas the mean derives from the optimal EM model.

The *compact protocol of robust EMMA* (Fig. 1b) combines steps of the extended protocol and automates the identification of plausible grain-size class limits for robust end-member extraction. After data input checks, the ranges of $\boldsymbol{l}$ (step 1) and $\boldsymbol{q}$ (step 2) are determined. These boundary conditions are used to evaluate multiple EMMA scenarios (step 3). Cluster limits can be identified by a kernel density estimate for all available grain-size modes (step 4) that are used to define robust end-members. Kernel density estimates are curves that depict the continuous empiric distribution of data, in this case grain-size mode classes, by sliding a window (the kernel) over the data and counting the number of values within it for each sliding step. The window size (or kernel bandwidth) is the parameter controlling the shape of the resulting curve. Here, a default kernel bandwidth of 1 % of the number of grain-size classes of the input data set is used. To identify mode cluster limits, the density curve needs to be cut off at a given threshold. Above that threshold, the limits bracketing

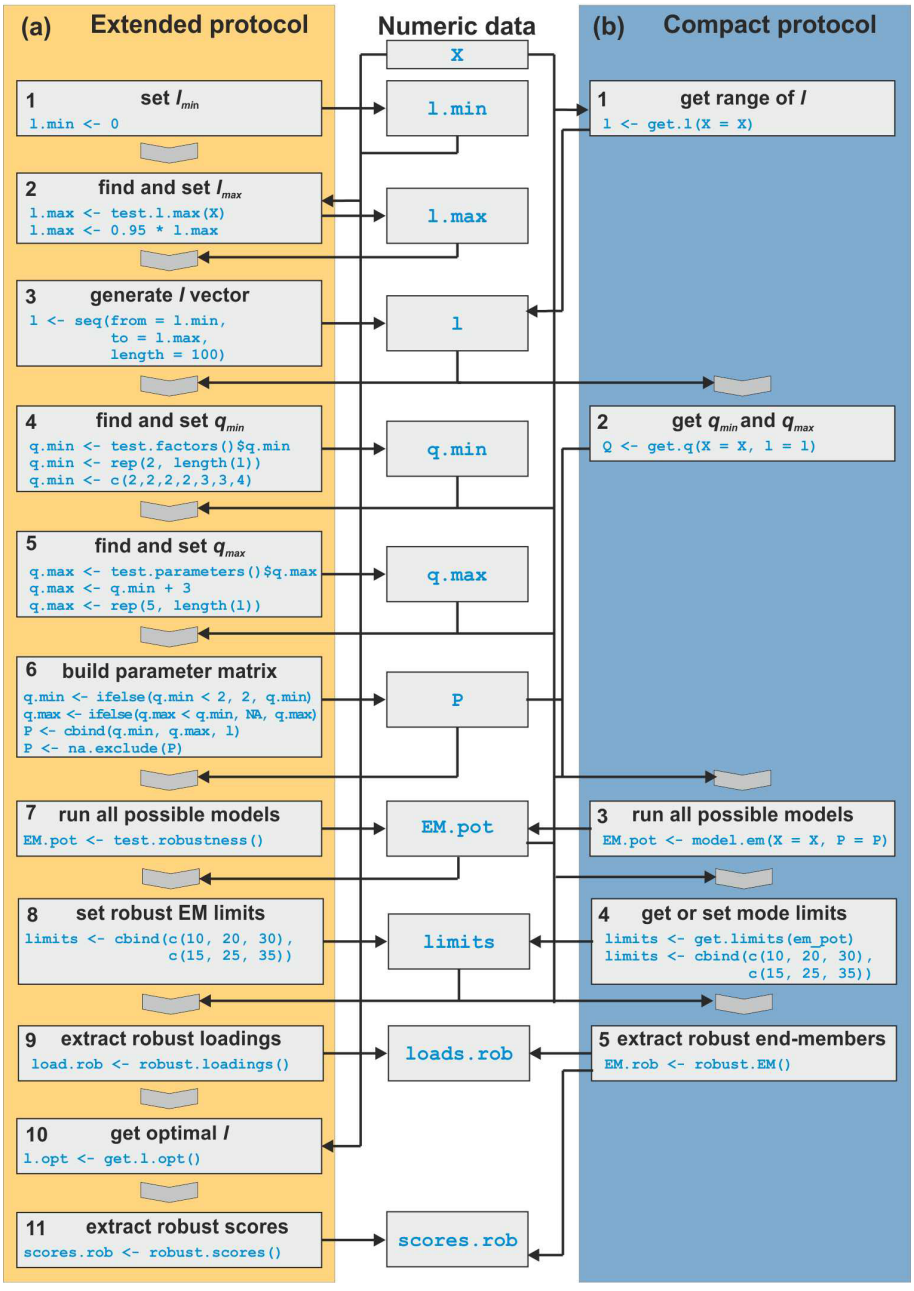

Figure 1. Flow chart of the two robust EMMA protocols. **(a)** Extended protocol with code for the entire modelling chain. **(b)** Compact protocol with minimal user input.

the modes can be derived. By default, the cut-off threshold is defined as the 0.7 quantile of the density values. These empirical default values were found to be appropriate during extensive tests with synthetic data sets during package development. However, they are not universal and may be adjusted when needed. With all modelled end-member loadings (from step 3) and the class limits (from step 4), the robust end-member loadings and scores can be extracted (step 5; Fig. 1).

3 Practical application: material and methods

3.1 Example data set

Sediment outcrops of four depositional environments were sampled near the city of Dresden, Germany (Fig. 2). These represent natural sedimentological end-members (EM_{nat}) of a floodplain section ($EM_{nat}1$, with main grain-size mode at 19 µm) of an Elbe River tributary, a loess deposit ($EM_{nat}2$, mode at 36 µm) of the Ostrau profile described by Meszner

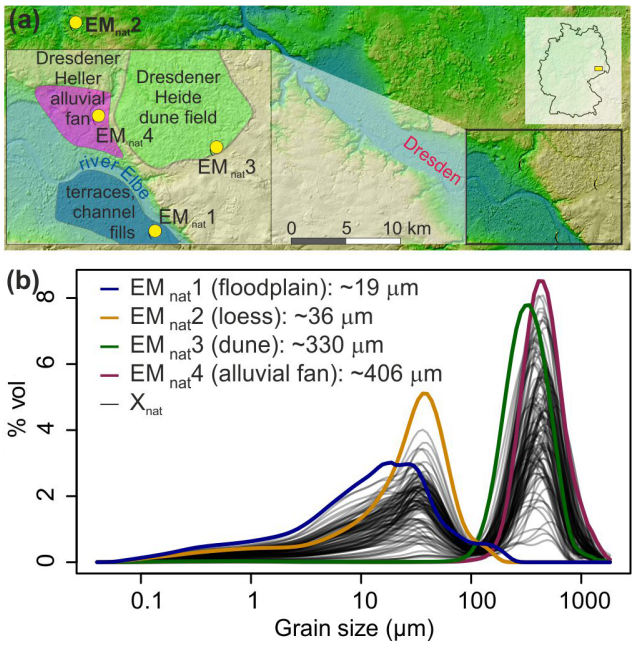

Figure 2. **(a)** Sample locations and sedimentological setting (according to the geological map, section Dresden, Sächsisches Landesamt für Umwelt, Landwirtschaft und Geologie; http://www.geologie.sachsen.de/geologische-karten-14041.html, last access: 10 May 2019); see kmz file in the Supplement. **(b)** Grain-size distributions of the four natural grain-size end-members (EM_{nat}) and the 100 resulting mixed samples (X_{nat}), i.e. the example data set of the EMMAgeo R package (Dietze and Dietze, 2019).

et al. (2013), a sandur dune ($EM_{nat}3$, mode at 330 µm) and a Weichselian alluvial fan ($EM_{nat}4$, mode at 406 µm; Fig. 2). These natural environments were selected to cover a broad range of transport regimes, grain-size distribution shapes, degrees of mode overlapping ($EM_{nat}4$ and $EM_{nat}3$) and number of modes ($EM_{nat}1$). Note that these samples are potentially composed of multiple grain-size populations themselves and are far from "ideal" for synthetic unmixing. We decisively chose this approach not only to compare the performance of different EMMA methods but also to explore drawbacks in the modelling procedure under such conditions.

Three parallel samples (0.3–2.0 g) per outcrop were chemically treated with 10 % NaCl, 15 % H_2O_2 and 1.25 mL $Na_4P_2O_7$, each for 48 h, and measured with a Beckman Coulter LS 13 320 Laser Diffraction Particle Size Analyzer at RWTH Aachen, delivering 116 classes (0.04–2000 µm). Between 7 and 16 aliquots per sample were investigated in triplicates. Grain-size distributions were derived applying the Mie theory with the following parameters: fluid refraction index: 1.33; sample refraction index: 1.55; imaginary refraction index: 0.1. The resulting median grain-size distributions (Fig. 2) were manually mixed in the lab to generate 100 samples with randomly assigned individual contributions. Within this data set $\mathbf{X}_{nat}$, 50 samples contained all four EM_{nat}, 25 were prepared without $EM_{nat}4$ material and a further 25 were prepared without $EM_{nat}1$. Hence, in contrast to other studies, we fully know the grain-size distributions of the underlying natural process end-members and their mixing ratios, which allows a detailed evaluation of performance and comparison of all available EMMA algorithms.

3.2 Model performance of different EM analyses

The example data set $\mathbf{X}_{nat}$ was decomposed with deterministic EMMA of EMMAgeo using `q=4` and `l=0`. Robust EMMA was run with both the extended and the compact protocol. To be as conservative and as unbiased as possible, both protocols were executed with the default parameterisations as suggested above and were only modified when results obviously prompted manual parameter adjustments.

To run the FORTRAN-based approach by Weltje (1997), provided by Jan-Berendt Stuut (personal communication, 2017), the grain-size classes of $\mathbf{X}_{nat}$ needed to be aggregated; i.e. the resolution decreased by a factor of 2. For consistent comparisons with the other approaches, the resulting end-member loadings were interpolated back to the initial grain-size resolutions (see Supplement). The down-sampling and subsequent up-sampling of all EM_{nat} values resulted in negligible artefacts with an average $R^2 > 0.999$. The modelled data set $\mathbf{X}'$ was computed by combining loadings and scores according to Eq. (1), excluding the error matrix $\mathbf{E}$.

Running the collection of the five RECA R scripts (Seidel and Hlawitschka, 2015) required manual installation of the additional package compositions (Van den Boogaart et al., 2014), e1071 (Meyer et al., 2017) and nnls (Mullen and van Stokkum, 2012), loading all scripts and manual screen input of the model parameters. RECA needs to be run completely to the end until consequences of parameter changes can be inspected. The decision on q is based on a q–R_n^2 plot (e.g. using the inflection point). Here, RECA was run with four end-members, a maximum convexity error of −6, confirmation of the first start model, 100 iterations and a weighting exponent of 1, as suggested by Seidel and Hlawitschka (2015).

AnalySize by Paterson and Heslop (2015) provides a MATLAB GUI, in which q is set manually. The numeric MATLAB output, end-member loadings and scores, was imported to R using the package R.matlab (Bengtsson, 2018).

Bayesian EMMA (BEMMA) in MATLAB (Yu et al., 2015) does not allow a predefined q to be specified. With repeated model runs, the number of output end-members changed unsystematically between two and four. Depending on q, the shape and mode positions of the unmixed distributions fluctuated, which prevented the output from different model runs from being grouped. Hence, we did not include BEMMA in this comparison.

3.3 Evaluation and validation criteria

The performance of all approaches was evaluated in two steps. First, we compared the original data set $\mathbf{X}_{nat}$ and the modelled data sets $\mathbf{X}'$ using (i) coefficients of determination (mean total R^2_t, sample-wise R^2_m, class-wise R^2_n) and (ii) the absolute differences between $\mathbf{X}_{nat}$ and $\mathbf{X}'$ (total MAD_t, sample-wise MAD_m, class-wise MAD_n). This comparison resembles the classical evaluation step when the true natural end-member composition is unknown.

Second, knowing which natural end-members have been mixed to create the example data set $\mathbf{X}_{nat}$, we compare (i) R^2 and MAD for EM_{nat} distributions and loadings (R^2_{n1} to R^2_{n4} and MAD_{n1} to MAD_{n4}), (ii) R^2 and MAD for mixing ratios and scores (R^2_{m1} to R^2_{m4} and MAD_{m1} to MAD_{m4}) and (iii) the absolute deviations of the mode positions of EM_{nat} distributions and loadings. For comparisons of EM_{nat} distributions with modelled loadings, all results were truncated to grain-size classes of EM_{nat} higher than 0.1 % vol and rescaled to 100 %. There are two reasons for this: first, due to the generally narrow grain-size distributions, EM_{nat} contained many grain-size classes of only zeros, which biases the resulting measures (Ciemer et al., 2018). This bias is severe: correlating, for example, two sequences of random values (e.g. 3.1, 5.2, 4.0 and 9.2, 8.3, 3.5) typically yields a very low correlation coefficient (e.g. $r = -0.065$). However, padding these sequences with zeros strongly increases the correlation coefficient (e.g. $r = 0.87$, including five zeros). Second, it is known that EMMA (Dietze et al., 2012), but also other approaches, causes spurious secondary modes directly below the mode positions of other end-members (Paterson and Heslop, 2015). The spurious modes are obviously not related to the underlying sedimentation regime and are not intended to be interpreted genetically (Dietze et al., 2014). As they would also bias the model comparison measures, we excluded them from model evaluation.

4 Results: the different model performances

4.1 Evaluation of model performance

4.1.1 Deterministic EMMA

Figure 3 shows the default graphical output after the EMMA algorithm has modelled the data set with four end-members. Panels a and b depict R^2 values (squared Pearson correlation coefficients) organised by grain-size class and sample. Overall, the data set was reproduced with a mean R^2_t of 0.969 and MAD_t of 0.2 % vol (Table 1). Panels c and d show modelled end-member loadings and scores. End-member loadings (EM1-4) had modes at 16, 40, 310 and 450 µm. Spurious secondary modes of less than 2.5 % vol are visible below primary modes of other end-members. Apart from the multimodal EM4, all end-members have a log-normal shape. Figure 3a shows that grain-size class-wise R^2_n decreases between 946 and 1830 and 117 and 177 µm, both grain-size class intervals that contribute less than 0.9 % vol to $\mathbf{X}$ (Fig. 2). Mean sample- and class-wise absolute deviations are shown in Table 1.

The scores of EM1 to EM4 accounted for 20 %, 20 %, 31 % and 29 % of the variance of $\mathbf{X}'$, respectively. Sample-wise R^2_m is 0.98 on average (Table 1). Four outliers had $R^2_m < 0.95$ (samples 16, 57, 64, 75; Fig. 3b). However, neither removing these samples nor changing the rotation type from Varimax to Quartimax or the oblique rotation Promax improved the modelling of loadings and scores (not shown).

4.1.2 Robust EMMA – extended and compact protocol

In the extended protocol, an l_{min} of zero was used according to Miesch (1976), and l_{max} was set to 0.37, i.e. 95 % of the modelled absolute l_{max} of 0.39 (see methods in Sect. 3). However, when using this value, negative loadings occurred. Therefore, the value was set to 80 %, yielding a more realistic and valid l_{max} of 0.31. With 20 values between l_{min} and l_{max}, q_{min} varied between 2 and 3 (Fig. 4a), and q_{max} showed a trend of decreasing $\boldsymbol{R}^2_t$ with increasing l (Fig. 4c, d), until even NA values were produced for some parameter combinations (blue graph, Fig. 4b). Accordingly, after a local optimum at q_{max} between 4 and 9 (open circles, Fig. 4b), adding more end-members leads to numerical instabilities.

Figure 5a shows all 223 end-member loadings from 96 EMMA runs that agree with the parameter space of `P`. Note that the protocol can be run with user-defined grain-size units (function argument classunits) or simply the raw grain-size class numbers (default, and used in the following sections for simplicity). Several end-members have main mode position clusters between grain-size class numbers 63 and 66, 74 and 77, 94 and 97 and 99 and 102 (orange polygons). These class limits were used to model the robust end-member loadings, excluding the negative loadings that were modelled due to l_{max} values that are too high. A fifth cluster at classes 71–73 exists (not marked), although the distribution of this end-member is rather broad and overlaps with the distribution shapes of the two other clusters in this range. It was rejected as a robust end-member (see below).

The resulting robust EM3 and EM4 loadings show high class-wise standard deviations (SDs) around the mode positions (Fig. 6a). EM1 has a continuously narrow uncertainty envelope (i.e. mean $\pm$ 1 SD), and EM2 shows the largest and most variable envelope. Mean class-wise SDs range from 0.06 (EM4) to 0.38 % vol (EM2). The main mode positions of the robust loadings are identical with those of deterministic EMMA; only the EM2 mode is one class off. Using the mean robust loadings, l_{opt} was 0.0163 when maximising R^2_t. Based on this, mean robust scores were modelled (Fig. 6b) with an average SD of 9.9 % vol, 7.8 % vol, 11.3 % vol and 9.5 % vol for EM1 to EM4.

With the compact protocol, the same parameter space (l_{min}, l_{max}, q_{min} and q_{max}) was calculated as with the extended protocol. Robust end-member definition is supported

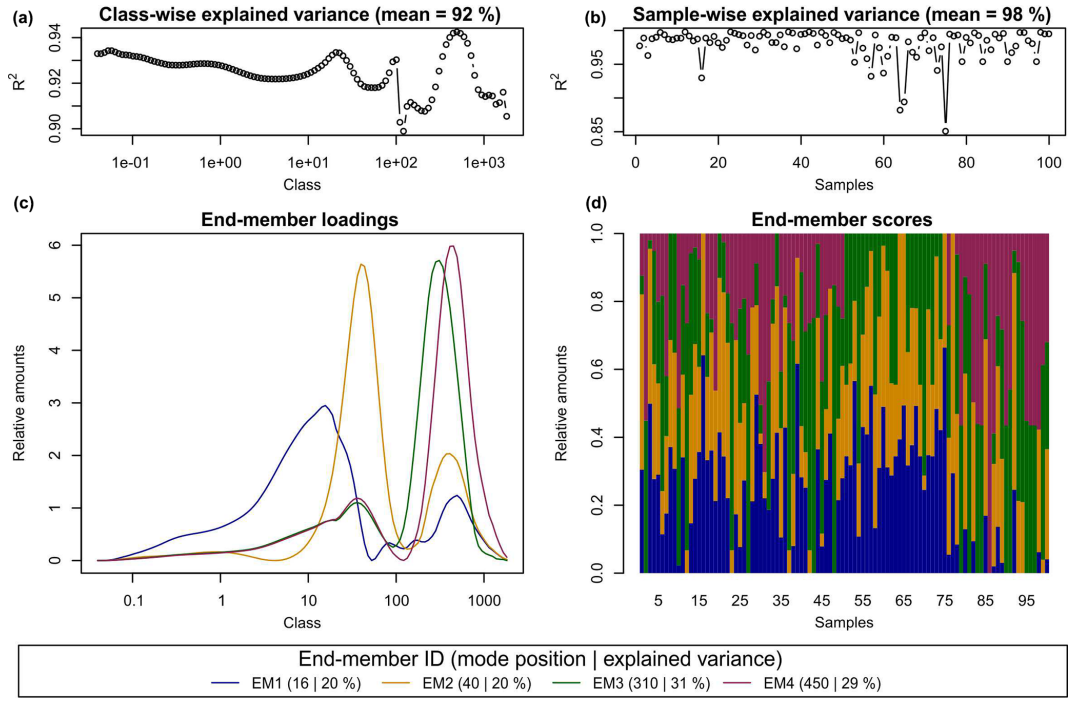

Figure 3. Default graphical output of the R function `EMMA()`. **(a, b)** Measures of model performance (i.e. class- and sample-wise R^2), **(c)** end-member loadings and **(d)** end-member scores. The legend presents the main mode positions (µm) and explained variance of each end-member (%).

Table 1. Comparison of model performance (total, sample-wise and grain-size class-wise coefficients of variation (R^2_t, R^2_m, R^2_n) and absolute deviation (MAD_t, MAD_m, MAD_n) of X_{nat} versus $\mathbf{X}'$). $EMMA_{det}$, $EMMA_{rob\_ext}$ and $EMMA_{rob\_cmp}$ refer to EMMAgeo deterministic, extended and compact robust models (see text). $EMMA_{weltje}$, RECA and AnalySize refer to end-member approaches in FORTRAN (Weltje, 1997), R (Seidel and Hlawitschka, 2015) and MATLAB (Paterson and Heslop, 2015), respectively.

Model	R^2_t	R^2_m	R^2_n	MAD_t	MAD_m	MAD_n
$EMMA_{det}$	0.969	0.98	0.925	0.15	0.155	0.145
$EMMA_{rob\_ext}$	0.964	0.974	0.92	0.171	0.186	0.156
$EMMA_{rob\_cmp}$	0.966	0.975	0.927	0.168	0.183	0.153
$EMMA_{weltje}$	0.978	0.981	0.837	0.17	0.186	0.155
RECA	0.868	0.886	0.684	0.302	0.338	0.266
AnalySize	0.995	0.995	0.916	0.065	0.072	0.058

by the plot output of the function `robust.EM()`. Figure 5b shows five clusters with mode positions at 13–16, 27–33, 38–47, 250–320 and 390–500 µm (i.e. class numbers 63–66, 71–74, 75–77, 95–97 and 100–102). The colour scheme reveals that the cluster at 27–33 µm (grey bar, Fig. 5b) systematically occurs when EMMA was run with three end-members (red curves, Fig. 5a). Clusters at 13–20 and 38–47 µm emerge especially when four end-members were included in a model run (green curves). A similar case exists for the two coarse end-members, at 250–320 and 390–500 µm. Hence, models with a value for `q` that is too small systematically merge distinct grain-size distributions into spurious, broad curves. Values for `q` that are too high instead caused spikey loadings (blueish, pink curves, Fig. 5b).

Defining the limits by the automatic kernel density estimate approach suggested only three out of four natural end-members as robust ones, combining all loadings around class 100 (Fig. 5b, black line). Setting the kernel bandwidth arbitrarily to 0.5 would allow separation of the two overlapping modes around $EM_{nat}2$ while missing $EM_{nat}1$ and misinterpreting the cluster around the two coarsest end-members (not shown). Thus, for strongly overlapping mode clusters, automatic class limit detection was not appropriate. Hence, we set the mode limits similar to the extended protocol to class numbers 63–66, 75–77, 94–97 and 99–102, changing the definition of EM2 by just one grain-size class (extended protocol: 74–77) to better exclude the cluster at 27–

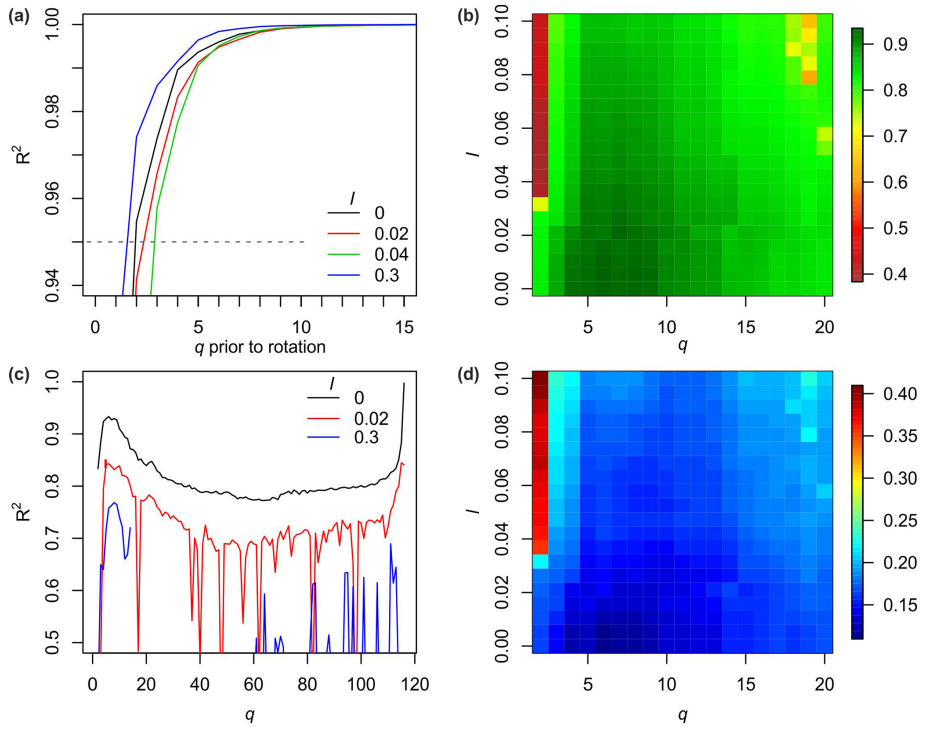

Figure 4. Parameter optimisation steps in the extended protocol of robust EMMA. **(a)** Model performance (coefficient of determination) with increasing number of factors prior to rotation (examples of weight transformation limits l; default output of the function `test.factors()`). **(b)** Mean total R^2_t of all likely q and l, default output of `test.parameter()`, 19 different q (2 to 20). **(c)** Examples of total R^2_t of EMMA-scenarios as a function of the number of end-members q (along the x axis) and three different l values. **(d)** Mean sample-wise model error E_n of all likely q and l values, optional output of `test.parameters()`, 20 different l values (0 to 0.1).

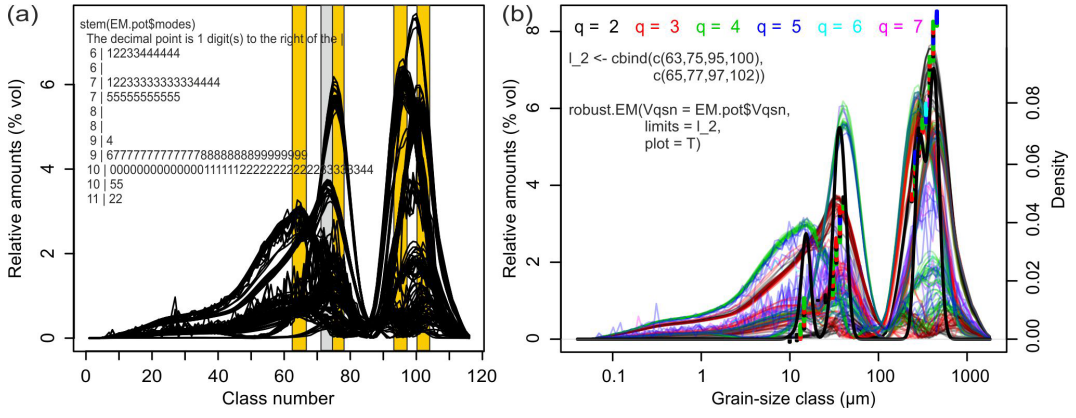

Figure 5. **(a)** Potential end-member loadings resulting from multiple EMMA runs with similarly likely parameter combinations. Distinct clusters of main mode positions define the grain-size class limits (orange bars) and allow calculation of the range of robust end-members by averaging the loadings with main modes that fall within the defined class limits. Note that there is no straightforward impression of the four input EM_{nat} values and the few, spikey loadings resulting from values of l that are too high. A stem-and-leaf plot of the mode clusters can be used to judge the appropriateness of the identified limits. **(b)** Default graphical output of the R function `model.EM()` assigns potential end-member loadings to the EMMA runs of **(a)**. Coloured lines show end-member loadings from EMMA models with different q (dots at respective main mode positions) and varying l values. The black line is a kernel density estimate of the main mode positions of all loadings, with a default bandwidth of 1.16, i.e. 1 % of the number of grain-size classes of the input data set and a default threshold to identify mode clusters (i.e. 0.016) that define three robust end-members (not shown). Manual setting of the limits avoids overlapping of the two coarse end-members and excludes the loadings of the grey bar.

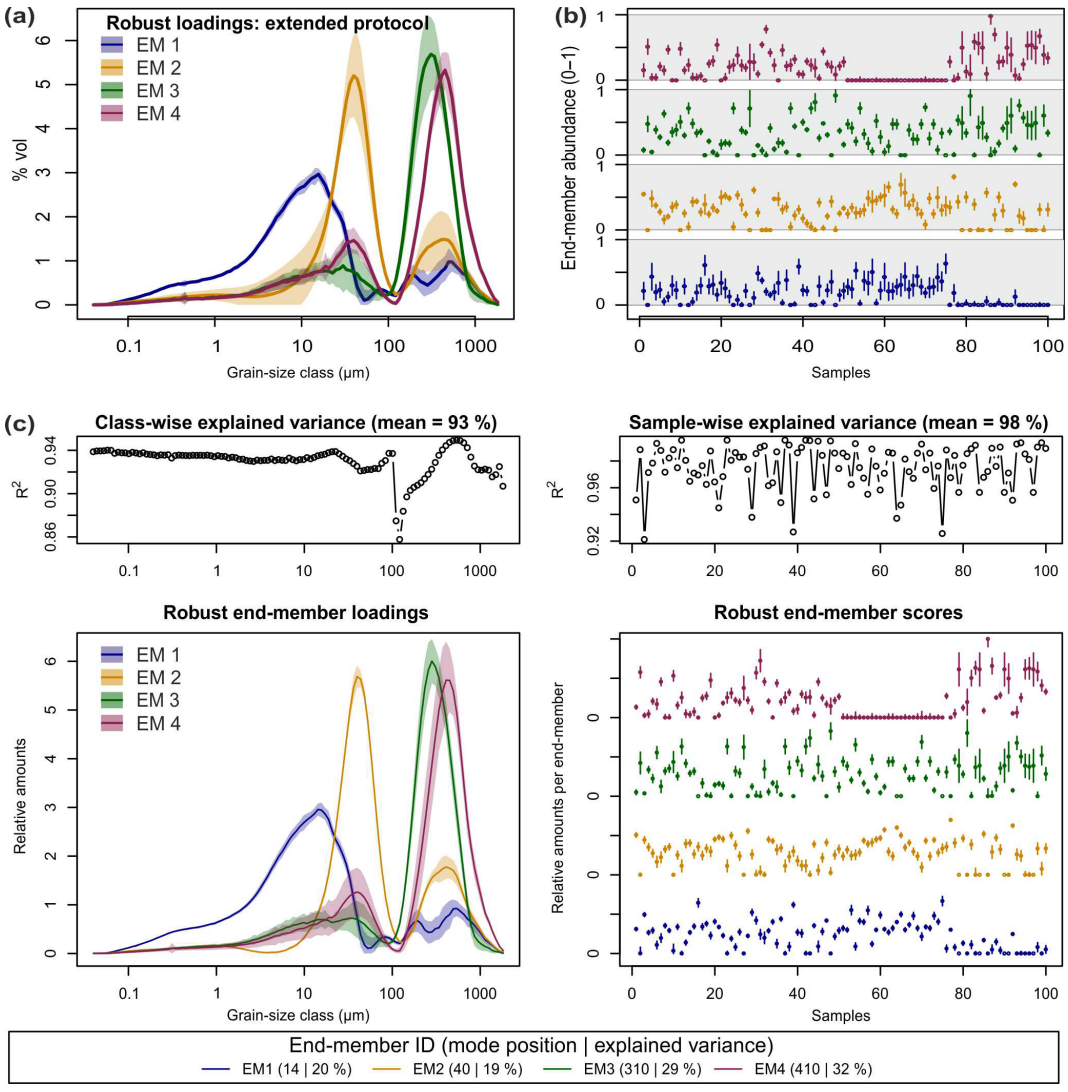

Figure 6. **(a)** Robust end-member loadings and **(b)** scores of the extended protocol. **(c)** Default graphical output of `robust.EM()` as part of the compact protocol, including class- and sample-wise explained variances **(a, b)** and a legend with main mode position and explained variance of each end-member. Mean robust loadings as line graphs, mean robust scores as panels of points. Polygons around loadings and bars around scores represent 1 standard deviation.

33 µm (red curves, Fig. 5b) and to assess varying robust end-member definitions.

The resulting end-members are shown in Fig. 6b. They are similar to the plotted output of the deterministic version (Fig. 3) but extended by uncertainty polygons, the different representation of scores and slightly different mode positions, grain-size class-wise R^2_n (0.93) and sample-wise R^2_m (0.98). Mean end-member contributions to the variance of the data set (20 %, 19 %, 29 % and 32 %) are almost identical to the deterministic version.

4.1.3 Comparison to other end-member unmixing algorithms

The full benchmark reveals that all approaches successfully model the data sets. The output of RECA shows difficulties in reaching the minimum convexity error of −6 with the initial 100 iterations, but by increasing the value to 200 iterations the issue was solved.

The average R^2_t values were higher than 0.868 in all cases, up to 0.995 (Table 1). Sample-wise R^2_m values were always higher than the grain-size class-wise R^2_n values. Deterministic EMMA yielded slightly better results than the two robust EMMA protocols, which in turn were very similar. The lowest (highest) and highest (lowest) R^2_t (MAD_t) values are related to RECA and AnalySize, respectively.

The main absolute deviations of $\mathbf{X}'$ from $\mathbf{X}_{nat}$ are associated with grain-size classes between 100 and 1000 µm, regardless of the model (Fig. 7). Except for AnalySize, all approaches show systematic underestimation of these grain-size classes of up to −2.5 % vol per class. Vice versa, finer grain-size classes between 1 and 100 µm are slightly overestimated by ca. 1 % vol per class. The effects of the applied sample mixing scheme of X_{nat} are clearly visible in all model results (Fig. 7). Samples 51 to 75 (without coarse $EM_{nat}4$) show an overestimation of coarse and underestimation of fine classes. Samples 76 to 100 (without fine $EM_{nat}1$) show the opposite picture. AnalySize yielded the overall best unmixing, with average deviations of ca. ±1 % vol.

4.2 Validation against known data set composition

The above criteria quantify how well the approaches modelled the data set (Eq. 1), whereas their ability to reproduce the true "mixed ingredients" is addressed here. The R^2 values between loadings and input EM_{nat} grain-size distributions (Table 2a) were on average between 0.4 and 0.99 and, thus, systematically larger than R^2 values linking scores and mixing ratios (0.77 to > 0.99; Table 2b). Both EMMAgeo and AnalySize performed less well in modelling one out of three EM_{nat} distributions (EM1 for EMMAgeo and EM4 for AnalySize). The MAD was below 0.8 % vol for all models and end-members, except for EM4 scores (AnalySize).

A graphical comparison of the grain-size class-wise deviations of input end-member distributions and modelled loadings (Fig. 8) shows that all EMMAgeo-based models underestimate the main mode grain-size classes (i.e. curves are below the 1 : 1 line). This is the result of the emergence of spurious modes that shift class-wise percentages (up to −3.2 % vol) from the main modes to classes around the spurious modes (up to 1.3 % vol) that actually contain no grains (vertically aligned points at zero x values). The other EMMA approaches also show mismatches between natural end-members and modelled loadings. Especially the alluvial fan $EM_{nat}4$ is affected, most severely in AnalySize. Percent volume (% vol) shifts due to spurious secondary modes also occur for the algorithm of Weltje (1997) and RECA. Overall, the latter approach yields the most accurate representations of the input distributions.

Concerning the reproduction of the initial mixing ratios (Fig. 9, Table 2b), variability among the models is higher, and all approaches show some unsystematic over- and underestimation, especially for EM in samples in which real mixing ratios were zero (vertical point clusters along the 0 % x axis; Fig. 9). Except for RECA and AnalySize, the opposite effect is also visible: the models suggest zero contribution from end-members that are actually present in a sample with up to ca. 20 % (horizontal points along the 0 % y axis; Fig. 9).

The modal grain-size classes of the four EM_{nat} were modelled with different levels of success (Fig. 8, legends). The main modes of the coarse end-members were detected with only one or two grain-size classes' difference, whereas finer end-members differed by up to three classes. Modal classes of $EM_{nat}2$ and $EM_{nat}3$ were correctly depicted by EMMA of Weltje (1997), RECA and AnalySize. Most models yielded a value of $EM_{nat}1$ that is slightly too coarse, deviating by one or two grain-size classes. $EM_{nat}4$ caused the largest scatter among the models.

5 Discussion

5.1 Operational modes of EMMAgeo

The functionality of EMMA has improved significantly since the introduction of the MATLAB algorithm of Dietze et al. (2012). Not only an increase in computation speed, which was already 1 to 3 orders of magnitude faster than for other algorithms (Paterson and Heslop, 2015), but also many new and detailed ways to explore end-members (with deterministic EMMA) and to estimate and describe associated uncertainties of all end-member components (with robust EMMA) were implemented. The plot output of both EMMA modes is a comprehensive visualisation of all relevant information. It allows direct process interpretation in terms of plausibility of loadings and scores, model performance and identification of outliers.

Both EMMA modes, deterministic and robust, result in consistently similar outputs. Deviations of individual modes of robust loadings from known EM_{nat} distributions by one or two grain-size classes are within the model uncertainty of robust EMMA. Therefore, a key step is the definition of robust end-members by setting the grain-size class limits that bracket robust, parameter-independent main modes, which overcomes the problem of relying on statistical measures like the inflection point of a q–R^2 graph (van Hateren et al., 2018). The workflow of robust EMMA offers ways to explore the ability of different kernel bandwidths and density thresholds, but in complicated cases, like the one provided in this study, expert knowledge-based limit definition might be the most practicable option. Hence, each data set should be considered individually, and deviations from common patterns may be significant in their own right (see discussion by van Hateren et al., 2018).

5.2 Performance test and validation

Unmixing quality is very high regardless of the model used, suggesting that all approaches in this benchmark are able to reproduce the input grain-size data set with unmixed end-member subpopulations. There is no model with an outstanding performance. Model deviations of < 1 % (especially for grain-size classes with > 0.1 % vol) are low in the light of uncertainties related to process interpretation (see below).

The validation against known input end-member composition showed that all EMMA approaches are equally applica-

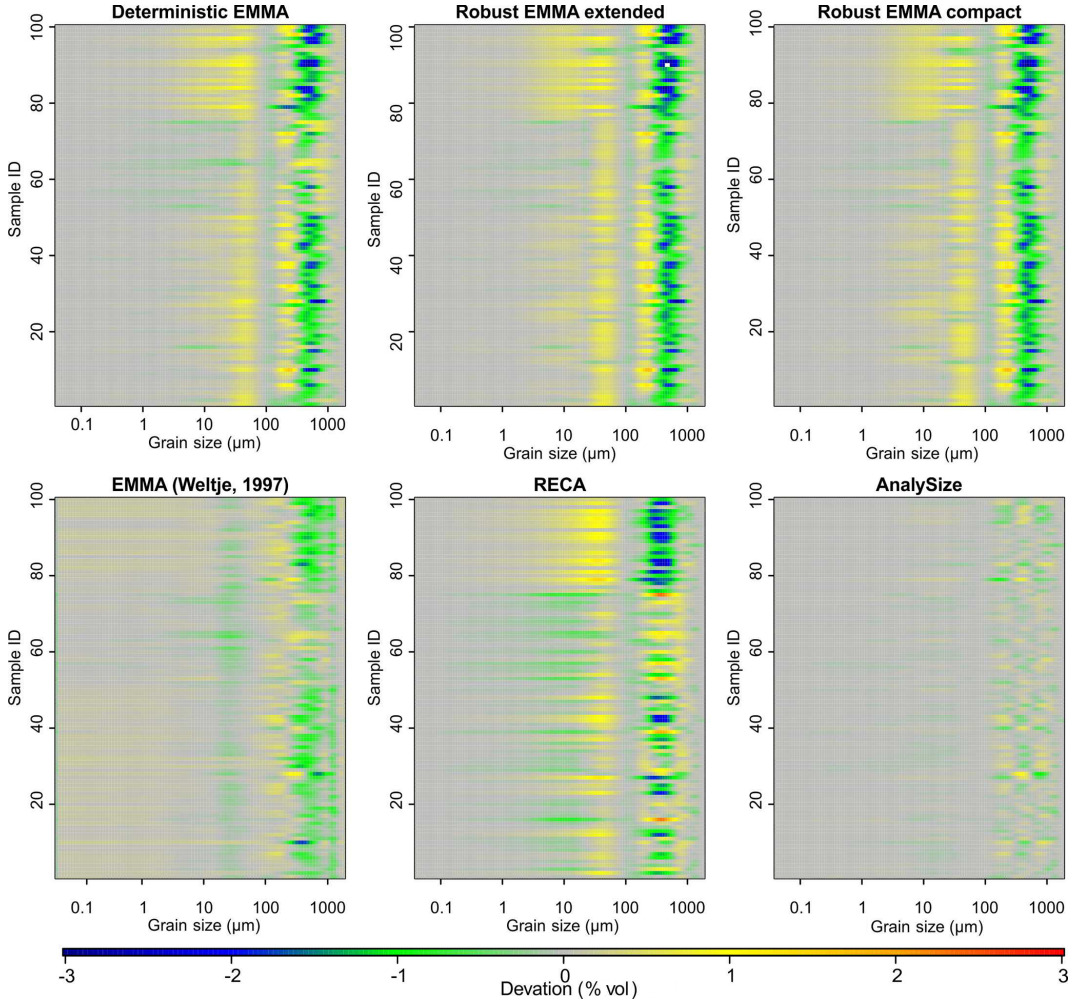

Figure 7. Model performance to unmix and reproduce the example data set X_{nat}. For each end-member model approach, the absolute difference MAD between modelled and original data set is shown.

ble. When comparing end-member loadings with the EM_{nat} distributions, R^2 mainly represents shifts in mode positions, whereas MAD reacts to both shifts in the modes of individual grain-size distributions and differences in the volume percentages per class. Yet, each algorithm has certain strengths depending on the specific dimension of the investigation: if the main goal is to identify the most likely q that builds an empirical data set, robust EMMA provides a set of tools that go beyond classical approaches (e.g. the inflection point of the q–R^2 plot) – allowing the inclusion of expert knowledge in the quantification and interpretation of grain-size subpopulations.

If the correct grain-size distribution shape of underlying process end-members is targeted, RECA of Seidel and Hlawitschka (2015) and EMMA by Weltje (1997) are most suitable from our benchmark study (Table 2a). RECA had problems with reaching the convexity error threshold, which could result from our data set with largely overlapping natural process end-members.

When quantifying the contribution of end-members to a given sample, robust EMMA, EMMA according to Weltje (1997) and AnalySize performed best (Table 2b). Robustly estimated scores using EMMAgeo reproduced original mixing proportions very well and in a range comparable to the other available end-member algorithms. However, as all approaches and earlier EMMA evaluations showed, very low and high scores ($< 20\,\%$ and $> 80\,\%$) of one end-member might be under- or overestimated within the compositional mixture (McGee et al., 2013). Hence, extremely high (e.g. $100\,\%$) contributions of one end-member to a sample should not be interpreted as complete absence of the other end-members but rather as the dominance of this one end-member (and vice versa).

If uncertainty estimates for both loadings and scores are considered important, then only robust EMMA is suitable. The inclusion of uncertainties for loadings and scores is a key precondition for propagating model results to further data analysis, for example to interpret grain-size end-members

Table 2. **(a)** Grain size class-wise coefficients of variation (R^2_n) and absolute deviation (MAD_n) of modelled end-member loadings compared to natural end-member distributions. **(b)** Sample-wise coefficients of variation (R^2_m) and absolute deviation (MAD_m) of modelled end-member scores compared to natural end-member mixing ratios.

(a)

Model	R^2_n1	R^2_n2	R^2_n3	R^2_n4	MAD_n1	MAD_n2	MAD_n3	MAD_n4
$\mathrm{EMMA}_{\mathrm{det}}$	0.765	0.811	0.922	0.872	0.094	0.082	0.076	0.084
$\mathrm{EMMA}_{\mathrm{rob\_ext}}$	0.752	0.807	0.941	0.884	0.096	0.081	0.068	0.097
$\mathrm{EMMA}_{\mathrm{rob\_cmp}}$	0.744	0.821	0.901	0.867	0.096	0.078	0.082	0.095
$\mathrm{EMMA}_{\mathrm{weltje}}$	0.988	0.975	0.723	0.702	0.04	0.051	0.096	0.095
RECA	0.745	0.403	0.595	0.837	0.116	0.165	0.125	0.072
AnalySize	0.98	0.974	0.761	0.701	0.045	0.049	0.088	0.091

(b)

Model	R^2_m1	R^2_m2	R^2_m3	R^2_m4	MAD_m1	MAD_m2	MAD_m3	MAD_m4
$\mathrm{EMMA}_{\mathrm{det}}$	0.773	0.93	0.989	0.999	0.5	0.827	0.303	0.097
$\mathrm{EMMA}_{\mathrm{rob\_ext}}$	0.778	0.925	0.97	0.978	0.477	0.83	0.499	0.531
$\mathrm{EMMA}_{\mathrm{rob\_cmp}}$	0.772	0.925	0.979	0.98	0.485	0.831	0.416	0.513
$\mathrm{EMMA}_{\mathrm{weltje}}$	0.975	0.993	0.988	0.92	0.166	0.133	0.478	0.906
RECA	0.917	0.966	0.978	0.947	0.272	0.284	0.427	0.686
AnalySize	0.985	0.999	0.97	0.787	0.116	0.037	0.625	1.633

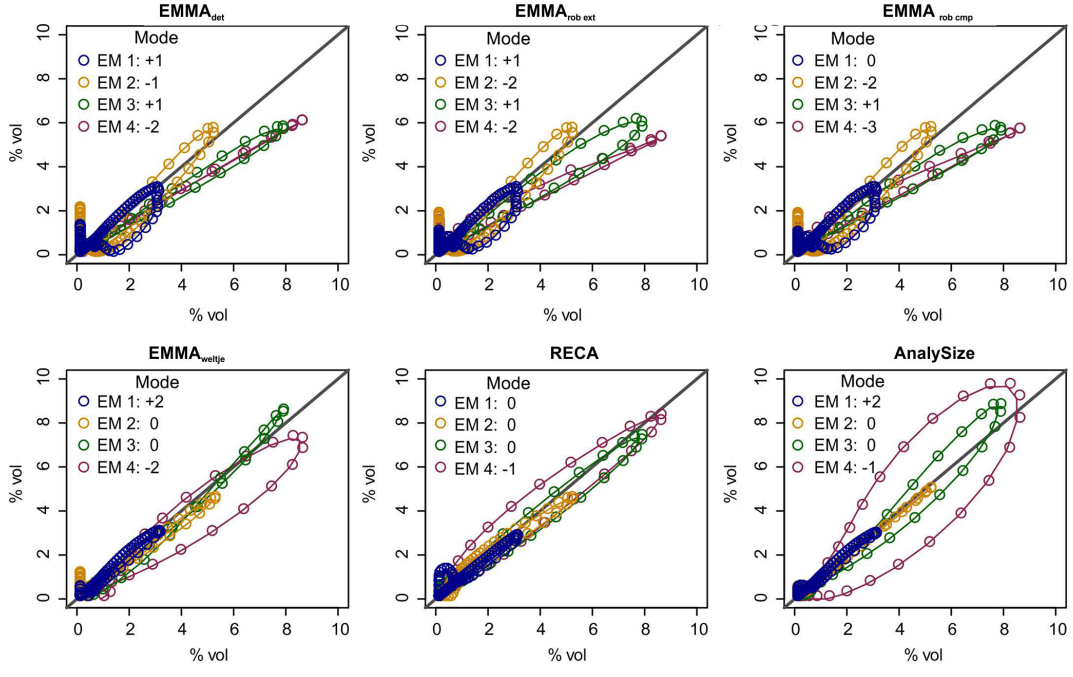

Figure 8. Natural versus modelled end-member grain-size distributions for all evaluated models. Deviation of main mode (in number of classes). x axes show $\mathbf{X}_{\mathrm{nat}}$ and y axes modelled $\mathbf{X}'$ values.

as proxies for sediment sources (loadings) in environmental archives as they evolve with time (scores). As van Hateren et al. (2018) emphasise, changes in the model results will inevitably result in diverging interpretations of the assumed sedimentary processes. Also, the interpretations of the scores in their spatial (samples across a landscape) or temporal (samples downcore) context will be affected. Thus, it is extremely important to provide some estimate of the inherent uncertainty in both the proxy definition and in the sample domain. So far only robust EMMA can deliver such information. Yet, necessary parameter estimates and diverging start conditions evidently exist in the other models too.

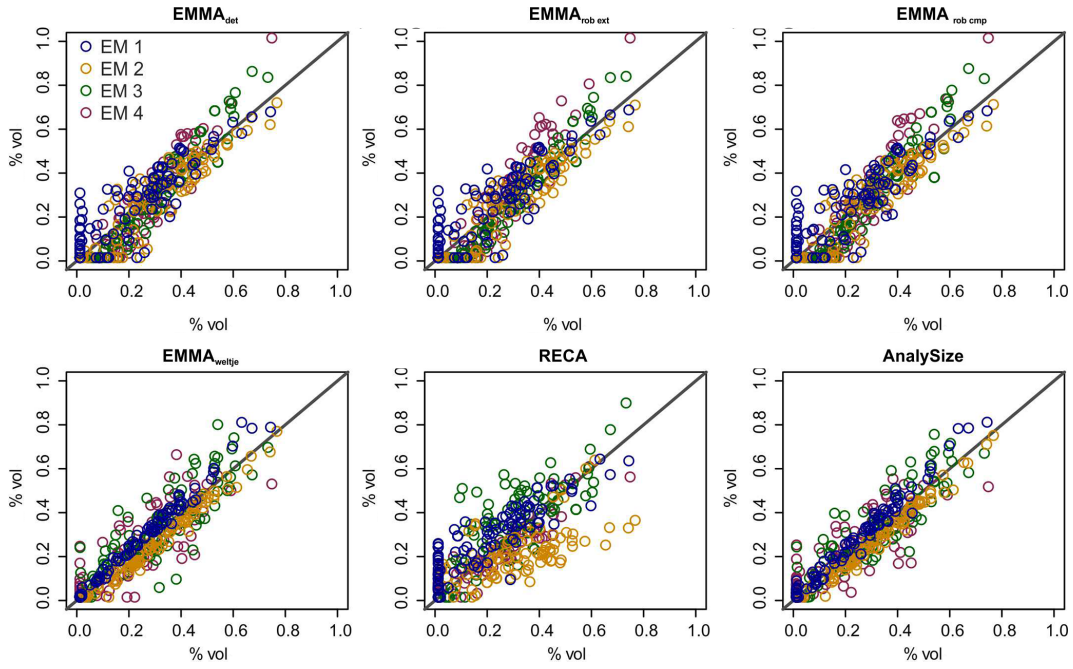

Figure 9. Natural versus modelled end-member mixing ratios for all evaluated models. x axes show $\mathbf{X}_{\text{nat}}$ and y axes modelled $\mathbf{X}'$ values.

If the distribution shape of an inherent natural grain-size end-member is known, EMMAgeo allows quantification of its contribution to the data set by including it as unscaled loadings in both deterministic and robust EMMA or by assigning the known main mode class limits when selecting robust end-members (step 4; Fig. 1b). Finally, if free and open-source software is a criterion – which is increasingly the case for journals and funding agencies (David et al., 2016; Munafò et al., 2017) – RECA and EMMAgeo remain the only options.

5.3 Comparison with other benchmark studies

In previous benchmark studies, EMMAgeo performed less well, which Paterson and Heslop (2015) attributed to the implementation of the non-negativity and sum-to-one constraints. van Hateren et al. (2018) pointed to the secondary modes as cause of the deviations of scores from the mixing ratios. We cannot confirm the poor performance of EMMAgeo in our study, as it is not fully clear how van Hateren et al. (2018) determined the EMMAgeo loading curves, which they evaluate graphically. They note that in EMMAgeo the q is not set by the inflection point of the q–R^2 relationship, but robust EMMA would lead to one q, and not a sequence of 2 to 5, as discussed in their study. Additionally, it is unclear which realisation from within the robust EMMA uncertainty range was evaluated by van Hateren et al. (2018). Accordingly, detailed introduction of the EMMA protocols is essential to avoid future misinterpretations.

Yet, the occurrence of artificial secondary modes below the main modes of the end-members is more pronounced in EMMAgeo compared to other unmixing algorithms. The inherent compositional data constraints lead to an intimate linkage of the distribution shape of one end-member with the distribution shapes of other loadings. However, when excluding hardly interpretable secondary modes from global measures of model quality, the performance of EMMA is well within the range of other available algorithms. As repeatedly noted in articles applying EMMAgeo (Dietze et al., 2012, 2014) but also highlighted for other approaches in the benchmark study of Paterson and Heslop (2015), secondary modes are model artefacts and should not be interpreted genetically.

However, to test the impact of artificial secondary modes on model performance, we modelled the EM_{nat} data set with user-defined end-members. We manually set the unscaled loadings outside the known primary end-member modes to zero and used these updated loadings for the modelling process (see Supplement for R code). Although the resulting end-member loadings are now free of secondary modes, the mixing ratios are only marginally better modelled (-1 % to 4 % deviation). Thus, such a truncation may help in tuning the shape of the modelled end-members but cannot improve deviations of the scores from mixing ratios. Still, the uncertainty ranges of the robust scores included the expected EM_{nat} mixing ratios (66.5 % of the samples are within the modelled 1 standard deviation range).

5.4 Constraints on end-member interpretation

Going beyond classical measures of grain-size properties, EMMA is well suited to quantify sedimentary processes from mixed sediment sequences in space and time. How-

ever, interpretation of grain-size end-members requires expert knowledge about the investigated sedimentary system. Hence, when applying EMMA to any set of grain-size data, the interpretability of the resulting end-members needs to be checked. For this, both end-member components should be considered: the shape and position of the main modes of the loadings and the spatio-temporal or stratigraphic context of the scores. For example, the effectiveness of a process in sorting sediment could be interpreted in the classical sense from the shape of the end-member loadings (excluding artificial modes), with broader peaks being more poorly sorted than narrow peaks (Friedman, 1961).

As any other statistical method, EMMA is a tool, and interpretation of grain-size end-members relies on contextual knowledge. There may be processes that contribute to the overall sediment composition and that are not size-selective or sort sediment of various grain-size classes in a typical way. For example, event-triggered turbidity currents in lakes caused problems in attributing a single sedimentary process to end-members in the study by Dietze et al. (2014) because the typical fining-upwards trend was also reflected by several end-members that contributed to samples of "normal" deposition.

Closely related is the constraint of stationarity in processes, which implies that through space and time each transport process must create an identical grain-size distribution. For example, fining of aeolian material from one distinct source area with downwind transport distance (Pye, 1995) might rather be explored by a gradual approach, e.g. by running EMMA in a moving window over a data set to detect shifts in stationarity.

Post-depositional processes that change grain-sizes, e.g. due to permafrost conditions or soil formation, could strongly disturb the original grain-size characteristics. In the worst case, a lacustrine sediment archive composed of different aeolian and fluvial sediment end-members (Dietze et al., 2013) can be affected by ongoing cryogenic and active-layer dynamics in a way that all modelled end-members were overlapping and peaking in similar grain-size classes – "erasing" primary signals related to sediment deposition. If post-depositional activity overprints the original depositional processes, EMMA can detect them as single end-members and would allow quantification of the intensity of the overprint, e.g. soil formation (Dietze et al., 2016) or weathering (Sun et al., 2002; Xiao et al., 2012).

Sediments affected by the processes mentioned above can affect end-member modelling in manifold ways. For example, EMMA could result in rather low explained variances, and the modes of affected end-member loadings would become broader and/or may even be better represented by additional but nevertheless spurious end-members. In the worst case, modes of end-member loadings overlap strongly or cannot be unmixed at all.

6 Conclusions

EMMAgeo allows the characterisation of multi-modal grain-size distributions by end-member subpopulations. New protocols allow a quick analysis, including modelling of associated uncertainties for both end-member loadings and scores. Using four known natural end-members, which represent typical sediment types found in terrestrial systems, the performance of EMMAgeo in unmixing the correct end-member distribution shapes and mixing ratios is within the same order as the performance of other available end-member modelling algorithms, which all perform very well. Hence, all of these algorithms are powerful tools for characterisation of different sediment source, transport, depositional and even post-depositional processes. In comparison to other algorithms, EMMAgeo is the only available open-source grain-size unmixing approach that includes uncertainty estimates. An inherent strength of the fully free R package is a large flexibility for users to modify the parameter settings and workflows with the new protocols, reproduce results and continue data evaluation.

Once genetically interpretable grain-size end-members are derived, their loadings can be described by classical descriptive measures (Folk and Ward, 1957; Blott and Pye, 2001). This allows a statistically robust determination and comparison of mean, sorting and shape measures across sites and data sets by describing and quantifying processes that sort sediment better or poorer than other processes.

Many future applications in the fields of Quaternary Science, sedimentology, geology, geomorphology and hydrology could gain new insights from applying EMMAgeo to compositional data sets that represent mixtures. In contrast to classical linear decomposition methods such as principle component analysis, EMMA has the potential to quantify (and not just qualify) different sources or processes of modern and past sedimentary environments that contribute to a sample set, including associated model uncertainties.

Code and data availability. The Supplement contains the example data set, end-member measurement data, mixing ratios and output of the other approaches included in the comparison. The R package EMMAgeo in its latest release version 0.9.6 (Dietze and Dietze, 2019; https://doi.org/10.5880/GFZ.4.6.2019.002) is available on the Comprehensive R Archive Network (R Core Team, 2017) and on GitHub. Please report any bugs and improvements to the maintainers of the package.

Supplement. The supplement related to this article is available online at: https://doi.org/10.5194/egqsj-68-29-2019-supplement.

Author contributions. ED and MD improved the original EMMA algorithm, workflows and auxiliary functionalities. ED

compiled the operational modes of EMMA and MD established the EMMAgeo package. Both authors wrote the paper.

Competing interests. The authors declare that they have no conflict of interest.

Special issue statement. This article is part of the special issue "Connecting disciplines – Quaternary archives and geomorphological processes in a changing environment". It is a result of the First Central European Conference on Geomorphology and Quaternary Sciences, Gießen, Germany, 23–27 September 2018.

Acknowledgements. Thomas Hösel and Claudia Ziener prepared the example data set. Philip Schulte performed grain-size analysis using the Laser particle sizer at RWTH Aachen. Jan-Berend Stuut provided the data from the FORTRAN code of Weltje (1997), and Mitch D'Arcy provided language editing. Kai Hartmann and Andreas Borchers supported the initial development of EMMA and Kirsten Elger the DOI and landing page coordination. Many users of former versions of the MATLAB and R scripts greatly helped to improve EMMAgeo.

Financial support. The article processing charges for this open-access publication were covered by a Research Centre of the Helmholtz Association.

References

Aitchison, J.: The statistical analysis of compositional data, Chapham and Hall, London, New York, 1986.

Bagnold, R. A. and Barndorff-Nielsen, O.: The pattern of natural size distributions, Sedimentology, 27, 199–207, 1980.

Bartholdy, J., Christiansen, C., and Pedersen, J. B. T.: Comparing spatial grain-size trends inferred from textural parameters using percentile statistical parameters and those based on the log-hyperbolic method, Sedimentary Geology From Particle Size to Sediment Dynamics, 202, 436–452, 2007.

Bengtsson, H.: R.matlab: Read and Write MAT Files and Call MATLAB from Within R, available at: https://CRAN.R-project.org/package=R.matlab (last access: 10 May 2019), 2018.

Bernaards, C. A. and Jennrich, R. I.: Gradient Projection Algorithms and Software for Arbitrary Rotation Criteria in Factor Analysis, Educ. Psychol. Meas., 65, 676–696, 2005.

Blott, S. J. and Pye, K.: GRADISTAT: a grain size distribution and statistics package for the analysis of unconsolidated sediments, Earth Surf. Process. Landforms, 26, 1237–1248, https://doi.org/10.1002/esp.261, 2001.

Borchers, A., Dietze, E., Kuhn, G., Esper, O., Voigt, I., Hartmann, K., and Diekmann, B.: Holocene ice dynamics and bottom-water formation associated with Cape Darnley polynya activity recorded in Burton Basin, East Antarctica, Mar. Geophys. Res., 2015, 1–22, https://doi.org/10.1007/s11001-015-9254-z, 2015.

Buccianti, A., Mateu-Figueras, G., and Pawlowsky-Glahn, V.: Compositional Data Analysis in the Geosciences: From Theory to Practice, Geological Society of London, London, 212 pp., 2006.

Ciemer, C., Boers, N., Barbosa, H. M. J., Kurths, J., and Rammig, A.: Temporal evolution of the spatial covariability of rainfall in South America, Clim. Dynam., 51, 371–382, 2018.

David, C. H., Gil, Y., Duffy, C. J., Peckham, S. D., and Venayagamoorthy, S. K.: An introduction to the special issue on Geoscience Papers of the Future, Earth Space Sci., 3, 441–444, 2016.

Dietze, E., Hartmann, K., Diekmann, B., Ijmker, J., Lehmkuhl, F., Opitz, S., Stauch, G., Wünnemann, B., and Borchers, A.: An end-member algorithm for deciphering modern detrital processes from lake sediments of Lake Donggi Cona, NE Tibetan Plateau, China, Sediment. Geol., 243–244, 169–180, 2012.

Dietze, E., Wünnemann, B., Hartmann, K., Diekmann, B., Jin, H., Stauch, G., Yang, S., and Lehmkuhl, F.: Early to mid-Holocene lake high-stand sediments at Lake Donggi Cona, northeastern Tibetan Plateau, China, Quaternary Res., 79, 325–336, 2013.

Dietze, E., Maussion, F., Ahlborn, M., Diekmann, B., Hartmann, K., Henkel, K., Kasper, T., Lockot, G., Opitz, S., and Haberzettl, T.: Sediment transport processes across the Tibetan Plateau inferred from robust grain-size end members in lake sediments, Clim. Past, 10, 91–106, https://doi.org/10.5194/cp-10-91-2014, 2014.

Dietze, M. and Dietze, E.: EMMAgeo: End-Member Modelling of Grain-Size Data, available at: https://cran.r-project.org/web/packages/EMMAgeo/ (last access: 10 May 2019), 2016.

Dietze, M. and Dietze, E.: EMMAgeo – R package. V. 0.9.6, GFZ Data Services, https://doi.org/10.5880/GFZ.4.6.2019.002, 2019.

Dietze, M., Dietze, E., Lomax, J., Fuchs, M., Kleber, A., and Wells, S. G.: Environmental history recorded in aeolian deposits under stone pavements, Mojave Desert, USA, Quaternary Res., 85, 4–16, 2016.

Flemming, B. W.: The influence of grain-size analysis methods and sediment mixing on curve shapes and textural parameters: Implications for sediment trend analysis, Sedimentary Geology From Particle Size to Sediment Dynamics, 202, 425–435, 2007.

Folk, R. L. and Ward, W. C.: Brazos River bar [Texas]; a study in the significance of grain size parameters, J. Sediment. Res., 27, 3–26, 1957.

Friedman, G. M.: Distinction between dune, beach, and river sands from their textural characteristics, J. Sediment. Res., 31, 514–529, 1961.

Gan, S. Q. and Scholz, C. A.: Skew Normal Distribution Deconvolution of Grain-size Distribution and Its Application To 530 Samples from Lake Bosumtwi, Ghana, J. Sediment. Res., 87, 1214–1225, 2017.

Hartmann, D.: From reality to model: Operationalism and the value chain of particle-size analysis of natural sediments, Sedimentary Geology From Particle Size to Sediment Dynamics, 202, 383–401, 2007.

Heslop, D., von Dobeneck, T., and Höcker, M.: Using non-negative matrix factorization in the "unmixing" of diffuse reflectance spectra, Mar. Geol., 241, 63–78, 2007.

Hunter, D. R., Richards, D. S. P., and Rosenberger, J. L.: Nonparametric Statistics and Mixture Models, World Scientific, The Pennsylvania State University, 2011.

Klovan, J. E. and Imbrie, J.: An algorithm and Fortran-iv program for large-scale Q-mode factor analysis and calculation of factor scores, J. Int. Ass. Math. Geol., 3, 61–77, 1971.

Lindsay, B. G. and Lesperance, M. L.: A review of semiparametric mixture models, J. Stat. Plan. Infer., 47, 29–39, 1995.

Macumber, A. L., Patterson, R. T., Galloway, J. M., Falck, H., and Swindles, G. T.: Reconstruction of Holocene hydroclimatic variability in subarctic treeline lakes using lake sediment grain-size end-members, Holocene, 28, 845–857, 2018.

McGee, D., deMenocal, P. B., Winckler, G., Stuut, J. B. W., and Bradtmiller, L. I.: The magnitude, timing and abruptness of changes in North African dust deposition over the last 20 000 yr, Earth Planet. Sc. Lett., 371–372, 163–176, 2013.

Meszner, S., Kreutzer, S., Fuchs, M., and Faust, D.: Late Pleistocene landscape dynamics in Saxony, Germany: Paleoenvironmental reconstruction using loess-paleosol sequences, Quaternary Int., 296, 94–107, 2013.

Meyer, D., Dimitriadou, E., Hornik, K., Weingessel, A., and Leisch, F.: e1071: Misc Functions of the Department of Statistics, Probability Theory Group (Formerly: E1071), available at: https://CRAN.R-project.org/package=e1071 (last access: 10 May 2019), TU Wien, 2017.

Miesch, A. T.: Q-mode factor analysis of compositional data, Comput. Geosci., 1, 147–159, 1976.

Mullen, K. M. and van Stokkum, I. H. M.: nnls: The Lawson-Hanson algorithm for non-negative least squares (NNLS), available at: https://CRAN.R-project.org/package=nnls (last access: 10 May 2019), 2012.

Munafò, M. R., Nosek, B. A., Bishop, D. V. M., Button, K. S., Chambers, C. D., Percie du Sert, N., Simonsohn, U., Wagenmakers, E.-J., Ware, J. J., and Ioannidis, J. P. A.: A manifesto for reproducible science, Nature Human Behaviour, 1, 0021, Tulsa, Oklahoma, USA, 2017.

Paterson, G. A. and Heslop, D.: New methods for unmixing sediment grain size data, Geochem. Geophys. Geosyst., 16, 4494–4506, 2015.

Prins, M. A. and Weltje, G. J.: End-member modeling of siliciclastic grain-size distributions: The late Quaternary record of aeolian and fluvial sediment supply to the Arabian Sea and its paleoclimatic significance, in: SEPM Special Publication, edited by: Harbaugh, J., 62, Society for Sedimentary Geology, 1999.

Pye, K.: The nature, origin and accumulation of loess, Quaternary Sci. Rev., 14, 653–667, 1995.

R Core Team: R: A language and environment for statistical computing, R Foundation for Statistical Computing, Vienna, 2017.

Schillereff, D. N., Chiverrell, R. C., Macdonald, N., and Hooke, J. M.: Hydrological thresholds and basin control over paleoflood records in lakes, Geology, 44, 43–46, 2016.

Schulte, P., Dietze, M., and Dietze, E.: How well does end-member modelling analysis of grain size data work?, EGU General Assembly Conference Abstracts, 1903, 2014.

Seidel, M. and Hlawitschka, M.: An R-Based Function for Modeling of End Member Compositions, Math. Geosci., 47, 995–1007, 2015.

Strauss, J., Schirrmeister, L., Wetterich, S., Borchers, A., and Davydov, S. P.: Grain-size properties and organic-carbon stock of Yedoma Ice Complex permafrost from the Kolyma lowland, northeastern Siberia, Global Biogeochem. Cy., 26, 1–12, 2012.

Stuut, J.-B. W., Prins, M. A., Schneider, R. R., Weltje, G. J., Jansen, J. H. F., and Postma, G.: A 300-kyr record of aridity and wind strength in southwestern Africa: inferences from grain-size distributions of sediments on Walvis Ridge, SE Atlantic, Mar. Geol., 180, 221–233, 2002.

Sun, D., Bloemendal, J., Rea, D. K., Vandenberghe, J., Jiang, F., An, Z., and Su, R.: Grain-size distribution function of polymodal sediments in hydraulic and aeolian environments, and numerical partitioning of the sedimentary components, Sediment. Geol., 152, 263–277, 2002.

Tjallingii, R., Claussen, M., Stuut, J.-B. W., Fohlmeister, J., Jahn, A., Bickert, T., Lamy, F., and Rohl, U.: Coherent high- and low-latitude control of the northwest African hydrological balance, Nat. Geosci., 1, 670–675, 2008.

Toonen, W. H. J., Winkels, T. G., Cohen, K. M., Prins, M. A., and Middelkoop, H.: Lower Rhine historical flood magnitudes of the last 450 years reproduced from grain-size measurements of flood deposits using End Member Modelling, CATENA, 130, 69–81, 2015.

Vandenberghe, J.: Grain size of fine-grained windblown sediment: A powerful proxy for process identification, Earth-Sci. Rev., 121, 18–30, 2013.

Vandenberghe, J., Lu, H., Sun, D., van Huissteden, J., and Konert, M.: The late Miocene and Pliocene climate in East Asia as recorded by grain size and magnetic susceptibility of the Red Clay deposits (Chinese Loess Plateau), Palaeogeogr. Palaeocl., 204, 239–255, 2004.

Vandenberghe, J., Sun, Y., Wang, X., Abels, H. A., and Liu, X.: Grain-size characterization of reworked fine-grained aeolian deposits, Earth-Sci. Rev., 177, 43–52, 2018.

Van den Boogaart, K. G., Tolosana, R., and Bren, M.: compositions: Compositional Data Analysis, available at: https://CRAN.R-project.org/package=compositions (last access: 10 May 2019), 2014.

van Hateren, J. A., Prins, M. A., and van Balen, R. T.: On the genetically meaningful decomposition of grain-size distributions: A comparison of different end-member modelling algorithms, Sediment. Geol., 375, 49–71, 2018.

Varga, G., Újvári, G., and Kovács, J.: Interpretation of sedimentary (sub)populations extracted from grain size distributions of Central European loess-paleosol series, Quaternary Int., 502, 60–70, https://doi.org/10.1016/j.quaint.2017.09.021, 2019.

Visher, G. S.: Grain size distributions and depositional processes, J. Sediment. Res., 39, 1074–1106, 1969.

Vriend, M. and Prins, M. A.: Calibration of modelled mixing patterns in loess grain-size distributions: an example from the northeastern margin of the Tibetan Plateau, China, Sedimentology, 52, 1361–1374, 2005.

Weltje, G.: End-member modeling of compositional data: Numerical-statistical algorithms for solving the explicit mixing problem, Math. Geol., 29, 503–549, 1997.

Weltje, G. J. and Prins, M. A.: Muddled or mixed? Inferring palaeoclimate from size distributions of deep-sea clastics, Sediment. Geol., 162, 39–62, 2003.

Weltje, G. J. and Prins, M. A.: Genetically meaningful decomposition of grain-size distributions, Sediment. Geol., 202, 409–424, 2007.

Wündsch, M., Haberzettl, T., Kirsten, K. L., Kasper, T., Zabel, M., Dietze, E., Baade, J., Daut, G., Meschner, S., Meadows, M. E.,

and Mäusbacher, R.: Sea level and climate change at the southern Cape coast, South Africa, during the past 4.2 kyr, Palaeogeogr. Palaeocl., 446, 295–307, 2016.

Xiao, J., Chang, Z., Fan, J., Zhou, L., Zhai, D., Wen, R., and Qin, X.: The link between grain-size components and depositional processes in a modern clastic lake, Sedimentology, 59, 1050–1062, 2012.

Yu, S.-Y., Colman, S. M., and Li, L.: BEMMA: A Hierarchical Bayesian End-Member Modeling Analysis of Sediment Grain-Size Distributions, Math. Geosci., 2015, 1–19, https://doi.org/10.1007/s11004-015-9611-0, 2015.

Connecting disciplines – Quaternary archives and geomorphological processes in a changing environment (proceedings of the Central European Conference on Geomorphology and Quaternary Sciences)

ISSN 0424-7116